



HAL
open science

Glycine/GABA mixed inhibitory synapses studied with super-resolution microscopy : differential regulation of GlyRs and GABAARs by excitatory activity

Xiaojuan Yang

► **To cite this version:**

Xiaojuan Yang. Glycine/GABA mixed inhibitory synapses studied with super-resolution microscopy : differential regulation of GlyRs and GABAARs by excitatory activity. *Neurons and Cognition [q-bio.NC]*. Université Paris sciences et lettres; East China normal university (Shanghai), 2019. English. NNT : 2019PSLEE012 . tel-02351605

HAL Id: tel-02351605

<https://theses.hal.science/tel-02351605>

Submitted on 6 Nov 2019

HAL is a multi-disciplinary open access archive for the deposit and dissemination of scientific research documents, whether they are published or not. The documents may come from teaching and research institutions in France or abroad, or from public or private research centers.

L'archive ouverte pluridisciplinaire **HAL**, est destinée au dépôt et à la diffusion de documents scientifiques de niveau recherche, publiés ou non, émanant des établissements d'enseignement et de recherche français ou étrangers, des laboratoires publics ou privés.



THÈSE DE DOCTORAT
DE L'UNIVERSITÉ PSL

Préparée à [École normale supérieure à Paris]
Dans le cadre d'une cotutelle avec [East China Normal University]

**Microscopie super-résolutive aux synapses inhibitrices mixtes:
régulation différentielle des GlyRs et des GABA_ARs par l'activité
excitatrice**

Glycine/GABA mixed inhibitory synapses studied with super-resolution
microscopy: differential regulation of GlyRs and GABA_ARs by excitatory
activity

Soutenue par

Xiaojuan YANG

Le 10 / 09 / 2019

Ecole doctorale n° 158

**L'école doctorale Cerveau-
Cognition-Comportement**

Spécialité

Neurosciences

Composition du jury :

Enrica Maria, PETRINI PU, Italian Institute of Technology	<i>Président</i>
Lydia, DANGLLOT CR, Université Paris Diderot	<i>Rapporteur</i>
Andrea, BARBERIS DR, Italian Institute of Technology	<i>Rapporteur</i>
Erin, SCHUMAN DR, Max Planck Institute for Brain Research	<i>Examineur</i>
Mathieu, COPPEY CR, Institut Curie	<i>Examineur</i>
Huimin, WANG DR, East China Normal University	<i>CoDirecteur de thèse</i>
Christian, SPECHT CR, École normale supérieure à Paris	<i>Directeur de thèse</i>

Invited member

Antoine Triller

DR, Institut de biologie de l'ENS à Paris

Abstract

Single molecule localization microscopy (SMLM) bypasses the diffraction limit by recording spatially and temporally separated single molecule signals, achieving a resolution of ~10-40 nm. Numerous studies of excitatory synapses using SMLM have revealed a heterogeneous intra-synaptic organization of synaptic proteins. Synaptic proteins form sub-synaptic domains (SSDs), in which the molecule density is higher than in the adjacent areas. Furthermore, pre- and post-synaptic SSDs can align into a trans-synaptic nanocolumn, which is proposed to be a regulatory element for synaptic strength and plasticity at excitatory synapses.

At mixed inhibitory synapses, GlyRs and GABA_ARs co-exist within the same post-synaptic density (PSD). However, little is known about how the two types of receptors are organized within the PSD, and whether their spatial relationship plays a role in the regulation of the GABAergic/glycinergic co-transmission. The inhibitory scaffold protein gephyrin provides binding sites for both GlyRs and GABA_ARs. Gephyrin has been shown to form SSDs at GABAergic synapses. However, it is unclear whether gephyrin forms SSDs at mixed inhibitory synapses, and if so, what roles these subdomains hold. Also, it is still unresolved whether trans-synaptic nanocolumns exist at inhibitory synapses and how GlyRs and GABA_ARs are aligned with pre-synaptic vesicle release sites.

To answer these open questions, I have adopted a two-color dSTORM imaging approach. My experimental results showed that the fluorescent dyes used for labeling had a strong impact on the characterization of synaptic clusters in dSTORM images. Thus, I carefully studied the methodology of two-color dSTORM imaging of synaptic clusters and developed an imaging and analysis strategy. I mainly adopted H-watershed method for SSD segmentation and intensity correlation quotient (ICQ) for evaluating the spatial relationships of synaptic proteins.

With the established two-color dSTORM methodology, I examined the intra-synaptic organization of GlyRs, GABA_ARs, gephyrin and RIM1/2 at mixed inhibitory synapses in a pair-wise manner. All these synaptic components exhibited heterogeneous distributions and formed SSDs within the synapse. GlyRs

and GABA_ARs were not fully intermingled, but sometimes occupied different spaces at mixed inhibitory synapses. Moreover, pre-synaptic RIM1/2 SSDs were aligned with post-synaptic gephyrin SSDs into trans-synaptic nanocolumns.

I also examined the effect of network activity on the spatial relationships of GlyRs, GABA_ARs, gephyrin and RIM1/2. The spatial correlation between GlyRs, GABA_ARs and gephyrin at mixed inhibitory PSDs was increased when elevating the excitatory activity by 4-AP treatment. In addition, GlyRs, but not GABA_ARs, exhibited a higher spatial correlation with pre-synaptic RIM1/2 after 4-AP treatment. However, the SSD counts per synapse of these synaptic proteins were not changed by 4-AP treatment. Therefore, the spatial organization of GlyRs and GABA_ARs within the mixed inhibitory synapses appears to be differentially regulated by network activity. This study thus provides a new angle for understanding the mechanisms underlying GABAergic/glycinergic co-transmission.

Keywords

Mixed inhibitory synapses, GlyR, GABA_AR, gephyrin, RIM1/2, co-transmission, subsynaptic domain (SSD), trans-synaptic nanocolumn, single molecule localization microscopy (SMLM), direct stochastic optical reconstruction microscopy (dSTORM), multi-color dSTORM.

Résumé

La microscopie de localisation de molécule unique (SMLM) contourne la limite de diffraction en enregistrant des signaux de molécule unique séparés dans l'espace et dans le temps, atteignant une résolution de ~10-40 nm. De nombreuses études de synapses excitatrices utilisant la SMLM ont révélé une organisation intra-synaptique hétérogène des protéines synaptiques. Il est intéressant de noter que les protéines synaptiques forment des domaines sous-synaptiques (SSD), dans lesquels la densité moléculaire est plus élevée que dans les zones adjacentes. En outre, les SSD pré- et post-synaptiques peuvent s'aligner dans une nanocolonne trans-synaptique, qui est proposée comme un élément régulateur de la force et de la plasticité synaptique aux synapses excitatrices.

Aux synapses inhibitrices mixtes, les GlyRs et les GABA_ARs coexistent dans la même densité post-synaptique (PSD). Cependant, on sait peu de choses sur la façon dont les deux types de récepteurs sont organisés au sein de la PSD et si leur relation spatiale joue un rôle dans la régulation de la co-transmission GABAergique/glycinergique. La géphyrine, protéine inhibitrice d'échafaudage, fournit des sites de liaison pour les GlyRs et les GABA_ARs. Il a été démontré que la géphyrine forme des SSD aux synapses GABAergique. Cependant, il n'est pas clair si la géphyrine forme des SSD aux synapses inhibitrices mixtes et, dans l'affirmative, quels rôles ces sous-domaines jouent. De plus, on ne sait toujours pas s'il existe des nanocolonnes trans-synaptiques aux synapses inhibitrices et comment les GlyR et les GABA_AR sont alignés avec les sites de libération vésiculaire présynaptique.

Pour répondre à ces questions ouvertes, j'ai adopté une approche d'imagerie dSTORM bicolore. Mes résultats expérimentaux ont montré que les colorants fluorescents utilisés pour le marquage avaient un fort impact sur la caractérisation des amas synaptiques dans les images dSTORM. Ainsi, j'ai soigneusement étudié la méthodologie d'imagerie dSTORM bicolore des grappes synaptiques et j'ai développé une stratégie d'imagerie et d'analyse. J'ai principalement adopté la méthode H-Watershed pour la segmentation SSD et le quotient de corrélation d'intensité (ICQ) pour évaluer les relations spatiales des protéines synaptiques.

Avec la méthodologie bicolore dSTORM, j'ai examiné l'organisation intra-synaptique des GlyRs, GABA_ARs, géphyrine et RIM1/2 aux synapses inhibitrices mixtes. Toutes ces composantes synaptiques présentent des distributions hétérogènes et forment des SSDs à l'intérieur de la synapse. Les GlyR et les GABA_AR ne sont pas complètement mélangés, mais peuvent occuper des espaces différents aux synapses inhibitrices mixtes. De plus, les SSDs de RIM1/2 présynaptiques sont alignées avec les SSDs de géphyrine post-synaptique dans des nanocolonnes trans-synaptiques.

J'ai également examiné l'effet de l'activité du réseau sur les relations spatiales des GlyRs, GABA_ARs, géphyrine et RIM1/2. La corrélation spatiale entre les GlyRs, les GABA_ARs et la géphyrine au niveau des PSD inhibiteurs mixtes a été augmentée lorsque l'activité excitatrice était élevée par un traitement par 4-AP. De plus, les GlyRs, mais pas les GABA_ARs, présentaient une corrélation spatiale plus élevée avec la RIM1/2 présynaptique après un traitement par 4-AP. Cependant, le nombre de SSD par synapse de ces protéines synaptiques n'est pas modifié par le traitement par 4-AP. Par conséquent, l'organisation spatiale des GlyRs et des GABA_ARs dans les synapses inhibitrices mixtes semble être régulée différemment par les changements de l'activité du réseau. Cette étude offre donc un nouvel angle de compréhension des mécanismes sous-jacents à la co-transmission GABAergique/glycinergique.

Mots clés

Synapses inhibitrices mixtes, GlyR, GABA_AR, géphyrine, RIM1/2, co-transmission, domaine sous-synaptique (SSD), nanocolonne trans-synaptique, microscopie de localisation de molécule unique (SMLM), microscopie de reconstruction optique stochastique directe (dSTORM), dSTORM multi-couleur.

Table of Contents

Abstract	i
Résumé	iii
List of Figures	ix
List of Tables	xi
Abbreviations	xii
Acknowledgement	xiii
1 Introduction	1
1.1 GABAARs and GlyRs: the two main inhibitory neurotransmitter receptors.....	1
1.1.1 The subunit composition of GABAARs and GlyRs	1
1.1.2 The lateral diffusion of the receptors underlying inhibitory synaptic plasticity	4
1.1.3 The physiological functions of GABA _A Rs and GlyRs and their implications in	
neurological disorders	5
1.2 Gephyrin: a master regulator at inhibitory synapses	7
1.2.1 The structure of gephyrin complex and their dynamics	7
1.2.2 The roles of gephyrin in the regulation of synaptic GlyRs and GABA _A Rs.....	9
1.3 Glycinergic and GABAergic mixed inhibitory synapses	10
1.3.1 The evidence of GABA _A R/GlyR colocalization and GABA/glycine co-release ..	11
1.3.2 The synaptic control of GABA/glycine co-transmission	13
1.4 Heterogeneity of intra-synaptic organization revealed by super-resolution optical	
microscopy	15
1.4.1 Super-resolution optical microscopy and stochastic optical reconstruction	
microscopy (STORM).....	15
1.4.2 The challenges of applying two-color dSTORM to synapses	19
1.4.2.1 Challenges posed by technical limitations	19
1.4.2.2 Challenges posed by the characters of synapses.....	21
1.4.3 Intra-synaptic heterogeneity and sub-synaptic domains as regulators of	
synaptic functions	23
1.5 Functional implications of intra-synaptic heterogeneity and SSDs in mixed	
inhibitory synapses	26
1.6 Aims of this study.....	27
2 Materials and methods	28
2.1 Primary spinal cord neuron culture	28
2.2 Conjugation of Cy3B dye to secondary antibodies	29
2.3 Pharmacological treatment and immunocytochemistry	30

2.4 Calcium imaging and data analysis.....	31
2.5 Conventional microscopy and data analysis	32
2.6 Two-color dSTORM imaging and analysis	32
2.6.1 Microscope setup.....	32
2.6.2 Sequential two-color dSTORM imaging	33
2.6.3 dSTORM image processing and data analysis	34
2.7 Statistical analysis.....	35
3 Results	36
3.1 Methodological evaluation: two-color dSTORM of synapses	36
3.1.1 An optimized sequential two-color dSTORM imaging protocol.....	36
3.1.1.1 Fluorescent beads as fiducial marker.....	38
3.1.1.2 Performance evaluation of chosen dyes.....	40
3.1.2 Two-color dSTORM data analysis protocol	42
3.1.2.1 Image-based data analysis workflow	43
3.1.2.2 Verification of the different intensity correlation approaches with an exemplary dataset.....	47
3.1.2.3 SRclusters: coordinates-based data analysis tool	51
3.1.3 The impact of low protein copy number on the imaging data	53
3.1.4 Dyes have a strong impact on the detected synaptic structure characterization	55
3.1.4.1 The impact of dyes on dSTORM synaptic clusters explained by their blinking profiles.....	55
3.1.4.2 The impact of reversing the dyes on the synaptic clusters in dSTORM images	60
3.2 The study of mixed inhibitory synapses with two-color dSTORM	64
3.2.1 Post-synaptic proteins are heterogeneously organized and exhibit SSDs at mixed inhibitory synapses in spinal cord neurons	64
3.2.1.1 GlyR and gephyrin are heterogeneously distributed at inhibitory PSDs... 64	
3.2.1.2 GABA _A Rs and GlyRs can occupy different spaces at mixed inhibitory PSDs	65
3.2.2 The copy numbers of synaptic GABA _A Rs and GlyRs are differentially regulated by neuronal activity.....	69
3.2.2.1 Calcium imaging showed the effect of TTX and 4-AP on the network activity of cultured spinal cord neurons.....	70
3.2.2.2 GABA _A Rs and gephyrin, but not GlyRs immuno-reactivity is regulated by changes in network activity.....	70

3.2.2.3 Gephyrin phosphorylation level but not the total molecular amount was reduced by increased neuronal activity.....	72
3.2.3 Intra-synaptic re-organization of GlyRs, GABA _A Rs and p-gephyrin during neuronal activity	76
3.2.3.1 The spatial association of synaptic GlyRs and p-gephyrin was increased after 4-AP treatment.....	76
3.2.3.2 GABA _A Rs exhibit increased spatial association with both p-gephyrin and GlyRs during increased neuronal activity.....	83
3.2.3.3 Summary of intra-synaptic re-organization at mixed inhibitory PSDs during neuronal activity.....	88
3.2.4 RIM1/2 forms pre-synaptic SSDs that are aligned with post-synaptic p-gephyrin SSDs.....	89
3.2.5 GlyRs and GABA _A Rs are differentially re-aligned to pre-synaptic vesicle release sites during increased neuronal activity	90
3.2.5.1 Pre-synaptic RIM1/2 content is not changed by increased neuronal activity with 4-AP	94
3.2.5.2 Increased spatial association of GlyRs but not GABA _A Rs with RIM1/2 after increasing neuronal activity	94
3.2.6 Summary of the results on mixed inhibitory synapses.....	97
4 Discussion.....	102
4.1 A critical review of sub-synaptic domains (SSDs)	102
4.1.1 What is a subsynaptic domain?	102
4.1.2 How to detect SSDs with SMLM	107
4.2 The intra-synaptic spatial organization of mixed inhibitory synapses and its functional implications.....	110
4.2.1 The intra-synaptic organization of GlyRs and GABA _A Rs at mixed PSDs are differentially regulated	110
4.2.1.1 The synaptic accumulation of GlyRs and GABA _A Rs at mixed PSDs are differentially regulated by excitatory activity.....	111
4.2.1.2 Increased intra-synaptic spatial correlation of GlyRs, GABA _A Rs and gephyrin at mixed PSDs by excitatory activity	112
4.2.2 Trans-synaptic nanocolumns at inhibitory synapses and potential roles of adhesion proteins	114
4.2.3 Differential trans-synaptic alignment of GlyRs and GABA _A Rs to pre-synaptic vesicle releasing sites.....	116
4.3 Limitations in the current study and alternative approaches	117
4.4 Future directions and perspectives	119
References	121

Appendix Table 1. Antibodies	143
Appendix Table 2. List of two-color dSTORM dataset	145
Appendix 3: SRclusters protocol	146
Appendix 4. Two-color 3D dSTORM	151
Appendix 5: Yang and Specht 2020	155
Appendix 6. Yang and Specht 2019	205

List of Figures

Figure 1. The basic structure of GABAARs and GlyRs	2
Figure 2. Gephyrin as the scaffold protein at inhibitory PSDs	8
Figure 3. Co-release and co-transmission of glycine and GABA at mixed inhibitory synapses	12
Figure 4. The basic principles of stochastic optical reconstruction microscopy (STORM).....	17
Figure 5. The challenges of applying SMLM to synapses	20
Figure 6. Sub-synaptic domains (SSDs) as regulators of synaptic function	25
Figure 7. Sequential two-color dSTORM imaging of synaptic proteins	37
Figure 8. Drift correction with beads as fiducial markers	39
Figure 9. Blinking profiles of the dyes conjugated to secondary antibodies.....	41
Figure 10. Image-based data analysis workflow	44
Figure 11. Verification of the different intensity correlation approaches with an exemplary dataset	48
Figure 12. SRclusters: a coordinates-based data analysis tool	52
Figure 13. The effect of low copy numbers of synaptic proteins on the cluster integrity in dSTORM images	54
Figure 14. The impact of dyes on dSTORM synaptic clusters explained by their blinking profiles	56
Figure 15. Strong impact of fluorescent dyes on the reconstructed synaptic clusters in dSTORM	58
Figure 16. Image-based analysis of dye reversal experiments of gephyrin in two-color dSTORM	61
Figure 17. Coordinate-based analysis of dye reversal experiments on gephyrin using SRclusters	63
Figure 18. The heterogeneous distribution of GlyR and gephyrin at the inhibitory PSDs in spinal cord neurons	66
Figure 19. The heterogeneous distribution of GABAARs and GlyRs at mixed inhibitory PSDs and their different spatial organization	68
Figure 20. The effect of TTX and 4-AP on neuronal activity in cultured spinal cord neurons demonstrated by calcium imaging	71
Figure 21. Reduced synaptic accumulation of GABAARs and gephyrin, but not GlyRs by 4-AP treatment	73

Figure 22. Reduced gephyrin phosphorylation level but not the total molecular amount at the inhibitory PSD by 4-AP treatment	75
Figure 23. Increased spatial correlation of p-gephyrin and GlyRs by 4-AP treatment	78
Figure 24. Increased spatial correlation of p-gephyrin and GlyRs by 4-AP treatment confirmed by reversed color experiments	80
Figure 25. Increased spatial correlation of GABAARs and p-gephyrin by 4-AP treatment, but not their SSD numbers	84
Figure 26. Increased spatial correlation of GABAARs and GlyRs by 4-AP treatment	86
Figure 27. Reconstructed two-color dSTORM images showing the alignment of RIM1/2 and p-gephyrin	91
Figure 28. The alignment of post-synaptic gephyrin SSDs with pre-synaptic RIM1/2 SSDs at inhibitory synapses	92
Figure 29. No change in the synaptic accumulation of RIM1/2 at mixed inhibitory synapses by 4-AP treatment	95
Figure 30. Increased spatial correlation of GlyRs and RIM1/2 by 4-AP treatment	96
Figure 31. No change in the spatial correlation of GABAARs and RIM1/2 by 4-AP treatment	98
Figure 32. The spatial correlation of synaptic proteins measured by ICQ	100

List of Tables

Table 1. Summary of the changes in synaptic molecule amount at mixed synapses with altered neuronal activity	101
Table 2. Summary of the changes in the spatial correlation between protein pairs with altered neuronal activity, measured by ICQ	101
Table 3. Size and protein copy numbers of SSDs and PSDs obtained with different experimental techniques	105

Abbreviations

dSTORM	Direct stochastic optical reconstruction microscopy
EAAT-3	excitatory amino acid transporter 3
GABA	Gamma aminobutyric acid
GABA _A Rs	GABA subtype A receptors
GAD	Glutamic acid decarboxylase
GAT-1	GABA transporter 1
GlyRs	Glycine receptors
GlyT2	Glycine transporter 2
KCC2	Potassium-chloride co-transporter 2
mIPSC	Miniature inhibitory post-synaptic current
Moco	Molybdenum cofactor
PAG	Phosphate-activated glutaminase
PALM	Photo-activated localization microscopy
pGLICs	Cys-loop ligand-gated ion channels
PSD	Post-synaptic density
PTMs	Post-translational modifications
SIM	Structured illumination microscopy
SMLM	Single molecule localization microscopy
SNAT	Sodium-coupled neutral amino acid transporter
SSD	Subsynaptic domain
STED	Stimulated emission depletion
TIRF	Total internal reflection fluorescence
TTX	Tetrodotoxin
uPAINT	Universal point accumulation imaging in nanoscale topography
VGAT	Vesicular GABA transporter (also known as VIAAT)
VIAAT	Vesicular inhibitory amino acid transporter
4-AP	4-aminopyridine

Acknowledgement

I would like to express my deep gratitude to Antoine Triller, for accepting me in this laboratory to pursue my PhD, for being a great mentor for my research, and for being very kind with me.

I own same gratitude to Christian Specht, for him always being very patient, encouraging and kind with me, for his generous helps and valuable advices.

My many thanks to Huimin Wang, who has been my supervisor since my bachelor's study. I am very grateful for her support over these years.

I would also like to acknowledge the help provided by Felipe Delestro Matos and Auguste Genovesio for developing the program SRclusters.

My appreciation is extended to the China Scholarship Council (CSC) for the financial support, as well as to the Programme of Sino-French Education for Research (PRoSFER) for the great opportunity of joint-education during my master study and PhD study.

My grateful thanks are also extended to my wonderful colleagues (friends), who have always been very supportive and encouraging. Thank you all for your help and your friendship! Special thanks to Valentin Lepetz for his help with Fiji and Icy software, and to Pablo Serna for his valuable discussions on statistics.

I would also like to express my gratitude to the staff from the Imaging Facility and Animal Facility at IBENS. My many thanks to Xavier Marques and Astou Tangara for their help with the microscopy, and to Sabrina Colasse for her help with the cell culture.

My great tributes to the rodents and their sacrifices!

Finally, I would like to thank my dear family and friends. I wish them health and joys.

Chapter 1

1 Introduction

In this chapter, I first introduced the two main inhibitory neurotransmitter receptors in the central nervous system, gamma aminobutyric acid (GABA) subtype A receptors (GABA_ARs) and glycine receptors (GlyRs). Their main scaffold protein at the inhibitory post-synaptic density (PSD), gephyrin, was also introduced. Then, I focused on the evidence for GABA/glycine co-release and GABA_AR/GlyR co-existence at mixed inhibitory synapses. The molecular mechanisms of GABA/glycine co-transmission and its implications in neuronal function were also discussed.

In the second part of the introduction, I introduced super-resolution optical microscopy, specifically single molecule localization microscopy (SMLM). In particular, I discussed the challenges in the application of SMLM to synaptic structures, which are imposed by both the inherent limitations of SMLM and the intrinsic properties of synapses. Despite of these limitations and pitfalls, detailed insights into the structures of small compartments such as synapses have been achieved. Therefore, I summarized the current studies on the intra-synaptic organization of synaptic proteins (e.g. subsynaptic domains, also referred to as SSDs), and talked about their potential roles in regulating synaptic plasticity.

Finally, based on the available evidence, I discussed the possible existence of SSDs at mixed inhibitory synapses, and their potential functional implications. This chapter closes with the aims of this study.

1.1 GABA_ARs and GlyRs: the two main inhibitory neurotransmitter receptors

1.1.1 The subunit composition of GABA_ARs and GlyRs

GABA_ARs and GlyRs belong to the superfamily of Cys-loop ligand-gated ion channels (pGLICs) (Kasaragod and Schindelin, 2018; Moss and Smart, 2001). Their subunits have a characteristic structure, which is composed of an extracellular N-terminus, four transmembrane domains (TM1-4) and a short extracellular C-terminus (Figure 1.A).

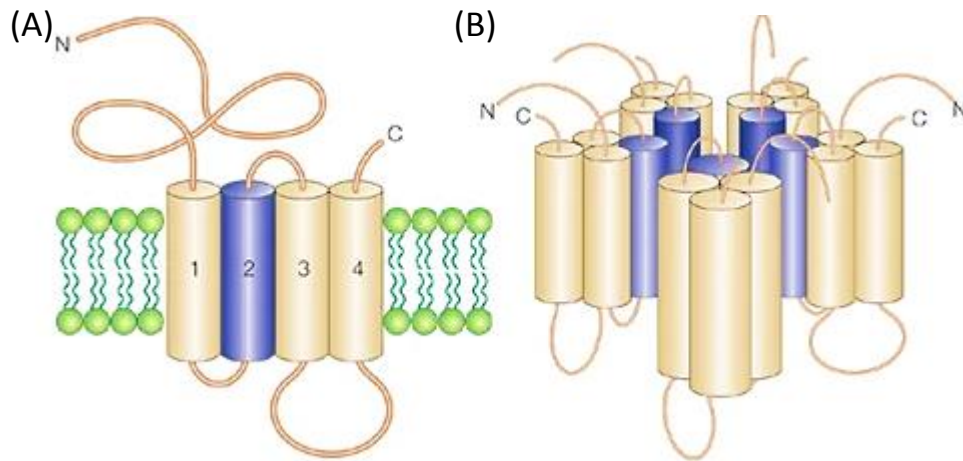


Figure 1. The basic structure of GABA_ARs and GlyRs.

(A) Each subunit of GABA_ARs and GlyRs has the characteristic structure of the Cys-loop ligand-gated ion channel superfamily. It starts with an extracellular N-terminus, followed by four transmembrane domains (TM1-4) and ends with a short extracellular C-terminus. A long intracellular loop is formed between TM3 and TM4. (B) The functional receptor complex consists of five subunits, and TM2 is known to form the ion channel in the middle. From Moss and Smart 2001.

A large intracellular loop is formed between TM3 and TM4. Functional GABA_ARs and GlyRs are pentamers. The five TM2 subunits facing the center form the lining of the ion channel, which selectively allows the passage of chloride ions (Figure 1.B). The influx of negatively charged chloride ions leads to a reduction of membrane potential, thus counteracting the effect of depolarizing (excitatory) currents.

GABA_ARs have a large variety of subunits. Nineteen subunits of eight different types have been identified, including α 1-6, β 1-3, γ 1-3, δ , ϵ , θ , π , and ρ 1-3. GABA_ARs are mainly heteropentamers, consisting of two α (α 1–6), two β (β 1–3) and either one γ (γ 1–3) or one δ subunit (Fritschy et al., 2012; Olsen and Seighart, 2008; Sigel and Steinmann, 2012). The GABA binding sites are located at the interface of α and β subunits. Therefore, GABA_AR pentamers encompass two GABA binding sites. The most common subunit composition in the mammalian brain is α 1 β 2 γ 2, followed by α 2 β 3 γ 2 and α 3 β 3 γ 2 (Knoflach et al., 2016; Nutt 2006). The synaptic clustering of GABA_ARs is dependent on the direct interaction of GABA_AR α 1-3 subunits and β 2-3 subunits with gephyrin, the main inhibitory scaffold protein (Kowalczyk et al., 2013; H. M. Maric et al., 2014; H. Maric, Mukherjee, Tretter, Moss, & Schindelin, 2011; G. Meyer, Kirsch, Betz, & Langosch, 1995; Mukherjee et al., 2011; Tretter et al., 2008, 2011, 2012). Moreover, another study showed that GABA_AR α 5 subunits also localize at synaptic sites through direct interaction with gephyrin (Brady & Jacob, 2015). GABA_AR γ 2 subunits do not bind gephyrin directly, but they are essential for the synaptic clustering of GABA_AR (Essrich et al., 1998). Recent studies have shown that γ 2-containing GABA_ARs cluster at inhibitory synapses through a gephyrin-independent mechanism. More specifically, GABA_AR γ 2 subunits interact with neuroligin-2 via GABA_AR regulatory Lhfp1 (GARLH) (Davenport et al., 2017; Heller et al., 2012; Yamasaki et al., 2017). While the majority of γ 2 subunits localize at the synaptic sites, they are also found at extra-synaptic sites, as well as α 1-2 and β 3 subunits (Kasugai et al., 2010). In contrast, δ subunit-containing GABA_ARs are believed to be exclusively located at extra-synaptic sites. These synaptic and extra-synaptic receptor populations produce two types of currents: phasic and tonic. Presynaptic release of GABA first activates synaptic receptors, inducing fast and transient (phasic) currents. The extracellular, diffuse GABA can

then activate extra-synaptic receptors, producing persistent (tonic) inhibitory currents.

GlyRs have relatively simple structure and composition. Only five subunits have been identified, including four α subunits (α 1-4) and one β subunit. The GlyR heteropentamers consists of α and β subunit, of which the stoichiometry is proposed to be either $2\alpha:3\beta$ or $3\alpha:2\beta$ (Burzomato et al. 2003; Durisic et al. 2012; Grudzinska et al. 2005; Langosch et al., 1988; Patrizio et al. 2017; Yang et al. 2012). GlyR β subunit has a strong affinity for the scaffold protein gephyrin, but none of the four α subunits directly binds to gephyrin. The β subunit therefore underlies the synaptic location of GlyRs, by its strong binding to the gephyrin scaffold (Kim et al., 2006). GlyRs can also form homopentamers with only α subunits, which localize at extra-synaptic sites and mediate tonic current (Dutertre et al., 2012; Legendre 2001; Lynch 2004).

1.1.2 The lateral diffusion of the receptors underlying inhibitory synaptic plasticity

Single Quantum-Dot tracking of GlyRs at the neuronal plasma membrane revealed that synaptic and extra-synaptic receptors are not stationary but undergo lateral diffusion in the membrane with different dynamics (Dahan et al., 2003). Lateral diffusion also leads to the translocation of the receptors between extra-synaptic and synaptic sites. Lateral diffusion is powered by both thermal Brownian diffusion and reversible trapping through receptor-scaffold interactions (Choquet and Triller 2013; Salvatico et al, 2015). At synaptic sites, the steric hindrance in the crowded environment and trapping by interacting with scaffold proteins can lower the synaptic receptor mobility, compared to extra-synaptic receptors (Li et al., 2016; Renner et al., 2012). Given that there is a substantial amount of extra-synaptic receptors (Kasugai et al., 2010), the lateral diffusion of membrane receptors provides a mechanism for the regulation of synaptic receptor content and synaptic plasticity, in addition to endocytosis and exocytosis (Gerrow and Triller, 2010; Triller and Choquet, 2008). It has been proposed that the fast trafficking of membrane receptors by lateral diffusion can replace the desensitized receptors at synaptic sites and thus participate in the high frequency synaptic activity, although this concept is still debated (Choquet, 2010; Delgado & Selvin,

2018). Nevertheless, the study of receptor dynamics has provided new ideas about synaptic plasticity (Dumoulin et al., 2010; Renner et al., 2008).

In hippocampal neurons, increased excitatory activity by several different pharmacological treatments resulted in larger diffusion coefficient of GABA_AR γ 2 subunits at both synaptic and extra-synaptic sites (Bannai et al., 2009). In addition, the mobility of synaptic GABA_ARs can be modulated by their agonists, antagonists and allosteric modulators. For instance, the GABA_AR agonist muscimol increases the diffusion coefficient of GABA_AR α 1, α 2, α 5 and γ 2 subunits, while the positive allosteric modulator diazepam abolishes the effect of muscimol and reduces the GABA_AR diffusion coefficient (Gouzer et al., 2014). During sustained neuronal activity by 4-AP treatment, diazepam reduced the lateral diffusion and stabilized GABA_ARs at synapses (Lévi et al., 2015). It is noteworthy that different regulation of GABA_AR subunit mobility was reported in these studies. This was also shown in a recent study revealing that the diffusion properties of GABA_ARs are dependent on the subunit composition (Hannan et al., 2019). Moreover, excitatory synaptic activity has been shown to modulate the diffusion dynamics of GlyRs. Reduced excitatory activity increased the diffusion coefficient of GlyR α 1 subunits, but not GABA_AR γ 2 subunits in spinal cord neurons (Lévi et al., 2008). Furthermore, increased microglia activity reduced the diffusion coefficient of GlyR α 1 subunits, but did not affect GABA_AR γ 2 subunits (Cantaut-Belarif et al., 2017). Taken together, the diffusion dynamics of GABA_ARs and GlyRs are differently regulated in spinal cord neurons, where both types of receptors can co-exist at the same inhibitory PSDs (see section 1.3). These data suggest that the lateral diffusion of inhibitory synaptic receptors indeed participates in the regulation of inhibitory neurotransmission.

1.1.3 The physiological functions of GABA_ARs and GlyRs and their implications in neurological disorders

During development, the intracellular chloride ion level is elevated in immature neurons. Therefore, the opening of the ion channels of GABA_ARs and GlyRs leads to chloride efflux. This causes depolarization of the neurons and increases the neuronal excitability (reviewed in Bowery and Smart 2006; Dutertre et al. 2012; Legendre 2001; Spitzer 2010). During the second postnatal week, a

transition from depolarizing to hyperpolarizing occurs. This is due to the increased expression of the potassium-chloride co-transporter (KCC2), which pumps chloride out of the cytosol (Kaila et al., 2014). In mature neurons, the activation of GABA_ARs and GlyRs thus causes chloride ion influx and therefore hyperpolarization of the membrane potential. The membrane hyperpolarization reduces the excitability of the neurons, thus inducing neuronal inhibition.

A balanced excitation and inhibition in the neuronal circuits is important for the brain function, and its disruption may underlie various neurological disorders. For example, an imbalance of excitation and inhibition is a shared pathophysiological mechanism for autism spectrum disorders and schizophrenia (reviewed in Gao and Penzes 2015; Nelson and Valakh 2015). Disrupted inhibitory control via GABAergic neurotransmission plays important roles in these pathologies (reviewed in Pizzarelli and Cherubini 2011; Selten et al, 2018). Moreover, the reduction in GABAergic neurotransmission is also a key feature of epilepsy, in addition to an elevated glutamatergic activity (reviewed in Bonansco and Fuenzalida 2016; Fukata and Fukata 2017; Treiman 2001; Wong 2010). The reduction in GABAergic inhibition leads to abnormally high neuronal activity, thus seizures. Promoting GABAergic inhibition, such as by benzodiazepines that are positive allosteric modulators of GABA_ARs can suppress seizures. GABA_ARs have been extremely important therapeutic targets for these neurological diseases.

GlyRs are mainly expressed in the hindbrain and spinal cord. They are also implicated in numerous neurological disorders involving the motor control and sensory information processing. For example, several missense mutations in the GlyR α 1 subunit gene underlie human hyperekplexia, also known as startle syndrome or stiff baby syndrome (Legendre, 2001; Lynch, 2004; Schaefer et al., 2018). Hyperekplexia is characterized by exaggerated startle response to mild stimuli and muscle rigidity. Moreover, the GlyR α 3 subunits has been implicated in the inflammatory pain sensation in the spinal cord dorsal horn (Betz & Laube, 2006; Harvey & Yee, 2013). GlyR α 3 knock out animals not only had lower glycinergic neurotransmission in response to inflammatory signals, but also reduced pain sensation (Harvey et al., 2004). So far, GlyRs are not as well investigated as GABA_ARs as therapeutic targets.

1.2 Gephyrin: a master regulator at inhibitory synapses

Gephyrin is expressed in almost all organisms, across bacteria, plants and animals. In mammals, it is detected in various non-neuronal tissues, including liver, heart, stomach and so on (Nawrotzki et al., 2012). Gephyrin is a moonlighting protein as it has multiple functions in the non-neuronal organs and the central nervous system. In non-neuronal cells, gephyrin is responsible for the last step of molybdenum cofactor (Moco) synthesis (Schwarz et al., 2009). Recently, gephyrin was also implicated in the regeneration of pancreatic β cell from α cells induced by the antimalarial drug artemisinin (Li et al., 2017). Though gephyrin is critical in non-neuronal cells, I will not further discuss this topic. Instead, I will focus on its roles in the central nervous system, where gephyrin is a key regulator at inhibitory synapses.

1.2.1 The structure of gephyrin complex and their dynamics

Gephyrin molecules are composed of three domains, the N-terminal G-domain, a linker (C-domain), and the C-terminal E-domain (Figure 2.A). Gephyrin is subject to many different types of post-translation modifications (PTMs), including phosphorylation, palmitoylation, SUMOylation, acetylation and nitrosylation. Among all the PTMs, the identified phosphorylation sites are almost exclusively located in the C-domain, including the prominent phosphorylation site at the serine amino acid residue at the position 270 (S270). The binding of the monoclonal antibody mAb7a is dependent on S270 phosphorylation (Kuhse et al., 2012). Moreover, gephyrin undergoes alternative splicing that controls its folding, receptor binding and synaptic clustering (Herweg & Schwarz, 2012). The splice-specific control of gephyrin clustering is thought to act through conformational changes in the C-domain.

Biochemical studies have shown that gephyrin molecules can form stable trimers through their G-domain interaction, and that weak E-domain interactions can also induce dimerization (Saiyed et al., 2007; Sola et al., 2004). Therefore, it has been proposed that gephyrin molecules form a hexagonal lattice under the post-synaptic membrane (Kneussel & Betz, 2000a, 2000b).

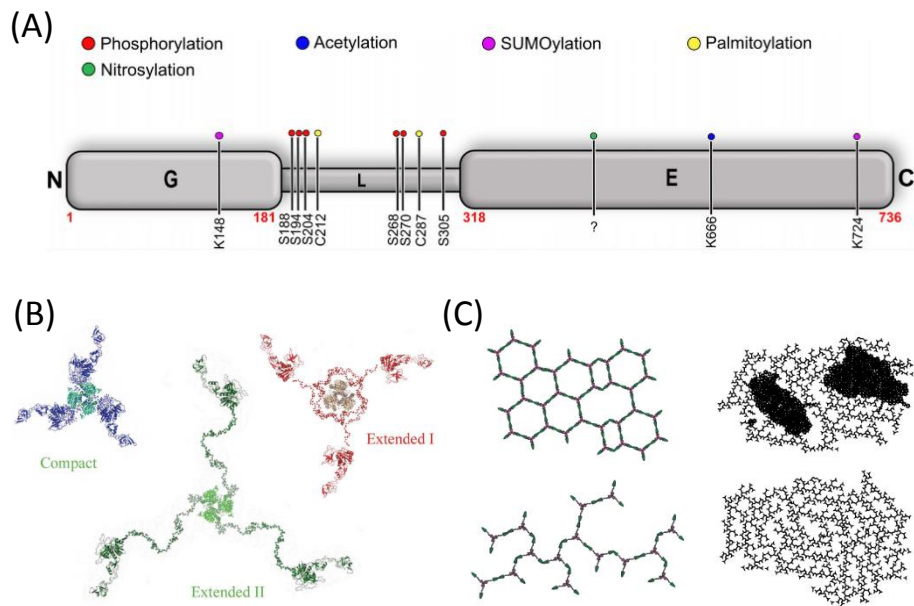


Figure 2. Gephyrin as the scaffold protein at inhibitory PSDs.

(A) The structure of gephyrin consists of an N-terminal G-domain, a linker domain (L, also known as C-domain) and a C-terminal E-domain. Gephyrin is subject to different types of post-translational modifications at different sites, such as phosphorylation, acetylation, palmitoylation, SUMOylation, nitrosylation. Most identified phosphorylation sites locate to the linker domain. From Kasaragod and Schindelin 2018. (B) Gephyrin forms stable trimers through the G-domain trimerization. The trimers can exhibit different compactness due to the different extension status of their linker domains. From Sander et al., 2013. (C) The stable gephyrin trimers are thought to assemble sub-membranous lattice with distinct compactness (left). It has been recently reported that gephyrin clusters can form subdomains that contain higher molecule density than the neighboring regions (right). From Groeneweg et al., 2018.

This hypothesis is consistent with the observation of a confined gephyrin distribution in a thin layer in electron microscopy (Triller et al., 1985). Structural analysis of gephyrin revealed that the trimers can have different compactness by the different extension status of the C-domain (Figure 2.B). This gives room to the possibility that synaptic gephyrin can be distributed heterogeneously in the planar lattice (Figure 2.C). Indeed, super-resolution optical imaging revealed the heterogeneous distribution of gephyrin molecules at the inhibitory PSDs (Pennacchietti et al., 2017a).

The fluorescence recovery after photobleaching (FRAP) of live cells has revealed the dynamics of synaptic scaffolds (reviewed in Specht and Triller 2008). FRAP imaging has shown that excitatory scaffold proteins such as PSD-95, GKAP and Shank are unstable at the synapses and have different turnover rates (Kuriu et al., 2006). Moreover, the dendritic spines undergo morphological changes regulated by actin skeleton in a calcium-dependent manner (reviewed in Oertner and Matus 2005). In addition, the spine head, PSD and pre-synaptic bouton exhibit correlated enlargement induced by two-photon glutamate uncaging (Meyer et al., 2014). Similarly, inhibitory synaptic scaffolds also undergo dynamic morphological changes. Venus tagged gephyrin clusters exhibit rapid lateral motion along the dendritic shafts on the time scale of seconds, and this movement is calcium dependent and controlled by the cytoskeleton (Hanus et al., 2006). Interestingly, YFP-tagged gephyrin clusters show fusing and splitting behavior that are resulted from their lateral movement on a time scale of hours (Dobie and Craig, 2011). Importantly, the lateral movement of gephyrin clusters is closely correlated with the pre-synaptic bouton marked by vesicular GABA transporter (VGAT) labeling (Dobie and Craig 2011; Kuriu et al., 2012). In other words, gephyrin scaffolds are not stationary, but mobile entities on the dendritic shaft. Recent super-resolution optical imaging further revealed the continuous morphological changes within gephyrin clusters (Rodriguez et al., 2017; Specht et al. 2013), which will be discussed in detail later.

1.2.2 The roles of gephyrin in the regulation of synaptic GlyRs and GABA_ARs

Gephyrin has been shown to play an important role in the regulation of GlyRs and GABA_ARs (reviewed in Alvarez 2017; Groeneweg et al. 2018; Kasaragod and

Schindelin 2018; Tyagarajan and Fritschy 2014). The phosphorylation, nitrosylation and palmitoylation of gephyrin has been implicated in the synaptic re-organization and plasticity of GABAergic synapses (Dejanovic et al. 2014; Dejanovic and Schwarz 2014; Zacchi et al., 2014). Gephyrin has a strong binding affinity for GlyR β subunits, but does not directly interact with GlyR α subunits (Kim et al., 2006). As a scaffold protein, gephyrin provides common binding sites for GlyR β subunits and GABA_AR α 1-3 and β 2-3 subunits, with lower affinity for the GABA_AR subunits (Kowalczyk et al., 2013; Maric et al., 2014; Maric et al., 2011; Meyer et al., 1995; Mukherjee et al., 2011; Tretter et al., 2008, 2011). The direct binding of receptors with gephyrin is important for their synaptic clustering and is dependent on the oligomerization of gephyrin (Calamai et al., 2009; Mukherjee et al., 2011). Moreover, the receptor binding pocket of gephyrin is in close proximity with the E-domain dimerization motif (Grünewald et al., 2018). Thus receptor binding may also contribute to the gephyrin clustering at synaptic sites.

1.3 Glycinergic and GABAergic mixed inhibitory synapses

The co-transmission of multiple neurotransmitters from pre-synaptic neurons is a common phenomenon in the mammalian central nervous system (reviewed in Granger et al., 2017; Tritsch et al., 2016; Vaaga et al., 2014). The co-release of GABA with other neurotransmitters such as glycine, glutamate and dopamine, as well as the cross-talk of GABA_ARs with the corresponding receptors, is likely to have a role in fine-tuning of synaptic transmission and plasticity (reviewed in Shrivastava et al., 2011; Tritsch et al. 2016). The disruption of the balanced co-transmission may underlie neurological disorders. For instance, the GABA/glutamate co-release has been implicated in animal models of depression as well as cocaine withdrawal (Meyer et al., 2016; Shabel et al., 2014), and the co-transmission of GABA/dopamine in the olfactory bulb might be modulated in Parkinson disease (Doty, 2012; Ross et al., 2008). However, the implications of co-transmission in neurological diseases are so far still poorly described and require further investigation.

In the context of my study, I am particularly interested in the co-release of glycine and GABA, which is a particular case of co-transmission. In this section, I

particularly introduced the evidence of GABA/glycine co-release and GABA_AR/GlyR co-existence at the same synapses, which are referred to as mixed inhibitory synapses. I also discussed about our current knowledge of the mechanisms underlying the regulation of mixed inhibitory synapses.

1.3.1 The evidence of GABA_AR/GlyR colocalization and GABA/glycine co-release

GABA and glycine are the two main inhibitory neurotransmitters mediating fast inhibition in the central nervous system (see review Bowery and Smart 2006). It was first described in spinal cord neurons that glycine and GABA are co-released from the same pre-synaptic terminal, and that their respective receptors, GlyRs and GABA_ARs, co-exist at the same post-synaptic density (Figure 3.A; Bohlhalter et al., 1994; Lévi et al. 1999; Mitchell et al., 1993; Todd et al. 1996; Triller et al., 1987). Here, I refer to these GABAergic and glycinergic synapses as mixed inhibitory synapses.

Numerous subsequent studies have investigated the GABA/glycine co-release in various regions in the central nervous system, including the auditory network (Fischl and Burger 2014; Lim et al., 2000; Lu et al., 2007; Moore and Trussell 2017; Nabekura et al. 2004; Nerlich et al. 2014), respiratory network (Rahman et al., 2013), brain stem motor nucleus (Muller et al., 2006; O'Brien and Berger, 2001; Russier et al., 2002), cerebellum (Dugué et al. 2005; Dumoulin et al., 2001; Rousseau et al. 2012), and even in a small population of hippocampal neurons (Lévi et al., 2004). The prevalence of the GABA/glycine co-transmission in the hindbrain and spinal cord emphasizes its functional importance for inhibitory regulation of the motor and sensory systems.

In the spinal cord, GABA/glycine co-transmission has been reported in the lamina I-II interneurons in the dorsal horn, and in the motor neurons and interneurons in the ventral horn (Geiman et al. 2002; Gonzalez-Forero et al. 2005; Jonas et al., 1998; Keller et al. 2001; Lévi et al. 1999; O'Brien and Berger 2001; Russier et al. 2002). The co-transmission mostly occurs during developmental stages, and starts to fade away during postnatal maturation (Geiman et al., 2002; Gonzalez-Forero and Alvarez, 2005; Keller et al., 2001). However, though less prominent,

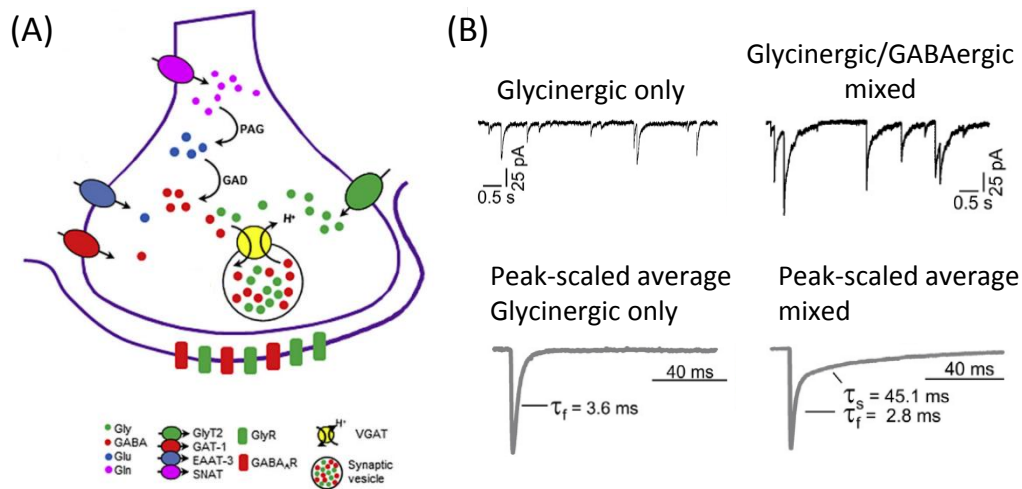


Figure 3. Co-release and co-transmission of glycine and GABA at mixed inhibitory synapses.

(A) The glycine and GABA mixed inhibitory synapses. GlyRs and GABA_ARs coexist at the same inhibitory PSDs. In the pre-synaptic terminals, the neurotransmitters glycine and GABA are loaded into the same vesicles, by a common vesicular transporter VGAT (also known as VIAAT). The cytosolic supplies of glycine and GABA are achieved through separate pathways. The cytosolic glycine is supplied by the uptake from the extracellular space through GlyT2. GABA is mostly synthesized from glutamate by the enzyme GAD. The uptake of GABA by GAT-1 can also contribute to its cytosolic content. In addition, the cytosolic glutamate can be transported from the extracellular space by EAAT-3, but mostly it is synthesized from glutamine by the enzyme PAG. Glutamine is transported into the cell by SNAT. From Aubrey 2016. (B) Glycinergic mIPSCs have lower peak amplitudes and a faster decay time, while glycinergic/GABAergic mixed mIPSCs have higher peak amplitudes and a slower decay time. In the peak-scaled average mIPSCs, mixed IPSCs exhibit a complex decay time course, containing a fast (f) and a slow (s) component. From Alvarez 2017.

GABA/glycine co-release is still observed in the adult animals (Chéry and De Koninck, 1999; Coull et al., 2003; Dufour et al., 2010). Furthermore, different isoforms of GlyRs and GABA_ARs have distinct expression levels. In the spinal cord dorsal horn, GlyR α 1 and β subunits are highly expressed while the expression of α 2 and α 3 subunits is relatively low (Anderson et al., 2009). GlyR α 3 expression is restricted to a population of neurons in the spinal cord dorsal horn (Harvey et al., 2004). GABA_AR α 2, β 3 and γ 2 subunits have relatively higher expression in the spinal cord neurons than the other GABA_AR subunits such as α 1 and β 2 subunits (Anderson et al., 2009). These GABA_AR subunits also exhibit region-specific expression levels between superficial dorsal horn and deep dorsal horn. Taken together, the evidence points out that the GABA/glycine co-transmission may play important roles in the sensory and motor control.

Electrophysiology experiments have also further demonstrated the co-release of GABA and glycine from the same pre-synaptic terminals and the same individual vesicles (Chéry and De Koninck, 1999; Jonas et al., 1998; O'Brien and Berger, 1999). Glycinergic and GABAergic mIPSCs have distinct kinetics, with glycinergic mIPSCs exhibiting larger amplitudes and fast decay, while GABAergic mIPSCs have a lower amplitude and a longer decay time (Figure 3.B). The combination of glycinergic and GABAergic transmission leads to elevated amplitudes and prolonged decay times, producing a stronger inhibition. The mixed glycinergic/GABAergic transmission may thus underlie the precise control of synaptic inhibition (Alvarez, 2017). Therefore, it is not surprising that the malfunction in the co-transmission of GABA and glycine has been implicated in numerous pathologies such as neuropathic pain, analgesia and amyotrophic lateral sclerosis (Coull et al. 2003; Imlach et al. 2016; Medelin et al. 2016; Takazawa et al. 2017; Takazawa and MacDermott 2010; Zeilhofer et al., 2009).

1.3.2 The synaptic control of GABA/glycine co-transmission

Our current knowledge about mixed inhibitory synapses mostly comes from electrophysiological studies, and relates to the pre-synaptic control of GABA and glycine neurotransmitters. There are only a handful of studies about the regulation of the respective receptors, GlyRs and GABA_ARs, at mixed inhibitory PSDs.

The pre-synaptic control of GABA and glycine neurotransmitter loading and release has been relatively well investigated (see review Aubrey 2016). The cytosolic supply of GABA and glycine in the pre-synaptic terminal is regulated by separate mechanisms. The supply of GABA is achieved by a combination of enzymatic biosynthesis from glutamate and the uptake by the relevant membrane transporters, while the supply of glycine is mostly dependent on its membrane transport (Figure 3.A). In contrast, the loading of GABA and glycine to the synaptic vesicles depends on the same vesicular transporter known as vesicular inhibitory amino acid transporter (VIAAT, or VGAT) (Chaudhry et al., 1998; Dumoulin et al., 1999; Gasnier, 2000; Wojcik et al., 2006). The sharing of a common vesicular transporter indicates that the release of GABA and glycine from the pre-synaptic terminals is under the same control by calcium signals. Therefore, the GABA/glycine content in individual vesicles and the number and distribution of the respective receptors at the post-synaptic density may be the main determinants of co-transmission. Indeed, the relative content of GABA and glycine within the vesicles has a large variability, with pure glycine-containing, pure GABA-containing and GABA/glycine-containing vesicles existing in the same pre-synaptic terminals (Aubrey and Supplisson, 2018; Katsurabayashi et al., 2004). Moreover, acute changes of cytosolic GABA or glycine concentrations rapidly change the IPSC amplitudes in an activity-independent manner (Apostolides and Trussell, 2013). This suggests that the vesicular GABA/glycine is not saturated, and that rapid modulation of evoked IPSCs can be achieved by modulating the vesicular and cytosolic neurotransmitter content. The cytosolic GABA and glycine content is most likely regulated by the glycine transporters (GlyT2) and glutamate transporters (EAAT3) (Apostolides and Trussell, 2013; Aubrey et al., 2007; Ishibashi et al., 2013). Therefore, the cause for the various profiles of vesicular content can be the different affinity of VIAAT for GABA and glycine (Juge et al., 2009; McIntire et al. 1997; Sagné et al., 1997). Another possibility could be that the expression level of VIAAT is different across individual vesicles, which remains to be examined.

At the mixed PSDs, the lateral mobility and synaptic accumulation of GlyRs, but not GABA_ARs, is regulated by NMDAR-dependent excitatory activity (Lévi et al., 2008). Moreover, microglia can tune the lateral mobility of GlyRs and glycinergic

IPSCs through prostaglandin E2, while it has no effect on GABA_ARs (Cantaut-Belarif et al., 2017). This evidence suggests that GlyRs and GABA_ARs are differentially regulated at mixed inhibitory synapses. Furthermore, gephyrin antisense oligonucleotides strongly reduce the amplitudes (and frequency) of glycinergic currents, but not GABAergic amplitudes (van Zundert et al., 2005). This indicates that gephyrin differentially modulates synaptic GlyRs and GABA_ARs. Since GlyRs and GABA_ARs bind to the same receptor binding sites of gephyrin with different affinities (see above), there is possibly a direct competition between GlyRs and GABA_ARs for the synaptic binding sites (Specht et al., 2013). However, other gephyrin-independent clustering mechanisms must also be taken into account.

The molecular mechanisms underlying mixed inhibitory synapses are still elusive, especially regarding the cooperation or competition between GlyRs and GABA_ARs. How GlyRs and GABA_ARs are differently regulated at the same PSD and what role gephyrin plays in this process is still poorly understood.

1.4 Heterogeneity of intra-synaptic organization revealed by super-resolution optical microscopy

1.4.1 Super-resolution optical microscopy and stochastic optical reconstruction microscopy (STORM)

In conventional optical microscopy, the lateral resolution is limited by the wavelength (λ) and the numerical aperture (NA) of the objective. The minimal distance between two resolvable points is several hundred nanometers due to the diffraction limit ($d \approx 0.61 \lambda/NA$). Therefore, conventional fluorescence microscopy cannot gain detailed information on sub-diffraction-limited structures such as synapses, which have a size of only a few hundred nanometers.

The advancement of several super-resolution optical microscopy techniques, such as stimulated emission depletion (STED), structured illumination microscopy (SIM) and single molecule localization microscopy (SMLM), have boosted the study of sub-diffraction-limited structures and provided us with novel insights into their ultra-structural details (reviewed in Hell et al. 2015; Laine et al. 2016; Schermelleh et al., 2010; Sieben et al. 2018; Sydor et al. 2015; Turkowyd et al.,

2016; Vangindertael et al. 2018). STED microscopy adopts donut-shaped illumination with excitation light in the center and a longer wavelength light to deplete the emission fluorescence at the perimeter (Klar et al., 2000). Thus, STED illumination only excites and records the signals from the fluorophores at the center of the illumination, and the super-resolution is achieved by tuning the laser powers to minimize the donut center. Super-resolution images are reconstructed after scanning the whole structure. SIM uses a different type of illumination structure with a known, high spatial frequency pattern to scan the samples (Gustafsson, 2000). This produces moiré fringe, from which the substructure information can be extracted and super-resolution images is therefore reconstructed. SIM and STED microscopy both circumvent the diffraction limit and achieve better resolution than conventional microscopy.

SMLM includes several related techniques, e.g. stochastic optical reconstruction microscopy (STORM), photo-activated localization microscopy (PALM) and universal point accumulation imaging in nanoscale topography (uPAINT) (Betzig et al. 2006; Giannone et al. 2010; Heilemann et al. 2008; Hess et al., 2006; Rust et al., 2006). These different forms of SMLM all share the same basic principles. A detailed discussion about the advantages and limitations inherent to each form is written in a book chapter in the forthcoming book *Single Molecule Microscopy in Neurobiology* edited by Yasushi Okada and Nobuhiko Yamamoto (also see Appendix 5). Here, I only discuss about STORM and PALM, which is more related in my project.

In particular, STORM techniques take advantage of the blinking behaviors of the fluorescent dyes and detect signals from a sparse subset of molecules that are temporally separated (Figure 4; Rust et al. 2006). During imaging, the fluorophores are first pushed into a non-fluorescent OFF state, then a sparse subset of fluorophores are activated by a low dose of UV light or spontaneously in the presence of reducing agents in the imaging buffer to gain a temporal separation of the signals. These sparse single detections are fitted mathematically during image processing, attaining a localization precision of ~10 nm. Super-resolution images can then be reconstructed by superimposing all the detections

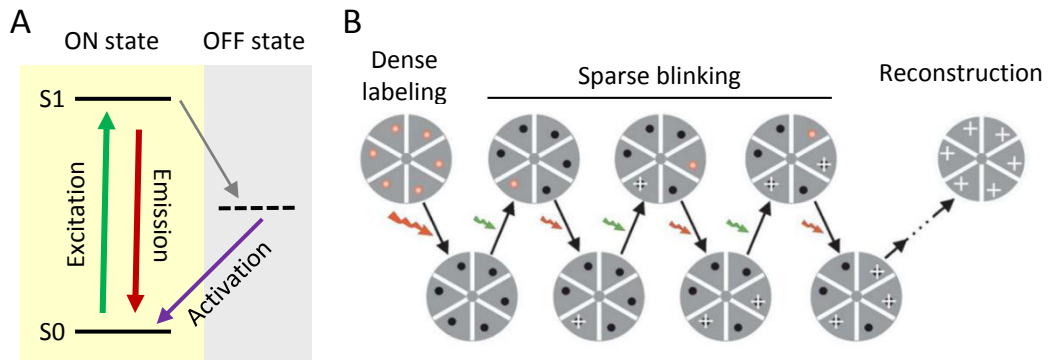


Figure 4. The basic principles of stochastic optical reconstruction microscopy (STORM).

(A) A simplified Jablonski diagram illustrating the ON/OFF blinking cycles of fluorescent dyes. After excitation to the S1 state, the fluorophores can either return to the ground state (S0) by emitting longer wavelength light, or they enter the non-fluorescence OFF state. Fluorophores in the OFF state are re-activated by UV light or spontaneously in the presence of reducing agents in the imaging buffer. (B) The diagram shows the working principles of STORM. The samples are densely labeled with fluorophores. At the beginning of the STORM imaging, a strong dose of illumination laser (red) is applied to bleach the ON state fluorophores. Then a small dose of activation laser (green) is applied to activate a subset of spatially separated fluorophores. These sparsely activated fluorescent signals are recorded under the red laser illumination. Taking advantage of the stochastic blinking of the fluorophores, tens of thousands of frames are recorded. Post-processing of the recordings obtains the localizations of the blinking events, from which the super-resolution dSTORM images are reconstructed. Form Rust et al., 2006.

from the recording. STORM can achieve a spatial resolution of single molecules of 10-40 nm.

The main difference between STORM and PALM is the labeling technique, where organic dyes are used in STORM and fluorescent proteins are used in PALM to label the target proteins (Betzig et al., 2006; Heilemann et al., 2008; Hess et al., 2006; Rust et al., 2006). Both organic dyes and fluorescent proteins can be induced to blink under different conditions. In STORM, the blinking of fluorescent dyes requires particular imaging buffers and high illumination intensity. In PALM, the blinking of fluorescent proteins is achieved by sequential photo-activation/conversion with UV light in buffered salt solutions. PALM is thus preferable for live-cell imaging, because the STORM imaging buffers are detrimental to living cells. However, labeling with fluorescent proteins requires the expression of recombinant fusion proteins, which may potentially change the target protein's function. Moreover, organic dyes usually have narrower excitation/emission spectra and higher photon emission compared to fluorescent proteins. Therefore, STORM is more suitable for multi-color imaging and to gain a better localization precision.

There are two versions of STORM imaging, N-STORM (Rust et al., 2006) and direct STORM (dSTORM) (Heilemann et al., 2008). N-STORM adopts a pair of dyes, one with a short wavelength (green) and another with a longer wavelength (red), to act as activator and reporter, respectively. The pair of dyes are conjugated to the same antibody at close proximity. During imaging, a red laser is used to excite the red dyes and to switch them into the OFF state, while a green laser at low intensity excites the green dyes that in turn activate the red fluorophores. Note that no UV light is needed in N-STORM. For dual-color imaging, the two target proteins are labeled with the same reporter dye (e.g. Alexa Fluor 647), but different activator dyes are used to selectively visualize the two targets (Bates et al., 2007). There are, however, a few drawbacks of using activator/reporter dye pairs in STORM. Firstly, it is difficult to control precisely the ratio of activator and reporter dyes on the same antibody. Secondly, by using two wavelengths for a single target protein, N-STORM leaves limited options of dyes for multi-color imaging. Thirdly and most importantly, the commonly used reporter dye Alexa

Fluor 647 can blink spontaneously in the imaging buffer without laser activation, making N-STORM susceptible to contaminating detections from the other channel. This is particularly problematic for dense structures such as synaptic protein assemblies, because there is no efficient way to identify and remove the contaminating detections. In dSTORM, only single fluorophores (reporter dyes) are used for one color imaging, and their activation is tuned by a low dose of UV light and reducing agents in the imaging buffer. The spectral separation of the fluorophores affords a larger choice of dyes, making dSTORM more favorable for implementing dual-color super-resolution imaging of synaptic proteins.

1.4.2 The challenges of applying two-color dSTORM to synapses

The superior resolving power of SMLM makes it a powerful tool to study small structures such as synapses. However, its application to synapses is accompanied by many challenges arising from the techniques themselves and from the particular properties of synapses.

1.4.2.1 Challenges posed by technical limitations

Several technical limitations are inherent to SMLM (Figure 5.A). Ideally, the target structures are densely labeled with fluorophores, and single molecule detections of these fluorophores are precisely localized. From the abundant localizations, the fine structure is then reconstructed (Figure 5. A1). This ideal scheme of SMLM can be hampered by many factors during experimental practice. First, the localization precision is generally limited in a range of 10-40 nm (Schermelleh et al., 2010; Sieben et al., 2018; Turkowyd et al., 2016). Limited localization precision can blur the fine structure of the targets and attenuate the resolution (Figure 5.A2). Second, the labeling density of fluorophores needs to be extremely high in order to obtain abundant localizations (Baddeley and Bewersdorf, 2018; Deschout et al., 2014; van de Linde et al., 2010; Shivanandan et al., 2015). This requirement is often compromised in biological samples due to the inefficiency of the labeling strategies, for example due to epitope masking. Sparse labeling leads to insufficient detections and therefore poorly represented target structures (Figure 5.A3). Third, many labeling strategies also suffer from the bulky size of the probes such as antibodies (Maidorn et al., 2016). The large size of the antibodies inevitably dis-locates the fluorophores from the epitopes, and consequently smears the detected structures

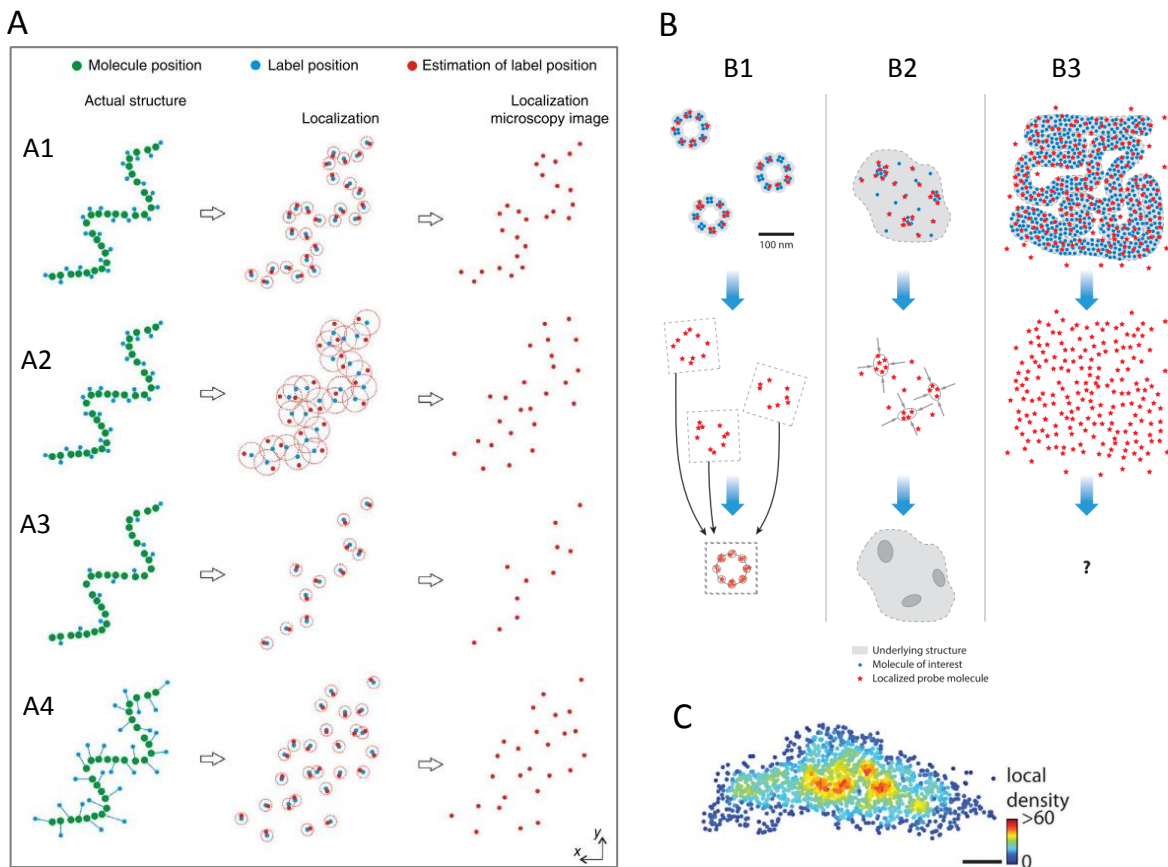


Figure 5. The challenges of applying SMLM to synapses.

(A) The challenges imposed by the technical limitations of SMLM. Except in the ideal situation (A1), the quality of SMLM images can be compromised by insufficient localization precision (A2), labeling density (A3), and the dislocation of the fluorophores due to the bulky size of probes (A4). From Deschout et al., 2014. (B) Different types of target structures as subjects of SMLM impose different requirements and challenges. For stereotypic structures, many images can be combined and averaged to gain detailed information (B1). For well-isolated complex structures, image averaging is not suitable and complex characterization approaches are needed (B2). For closely-spaced complex structures, little information can be extracted (B3). From Baddeley and Bewersdorf, 2018. (C) The intra-synaptic organization of a PSD-95 cluster. Resolving its intra-synaptic organization is faced with both technical and biological challenges. Scale bar 100 nm. From MacGillavry et al., 2013.

(Figure 5.A4). Fourth, the photo-blinking behavior of fluorophores is a major concern in SMLM. The blinking performance of fluorophores is dependent on their photo-physical and photo-chemical properties and can be modulated with imaging buffer components and by adjusting the strength of the laser illumination (Annibale et al., 2011; Dempsey et al., 2011; Endesfelder et al., 2011; Ha and Tinnefeld, 2012; Lehmann et al., 2016; van de Linde et al., 2010, 2011; Nahidiazar et al., 2016; Pennacchietti et al., 2017b; Wang et al., 2014). Sub-optimal imaging conditions cause clustering artefacts that lead to false representation of the target structure (Annibale et al., 2011a; Burgert et al, 2015; Endesfelder and Heilemann, 2014). Besides, the photo-switching of fluorophores can give rise to repetitive detections of the same molecule, and the stochasticity of the blinking behavior adds to the uncertainty in the reconstructed structures. As a result, targets with identical structure may not give rise to the same spatial representation or number of detections (Figure 5.B1).

In the scheme of multicolor SMLM, each channel submits to the same challenges mentioned above. However, additional sources of errors due to the multicolor scheme increase the difficulties in SMLM, such as the registration of two channels (Annibale, Scarselli, Greco, & Radenovic, 2012). Specifically, among different sources of artifacts in two-color dSTORM, the compatibility of fluorescent dyes in the same imaging system is a key player during data acquisition (Dempsey et al. 2011; Nahidiazar et al. 2016; Xu et al., 2017). Even under optimized imaging conditions, various dyes can produce different representations of the same structure (Dempsey et al., 2011). In conclusion, two-color dSTORM is faced with greater challenges and optimizations need to be taken for reliable data acquisition and interpretation.

1.4.2.2 Challenges posed by the characters of synapses

Different biological structures have distinctive features that introduce particular concerns in SMLM (Figure 5.B). Baddeley and Bewersdorf classified the analyzed structures into three categories (Baddeley and Bewersdorf, 2018). For well-isolated stereotypic structures such as the nuclear pore complex (NPC), many detected structures can be combined and averaged to gain finer structural information (Figure 5.B1). This averaging strategy can compensate for the technical limitations

in SMLM in order to resolve the accurate structures, lowering the demands for detection efficiency. However, this requires accurate averaging algorithms during the image processing. For well-isolated complex structures such as gene loci and synapses, each detected structure needs to be treated as individuals rather than be averaged due to the large variability of these structures (Figure 5.B2). To segment these individual complexes from the whole image and to characterize their variable structural features is very demanding in terms of image processing and statistical analysis (Nicovich et al., 2017). For closely spaced complex structures such as condensed chromatin, resolving the structure is difficult and only limited information can be extracted from the SMLM data (Figure 5.B3). This classification of analyzed structures is a good way to illustrate the different difficulties in SMLM applications.

The study of synapses using SMLM imaging is particularly challenging due to the technical limitations discussed above, as well as the special properties of synapses. From an ultra-structural point of view, the unique character of synaptic protein assemblies pose particular challenges to the acquisition of reliable SMLM data and to the data interpretation. First of all, the size of synapses is of the same order as the diffraction limit, with only a few hundred nanometers in diameter, which makes it difficult to obtain temporally and spatially separated sparse blinking events during imaging (Harris and Stevens, 1989; Harris and Weinberg, 2012; Specht et al., 2013). Even when the overall blinking in the field of view (FOV, here referring to the whole images under the recording) is sparse, there can still be many overlapping blinking events at synaptic sites. The assignment of multiple signals to a single detection necessarily causes wrong representations in the super-resolved image. Second, synapses have large variability in the cluster morphology and protein copy numbers (Fukazawa and Shigemoto 2012; Masugi-Tokita et al. 2007; Nusser et al., 1997, 1998; Sheng and Kim 2011; Specht et al. 2013; Sugiyama et al. 2005; Tarusawa et al. 2009). As a consequence, individual synaptic clusters cannot be combined and population averaging is not applicable. Each synaptic cluster needs to be treated individually, which increases the difficulties of data analysis. Furthermore, given the stochastic nature inherent to dSTORM, the variations in detection efficiency and localization density of synaptic clusters in the same images (i.e. FOVs) can be large, not to mention the variations among different images (i.e.

FOVs). Third, even though synapses are densely packed compartments, the copy numbers of many of their components are quite small, with receptors in the order of tens and scaffold proteins in order of hundreds of molecules per. Small numbers of target proteins make it difficult to attain sufficiently dense labeling and hence efficient sampling of the synapse in order to reconstruct a representative super-resolution image. Fourth, synaptic proteins undergo dynamic changes and reorganization during synaptic plasticity, which adds to the difficulties of SMLM data interpretation. Given the variability and plasticity of synapses, high throughput analysis of large number of synapses are needed for meaningful data interpretation. Fifth, the characterization of the internal synaptic organization from the dSTORM data is subject to the difficulties faced by the third category structures (closely spaced complex structures) (Figure 5.C).

In addition to the aspects mentioned above, the detection of two synaptic components in parallel dramatically increases the complexity of the experiments. On the one hand, it requires the achievement of good imaging quality of two channels, which is depend on the compatibility of fluorescent dyes, imaging buffer, laser and microscope setups. On the other hand, it demands the implementation of more complicated data processing and analysis tools. In summary, extraordinary scrutiny is required to assess the quality of the imaging data and the image processing methods in the study of synaptic structures.

1.4.3 Intra-synaptic heterogeneity and sub-synaptic domains as regulators of synaptic functions

Despite of all the challenges and difficulties, synapses are of great interest in SMLM due to their small size and important roles in neuronal activity. SMLM investigations have provided important insights into synaptic function. Dani and colleagues have examined pre- and post-synaptic protein assemblies with SMLM, confirming a layered molecular organization of different synaptic components (Dani et al., 2010). This arrangement may explain the different kinetic properties of excitatory scaffold proteins, where proteins that are located at a greater distance from the synaptic membrane have faster exchange rates (Kuriu et al. 2006; Sharma et al., 2006). SMLM has also been used to determine the absolute numbers of scaffold proteins and neurotransmitter receptor complexes at

synapses, providing new types of quantitative information about the regulation of synaptic structure and function (Fricke et al. 2015; Patrizio et al. 2017; Specht et al. 2013).

A very interesting discovery is the observation of sub-synaptic domains (SSDs) with super-resolution optical microscopy. In 2013, several groups reported independently that different synaptic proteins are distributed heterogeneously at synapses (MacGillavry et al., 2013; Nair et al., 2013; Specht et al., 2013). SMLM images showed that the excitatory scaffold protein PSD-95 occupies subdomains within the post-synaptic density that regulate AMPAR clustering (MacGillavry et al., 2013; Nair et al., 2013). The existence of PSD-95 subdomains was confirmed with STED microscopy both in vitro and in vivo (Broadhead et al., 2016; Dzyubenko et al., 2016; Hruska et al., 2018; Masch et al., 2018; Wegner et al., 2018). Likewise, sub-synaptic domains of gephyrin were shown to play a role in inhibitory plasticity at GABAergic synapses (Pennacchietti et al., 2017a). These findings point towards a mechanism whereby sub-synaptic domains drive the recruitment of neurotransmitter receptors to specific locations within the PSD, thus regulating synaptic transmission. Furthermore, using multicolor 3D-STORM, Tang and colleagues demonstrated that the sub-synaptic domains of several pre-synaptic proteins are aligned with those of post-synaptic proteins, an arrangement that is referred to as trans-synaptic nanocolumn (Tang et al., 2016). Therefore, it was proposed that the subsynaptic spatial organization can regulate the synaptic strength and plasticity (Figure 6.A). Synaptic adhesion molecules are likely to coordinate these trans-synaptic complexes. SMLM and STED microscopy have also shown that pre-synaptic proteins of the active zone (AZ) and synaptic adhesion proteins display sub-synaptic distributions (Chamma et al., 2016 a, b; Glebov et al. 2017; Haas et al. 2018; Perez de Arce et al. 2015; Tang et al. 2016). These exciting observations not only demonstrate the power of SMLM to visualize the ultra-structures of synapses, but also point towards possible roles of sub-synaptic domains in synaptic function (reviewed in Biederer et al., 2017; Chen et al., 2018; Liu et al, 2017; Scheefhals and MacGillavry 2018).

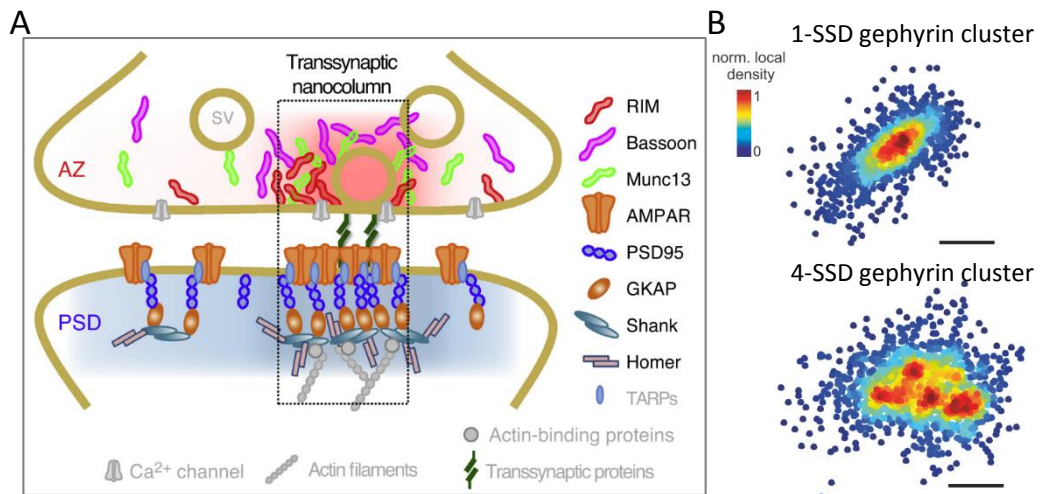


Figure 6. Sub-synaptic domains (SSDs) as regulators of synaptic function.

(A) Several important protein types at excitatory synapses are organized into sub-synaptic domains (SSDs), such as receptors, adhesion and scaffold proteins. The pre-synaptic SSDs and post-synaptic SSDs appear to be aligned in trans-synaptic nanocolumns. From Tang et al. 2016 and Chen et al., 2018. (B) At inhibitory synapses, gephyrin clusters are organized heterogeneously and can have several SSDs. Scale bar: 100 nm. From Pennacchietti et al., 2017.

1.5 Functional implications of intra-synaptic heterogeneity and SSDs in mixed inhibitory synapses

Electron microscopy of symmetric synapses has revealed a discontinuous network of filaments at the inhibitory PSD and in the synaptic cleft (High et al., 2015; Linsalata et al., 2014). Super-resolution optical microscopy confirmed that the inhibitory scaffold protein gephyrin forms heterogeneous distributions and sub-synaptic domains (Figure 6.B; Dzyubenko et al. 2016; Pennacchietti et al., 2017a; Specht et al. 2013). SMLM imaging in cultured hippocampal neurons further revealed that extra-synaptic gephyrin molecules are recruited to synaptic sites during NMDA-induced inhibitory long-term potentiation (Pennacchietti et al., 2017a). The increase in molecule density was accompanied by an increased fraction of gephyrin clusters with multiple SSDs. More recently, Crosby et al conducted a comprehensive analysis of pre- and postsynaptic components using 3D-SIM, reaching a resolution of ~120 nm laterally and ~300 nm axially (Crosby et al., 2019). It was shown that GABA_ARs form SSDs with an average diameter of ~300 nm that are closely associated with SSDs of gephyrin and pre-synaptic RIM1/2. This implies the existence of trans-synaptic nanocolumns as an organizing principle of inhibitory synapses. Given that the measured size of the SSDs was close to the resolution limit, the concept of nanocolumns at inhibitory synapses will require further validation. Nonetheless, these studies strongly suggest that the internal organization of inhibitory synapses plays an important role in regulating synaptic transmission.

At mixed inhibitory synapses, GlyRs and GABA_ARs co-exist at the same PSDs that are juxtaposed to the pre-synaptic terminals where GABA and glycine are co-released from the same vesicles (Figure 3). Once released from the pre-synaptic terminals, the neurotransmitters can diffuse quickly in the synaptic cleft. The effective range for the neurotransmitters to activate their receptors is about 125 nm in radius (Delgado & Selvin, 2018). This creates a particular situation, where the exact position of GlyRs and GABA_ARs relative to the presynaptic vesicle release site can have a strong impact on the efficacy of the agonists and thus the activity of the receptors. However, we do not yet know whether GlyRs and GABA_ARs are totally intermingled or whether they form SSDs at mixed synapses.

And if they do form distinct SSDs, how are they related to the SSDs of gephyrin, as well as the pre-synaptic machinery? Through its capacity to resolve the spatial organization at single molecule level, SMLM may provide answers to these open questions.

1.6 Aims of this study

As discussed above, my goal was to investigate the spatial relationship between GlyRs and GABA_ARs, as well as between the receptors and gephyrin at mixed inhibitory synapses. Due to the co-existence of GlyRs and GABA_ARs at the same PSDs, the spatial relationship between the two receptors and the pre-synaptic vesicle release sites can be important for tuning the efficacy of GlyRs and GABA_ARs. Thus, I have also examined the spatial relationship between the receptors and the vesicle release sites. My ultimate objective is to understand how neuronal activity regulates and is regulated by the spatial relationship of inhibitory synaptic components.

To realize this investigation, I first adopted the primary spinal cord neuron culture as an appropriate model for mixed inhibitory synapses. In cultured spinal cord neurons, about 70% of the inhibitory synapses are mixed inhibitory synapses (Dumoulin et al., 2000). Secondly, I developed an optimized two-color dSTORM imaging and data analysis protocol that is suitable for the synaptic structures. Thirdly, based on this methodology of two-color dSTORM imaging of synapses, I carefully examined the ultra-structure of synaptic protein assemblies and their spatial relationships at mixed inhibitory synapses. I was especially interested in the changes of the spatial relationship between synaptic components during altered neuronal network activity. To this aim, I used pharmacology approaches to change the excitatory activity. My experimental results provide a novel perspective for understanding the mechanisms underlying mixed inhibitory synapses.

Chapter 2

2 Materials and methods

2.1 Primary spinal cord neuron culture

All procedures using animals follow the regulations of the French Ministry of Agriculture and the Direction départementale des services vétérinaires de Paris (Ecole Normale Supérieure, Animalerie des Rongeurs, license B 75-05-20).

Primary spinal cord neuron cultures were prepared from embryonic Sprague Dawley rats on day 14 of gestation (E14) as described previously (Specht et al., 2013), with some modifications.

Glass coverslips (18 mm in diameter, thickness 0.16 mm, No. 1.5, VWR #6310153) were cleaned with ethanol, air-dried, and then coated with 70 µg/ml poly-DL-ornithine diluted in sterile water overnight. On the day of cell culture, the pregnant rat was euthanized and the embryos were collected and dissected to obtain the spinal cord tissues. The tissues were incubated with 0.25% Trypsin-EDTA (Life Technologies, Cat.No. 25200-056) diluted in HBSS to a final concentration of 0.005%, supplemented with 20 mM HEPES and 0.006 g/ml glucose (HBSSc medium) at 35°C for 10 minutes. After washing away the Trypsin-EDTA, the tissues were dissociated by pipetting in HBSSc medium in the presence of DNase at a final concentration of 50 µg/ml and then 20µg/ml (two rounds). Dissociated cells were combined and collected by centrifuging the supernatant on a layer of 4% BSA containing medium (BSA (Sigma, Cat.No. A3311) diluted in Leibovitz's L-15 medium (Gibco, Cat.No. 11415-049)) at 1000 rpm for 8 min. Cells were then resuspended and plated on the coverslips at a density of 6×10^4 cells/cm² in Neurobasal medium (ThermoFisher), supplemented with B-27, 2 mM glutamax, and antibiotics (5 U/ml penicillin and 5 µg/ml streptomycin). Cultures were kept at 37°C with 5% CO₂ in the incubator. The culture medium was replenished twice a week by replacing half of the volume with BrainPhys neuronal medium (Stemcell Technologies) supplemented with SM1 and antibiotics. Usually, spinal cord neurons developed mature neurites after two weeks in culture, at which point they were used for immunocytochemistry.

2.2 Conjugation of Cy3B dye to secondary antibodies

Unconjugated secondary antibodies, including donkey anti-mouse IgG (Jackson ImmunoResearch, #715-005-151), donkey anti-rabbit IgG (Jackson ImmunoResearch, #711-005-152), donkey anti-rat IgG (Jackson ImmunoResearch, #712-005-153), donkey anti-guinea pig IgG (Jackson ImmunoResearch, #706-005-148) were coupled with Cy3B mono-reactive N-hydroxysuccinimide (NHS) ester (PA63101, GE Healthcare) according to the supplier's protocol.

The reaction mix, containing 35 μl secondary antibody solution ($\sim 44 \mu\text{g}$ IgG), 5 μl Cy3B NHS ester solution (10 mg/ml in DMSO) and 10 μl NaHCO_3 (0.5 M), was incubated on a shaking incubator for 30 minutes and protected from light. During this time, an NAP-5 column (Illustra NAP-5 columns, #17085302, GE Healthcare) was equilibrated with PBS buffer. After the chemical crosslinking of the dye to the antibody, 150 μl of PBS were added to the reaction mix, and the combined 200 μl reaction volume was loaded onto the NAP-5 column. The Cy3B-conjugated antibodies were separated from the excess of unreacted NHS esters by size exclusion through the addition of 550 μl PBS (flow-through). Finally, the antibody fraction was eluted by addition of another 200 μl PBS. To characterize the labeling efficacy, the absorption of IgG protein was measured at 280 nm and that of the Cy3B dye was measured at 559 nm with a spectrophotometer (NanoDrop ND-1000 Spectrophotometer). The molar concentrations of the IgG and the Cy3B dyes were calculated according to the Lambert-Beer law:

$$A_{\lambda} = \epsilon c l$$

where A_{λ} is the absorption at the indicated wavelength λ , ϵ the molar extinction coefficient, c the concentration and l the path length (1 mm). A molar extinction coefficient of $195000 \text{ M}^{-1}\text{cm}^{-1}$ was estimated for IgG and $130000 \text{ M}^{-1}\text{cm}^{-1}$ for the Cy3B dye. From the molar concentration, the number of dyes per IgG was calculated. The estimated dye/IgG ratio was between 3 and 5 for all the experiments.

2.3 Pharmacological treatment and immunocytochemistry

Tetrodotoxin citrate (TTX, Cat. No. 1069, Tocris) stock solution (1 mM in sterile water) and 4-aminopyridine (4-AP, Cat.No.0940, Tocris) stock solution (5 mM in sterile water) were prepared and stored at -20°C. For drug treatment, 1 µl of the stock solution of TTX was diluted in the culture medium of the cells to reach a final concentration of 1 µM. 4-AP was applied in the same way at a final concentration of 50 µM. TTX and 4-AP were always applied simultaneously to different coverslips on the same 12-well plate. The cells were then placed back in the incubator for one hour before fixation.

Spinal cord neurons were fixed with 100% methanol at -20°C for 10 minutes or with pre-warmed (37°C) 4% paraformaldehyde (PFA) in PBS for 15 minutes. After several washes with PBS, unspecific binding sites were blocked with 3% BSA in PBS (blocking buffer) for at least 30 minutes. The cells were then incubated with primary antibodies diluted in the blocking buffer for 1 hour at room temperature, or overnight at 4°C. After several washing steps in PBS, the cells were incubated with the secondary antibodies diluted in the blocking buffer for 1 hour at room temperature, protected from light. All samples were washed with PBS before imaging.

The following primary antibodies were used for labeling: mouse monoclonal mAb7a (Synaptic Systems, #147011), rat monoclonal mAb7a (Synaptic Systems, #147208), and rabbit polyclonal (Synaptic Systems, #147002) antibodies against gephyrin, mouse monoclonal antibody against GABA_AR β3 (UC Davis/NIH NeuroMab Facility, #75-149, RRID: AB_2109585), rabbit polyclonal antibody against RIM1/2 (Synaptic Systems, #140203), guinea pig polyclonal antibody against RIM1/2 (Synaptic Systems, #140205), and custom-made rabbit polyclonal antibody against GlyRα1 (A. Triller lab, #2353). The primary antibodies were all diluted at 1:500. For the secondary antibodies, commercially available Alexa Fluor 647 (A647)-conjugated, Cy3-conjugated, Alexa Fluor 568 (A568)-conjugated and Alexa Fluor 488 (A488)-conjugated secondary antibodies (1:500 or 1:1000 dilution), as well as the custom-made Cy3B-conjugated secondary antibodies (1:50 to 1:100 dilution) were used (see 2.2 chemical dye conjugation). The combination of secondary antibodies in each experiment was chosen to

recognize the corresponding primary antibodies with minimal cross-reactivity with other primary antibodies. For a full list of the antibodies used in this study, see Appendix Table 1.

2.4 Calcium imaging and data analysis

Fluo-4 acetoxymethyl (AM) ester (F14201, Life Technologies) stock solution (0.5 mM in DMSO) was diluted in the culture medium of the cells to reach a final concentration of 0.5 μ M. Cells were placed back in the incubator for 10 min, after which the medium was replaced with pre-warmed imaging medium, containing 130 mM NaCl, 5 mM KCl, 2 mM CaCl₂, 1 mM MgCl₂, 30 mM glucose, and 10 mM HEPES. The coverslip was then mounted in an open imaging chamber on an inverted Nikon Eclipse Ti microscope, equipped with a 20 \times objective and an EMCCD camera (Andor iXon 897 Ultra). A 2 \times 2 binning of the pixels was applied to gain an effective image pixel size of 1.6 μ m. A mercury lamp (Intensilight C-HGFIE, Nikon) was used for illumination, combined with the appropriate excitation filter (FF02-485/20) and emission filter (FF01-525/30). Time lapse images of the calcium signals were recorded at 10 Hz for 3 min at room temperature, with the aid of NIS-Elements software (Nikon). To compare the calcium signals before and after the treatment, we first recorded 3 min-long movie of the basal calcium signals without treatment. Then, TTX or 4-AP was applied in the imaging buffer to reach a final concentration of 1 μ M or 50 μ M, respectively. Five minutes after the administration of the drug, another 3-min long movie was recorded. A third movie was recorded between 18 and 21 minutes.

The calcium signals were measured by drawing mask regions of the cell bodies manually and then measuring the integrated fluorescence intensity in the regions using Fiji (Schindelin et al., 2012). Background was subtracted from the calcium signals, and the amplitude of the calcium signals at the soma was expressed as $\Delta F/F$. A custom written program (gift from Anastasia Ludwig, IBENS/University of Helsinki) in Matlab 2012b (MathWorks) was used to detect the frequency and peak amplitude of the calcium signals.

2.5 Conventional microscopy and data analysis

After immunostaining, the coverslips were mounted in an open imaging chamber on the Nikon Ti microscope, equipped with a 100× oil objective (NA=1.49). An additional 1.5× lens was inserted in the emission light path to gain a 150× magnification, achieving an effective image pixel size of 107 nm. The mercury lamp was used for illumination, with appropriate band pass filters in the excitation and emission light path in the far-red (excitation FF01-650/13, emission FF02-684/24), red (exci. FF01-560/25, emi. FF01-607/36) and green (exci. FF02-485/20, emi. FF01-525/30) channels. The intensity of the illumination was set to avoid any pixel saturation and to have proper brightness of the synaptic clusters. Ten or twenty images were taken with an exposure time of 50 ms, and always in the order of far-red, followed by the red and the green channels. For a given set of experiments, all the imaging parameters were kept constant.

The stacks of images were combined by average projection of the ten (or twenty) frames in Fiji. Then, binary masks of the clusters were produced with the wavelet function of the Spot detector in Icy, using a size filter to remove the clusters smaller than 3 pixels (De Chaumont et al., 2012). The integrated intensity within the binary masks were measured by a lab-made program (Hennekinne et al., 2013) written in Matlab (MathWorks). Cluster intensities were not corrected for background. For comparing the relative amount the proteins, binary clusters produced from one of the channels were used as masks for all the channels imaged.

2.6 Two-color dSTORM imaging and analysis

2.6.1 Microscope setup

The stochastic optical reconstruction microscopy (STORM) setup is built on the inverted Nikon Eclipse Ti microscope with a perfect focusing system (PFS) to minimize the axial drift of the microscope stage, and equipped with a 100× oil immersion objective (HP APO TIRF 100× oil, NA 1.49, Nikon). The setup includes several continuous laser lines with emission wavelengths at 640 nm, 561 nm, 532 nm, 488 nm and 405 nm (Coherent), with nominal maximum power of 1W, 1W, 500 mW, 500 mW and 120 mW, respectively. The lasers are combined

in an external platform and controlled via an acousto-optic tunable filter (AOTF) to apply fast illumination pulses and to set the laser intensity. The laser beam is expanded with a total internal reflection fluorescence (TIRF) arm that focuses the beam on the back focal plane of the objective and that controls the inclination angle of the excitation. The emission light is captured with an electron multiplying charge-coupled device (EMCCD) camera using a multiple wavelength dichroic mirror and appropriate band pass filters (Semrock FF02-684/24 for A647, FF01-607/36 for Cy3B) in the emission light path. Conventional fluorescence images were taken with a mercury lamp (Intensilight C-HGFIE, Nikon) that emits a broad spectrum of wavelengths, using the corresponding band pass filters (FF01-650/13 for A647, FF01-560/25 for Cy3B) in the excitation light path (see 2.5). All the elements of the microscope are controlled by NIS-Elements software (Nikon).

2.6.2 Sequential two-color dSTORM imaging

The direct STORM (dSTORM) imaging workflow is illustrated in Figure 7.A. On the day of imaging, immuno-labeled neurons on glass coverslips were incubated with 100 nm multicolor beads (Tetraspeck, ThermoFisher, Cat. No. T7279) diluted in PBS for 5-30 minutes (concentration at $\sim 10^9$ particles/ml). After washing with PBS to remove the unattached beads, the coverslips were mounted on glass slides with a cavity (diameter 15-18 mm, depth 0.6-0.8 mm) containing freshly prepared Gloxy imaging buffer (0.5 mg/ml glucose oxidase, 40 μ g/ml catalase, 0.5 M D-glucose, 50 mM β -mercaptoethylamine (MEA) in PBS, pH 7.4). Gloxy buffer was freshly prepared on every day of imaging, and degassed with N₂. The coverslips were sealed on the glass slides with silicone rubber (Picodent twinsil speed 22).

Under the microscope, we searched for field of view (FOV) containing several synaptic clusters and multicolor beads that served as fiducial markers. During this time, the sample was illuminated with the mercury lamp instead of the lasers to minimize the bleaching of the fluorophores. Reference images (epifluorescence images) were taken in the far-red and in the red channel with the lamp, and also in the green channel when triple labeling was performed. The effective magnification of these images was 100x, resulting in a pixel size of 160 nm.

Sequential two-color dSTORM was then carried out first in the far-red channel for A647 signals, followed by the red channel for Cy3B. In the beginning of each recording, the field of view was briefly pre-bleached to push the fluorophores into the OFF state and to dampen the brightness of the beads. Then, 10000 to 30000 frames were recorded with an exposure time of 50 milliseconds. The frame numbers were adjusted and kept constant for each set of experiments to ensure comparability of the recordings. We used highly inclined laser illumination rather than total internal reflection fluorescence (TIRF) to reduce the background fluorescence while avoiding interferences and inhomogeneous illumination. The estimated illumination intensity on the field of view was ~ 1 kW/cm² for the 640 nm laser, and ~ 2 kW/cm² for the 561 nm laser. The blinking of Cy3B was supported by low-intensity activation with the 405 nm laser (~ 0.03 to 0.30 kW/cm²). The total acquisition time needed for each ROI was about half an hour to one hour.

2.6.3 dSTORM image processing and data analysis

The most critical processing steps of the raw imaging data comprise single particle detection, drift correction, two-channel registration and image reconstruction (Figure 7). Single particle detection was realized by using an adapted version of the multiple-target tracing (MTT) program (Sergé et al., 2008) in Matlab 2012b (MathWorks), as described by Izeddin et al (Izeddin et al., 2011). In this program, a Gaussian fitting was applied to each fluorophore signal to determine its coordinates and intensity (number of photons collected). The localization precision of A647 and Cy3B signals was estimated from the signal intensities, using the detections of individual fluorophores at synapses imaged under the two-color dSTORM mode as follows:

σ / \sqrt{n} , where σ is the width (standard deviation) of the Gaussian fit of the detections, and n is the number of photons. The localization precision obtained was 6 ± 3 nm for A647 signals, and 7 ± 2 nm for Cy3B signals ($n = 12$ synapses).

The lateral drift was corrected with the program PALMvis (Lelek et al., 2012) in Matlab 2012b using the multicolor beads as fiducial markers. A sliding window of 100 to 1000 frames was applied to calculate the average position of the beads

throughout the recording. The systematic x/y drift over time was thus estimated with a temporal resolution of 5-50 s based on the average displacement of the beads (Figure 8). The calculated drift of the stage was then applied to the whole image to correct the coordinates of all the single fluorophore localizations in each image frame. At this stage, we obtain the final coordinates of the localizations in both channels. The coordinates-based data was then imported into the SRclusters program (Delestro and Genovesio, IBENS, unpublished) for the two-channel registration by aligning the positions of the beads in the two channels, followed by further cluster analysis (Figure 12). Cluster analysis in SRclusters includes cluster size measurement, spatial correlation analysis and SSD segmentation (see section 3.1.2.3).

Alternatively, the drift-corrected coordinates-based data are converted into rendered super-resolution images by representing each localization as a Gaussian function with the same intensity and standard deviation. The standard deviation $\sigma = 15$ nm was used even though the estimated localization precision was 6-7 nm, in order to account for the less bright detections. Super-resolution images are generally displayed with a pixel size of 10 nm to balance file size versus representation precision. Finally, the two super-resolution images were aligned using the TurboReg plugin (Thevenaz et al., 1998) in Fiji before further cluster analysis (Figure 10, see section 3.1.2.1).

2.7 Statistical analysis

All statistical analysis was performed in Microsoft Excel (Microsoft). Student's t-test or Kolmogorov-Smirnov test was used for significance test. Paired t-test was used for the calcium imaging data to compare signals between different time points. Data are generally represented in the form of cumulative probability distributions, or as bar graphs showing the median and quartiles of the distribution (calcium imaging data), or the mean \pm standard deviation.

Chapter 3

3 Results

As discussed in the introduction, the application of two-color dSTORM to synaptic structures is faced with challenges from both inherent technical limitations and biological constraints. In my project, the first step was to obtain an optimized two-color dSTORM imaging protocol and analysis tools that are suited for synaptic structures. Then this methodology was applied to investigating the ultrastructure of mixed inhibitory synapses, in order to understand the mechanisms underlying the inhibitory co-transmission. The results are presented in two parts in the following, methodological results followed by results on mixed inhibitory synapses.

3.1 Methodological evaluation: two-color dSTORM of synapses

We adopted two-color dSTORM imaging to study the endogenous synaptic proteins at mixed inhibitory synapses in dissociated spinal cord neurons. With respect to the multifaceted challenges arising from the technical limitations and the unique synaptic characters, we carefully optimized the protocol, involving the sample preparation, image acquisition and data analysis. A full discussion of the optimization concerning the choice of fluorophore pairs, labeling strategies, imaging parameters, quality assessment and data analysis is synthesized in a chapter in the forthcoming book *Single Molecule Microscopy in Neurobiology* edited by Yasushi Okada and Nobuhiko Yamamoto in Springer Neuromethods series (See appendix: YANG and Specht, Practical guidelines for two-color SMLM of synaptic proteins in cultured neurons). Here, the optimized protocol from imaging to data analysis is introduced, supported by experimental data. These results address the importance of performing control experiments in SMLM and our strategies presented here can be easily adapted to other SMLM studies.

3.1.1 An optimized sequential two-color dSTORM imaging protocol

After some trials and failures in testing the fluorescent dye pairs, imaging buffers, laser illumination schemes and relevant imaging parameters, one configuration stood out to be a good choice (Figure 7). We chose Alexa Fluor 647 (A647) in the

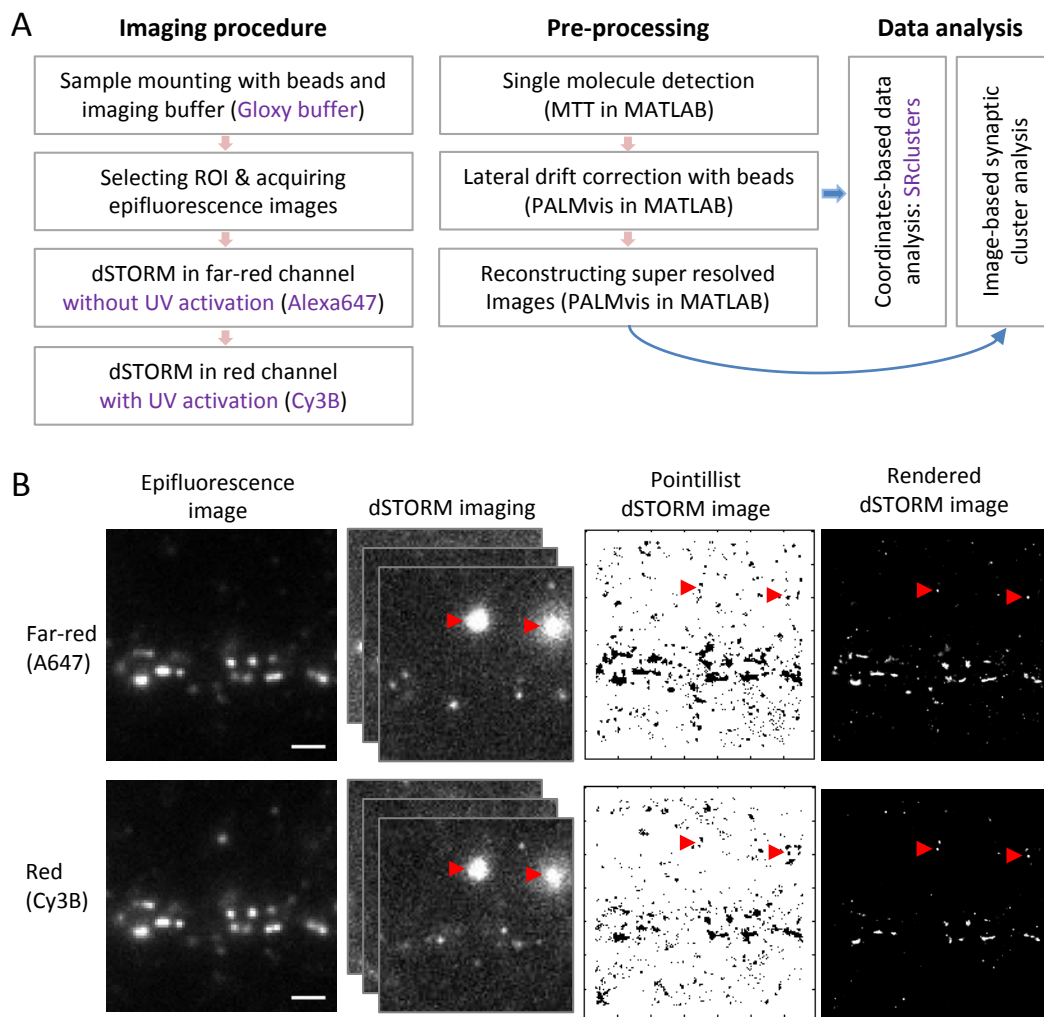


Figure 7. Sequential two-color dSTORM imaging of synaptic proteins.

(A) Experimental workflow for two-color dSTORM imaging and data processing. (B) Representative images of two-color dSTORM recordings. From left to right: epifluorescence reference images, acquisition of image stacks with single fluorophore blinking events, pointillist dSTORM images reconstructed from single fluorophore localizations (after drift correction), and rendered super-resolution images in the far-red (A647) and the red (Cy3B) channels. Arrowheads point to beads in the region of interest (ROI) used for drift correction. Scale: 2 μ m.

far-red channel and Cy3B in the red channel (see Methods for sample preparation and imaging procedure). A647 and Cy3B are both carbocyanine dyes and are very sensitive to oxygen bleaching and to UV activation (Dempsey et al., 2011). The imaging buffer contains an oxygen-scavenging system for the removal of oxygen achieved by Glucose Oxidase and Catalase, and also the reducing agent β -mercaptoethylamine (MEA) to help the photo-switching of the dyes (Gloxy buffer) (Dempsey et al., 2011; Izeddin et al., 2011; Nahidiazar et al., 2016). We found that A647 dyes generally have more photo-switching cycles and can produce good detections of the synapses without UV activation in the Gloxy buffer compared to Cy3B. Hence, in our sequential two-color imaging procedure, we first record A647 signals without UV activation and then record Cy3B signals with fine-tuned UV activation. Moreover, in order to correct the lateral drift and to accurately register the two channels in the imaging data, we incubated the samples with fluorescent beads before mounting the coverslip on the microscope. The beads were detected continuously during the image recording, and were used as fiducial markers for drift correction and two-channel registration.

3.1.1.1 Fluorescent beads as fiducial marker

Drift correction and two-channel registration are important factors for reconstructing super-resolution images as well as co-localization analysis of synaptic components (Annibale et al., 2012). Since the recordings can take up to 30 minutes, the microscope stage can drift dramatically in the x/y plane due to mechanical and thermal effects (Figure 8.A). The perfect focusing system of our Nikon Ti microscope minimizes the drift in the axial direction. However, the lateral drift can still lead to false structural representations that demand correction. For stereotypic or densely labeled structures, the drift correction can be achieved by using the structures themselves as landmarks. But in the case of sparse synaptic clusters, there are too few detections for precise drift correction using the clusters themselves. Beads which are stably attached to the coverslip and continuously detected during the recording track the lateral drift of the stage precisely and therefore are better option for drift correction in fixed samples (Figure 8.B). For sequential two-color dSTORM, two-channel registration is also mandatory, because both lateral drift and spectral differences result in a mismatch between the reconstructed images in the two channels. Using beads as independent fiducial

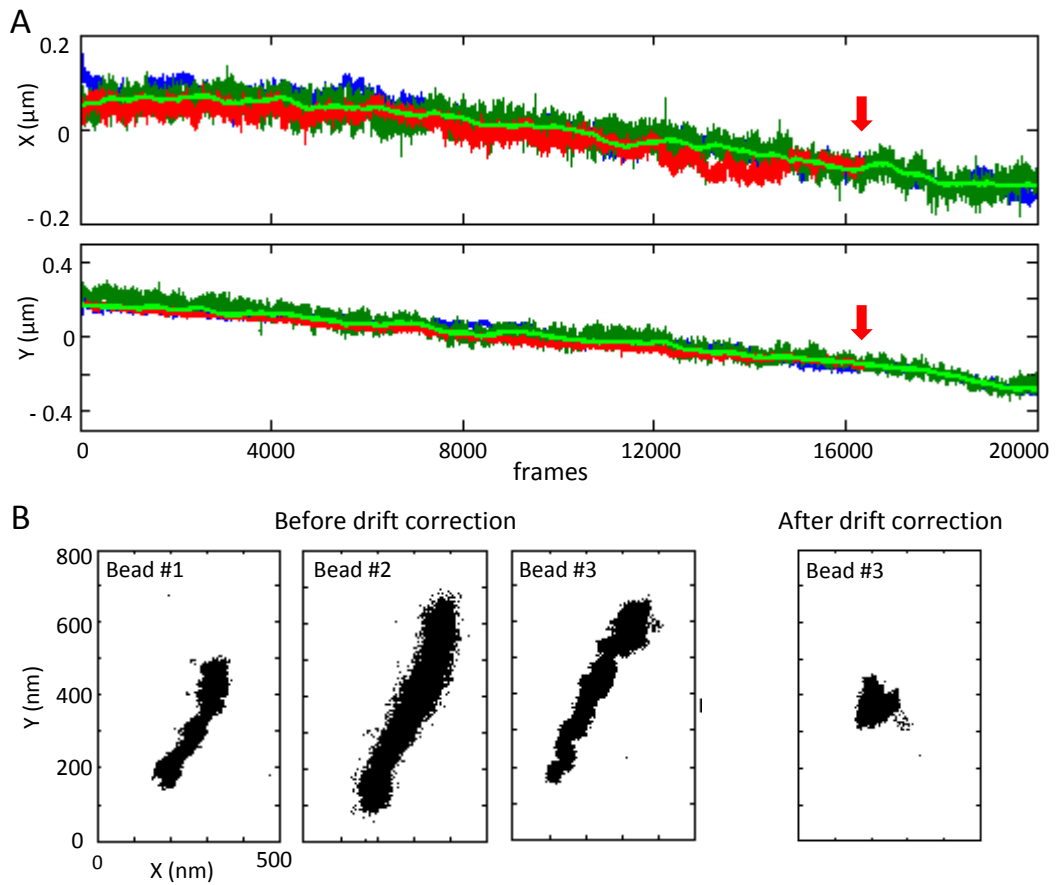


Figure 8. Drift correction with beads as fiducial markers.

(A) Apparent drift in the X and Y directions of three beads that were attached to the coverslip (red, green and blue traces). The bright green trace represents the average drift of the three beads, calculated with a sliding window of 500 frames. (B) Projection of the detection coordinates of the three beads before drift correction (left panels) and bead #3 after drift correction (right). Note that the lateral drift of the beads can differ; bead #1 is lost after frame 16000, and #2 is less bright and therefore has lower localization precision.

markers are more precise in the two-channel alignment than using the synaptic clusters. In conclusion, beads are important tools in our two-color dSTORM protocol.

3.1.1.2 Performance evaluation of chosen dyes

In addition to the signal to noise ratio (SNR), the dSTORM image quality depends largely on the photo-blinking behavior of the dyes, which is influenced by many factors (e.g. chemical traits of the dyes, imaging buffer composition, laser power). The evaluation of the individual factors is important for understanding their influence on the quality of the dSTORM data. However, the final image quality depends on the combined effect of these factors that are heavily inter-dependent. To assess the performance of the dyes, we carried out the optimized two-color dSTORM protocol using two secondary antibodies, conjugated with either A647 or Cy3B.

Clean glass coverslips were incubated for one hour with A647-conjugated donkey anti-mouse IgG and Cy3B-conjugated donkey anti-rabbit IgG that were diluted in 3% BSA and mounted with beads and Gloxy buffer. We then performed sequential two-color dSTORM imaging of these secondary antibodies. We characterized the clusters produced by single secondary antibodies in the two channels. Both A647-IgG and Cy3B-IgG produced nanometer scale clusters with a wide variability in the number of detections per cluster as well as cluster size (Figure 9.A). From the temporal profiles of the blinking events of a single secondary antibody probe, we can infer the photophysical behavior of the dyes. For A647, the blinking events are brief and dispersed across the entire recording (Figure 9.B). Cy3B fluorophores on the other hand display relatively few blinking events across the recording. Some Cy3B dyes showed persistent ON times, resulting in bursts of repetitive detections of a single blinking event, contributing to artifactual cluster identification. As a consequence, Cy3B produces detection densities that are less quantitative than those of A647. The diameter of the clusters produced by single IgG in both channels is around 40 to 120 nm (Figure 9.C), which corresponds to the localization precision of the fluorophores. These apparent clusters are also similar to the size of the subsynaptic domains (SSDs) proposed for synaptic proteins (Haas et al., 2018; Macgillavry et al., 2013; Nair et al., 2013; Tang et al., 2016). Therefore, the

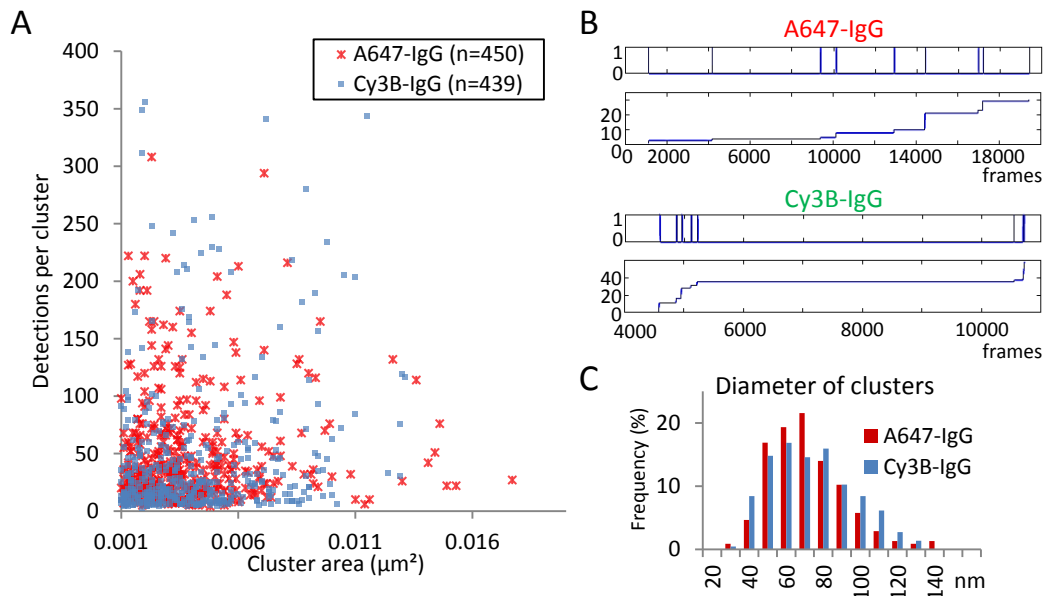


Figure 9. Blinking profiles of the dyes conjugated to secondary antibodies.

Two-color dSTORM imaging was done on sparsely distributed secondary antibodies coupled with Alexa Fluor 647 (A647-IgG) or Cy3B (Cy3B-IgG). (A) A large variability in the number of detections and cluster area for each dye-coupled IgG was observed. (B) Representative time traces of single A647-IgG and Cy3B-IgG detections in dSTORM show that the blinking of Alexa 647 is more dispersed than that of Cy3B (the upper boxes show the number of detections per frame, the lower boxes the cumulative detections). (C) Dye-coupled IgGs produce apparent nanoclusters with diameters ranging from 40 nm to 120 nm, as a result of multiple detections with limited localization precision.

detection density and the size of the clusters from single probes have to be taken into account during data analysis and data interpretation when characterizing subsynaptic domains.

3.1.2 Two-color dSTORM data analysis protocol

The first-hand data produced from SMLM recordings are the coordinates of the single molecule detections and the fluorescence intensity of the single signals. From the coordinates of the single molecules, an image containing the super-resolved fine structures can be rendered, with the pixel intensity representing the localization density (Coltharp et al., 2014). Both types of datasets are very useful for statistical analysis. Nevertheless, each type has its own strengths and drawbacks during analysis in practical terms.

The coordinates-based data in principle make the best use of single molecule localizations. However, the localization precision is usually neglected in the analytical methods developed so far. Moreover, cluster segmentation, feature extraction and spatial correlation analysis on the coordinates-based data demand qualified programming skills. On the other hand, the rendered super-resolution images give more intuitive information, and can be analyzed using common image processing tools that are widely known to researchers. More importantly, in the rendered images, pixel values represent the density of the localizations, taking into account the average localization precision. Since the SMLM coordinates are not the actual positions of the fluorophores but only calculated positions, they can also be understood as localization probabilities. The inclusion of the localization precision in image rendering thus produces more realistic representations. In addition, pixels that do not contain any localizations have the value of zero. In other words, there is no background in the rendered super-resolution images. Thus, there is no need for background subtraction or thresholding, which is often one of the major difficulties in fluorescent image processing.

In terms of available analysis tools, there are some open-source software for coordinates-based data, such as Clus-Doc and LAMA (Andronov et al., 2016; Levet et al., 2015; Malkusch & Heilemann, 2016; Pigeon et al., 2016). However, these tools are not very suited to the specific demands of synaptic clusters. In our

case, we did not find any available analysis tools that would allow us to perform individual synapse-based analysis, which is essential for the comparison of two synaptic proteins at the same synapse (e.g. GlyRs and GABA_ARs at mixed synapses). As for the rendered images, individual synaptic clusters can be obtained and characterized with commonly used image processing tools, such as Fiji (Schindelin et al., 2012) and Icy (De Chaumont et al., 2012). Image-based analysis of synaptic clusters is relatively straightforward and less demanding on programming skills. Therefore, we have built up a complete analysis workflow for image-based data analysis (Figure 10). In addition, we also developed a coordinate-based data analysis program together with the bioinformatics platform in our institution (Delestro and Genovesio, IBENS, Figure 12).

3.1.2.1 Image-based data analysis workflow

There are three main parts in this workflow: image alignment, segregation of the image into individual synaptic clusters, and synaptic cluster characterization (Figure 10.A).

Images requiring alignment include the rendered images from the two channels and the mask images produced from the epifluorescence images (Figure 10.B). The rendered images from the two channels have substantial mismatch due to the chromatic difference between the two channels and also the drift correction. The conventional epifluorescence images captured right before dSTORM imaging are used as references in order to identify synaptic clusters and to create binary masks for synaptic clusters. We adopt the combined mask image from the binary images to ensure the inclusion of the whole synaptic clusters from both channels (Figure 10.B). In this part of the workflow, the rendered images and the combined mask images are aligned with the aid of TurboReg plugin (Thevenaz et al., 1998) in Fiji.

In the second part, the regions of interest (ROIs) representing individual synaptic clusters are chosen from the aligned mask images. These ROIs are applied to the aligned rendered images in order to crop the individual synaptic clusters in Fiji. On the images of individual synaptic clusters, regions outside the ROIs are cleared and the clusters with saturated pixels are removed from the analysis. The clusters with saturated pixels could be artefacts on the coverslip, or they could be caused by

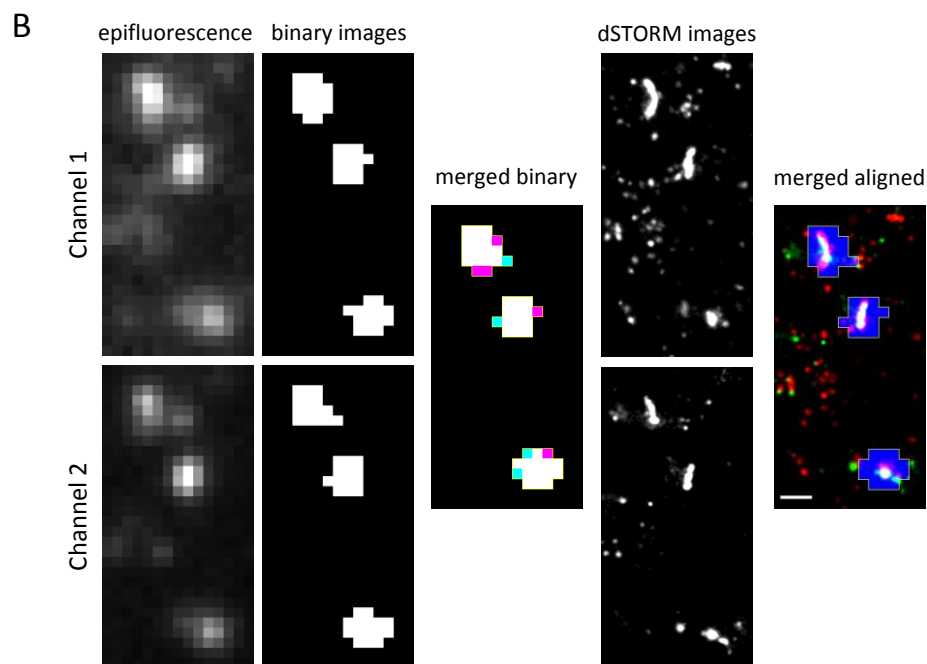
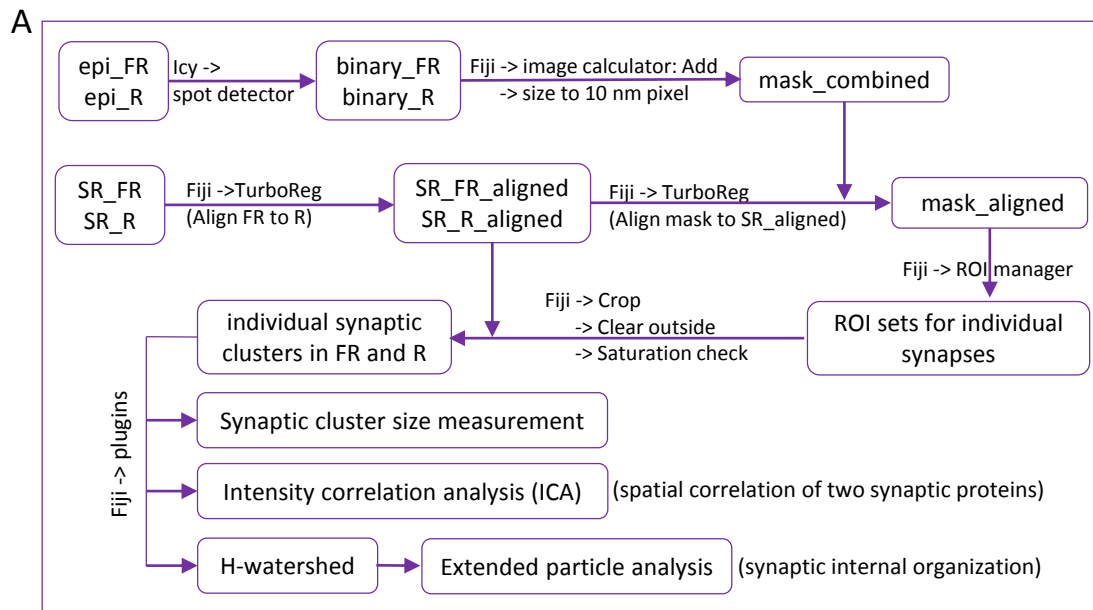


Figure 10. Image-based data analysis workflow. (continued in next page)

(continued)

Figure 10. Image-based data analysis workflow.

(A) The pipeline of data analysis using rendered images, starting from top-left and following the arrows. (B) Example images illustrating the synaptic masks and image alignment. Left: epifluorescence images and their derived binary images (channel 1 in magenta, channel 2 in cyan); right: dSTORM images and the alignment with the masks (channel 1 in red, channel 2 in green, masks in blue and outlined in yellow). Note that the summed area of the binary clusters from the two channels is used for the masks. Scale bar: 500 nm.

repetitive detections of some persistent blinking events (e.g. beads). At this point, we obtained individual synaptic cluster pairs of two synaptic proteins (e.g. GlyR and gephyrin), on which we can perform further cluster characterization.

The third part includes measuring the super-resolution synaptic cluster size, the spatial correlation between the two channels and the internal synaptic organization of the two target proteins.

To measure the cluster size, we applied a mild thresholding on the individual synaptic clusters and used Fiji *Measure* function. The purpose of thresholding is to reduce the impact from outlier detections around the synapses while remaining the most of the synaptic cluster area.

To characterize the spatial correlation of two synaptic proteins, we employed the intensity correlation analysis (ICA) plugin (Khanna et al., 2006; Li et al., 2004). The ICA plugin incorporates several different correlation analysis methods, including intensity correlation quotient (ICQ), Pearson's correlation coefficient (PCC), Mander's overlap coefficient (MOC) and Mander's correlation coefficient (MCC). ICQ measures the frequency of pixels which co-vary in intensity relative to their mean intensity in the two channels. ICQ values range between -0.5 and +0.5, where -0.5 indicates a mutually exclusive distribution, zero a random distribution, and +0.5 a perfectly positive correlation between the two proteins (Li et al., 2004). PCC and MOC measure the linear correlation of the pixel intensity from the two channels (Dunn et al., 2011; McDonald and Dunn 2013). They are mathematically similar, except that MOC uses absolute intensity values and PCC uses the deviation from the mean intensity. PCC values range from -1 to +1, with +1 indicating perfect positive correlation. Values that are negative or close to zero are difficult to interpret in fluorescent images. MOC values range from 0 to +1, with larger values indicating better correlation. MCC (MCC1 and MCC2) calculates the percentage of the total intensity in one channel which overlaps with the non-zero pixels in the second channel, and vice versa. These methods adopt different principles and have their own merits and drawbacks. The use of several methods together can compensate the drawbacks and provide more information about the data.

To characterize the internal synaptic organization of target proteins, we set out to

segment the synaptic clusters into subsynaptic domains (SSD). An H-watershed method was adopted to segment SSDs by using the interactive H-watershed plugin developed by Benoit Lombardot (http://imagej.net/Interactive_Watershed) in Fiji. H-watershed finds local maxima with one parameter, H, allowing the detection of intensity peaks and the segmentation of the subdomains from the whole synapse. After SSD segmentation, the features of the binary SSDs are extracted using extended particle analyzer (Brocher, 2014) in Fiji. The number of SSDs per synapse and the size of the SSDs are obtained, which reflect the intra-synaptic protein organization.

3.1.2.2 Verification of the different intensity correlation approaches with an exemplary dataset

The methods provided in ICA plugin (i.e. PCC, MOC, MCC, ICQ) all have their own limitations in measuring the correlation of fluorescent signals in the two channels. Therefore, we tested the analytical capability of these methods using our experimental data.

We stained the synapses for RIM1/2 and gephyrin and then conducted two-color dSTORM on these samples. Because RIM1/2 is not specific to inhibitory synapses but also exists at excitatory synapses, we can divide the synapses into two groups: one group with both RIM1/2 and gephyrin staining, and the other group with only RIM1/2 staining (Figure 11.A). The classification of the two groups was based on the binary masks produced from the epifluorescence images. The synapses with overlapping binary masks are classified into group one, and the synapses with only RIM1/2 masks are classified into group two. Due to the image thresholding, RIM1/2 clusters with very weak gephyrin staining are also attributed to group two. This is not a problem in our test. In fact, RIM1/2 clusters with weak gephyrin staining can mimic the situation where synaptic protein (e.g. neurotransmitter receptor) levels are reduced under certain experimental conditions. Moreover, due to the stochastic blinking behavior of the dyes, the weakly stained synapses can sometimes be detected with high localization density, producing bright dSTORM clusters comparable to those of brightly stained synapses. This can cause error in the comparison of spatial correlation between different experimental conditions (e.g. pharmacological treatment). Therefore, we took into account these two groups of

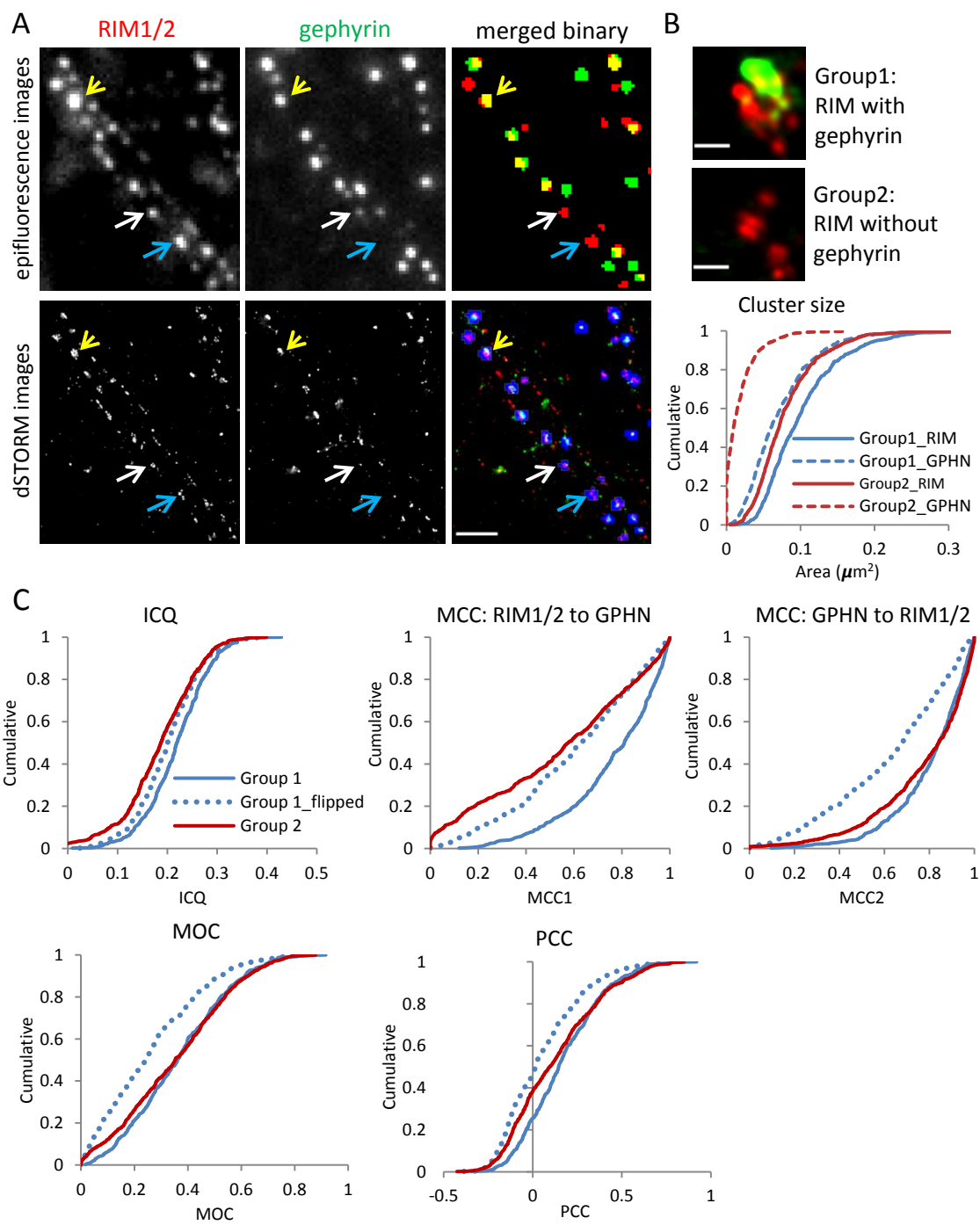


Figure 11. Verification of the different intensity correlation approaches with an exemplary dataset. (continued in next page)

(continued)

Figure 11. Verification of the different intensity correlation approaches with an exemplary dataset.

(A) Epifluorescence and dSTORM images illustrating the criteria for classifying the two groups of clusters: RIM1/2 with gephyrin (group 1) and RIM1/2 without gephyrin (group 2). Group 1 includes all the clusters with both RIM1/2 and gephyrin well stained (yellow arrow), producing overlapping binary clusters; group 2 includes clusters with RIM1/2 well stained but no gephyrin staining (blue arrow) or very weak gephyrin staining (white arrow), thus producing no binary gephyrin clusters. RIM1/2 was labeled with A647 and gephyrin with Cy3B. Scale bar: 2 μ m. (B) Individual synaptic cluster pairs were obtained and measured for their area. Example synaptic cluster pairs from the two groups are shown on the top, and the cluster size is shown on the bottom. Scale bar 200 nm. (C) The spatial correlation of RIM1/2 and gephyrin clusters was measured with several approaches incorporated in the ICA plugin. The spatial correlation of RIM1/2 and gephyrin clusters in group 1 was significantly reduced when gephyrin clusters were flipped vertically, measured by all the approaches (t-test, $p < 0.00001$). Group 1 has stronger spatial correlation than group 2 as measured by ICQ (t-test, $p < 0.00001$) and MCC (t-test, MCC1, $p < 0.00001$; MCC2, $p = 0.015$). MOC does not detect a difference between group 1 and group 2 (t-test, $p = 0.296$), and PCC values are mostly negative or close to zero in the two groups. Note that in the ICQ measurement, about 2% of the values in group 2 are negative and are cut off from the curve. Number of synapses: group 1, $n = 536$; group 2, $n = 709$; from three independent experiments.

cluster pairs in our test.

We carried out the analysis workflow as described above. We first measured the size of the synaptic clusters to verify the two groups of synapses (Figure 11.B). As expected, the area of gephyrin clusters from group two is dramatically smaller than that of group one, because there was none (~20% of the clusters) or very few detections of gephyrin in group two.

Next, we compared the spatial correlation of the super-resolution clusters in the two channels between group one and group two (Figure 11.C). ICQ measured a higher correlation in group one than group two. MCC measurement also showed a significant difference between the two groups. In the MCC test, the fraction of RIM1/2 signals co-localized with gephyrin is much higher in group one than in group two. This is because there are strong gephyrin signals in group one to produce large overlaps with RIM1/2. On the other hand, the fraction of gephyrin signals co-localized with RIM1/2 is similar in the two groups, even though gephyrin signals were dramatically different. This is because RIM1/2 signals were strong in both groups and produced large overlaps to include most of the gephyrin signals in both conditions. PCC and MOC did not detect a difference of spatial correlation between the two groups. Given that the detections of gephyrin clusters in group two are very few, as also seen from the cluster size, it is reasonable that the spatial correlation between gephyrin clusters and RIM1/2 clusters in group two could be lower than that of group one. Thus, the impact of few detections in one channel on the spatial correlation was detected by ICQ and MCC.

Furthermore, we vertically flipped the gephyrin clusters in group one, in order to verify the robustness of these spatial correlation approaches. This flipping created a situation where the clusters were somewhat scrambled, mimicking a negative control with low spatial correlation. Indeed, the spatial correlation of group one was reduced after flipping the gephyrin clusters, which was shown by all the four methods (Figure 11.C). This means that these methods are able to test the change in the spatial correlation between two synaptic clusters.

MOC treats the pixels with low red and high green signals as equal to median red and median green signals, where the latter apparently has better correlation. Thus,

MOC measures mostly co-occurrence. PCC is similarly calculated as MOC, except that PCC normalizes the signals to its mean in each channel. Though PCC values close to +1 can mean perfect positive correlation, values close to -1 do not mean negative correlation and values close to zero are difficult to interpret in fluorescent images. ICQ counts the pixels which increase or decrease in synchrony in the two channels, thus it measures the co-variation of signals. However, the pixels with intensity close to the mean and the pixels with much higher intensity are treated as the same. MCC provides a more straightforward colocalization measurement and it is easy to interpret. The major drawback of MCC is that it is very sensitive to background noise, because it takes all the non-zero pixels in one channel to produce the mask for the other channel. Taken together with the results in our test, we employed the ICQ and MCC tests in our following experiments as a measure of spatial correlation.

3.1.2.3 SRclusters: coordinates-based data analysis tool

Super-resolution cluster analysis (SRclusters) is a tool developed in collaboration with Delestro and Genovasio (IBENS) for the characterization of clusters using coordinate-based data (Figure 12). It is written in Python language and based on a Jupyter Notebook. The main algorithms adopted here are the density-based spatial clustering of applications with noise (DBSCAN) and the nearest neighbor distance (NND). DBSCAN needs two pre-defined parameters: the search radius (ϵ) and the minimal number of points (*minPts*). NND needs one pre-defined parameter: the number of nearest neighbors (x). It then calculates the average distance between each point and its x neighbors. With these two algorithms, the segmentation of clusters and characterization of spatial correlation are enabled in SRclusters. A user manual is shown in the Appendix 3.

There are four steps in the SRclusters program (see Appendix 3). Step one performs the segmentation of the clusters by DBSCAN and the registration of the two channels by aligning the bead as fiducial marker (Figure 12.A-B). Step two removes the beads from the clusters by thresholding the persistence of detections in the recording. Beads are generally detected throughout the whole recording and have high persistence of detections. Step three detects the cluster pairs from the two channels based on their centroid distance. Only the paired clusters are passed

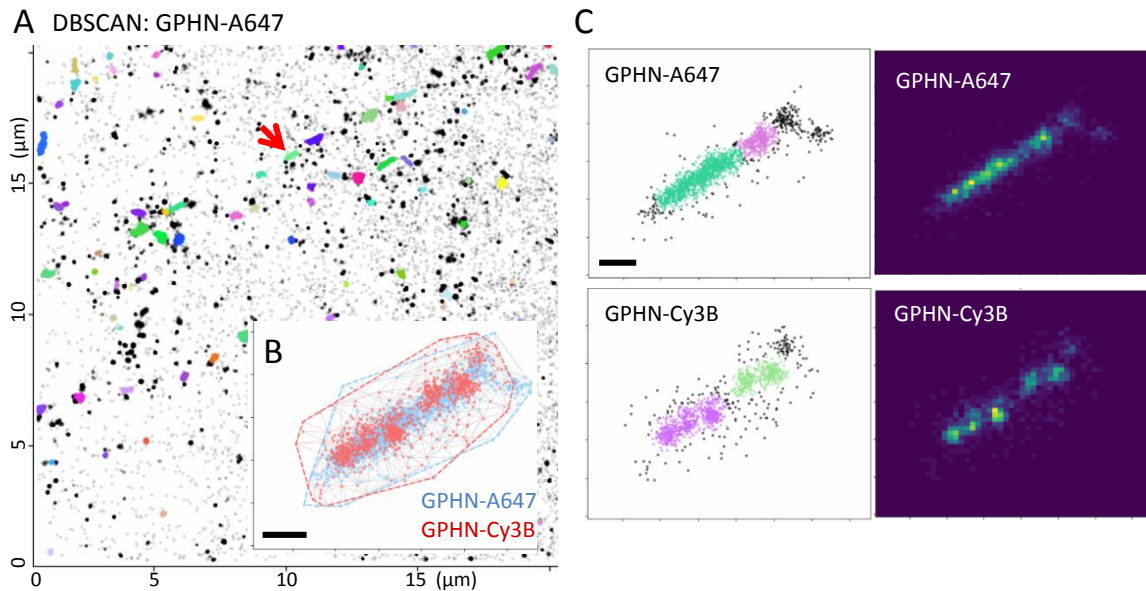


Figure 12. SRclusters: a coordinates-based data analysis tool.

(A) Pointillist image showing gephyrin molecules detected with Ae647, and the cluster segmentation with DBSCAN. Color-coded clusters are segmented gephyrin clusters; small black clusters and grey points are considered as noise. (B) The aligned gephyrin cluster pair detected in the two channels, corresponding to the cluster indicated by the red arrow in (A). Scale bar: 100 nm. (C) The same gephyrin cluster pair as in (B) displayed separately, either as pointillist image (left) or density hot map (right). The colored subdomains in the left are gephyrin SSDs segmented with density-weighted DBSCAN. Scale bar: 100nm.

onto step four. In this last step, we characterize the spatial correlation of the paired clusters, the features of the clusters and the subsynaptic domains (SSDs). The spatial correlation of the paired clusters is characterized with NND. For each point (i) in the first channel, the algorithm searches for the x nearest neighbors in the second channel, and calculates the mean distance for that point (NND_i). Then the NND_i of all the points in the first channel are averaged (MEANNND_{channel-1}). This is also performed for the second channel to obtain the mean of the NND_i of all the points in the second channel (MEANNND_{channel-2}). Then, the absolute difference between the means of the inter-cluster NND of the two channels (|MEANNND_{channel-1} - MEANNND_{channel-2}|) is assigned as the NND distance score for the spatial correlation. The score has a scale in nanometers and a smaller value indicates higher spatial correlation. Furthermore, the SSDs are segmented at individual synaptic clusters by a modified DBSCAN algorithm (Figure 12.C). The user defined minPts is weighted by its cluster density to generate the effective minPts (i.e. effective minPts = user define minPts × cluster density). In the end, the features of synaptic clusters and SSDs are extracted, including the number of points, area and localization density. Therefore, SRclusters can provide us with information from the coordinate-based data (see section 3.1.4.2).

3.1.3 The impact of low protein copy number on the imaging data

The low copy number of synaptic proteins impede the requirement of dense labeling in STORM. This challenge can be more evident when the synaptic protein is down-regulated under certain conditions such as altered neuronal network activities. When the synaptic cluster is weakly labeled with fluorescent dyes and the dyes do not have many blinking cycles, the majority of fluorescent signals can be lost during the pre-bleaching step and only a few detections are obtained during the recording. When rendered, the few localizations will give rise to very weak clusters. For instance, we compared the rendered clusters of gephyrin and GABA_ARs both labeled with Cy3B. In this case, gephyrin clusters were densely labeled and had good brightness and contrast, while GABA_AR clusters were weakly labeled and had poor brightness and contrast (Figure 13). Though gephyrin clusters detected with Cy3B gave rise to clear and complete clusters in the dSTORM image, GABA_ARs detected with Cy3B failed to show clear clusters. Noticeably, there were many bright clusters at non-synaptic sites in the dSTORM image of GABA_AR-Cy3B,

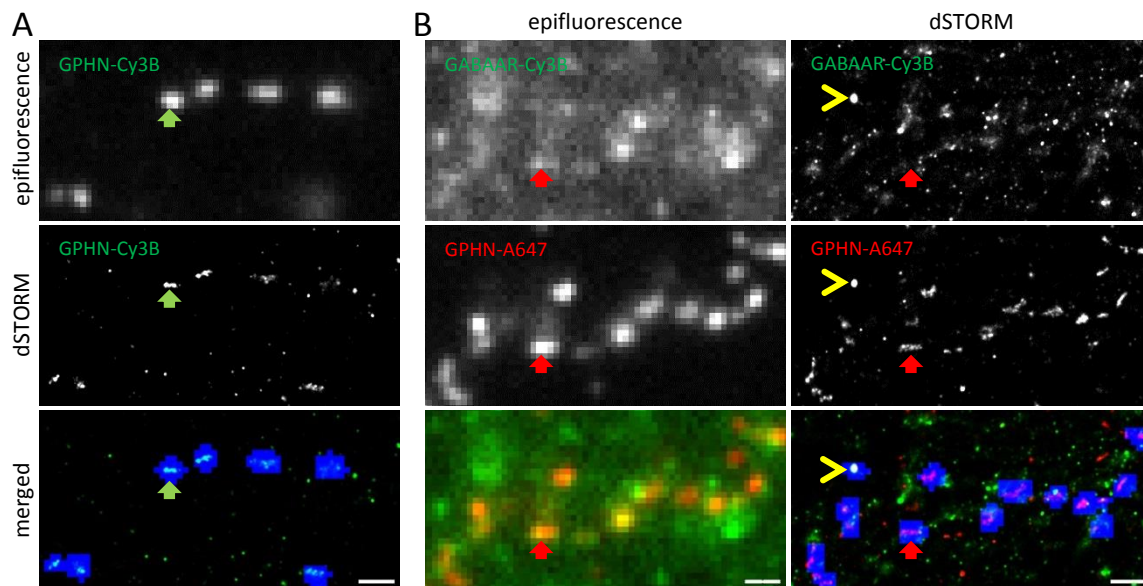


Figure 13. The effect of low copy numbers of synaptic proteins on the cluster integrity in dSTORM images.

(A) Gephyrin clusters that were labeled with IgG-Cy3B showed good brightness and contrast in the epifluorescence image, thus also produce nice super-resolution clusters in the dSTORM image (green arrow). (B) When the same secondary IgG-Cy3B was used to label GABA_AR, some GABA_AR clusters were only weakly stained, and had a poor contrast (top left). Synaptic GABA_AR clusters could barely be identified from the dSTORM image, especially with many signals in the surroundings (top right). Gephyrin was stained with Alexa 647 to confirm the identity of synaptic clusters in the images (middle). Red arrow indicates an example synapse. Yellow arrowhead points to a bead in the ROI, showing that the images were properly aligned. Scale bar: 1 μm. Note that the brightness and contrast in the Cy3B channel was differently adjusted in (A) and (B) to ensure visibility of the clusters.

which did not co-localize with gephyrin clusters in the dSTORM image. These bright clusters might reflect the extra-synaptic GABA_ARs, which were weakly stained but repetitively detected in the dSTORM recording. As a consequence, the weak synaptic clusters could be overwhelmed by the extra-synaptic detections during the image rendering. Therefore, the weak immuno-labeling due to the low protein copy number at synaptic sites can result in a few detections, challenging the cluster integrity in dSTORM images and causing uncertainty in the cluster characterization.

3.1.4 Dyes have a strong impact on the detected synaptic structure characterization

3.1.4.1 The impact of dyes on dSTORM synaptic clusters explained by their blinking profiles

Given the different blinking behaviors of the various dyes, the same structures may be detected and represented differently in the super-resolution images (Dempsey et al., 2011). Indeed, we found that the reconstructed structures of the same gephyrin clusters labeled with both A647 and Cy3B showed similar but not identical cluster patterns (Figure 14.A). In this experiment, gephyrin was labeled with both A647 and Cy3B through a common primary antibody and two secondary antibodies conjugated with either A647 or Cy3B. Favorably, the two clusters reconstructed from A647 and Cy3B detections showed similar overall shape and size, and they overlapped well with each other. However, the internal signal distribution of the clusters showed different levels of heterogeneity and different patterns of organization. The pointillist images of the clusters confirmed this discrepancy (Figure 14.B). From the coordinate-based data, we could look into the temporal profiles of the localizations in the corresponding clusters (Figure 14.C). Gephyrin clusters detected with A647 contained abundant localizations that were detected throughout the recording. The number of localizations over time had a smooth increment, demonstrating that the detections were well separated temporally. On the other hand, gephyrin clusters detected with Cy3B showed detection bursts and gaps in the profile. Sometimes there were no detections at all across hundreds of frames, while at other times bursts of detections happened. This created a heterogeneous profile of the localizations in the cluster. If we zoomed into the dense

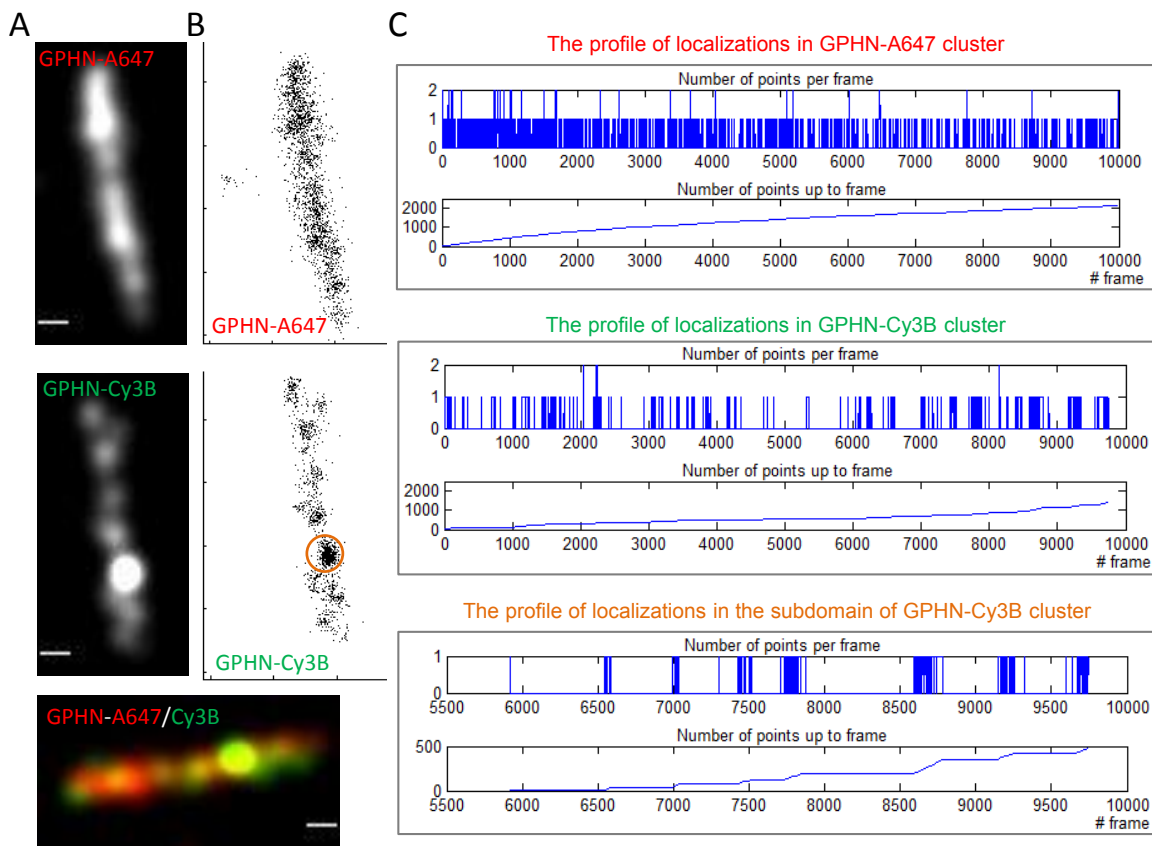


Figure 14. The impact of dyes on dSTORM synaptic clusters explained by their blinking profiles.

(A) The reconstructed dSTORM images of the same gephyrin cluster detected with A647 (top) and Cy3B (middle) are not identical. A647 or Cy3B conjugated secondary antibodies which recognize the same primary gephyrin antibody m7a were used. The merged image is rotated by 90° to the left. Scale bar: 100nm. (B) Pointillist images of the same two clusters. (C) The localization profiles of the clusters. Gephyrin cluster detections with A647 increase linearly over time (top), while GPHN-Cy3B localization profile shows gaps and bursts (middle). The dense subdomain in the GPHN-Cy3B cluster (orange circle in B) in fact is caused by repetitive detections of a few blinking events only.

subdomain in the gephyrin-Cy3B cluster, we found that most of the localizations in this subdomain were concentrated in a few bursts. The bursts of detections likely resulted from the persistent fluorescence of the Cy3B dyes during the ON phase of the blinking cycles. It is noteworthy that the profiles of the localizations from A647 and Cy3B shown here corresponds well with their blinking behavior characterized with secondary antibodies (Figure 9). In sum, different dyes may produce non-identical cluster patterns even for the same object.

Next, we quantitatively assessed the discrepancy of the cluster patterns detected with A647 and Cy3B. GlyRs were labeled, via one common primary antibody and two secondary antibodies conjugated with either A647 or Cy3B. GlyR clusters were well stained with good brightness and contrast in both channels according to the epifluorescence images (Figure 15.A). In the dSTORM images, GlyR-A647 clusters were generally well reconstructed. However, not all the GlyR-Cy3B clusters were properly reconstructed in the dSTORM image (Figure 15.A). As expected, the reconstructed GlyR clusters from A647 and Cy3B detections showed similar overall shape but differential internal signal distribution (Figure 15.B). However, the measured size of the same GlyR clusters is much larger with A647 ($0.107 \pm 0.052 \mu\text{m}^2$, mean \pm SD) than with Cy3B ($0.044 \pm 0.036 \mu\text{m}^2$) (Figure 15.C). We further looked into the internal organization of the GlyR clusters detected by these two dyes. We applied H-watershed to segment the subsynaptic domains (SSDs) in GlyR-A647 and GlyR-Cy3B clusters, with the same parameters for both channels (Figure 15.D). The SSD numbers per synaptic cluster in GlyR-A647 and GlyR-Cy3B had a moderate correlation (Pearson's method, $R^2 = 0.302$). The average number of SSDs per synapse in the two channels were similar (GlyR-A647: 2.31 ± 1.23 ; GlyR-Cy3B: 2.20 ± 1.40). Notably, the measured size of the SSDs in GlyR-A647 ($0.031 \pm 0.023 \mu\text{m}^2$) is much larger than those in GlyR-Cy3B ($0.011 \pm 0.011 \mu\text{m}^2$). Altogether, our data showed that the different photophysical properties of A647 and Cy3B dyes have strong impact on the quantification of synaptic clusters in dSTORM images.

In the two experiments discussed above, we cannot rule out that the competition between the two secondary antibodies for the primary antibody binding sites can influence this observed discrepancy. However, we did not observe exclusive spatial

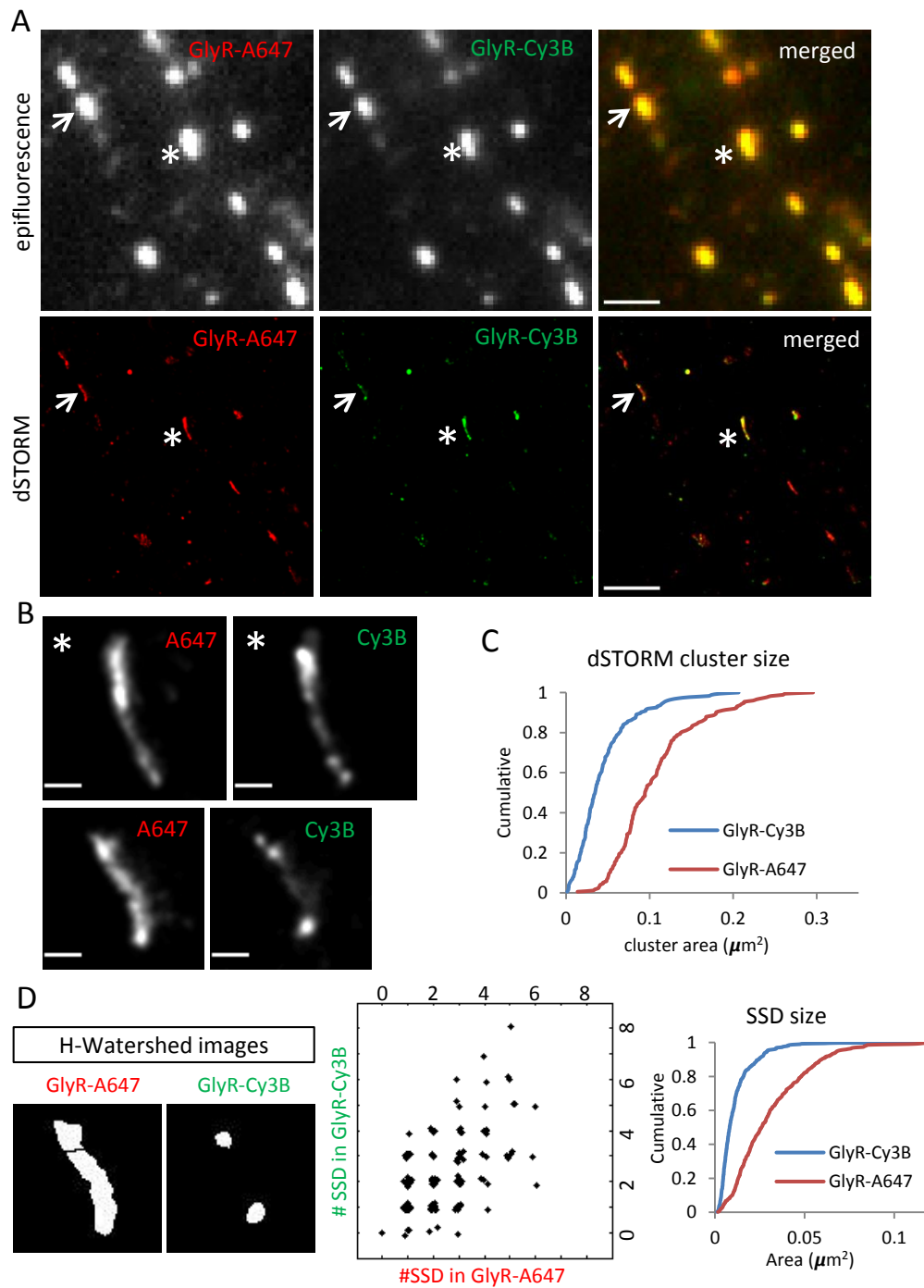


Figure 15. Strong impact of fluorescent dyes on the reconstructed synaptic clusters in dSTORM. (continued in next page)

(continued)

Figure 15. Strong impact of fluorescent dyes on the reconstructed synaptic clusters in dSTORM.

(A) GlyR clusters were labeled with the same primary antibody and two different secondary antibodies (GlyR-A647 and GlyR-Cy3B). The stained clusters showed good brightness and contrast in the two channels and also good overlapping in the epifluorescence images. In dSTORM, GlyR-A647 clusters are generally well detected and reconstructed. But GlyR-Cy3B clusters are not all as well reconstructed. Scale bar: 2 μ m. (B) Close view of the two marked synapses in (A), with one synapse with good reconstruction in both channels (top) and one with poor reconstruction in the Cy3B channel (bottom). Scale bar: 200 nm. (C) The size of GlyR-Cy3B clusters ($0.044 \pm 0.036 \mu\text{m}^2$) is dramatically smaller than that of GlyR-A647 ($0.107 \pm 0.052 \mu\text{m}^2$, t-test, $p < 0.00001$). Note that the same thresholding was used for both channels during the size measurement. (D) The internal heterogeneity of the clusters detected in the two channels is not the same. SSDs are segmented with the H-watershed approach (left). The SSD counts of the same GlyR cluster detected in two channels have a good agreement in the SSD numbers (middle; Pearson's $R^2=0.302$). The SSD size shows significant differences in line with the whole cluster size. The measured size of the SSDs in GlyR-A647 ($0.031 \pm 0.023 \mu\text{m}^2$) is much larger than those in GlyR-Cy3B ($0.011 \pm 0.011 \mu\text{m}^2$) (right, t-test, $p < 0.00001$, 416 subclusters for GlyR-A647 and 396 subclusters for GlyR-Cy3B). Number of synapses: $n=180$, from two independent experiments.

distribution of A647 and Cy3B signals in the same synapse, which could have resulted from the antibody binding competition. Besides, GlyR-A647 and GlyR-Cy3B showed good spatial correlation. Therefore, antibody binding competition may contribute to, but cannot be the main cause of the observed discrepancy in the dSTORM clusters.

3.1.4.2 The impact of reversing the dyes on the synaptic clusters in dSTORM images

Given the impact of dyes on the detection of the same synaptic clusters in dSTORM, we further assessed the effect of reversing the pair of dyes on the synaptic clusters. We used two different primary antibodies which recognized different epitopes on gephyrin. Primary mouse monoclonal mAb7a (m7a) and rabbit polyclonal antibodies against gephyrin (rbGPHN) were labeled, in one case with Cy3B-conjugated donkey anti-mouse IgG and A647-conjugated donkey anti-rabbit IgG (condition 1), and in the other case with A647-conjugated donkey anti-mouse IgG and Cy3B-conjugated donkey anti-rabbit IgG (condition 2) (Figure 16). In agreement with our observations in Figure 15, gephyrin clusters detected with A647 and Cy3B exhibited similar overall shape but differential internal organization (Figure 16.A). Also, the size of the gephyrin clusters detected with A647 was consistently larger than those with Cy3B, regardless of the primary antibodies (rbGPHN-A647: $0.090 \pm 0.047 \mu\text{m}^2$; m7a-Cy3B: $0.040 \pm 0.022 \mu\text{m}^2$; m7a-A647: $0.079 \pm 0.036 \mu\text{m}^2$; rbGPHN-Cy3B: $0.051 \pm 0.027 \mu\text{m}^2$). Importantly, the spatial correlation in the second condition was significantly stronger than that in the first condition, as judged from the ICQ values (Figure 16.B). MCC analysis also revealed differences in the level of overlap from one channel to the other between the two labeling conditions. This raised alert to that the spatial correlation level can be changed simply by reversing the dyes on the target proteins.

On the other hand, we segmented the subsynaptic domains (SSDs) of gephyrin clusters (Figure 16.C). Taking into account the effects of the fluorophores as revealed in Figure 15, we adopted different H-watershed parameters that were optimized for A647 and Cy3B channels. In each labeling condition, there was a weak correlation of the SSD counts per synapse in the two channels (Pearson's, $R^2=0.103$ for condition 1, $R^2=0.096$ for condition 2). In fact, the SSD numbers per

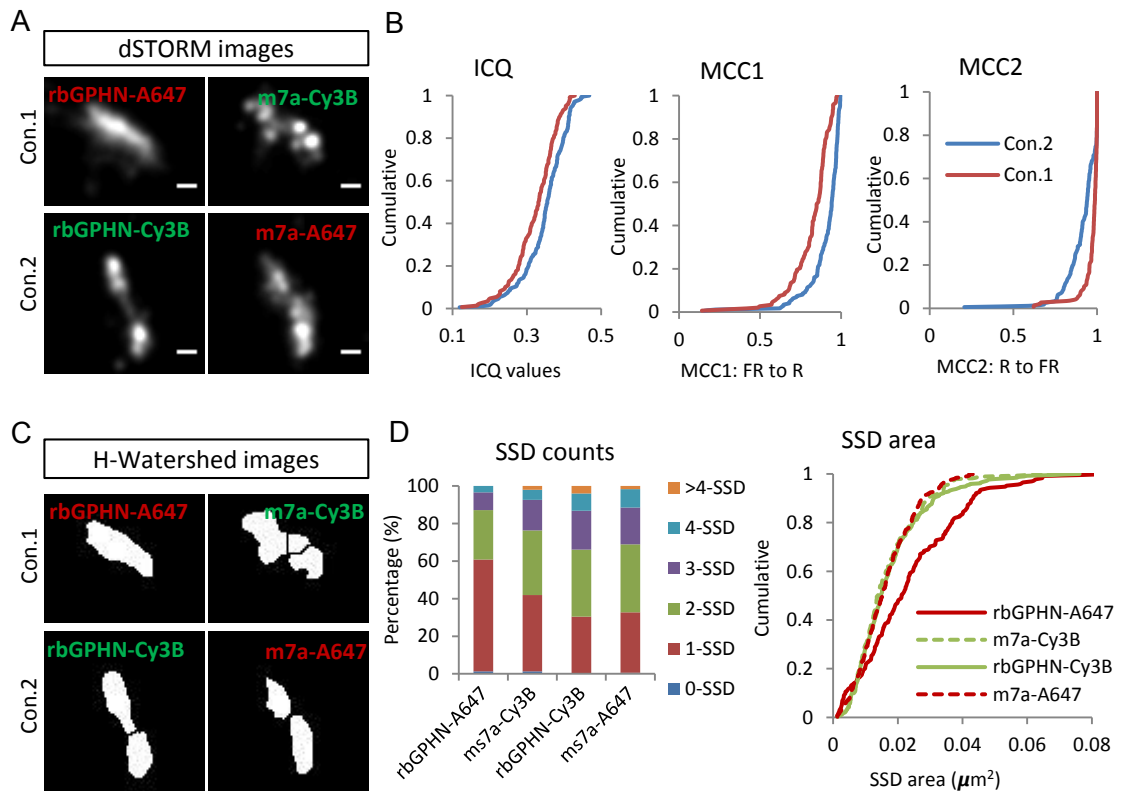


Figure 16. Image-based analysis of dye reversal experiments of gephyrin in two-color dSTORM.

(A) Gephyrin was labeled with two different primary antibodies, followed by two combinations of secondary antibodies. Scale bar: 100 nm. (B) The antibody combination rbGPHN-Cy3B/m7a-A647 (condition 2, $n = 174$ synapses) gave a significantly higher spatial correlation of gephyrin clusters in the two channels than the combination with reversed dyes (condition 1, rbGPHN-A647/m7a-Cy3B, $n = 148$), as shown by ICQ (t-test, $p < 0.001$). The MCC test (MCC1 and MCC2) also shows a significant difference of the overlap between the two channels (t-test, $p < 0.00001$ for both). (C) The segmented SSDs by H-watershed. (D) SSD counts per cluster for rbGPHN and m7a antibodies are influenced by the dyes different (rbGPHN-A647: 1.5 ± 0.8 ; m7a-Cy3B: 1.9 ± 1.1 ; m7a-A647: 2.1 ± 1.1 ; rbGPHN-Cy3B: 2.2 ± 1.2). SSD area detected by rbGPHN-A647 were significantly larger than by m7a-Cy3B (t-test, $p < 0.00001$), while the difference was not detected with the other antibody combination (t-test, $p = 0.064$).

synapse measured in the different conditions were very different (rbGPHN-A647: 1.5 ± 0.8 ; m7a-Cy3B: 1.9 ± 1.1 ; m7a-A647: 2.1 ± 1.1 ; rbGPHN-Cy3B: 2.2 ± 1.2) (Figure 16.D). Interestingly, the sizes of SSDs probed with rbGPHN-A647 were much larger than with m7a-Cy3B in the first condition. However, this difference was not seen in the second condition with reversed dye labeling. Therefore, the spatial correlation measurement and the SSD characterization can be influenced simply by reversing the dyes for the labeling.

To further validate our conclusions from the image-based analysis, the coordinate-based dataset from the same experiments was analyzed using SRclusters (Figure 17.A). The hull area of rbGPHN-A647 clusters was much larger than m7a-Cy3B clusters, while m7a-A647 clusters and rbGPHN-Cy3B clusters did not show much difference in size (rbGPHN-A647: $0.200 \pm 0.072 \mu\text{m}^2$; m7a-Cy3B: $0.090 \pm 0.050 \mu\text{m}^2$; m7a-A647: $0.121 \pm 0.055 \mu\text{m}^2$; rbGPHN-Cy3B: $0.120 \pm 0.066 \mu\text{m}^2$). It should be noticed that the hull area measured with SRclusters is about twice as large as the area measured in the image-based clusters. The reason is that the hull area includes all the outlier points surrounding the clusters, without thresholding. The spatial correlation level in the second labeling condition was consistently higher than in the first labeling condition as revealed by the score values (smaller score values indicate stronger spatial correlation) (Figure 17.B). The SSD counts per synapse did not show differences among the different labeling conditions (rbGPHN-A647: 1.9 ± 1.2 ; m7a-Cy3B: 1.7 ± 1.0 ; m7a-A647: 1.9 ± 1.1 ; rbGPHN-Cy3B: 2.0 ± 1.1) (Figure 17.C). However, the size of SSDs measured with the hull area confirmed the difference in size in the image-based analysis. In sum, the coordinate-based data analysis further confirmed that dyes have strong impacts on the characterizations of the detected synaptic clusters.

Apart from the impacts of the dyes on the detected clusters, these experiments also suggested that the gephyrin populations targeted by the two primary antibodies are not identical. If we assume that rbGPHN and m7a antibodies probe the same population of gephyrin molecules, it would be expected that the two labeling conditions would yield similar results in the spatial correlation and SSD measurements. However, it was not the case in our results. In fact, there was an obvious difference in the spatial correlation and SSD size between the two labeling

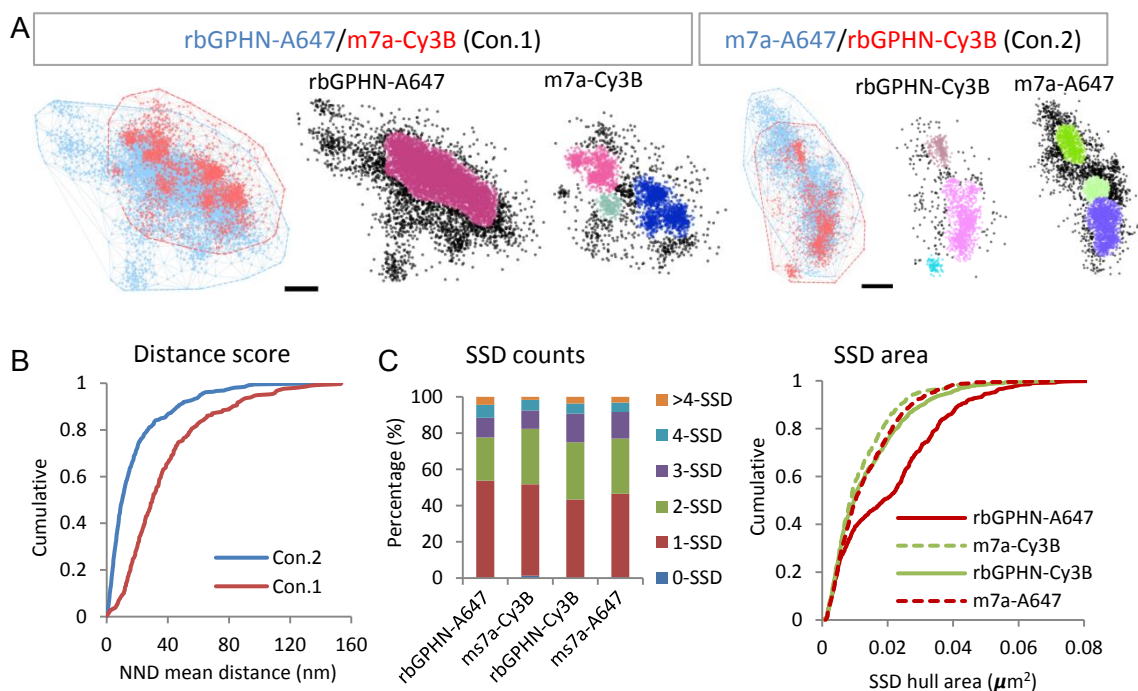


Figure 17. Coordinate-based analysis of dye reversal experiments on gephyrin using SRclusters.

(A) Pointillist images showing the aligned gephyrin clusters detected in the two channels and individual clusters segmented into SSDs in the two labeling conditions. Scale bar: 100 nm. (B) Smaller distance score in condition 2 (18 ± 21 nm) indicates a stronger spatial correlation of gephyrin clusters detected in the two channels than in condition 1 (38 ± 29 nm, t-test, $p < 0.00001$). (C) SSD counts per cluster are affected by the dyes, but to a lesser extent with the segmentation method in SRclusters (rbGPHN-A647: 1.9 ± 1.2 ; m7a-Cy3B: 1.7 ± 1.0 ; m7a-A647: 1.9 ± 1.1 ; rbGPHN-Cy3B: 2.0 ± 1.1) than that with H-Watershed (See Figure 16.D). The SSD hull area of rbGPHN-A647 ($0.021 \pm 0.016 \mu\text{m}^2$) is much larger than that of m7a-Cy3B ($0.012 \pm 0.010 \mu\text{m}^2$) in condition 1 (t-test, $p < 0.00001$). In condition 2, rbGPHN SSD area ($0.014 \pm 0.012 \mu\text{m}^2$) is larger than that of m7a SSD ($0.013 \pm 0.010 \mu\text{m}^2$) as well, but only with a small trend (t-test, $p = 0.261$). Note that the overall trend is similar as that in Figure 16.D. The dataset in this figure is the same as in Figure 16.

conditions. One possible explanation is that rbGPHN and m7a antibodies probe different sub-populations of gephyrin molecules. Indeed, the polyclonal rbGPHN antibodies target at the gephyrin E-domain, while the monoclonal m7a antibodies are known to target at a phosphorylated epitope (pS270) in gephyrin C-domain (Kuhse et al., 2012). In addition, Cy3B dyes tend to produce more granular clusters, while A647 dyes tend to produce more homogeneous clusters. Taken together the effects of the dyes and the primary antibodies, the different results of labeling condition one and condition two suggest that not all the gephyrin S270 sites are phosphorylated and that the pS270 sites may be distributed heterogeneously at the gephyrin lattice at the PSDs.

3.2 The study of mixed inhibitory synapses with two-color dSTORM

3.2.1 Post-synaptic proteins are heterogeneously organized and exhibit SSDs at mixed inhibitory synapses in spinal cord neurons

3.2.1.1 GlyR and gephyrin are heterogeneously distributed at inhibitory PSDs

In cultured spinal cord neurons, the majority of inhibitory synapses contain GlyRs (Dumoulin et al., 2000). Gephyrin as a scaffold protein for GlyRs has been described to have highly heterogeneous distribution and form SSDs (Pennacchietti et al., 2017a; Specht et al. 2013). Given the strong binding between GlyRs and gephyrin, we would expect that GlyR distribution exhibits similar heterogeneity at synaptic sites. To investigate the intra-synaptic organization of GlyRs at the PSD, we conducted two-color dSTORM imaging of GlyRs labeled with Cy3B and gephyrin with A647. The reconstructed clusters of GlyRs and gephyrin revealed the heterogeneity in the distribution of both proteins at synaptic sites (Figure 18.A). Generally speaking, the distribution of GlyRs matched well with gephyrin clusters. Meanwhile, from the intra-synaptic view, GlyRs form synaptic subdomains. The GlyR SSDs sometimes co-localize with gephyrin SSDs, and sometimes locate beside the gephyrin SSDs. To some extent, this mismatch can be explained by the three dimensional orientation of the synapses. Some of the PSDs were parallel to the imaging focal plane, exhibiting *en face* view, while others were seen from the side view (Figure 18.A). Given that only pS270 gephyrin molecules were labeled in this experiment, the mismatch of GlyR SSDs and

gephyrin SSDs suggests that the formation of GlyR SSDs may not be fully dependent on gephyrin phosphorylation. The GlyR SSDs which are beside the gephyrin SSDs in these synapses may be the ones stabilized by other non-phosphorylated gephyrin molecules. In other words, despite the direct interaction between GlyRs and gephyrin, their distribution at the PSDs is not perfectly matched.

We further characterized the number of SSDs for both GlyR and gephyrin clusters. Most of the gephyrin synaptic clusters had one to three SSDs, while the majority of GlyR synaptic clusters had one to four SSDs (Figure 18.B). The SSD counts for gephyrin and GlyR clusters showed a weak positive correlation. Moreover, the SSD counts of either gephyrin or GlyR synaptic clusters positively correlated with their synaptic cluster size (Figure 18.C), which is consistent with previous studies (Crosby et al., 2019; Fukata et al., 2013; Hruska et al., 2018; Nair et al., 2013). To summarize, our data suggest that GlyRs are organized heterogeneously and form SSDs at the inhibitory PSDs in spinal cord neurons.

3.2.1.2 GABA_ARs and GlyRs can occupy different spaces at mixed inhibitory PSDs

In cultured spinal cord neurons, GABA_ARs and GlyRs co-exist at ~70% of the inhibitory PSDs (Dumoulin et al., 2000). Whether these two types of receptors are homogeneously intermingled or they exclusively occupy different spaces at the PSD is not known. To investigate how these two types of receptors are organized at the same PSDs, we conducted two-color dSTORM imaging of GABA_ARs and GlyRs at the mixed inhibitory synapses. GABA_ARs were labeled with A647 and GlyRs with Cy3B. The reconstructed dSTORM images revealed that GABA_ARs have heterogeneous distribution and form SSDs at the inhibitory PSDs (Figure 19). The reconstructed structures of GlyR clusters further confirmed that GlyRs are heterogeneously distributed. Interestingly, GABA_ARs and GlyRs are not fully inter-mingled at the PSD, and they exhibit different patterns of spatial organization. GABA_ARs and GlyRs can occupy different spaces, as well as overlap with each other at the PSD. These observations raise the possibility that the spatial organization of GABA_ARs and GlyRs may be differentially regulated and can play a role in tuning the synaptic co-transmission.

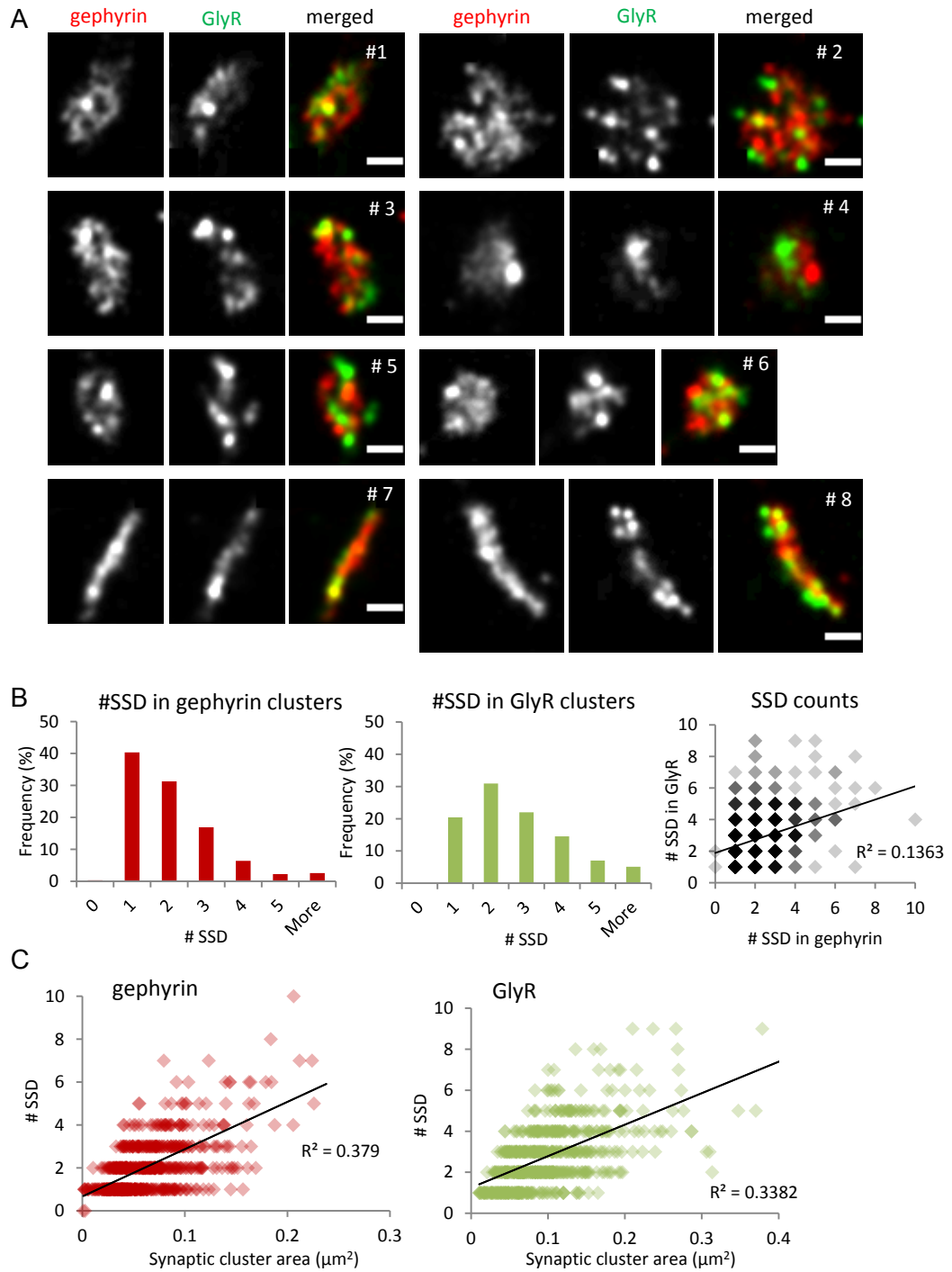


Figure 18. The heterogeneous distribution of GlyR and gephyrin at the inhibitory PSDs in spinal cord neurons. (continued in next page)

(continued)

Figure 18. The heterogeneous distribution of GlyR and gephyrin at the inhibitory PSDs in spinal cord neurons.

(A) Representative dSTORM images of synaptic GlyR and gephyrin clusters with putative *en face* view (#1-6) or side view (#7-8), showing the heterogeneity of the clusters and the spatial relationship between GlyR SSDs and gephyrin SSDs. Gephyrin was labeled with A647 and GlyR with Cy3B. Scale bar: 200 nm. (B) The SSD counts of GlyR and gephyrin clusters. There is a weak correlation between GlyR SSD counts and gephyrin SSD counts (Pearson's, $R^2= 0.136$). (C) Both gephyrin and GlyR SSD counts are moderately correlated with their synaptic cluster size (Pearson's, $R^2=0.379$ and $R^2=0.338$, respectively). Number of synapses: $n=627$, from three independent experiments.

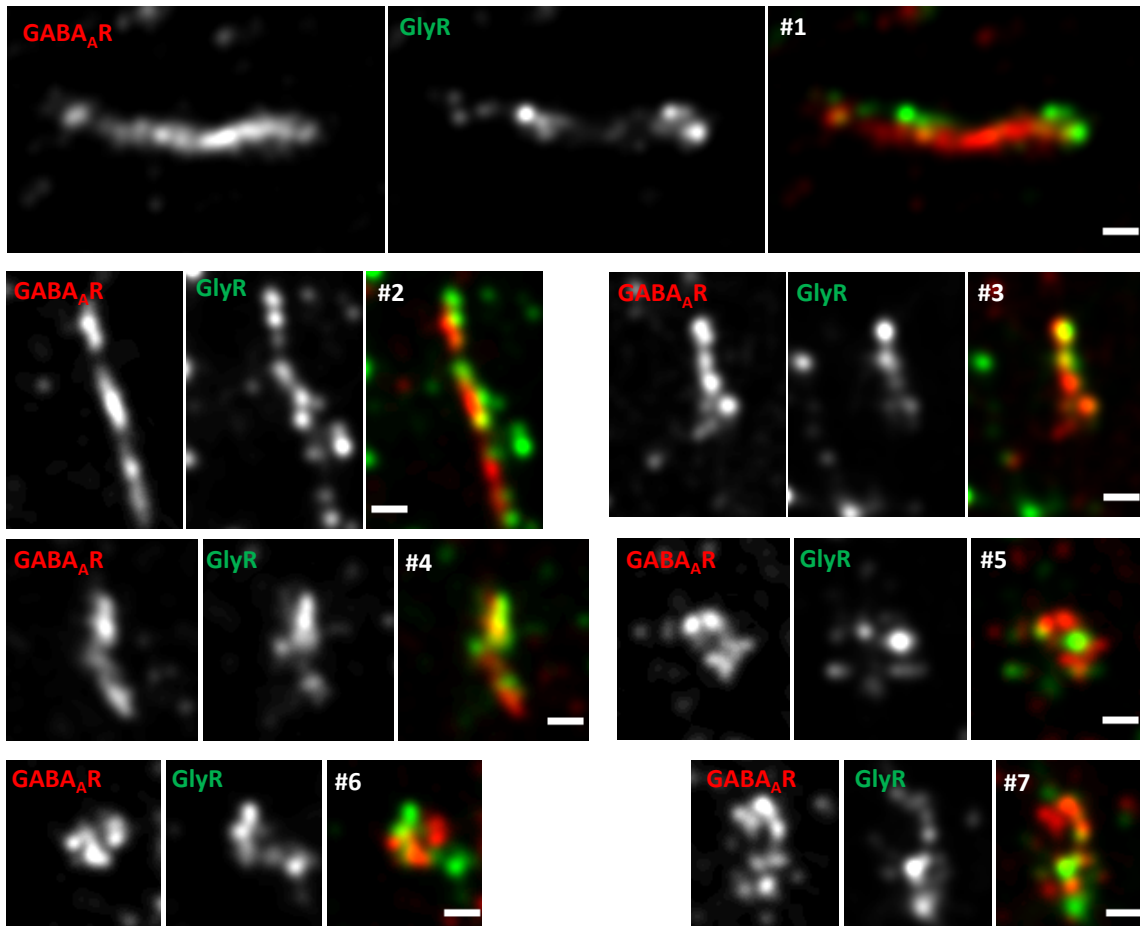


Figure 19. The heterogeneous distribution of GABA_ARs and GlyRs at mixed inhibitory PSDs and their different spatial organization.

Two-color dSTORM images of GABA_AR clusters (red) and GlyR clusters (green) at mixed synapses. GABA_ARs were labeled with A647 and GlyRs with Cy3B.

Scale bar: 200 nm.

In sum, our data provided the first evidence for the intra-synaptic organization of the key proteins at mixed inhibitory synapses, namely GABA_ARs, GlyRs and gephyrin. These three synaptic proteins are heterogeneously distributed and form SSDs. And they have different spatial organization patterns at the PSD. Their distinct spatial organization patterns suggest that intra-synaptic protein redistribution might serve as a regulator for neuronal activity. Previous studies have shown that GABA_ARs and GlyRs can be differentially regulated by neuronal activity in spinal cord neurons (Cantaut-Belarif et al., 2017; Lévi et al. 1999, 2008). Therefore, we next undertook an investigation of the intra-synaptic spatial organization of GABA_ARs and GlyRs under different neuronal network activities.

3.2.2 The copy numbers of synaptic GABA_ARs and GlyRs are differentially regulated by neuronal activity

Before the examination of the intra-synaptic protein organization at mixed inhibitory synapses, a fundamental question to be answered first is: how is the amount of the synaptic proteins regulated in response to different levels of neuronal activity? To answer this question, we adopted pharmacological methods to modulate the overall network activity in the cultured spinal cord neurons. We then used conventional epifluorescence microscopy to measure the total amount of synaptic proteins at inhibitory synapses. As widely used approach in biology, conventional fluorescence microscopy does not require the bleaching and switching of fluorescent signals. Therefore, conventional fluorescence imaging has less stochasticity in the measurement of synaptic protein quantity when compared to dSTORM imaging.

To modify the neuronal activity, we used TTX and 4-AP as pharmacological agents in our experiments. Tetrodotoxin (TTX) potently blocks voltage-gated sodium channels, thus blocking the action potential and diminishing the neuronal activity (Narahashi, 2008). 4-aminopyridine (4-AP) blocks voltage-gated potassium channels which are responsible for the repolarization during action potential, thus prolonging the action potential and increasing the neuronal activity (Zhang and McBain, 1995). TTX and 4-AP thus modulate the neuronal activity in opposite directions without directly interfering with the inhibitory synaptic proteins. We first evaluated the neuronal activity of spinal cord neurons with TTX

or 4-AP treatment using calcium imaging. Then, we investigated the effect of the altered neuronal activity on the protein copy numbers at mixed inhibitory synapses.

3.2.2.1 Calcium imaging showed the effect of TTX and 4-AP on the network activity of cultured spinal cord neurons

We compared the calcium signals of cultured spinal cord neurons before and after the administration of either TTX (1 μ M) or 4-AP (50 μ M). Calcium signals were recorded before, 5 min after and 20 min after the drug administration, with each recording lasting 3 min. Before the application of TTX or 4-AP, neurons had moderate level of activity (Figure 20.A). Five minutes after the drug application, the activity levels were clearly reduced by TTX, while the activity levels were dramatically increased by 4-AP. The effect was still present after 20 min as shown in the example signal traces. Moreover, we quantified the amplitude and frequency of the calcium signals (Figure 20.B). 4-AP significantly increased the calcium signal frequencies, but did not have strong effect on the amplitude. Because TTX abolished all the neuronal activity, we only took into account the calcium signals before the treatment. The frequency and amplitude of the calcium signals before treatment were similar in the two conditions as expected. In sum, TTX and 4-AP as pharmacological agents and their concentration used here are suitable to modulate the neuronal activity level of spinal cord neurons.

3.2.2.2 GABA_ARs and gephyrin, but not GlyRs immuno-reactivity is regulated by changes in network activity

Mature spinal cord neurons between DIV 14 and DIV 18 were used. TTX or 4-AP was diluted in the culture maintenance medium to the final concentration of 1 μ M and 50 μ M, respectively. Non-treated neurons from the same culture plate were used as control condition. After drug administration, cells were placed back in the incubator for one hour before fixation. We performed triple immunocytochemistry to stain GABA_ARs, GlyRs and gephyrin (m7a) simultaneously at mixed inhibitory synapses, which allowed us to compare directly their relative amount at the same synapses. Binary gephyrin clusters were used as masks to calculate the integrated intensity for all the three proteins.

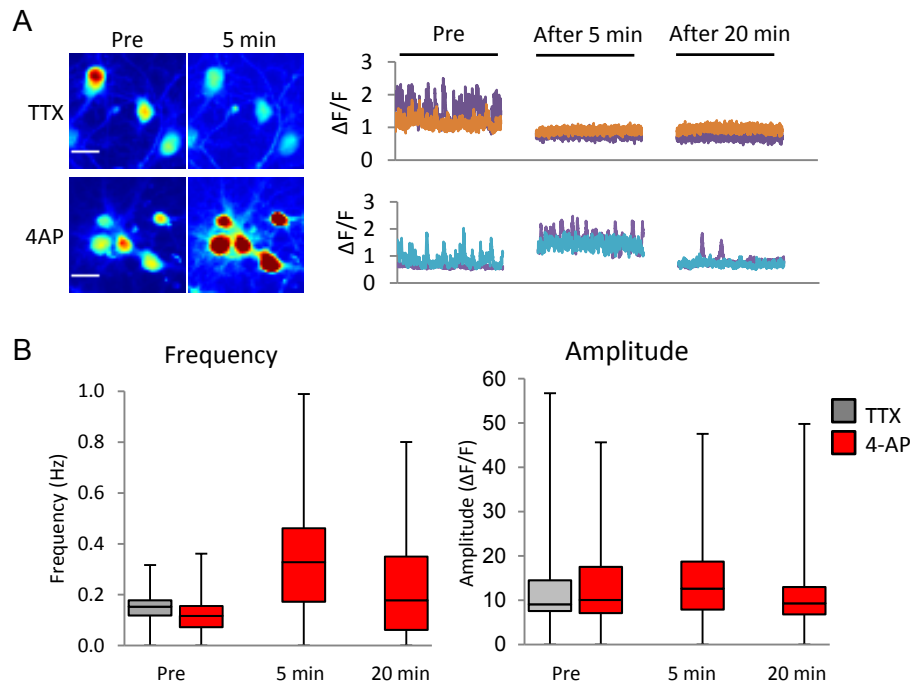


Figure 20. The effect of TTX and 4-AP on neuronal activity in cultured spinal cord neurons demonstrated by calcium imaging.

(A) Calcium signals are decreased after TTX treatment and increased after 4-AP treatment (left). On the right, time-lapse imaging of calcium signals showed the changes in neuronal activity for different cells (represented by different colors; top: TTX, bottom: 4-AP). Scale bar: 20 μm . (B) Quantification of the amplitude and frequency of the calcium signals. TTX blocks all the neuronal activity after its application, as judged by the lack of calcium signals. Five minutes after 4-AP treatment, the frequency was greatly increased (paired t-test, $p < 0.00001$) and the amplitude was slightly increased (paired t-test, $p = 0.025$). Number of cells: $n = 117$ in 4-AP treatment and $n = 70$ in TTX treatment, from three independent experiments.

In agreement with the previous studies in our laboratory (Dumoulin et al., 2000), GABA_ARs and GlyRs co-localized at most of the inhibitory PSDs marked by gephyrin clusters in spinal cord neurons (Figure 21.A). After 4-AP treatment, the integrated intensity of synaptic gephyrin and GABA_AR clusters were reduced comparing to the control condition, with a larger extent for gephyrin. However, the integrated intensity of synaptic GlyR clusters was not or only marginally reduced (Figure 21.B). On the other hand, TTX treatment did not have a strong impact on the accumulation of gephyrin or the receptors at the synaptic sites, compared to the control condition. To compare how the three proteins were affected at the same PSDs, we calculated the ratio of the integrated intensity of gephyrin and GABA_AR clusters over GlyR clusters at each synapse (Figure 21.C). The intensity ratio of gephyrin/GlyR showed that the intensity of gephyrin was reduced after 4-AP treatment, with respect to GlyRs at the same PSD. The lower intensity ratio of GABA_AR/GlyR indicated that GABA_ARs were removed to a larger extent than GlyRs from the same PSD in response to 4-AP treatment. The intensity ratio of GABA_AR/gephyrin was increased after 4-AP treatment. This suggested that gephyrin was reduced to a larger extent than GABA_ARs at the same PSD. In conclusion, increased neuronal activity by 4-AP treatment differentially regulated GABA_AR and GlyR amounts at mixed inhibitory synapses, while reduced neuronal activity by TTX treatment did not have a strong effect on their synaptic contents.

3.2.2.3 Gephyrin phosphorylation level but not the total molecular amount was reduced by increased neuronal activity

The primary antibody m7a that was used in the previous experiments detects gephyrin molecules which are phosphorylated at S270 sites in the C-domain (Kuhse et al. 2012). The phosphorylation at S270 sites has been shown to play an important role in regulating receptor clustering and inhibitory signaling (Groeneweg et al., 2018). The result in Figure 21 revealed that gephyrin immunoreactivity at synapses was reduced by 4-AP treatment. However, it did not determine whether gephyrin molecules were removed from synaptic sites or only the phosphorylation level was reduced in response to 4-AP treatment. Therefore, we conducted double immunocytochemistry of gephyrin with m7a antibody and another antibody recognizing gephyrin E-domain (rbGPHN). In principle,

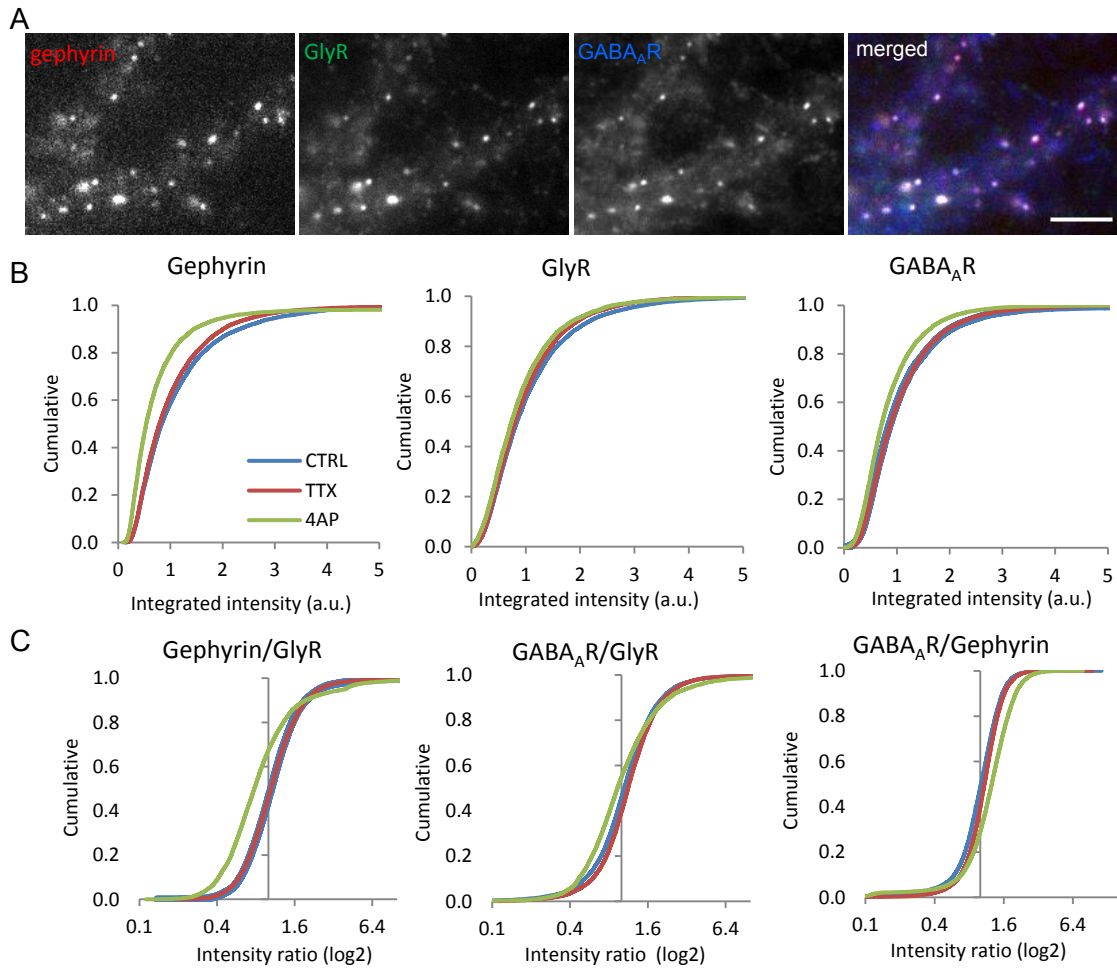


Figure 21. Reduced synaptic accumulation of GABA_ARs and gephyrin, but not GlyRs by 4-AP treatment.

(A) Triple staining of gephyrin, GlyRs and GABA_ARs at mixed inhibitory synapses. Scale bar: 5 μ m. (B) Fluorescence intensity of the synaptic clusters reveals the reduction of gephyrin and GABA_ARs, but not GlyRs after 4-AP treatment. Kolmogorov-Smirnov test with alpha at 0.01, significant between TTX and 4-AP conditions for gephyrin, GlyRs and GABA_ARs. (C) The intensity ratio of gephyrin/GlyR and GABA_AR/GlyR reveals the correlated change of these proteins at the same PSDs. Kolmogorov-Smirnov test with alpha at 0.01, significant between TTX and 4-AP conditions for gephyrin/GlyR, GABA_AR/GlyR and GABA_AR/gephyrin. Number of synapses: n=8856 in non-treated (CTRL) group, n=9416 in TTX condition, n=6949 in 4-AP condition; from three independent experiments.

rbGPHN antibodies should detect the entire gephyrin content (total gephyrin), while m7a antibodies detect the S270 phosphorylated gephyrin (p-gephyrin).

As expected, gephyrin clusters stained with rbGPHN and m7a matched very well with each other (Figure 22.A). We quantified the colocalization level of gephyrin clusters stained with the two different primary antibodies. For the large puncta, the binary clusters from the two channels always overlapped. The small puncta generally had low intensity and sometimes low contrast. Thus some of the small puncta were not detected in the second channel. Overall, the percentage of total gephyrin puncta overlapped with p-gephyrin puncta was around 85%, while that of p-gephyrin with total gephyrin was around 50% (Figure 22.B). The rbGPHN antibodies might also stain the extra-synaptic gephyrin molecules, increasing the fluorescence in the dendrites and decreasing the contrast of synaptic gephyrin clusters. On the other hand, the m7a antibodies might have high efficiency in recognizing their epitopes at gephyrin clusters. Thus, many small gephyrin clusters would be quantified with m7a staining but not with rbGPHN staining, which could result in a lower percentage in m7a (rbGPHN+) than in rbGPHN (m7a+) colocalization. Note that the treatment did not have dramatic effect on the degree of colocalization. Furthermore, we quantified the integrated intensity of the gephyrin clusters stained with these two primary antibodies. The total gephyrin stained with rbGPHN was not changed with either TTX or 4-AP treatment, while the gephyrin phosphorylation level was reduced by 4-AP treatment compared to TTX (Figure 22.C). The intensity ratio of p-gephyrin over total gephyrin per synapse was also reduced by 4-AP treatment versus TTX, confirming that gephyrin was dephosphorylated rather than removed from the synapses after 4-AP treatment. In addition, TTX treatment did not have much effect on the gephyrin cluster intensity compared to control condition.

In conclusion, increased neuronal activity by 4-AP treatment differentially regulates different synaptic proteins at mixed inhibitory synapses in spinal cord neurons. The GABA_AR amount was reduced by 4-AP treatment while the GlyR amount was not changed. Gephyrin remained at synaptic sites after 4-AP treatment. However, its phosphorylation level at the S270 site was dramatically decreased. These results suggest that gephyrin molecules probably form a stable

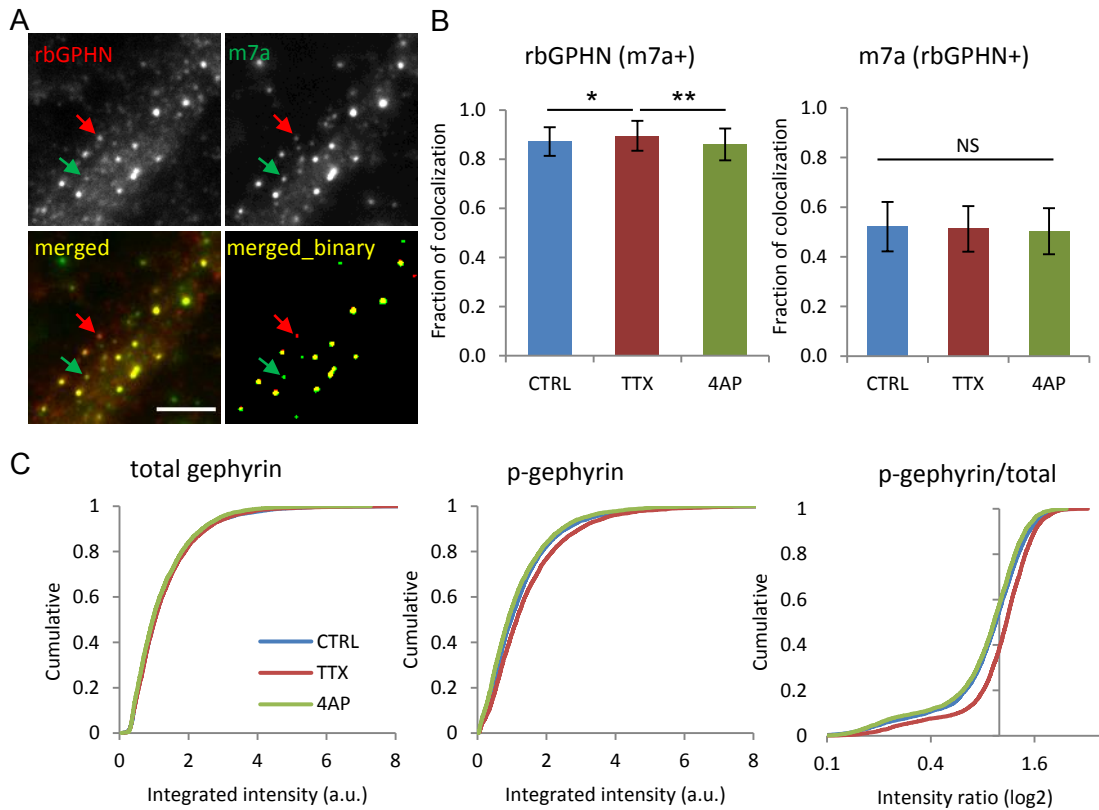


Figure 22. Reduced gephyrin phosphorylation level but not the total molecular amount at the inhibitory PSD by 4-AP treatment.

(A) Double staining of gephyrin with one antibody (rbGPHN) recognizing the gephyrin E-domain and another one (m7a) recognizing S270 phosphorylated gephyrin. Arrows point to weakly stained synapses, of which one produces only a rbGPHN mask (red arrow) and the other one produces only m7a mask (green arrow). Scale bar: 5 μm . (B) The colocalization level of the binary synaptic masks of rbGPHN and m7a clusters. Even though the colocalization level of rbGPHN with m7a showed a difference (t-test, $p < 0.05$ between CTRL and TTX, $p < 0.01$ between TTX and 4-AP), the treatment did not have a strong effect on the colocalization between rbGPHN and m7a. (C) The fluorescence intensity of total gephyrin was not changed by the treatment, whereas the p-gephyrin was reduced after 4-AP treatment (compared to TTX, Kolmogorov-Smirnov test, $p < 0.01$). The intensity ratio of p-gephyrin over total gephyrin shows that the gephyrin phosphorylation level was also reduced at the PSDs (Kolmogorov-Smirnov test, $p < 0.01$). Number of synapses: $n=3946$ in CTRL condition, $n=4040$ in TTX condition, $n=3818$ in 4-AP condition, from two independent experiments.

lattice at mixed inhibitory synapses, providing binding sites for receptors. Meanwhile, the phosphorylation level of gephyrin is closely regulated by neuronal activity. And the accumulation of GABA_ARs at mixed synapses is probably more associated with gephyrin phosphorylation level than that of GlyRs.

As shown before, GABA_ARs, GlyRs and gephyrin are heterogeneously distributed at mixed inhibitory PSDs. Since their copy numbers and phosphorylation status are differentially regulated in response to neuronal network activity, they may also undergo spatial re-organization during the altered activity. Next, we employed two-color dSTORM to investigate the intra-synaptic organization and the relative spatial correlation of the receptors and gephyrin after altering the neuronal activity by TTX and 4-AP.

3.2.3 Intra-synaptic re-organization of GlyRs, GABA_ARs and p-gephyrin during neuronal activity

The treatment of cultured spinal cord neurons with TTX and 4-AP was done as above. The fixed and immuno-stained samples were subjected to two-color dSTORM imaging afterwards. We compared the spatial distribution of GlyRs, GABA_ARs and gephyrin in a pair-wise manner as described in the methodology section. Note that the uncertainty of the neuronal baseline activity level in the non-treated coverslips was observed in our experiments and shown in Figure 21 and Figure 22. Therefore, we did not use the non-treated cells as control condition in the following two-color dSTORM experiments. Instead, we directly compared 4-AP treatment to TTX treatment conditions as representative of high and low neuronal activity levels, respectively.

3.2.3.1 The spatial association of synaptic GlyRs and p-gephyrin was increased after 4-AP treatment

We first performed two-color dSTORM imaging of p-gephyrin labeled with A647 and GlyRs labeled with Cy3B after treatment. Both gephyrin and GlyR clusters showed heterogeneous distribution at synapses and exhibited subsynaptic domains (SSDs), consistent with our earlier description (Figure 23.A, also see Figure 18). The overall size of gephyrin clusters was reduced by 4-AP treatment compared to TTX condition, while GlyR cluster size was not changed (Figure 23.B). This is in

line with the reduced immuno-reactivity of gephyrin clusters and sustained immuno-reactivity of GlyR clusters in our earlier results. The ICQ measurement indicated that the spatial association of GlyRs and gephyrin was increased by 4-AP treatment (Figure 23.C). This increased correlation in ICQ measurement can be attributed to the specific re-organization of synaptic GlyRs and p-gephyrin, because low level of proteins in one channel actually cause a decrease in the ICQ values (see Figure 11). MCC measurements did not indicate any differences between the two groups, suggesting that the overall overlap of one protein inside the boundary of the other protein assembly had not changed. Furthermore, we characterized the intra-synaptic distribution pattern of gephyrin and GlyRs by counting the SSDs. Neither gephyrin SSD nor GlyR SSD counts per synapse showed a difference between the two treatment groups (Figure 23.D). However, the gephyrin SSD area was reduced and the GlyR SSD area was increased by the 4-AP treatment, which is in agreement with internal re-organization of synaptic proteins.

As discussed in section 3.1.4, different dyes can have a strong impact on the detected synaptic clusters, influencing the spatial association and SSD measurements. In the case of p-gephyrin labeled with A647 and GlyRs with Cy3B, gephyrin clusters would be detected with less heterogeneity and more completeness due to the superior blinking properties of A647. This could potentially have an impact on the comparison between the two experimental conditions. Therefore, we reversed the dyes on gephyrin and the GlyRs for two-color dSTORM imaging to validate the effects of the treatment.

In the reversed color experiments, p-gephyrin was labeled with Cy3B and GlyR with A647 for dSTORM imaging (Figure 24.A). As expected, the cluster size was dramatically affected by the dyes (Figure 24.B). Different from the previous measurements, gephyrin cluster size was not decreased by 4-AP treatment in this case, while GlyR cluster size was slightly increased by 4-AP treatment. The spatial correlation measurements showed a trend towards higher ICQ values, which was consistent with the previous results (Figure 24.C). However, MCC measured an increase of gephyrin overlap with GlyRs by 4-AP treatment, in contrast to the earlier MCC measurements. On the other hand, the numbers of

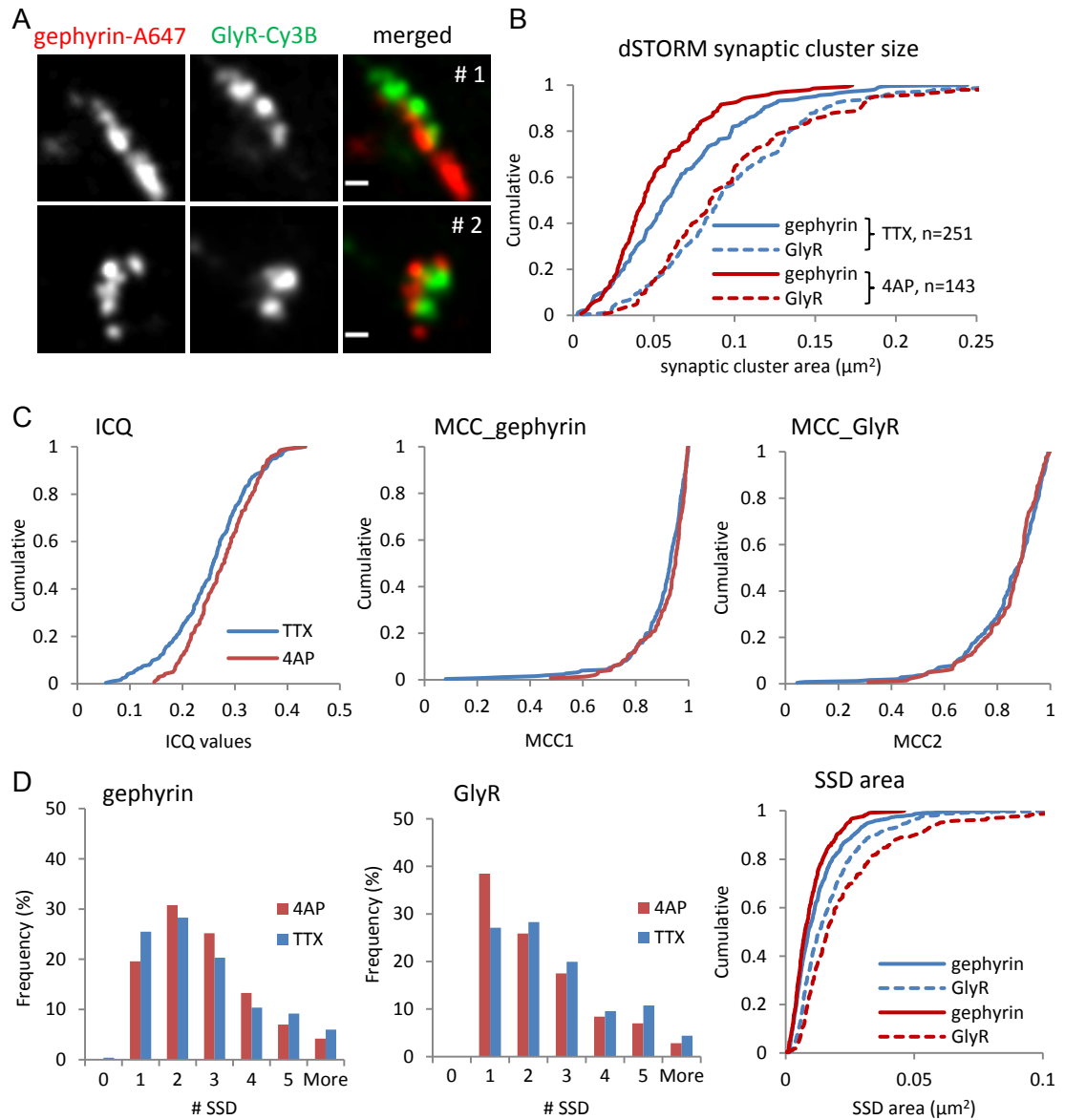


Figure 23. Increased spatial correlation of p-gephyrin and GlyRs by 4-AP treatment. (continued in next page)

(continued)

Figure 23. Increased spatial correlation of p-gephyrin and GlyRs by 4-AP treatment.

(A) Synaptic clusters of phosphorylated gephyrin labeled with A647 and GlyRs labeled with Cy3B in dSTORM images. Scale bar: 100 nm. (B) 4-AP treatment decreased gephyrin cluster area (t-test, $p < 0.001$), but not that of GlyRs (t-test, $p=0.785$). (C) The spatial correlation measurement of p-gephyrin and GlyRs. 4-AP treatment increased the spatial correlation compared to the TTX condition as judged by ICQ (left, t-test, $p < 0.01$). MCC test showed a minor increase of gephyrin overlapping with the GlyRs (middle, t-test, $p=0.125$), but not GlyRs overlapping with gephyrin (right). (D) The SSD measurements of gephyrin and GlyR clusters in the dSTORM images. No difference in the SSD counts was detected between the two treatment conditions. Gephyrin SSD area is decreased (t-test, $p < 0.0001$) and GlyR SSD area is increased (t-test, $p < 0.00001$) by 4-AP treatment. Number of synapses: $n=251$ in TTX condition, $n=143$ in 4-AP condition, from three independent experiments.

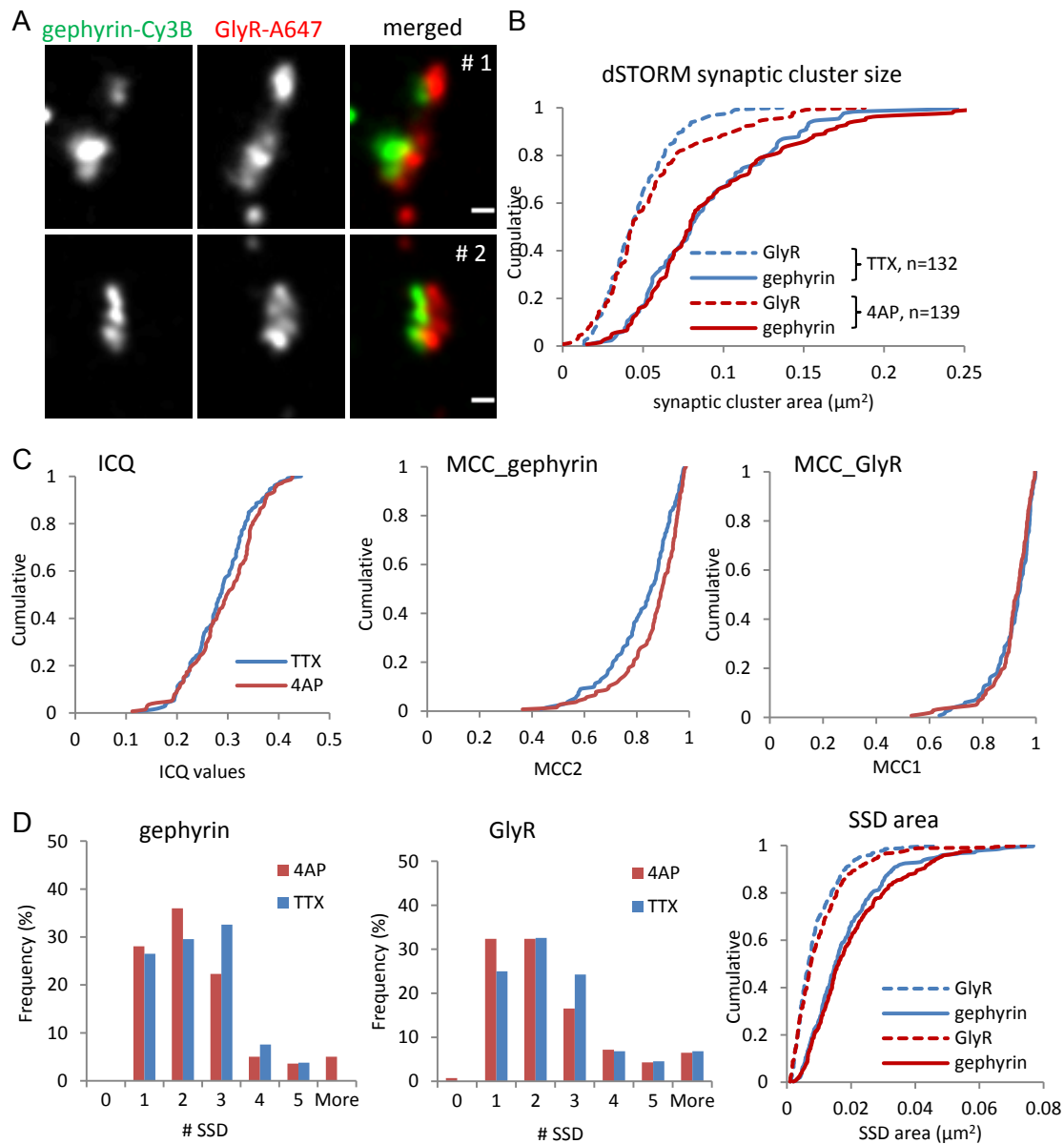


Figure 24. Increased spatial correlation of p-gephyrin and GlyRs by 4-AP treatment confirmed by reversed color experiments. (continued in next page)

(continued)

Figure 24. Increased spatial correlation of p-gephyrin and GlyRs by 4-AP treatment confirmed by reversed color experiments

(A) Synaptic clusters of p-gephyrin labeled with Cy3B and GlyRs with A647 in dSTORM images. Scale bar: 100 nm. (B) No difference in gephyrin cluster area is detected between the two conditions (t-test, $p=0.407$), and GlyR cluster size is slightly larger in 4-AP than TTX condition (t-test, $p=0.039$). (C) Spatial correlation measurement of gephyrin and GlyRs. ICQ showed a small but not significant increase in the spatial correlation after 4-AP treatment (left, t-test, $p=0.253$). MCC test showed a significant increase of gephyrin overlapping with GlyR (middle, t-test, $p=0.0038$), but not for GlyR overlapping with gephyrin (right). (D) The SSD measurements of gephyrin and GlyR clusters in the dSTORM images. No difference in the SSD counts was detected between the two treatment conditions. Gephyrin SSD area is marginally larger in 4-AP than in TTX condition (t-test, $p=0.129$), as well as GlyR SSD area (t-test, $p=0.0195$). Number of synapses: $n=132$ in TTX condition, $n=139$ in 4-AP condition, from two independent experiments.

SSDs per gephyrin or GlyR cluster did not differ between the two treatment groups, consistent with earlier results (Figure 24.D). Moreover, the SSD area was strongly affected by the dyes as well, but did not show a difference between conditions. In fact, the SSD area always showed similar trend as the synaptic cluster area. This means that the dyes have an impact not only on the synaptic cluster size measurement, but also on the SSD size measurement.

In summary, by reversing the dyes on the target proteins, we again manifested the strong impact of the dyes on the synaptic cluster measurements. Favorably, ICQ measurements were consistent in the two scenarios with reversed dyes. This suggests that the spatial correlation between GlyRs and gephyrin increased after 4-AP treatment, and that ICQ values are good read-out for these ultra-structural changes. In addition, SSD counts for gephyrin and GlyR clusters per synapse were not changed in both scenarios by the treatment. It is necessary to point out that some analysis methods may not be robust enough for the synaptic colocalization measurement in dSTORM images. Even though MCC was able to indicate the colocalization difference between RIM1/2 with gephyrin at synapses and RIM1/2 without gephyrin (Figure 11), it failed to produce consistent results when the dyes were reversed on gephyrin and GlyRs (Figure 23 and Figure 24). Moreover, the measured synaptic cluster size and SSD size were strongly affected by the dyes. Therefore, in the following experiments, we did not take the MCC and cluster size measurements into consideration for understanding the synaptic organization. But we included these data in the figures in order to fully present the results.

Taken together these results, the spatial correlation between GlyRs and p-gephyrin was increased by 4-AP treatment as measured with ICQ. The SSD counts of GlyR and p-gephyrin clusters did not change. As shown in Figure 22, the gephyrin phosphorylation level was largely reduced by 4-AP treatment while the total gephyrin molecules stayed constant. Therefore, the SSD counts likely reflect the internal synaptic heterogeneity, rather than the structural units as synaptic building blocks. In conclusion, these results suggest that GlyRs and p-gephyrin may undergo intra-synaptic re-distribution toward a stronger spatial association during increased neuronal activity.

3.2.3.2 GABA_ARs exhibit increased spatial association with both p-gephyrin and GlyRs during increased neuronal activity

The synaptic GABA_AR content was significantly lower after increasing the neuronal activity with 4-AP treatment, compared to the TTX treated condition (Figure 21). GABA_AR molecules might be removed from the PSD sites either randomly or from particular sites. In order to resolve which population of GABA_ARs were removed from the synaptic sites, we examined the spatial relationship of GABA_ARs with p-gephyrin and with GlyRs by pairwise two-color dSTORM experiments.

First, we conducted two-color dSTORM imaging of p-gephyrin labeled with A647 and GABA_ARs with Cy3B (Figure 25.A). The higher ICQ values after 4-AP treatment indicated that the spatial correlation between GABA_ARs and p-gephyrin was increased (Figure 25.C). The increase in ICQ values is probably due to a specific re-organization of synaptic proteins, because low protein level in one channel actually causes a reduction in the ICQ values (see Figure 11). GABA_AR SSD and p-gephyrin SSD numbers per synapse were not changed (Figure 25.D). These results suggest that GABA_AR molecules were not removed randomly from the PSD. GABA_ARs may be lost at the sites where p-gephyrin level is decreased, thus leaving the remaining GABA_ARs and p-gephyrin with higher spatial correlation. Another possibility is that the retained GABA_ARs may undergo re-distribution to associate more closely with the remained p-gephyrin sites.

Next, we conducted two-color dSTORM imaging of GlyRs labeled with A647 and GABA_ARs with Cy3B (Figure 26.A), in order to examine the change in their spatial correlation. ICQ measurements indicated that the spatial correlation of GABA_ARs and GlyRs was also increased by the 4-AP treatment (Figure 26.C). The GABA_AR SSD and GlyR SSD counts were again not changed (Figure 26.D). Given that the spatial association of p-gephyrin with GlyRs and GABA_ARs were both increased after 4-AP treatment, it is not surprising that GlyRs and GABA_ARs have a stronger correlation as well after 4-AP treatment. Because the GlyR amount is not changed and the GABA_AR amount is reduced at synaptic sites by 4-AP treatment, it is possible that GABA_ARs may be prevented to leave from the

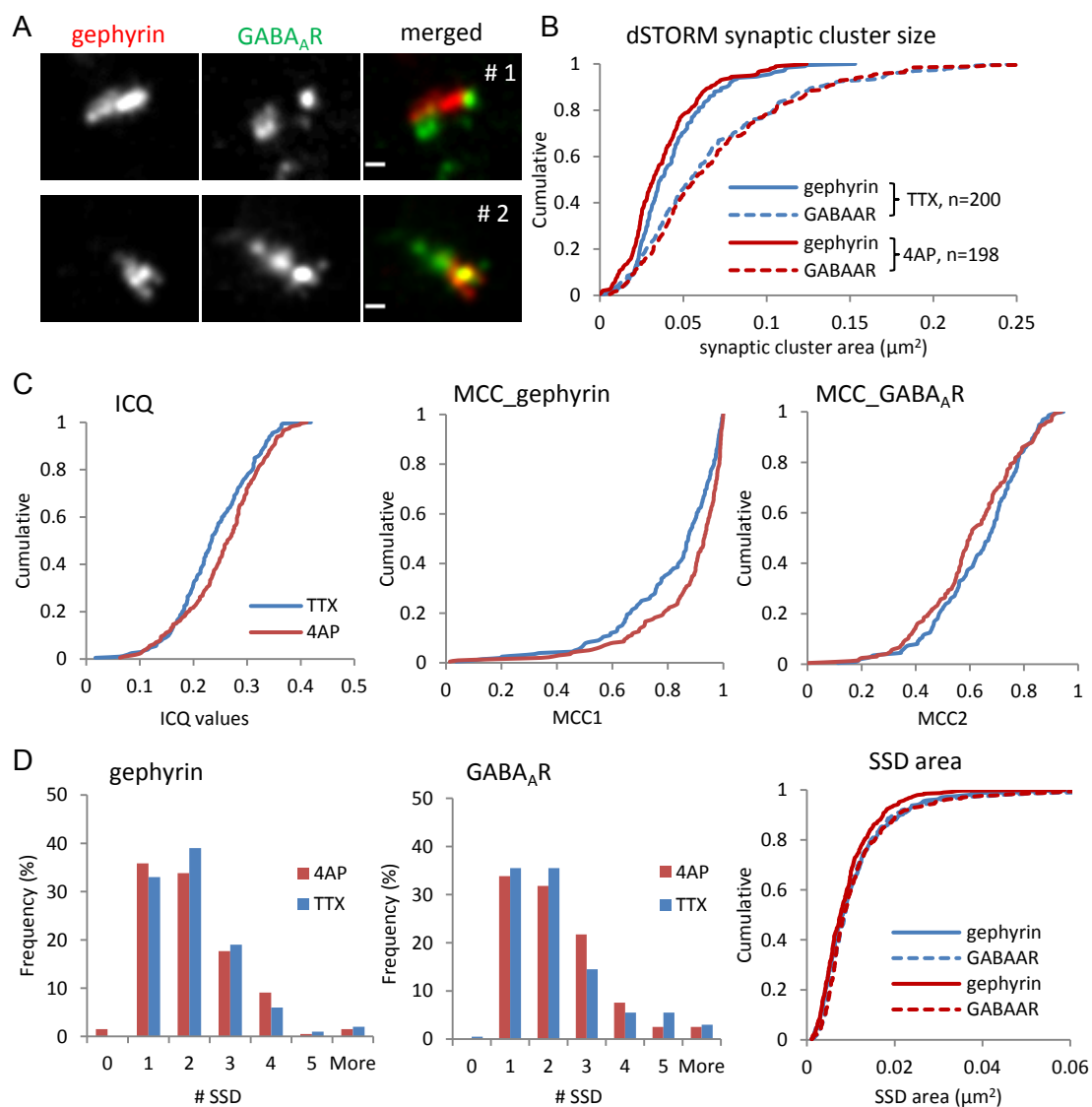


Figure 25. Increased spatial correlation of GABA_ARs and p-gephyrin by 4-AP treatment, but not their SSD numbers. (continued in next page)

(continued)

Figure 25. Increased spatial correlation of GABA_ARs and p-gephyrin by 4-AP treatment, but not their SSD numbers.

(A) Synaptic clusters of gephyrin labeled with A647 and GABA_ARs labeled with Cy3B in dSTORM images. Scale bar: 100 nm. (B) The size of gephyrin and GABA_AR clusters in dSTORM images. (C) The spatial correlation measurement of gephyrin and GABA_ARs. ICQ measured an increase of spatial correlation by 4-AP treatment compared to TTX condition (t-test, $p < 0.05$), while MCC showed an increase of p-gephyrin overlapping with GABA_ARs (t-test, $p < 0.01$) and a small decrease of GABA_ARs overlapping with p-gephyrin (t-test, $p=0.0558$). (D) The SSD measurements of gephyrin and GABA_AR clusters in the dSTORM images. No difference in the SSD counts was detected between the two treatment conditions. Gephyrin SSD area was smaller in 4-AP condition than in TTX condition (t-test, $p < 0.01$). Number of synapses: $n=200$ in TTX, $n=198$ in 4-AP conditions, from three independent experiments.

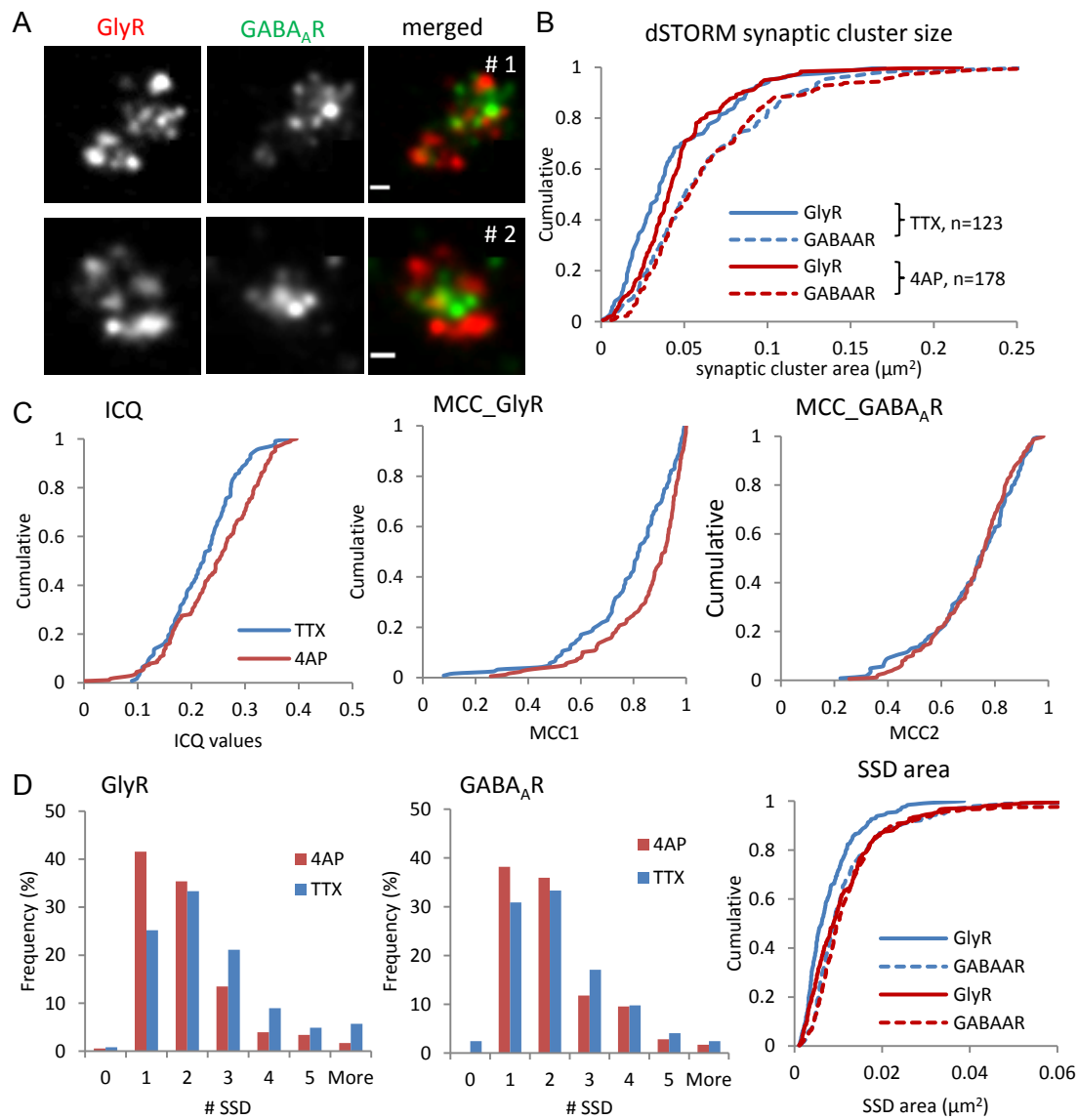


Figure 26. Increased spatial correlation of GABA_ARs and GlyRs by 4-AP treatment.
(continued in next page)

(continued)

Figure 26. Increased spatial correlation of GABA_ARs and GlyRs by 4-AP treatment.

(A) Synaptic clusters of GlyRs labeled with A647 and GABA_ARs labeled with Cy3B in dSTORM images. Scale bar: 100 nm. (B) The size of GlyR and GABA_AR clusters in dSTORM images. (C) Spatial correlation measurement of GlyRs and GABA_ARs. ICQ measured an increase of spatial correlation by 4-AP treatment compared to TTX (t-test, $p < 0.01$), while MCC showed an increase of GlyRs overlapping with GABA_ARs (t-test, $p < 0.001$) and no difference of GABA_ARs overlapping with GlyRs. (D) The SSD measurements of GlyR and GABA_AR clusters in the dSTORM images. No difference in the SSD counts was detected between the two conditions. GlyR SSD area is smaller in TTX than in the 4-AP condition (t-test, $p < 0.00001$). Number of synapses: $n=123$ in TTX, $n=178$ in 4-AP conditions, from two independent experiments.

synaptic sites in those regions that are also occupied by GlyRs, which would also explain the higher spatial correlation.

3.2.3.3 Summary of intra-synaptic re-organization at mixed inhibitory PSDs during neuronal activity

To recapitulate, the earlier epifluorescence microscopy experiments demonstrated that the synaptic content of GABA_ARs and p-gephyrin are reduced after increasing neuronal activity by 4-AP treatment, while the amount of GlyRs and total gephyrin are not changed. Two-color dSTORM experiments further revealed that the spatial correlation among GABA_ARs, p-gephyrin and GlyRs is increased after the 4-AP treatment. Taken together these results, we hypothesize that gephyrin molecules form a stable lattice as scaffold for the neurotransmitter receptors at inhibitory PSDs, providing strong binding sites for GlyRs and relatively weak binding sites for GABA_ARs. When the neuronal activity is increased, the phosphorylation level of gephyrin is reduced at specific subsynaptic sites. This does not have an effect on the GlyR content, due to their strong binding to the gephyrin scaffold. GlyRs are therefore less affected by the de-phosphorylation of gephyrin. In contrast, GABA_ARs appear to be more sensitive to gephyrin de-phosphorylation and are thus removed from the sites where gephyrin is dephosphorylated. At the same time, the remaining GABA_ARs and GlyRs may undergo re-distribution to better associate with the remaining p-gephyrin sites, in order to maintain certain level of inhibitory strength. This interpretation is further explored in the discussion.

Following our observations of the intra-synaptic re-organization at mixed inhibitory PSDs, an interesting question is: how does this relate to pre-synaptic components and influence the synaptic transmission? At the pre-synaptic active zone (AZ), the vesicle releasing site is dependent on a few key proteins (Südhof, 2012). RIM1/2 is an important component to indicate the vesicle releasing site, owing to its proximity to the pre-synaptic membrane and its heterogeneous subsynaptic distribution at the AZ (Dani et al., 2010; Glebov et al., 2017). A recent study has shown that RIM1/2 indeed dictates the evoked vesicle fusion sites and that post-synaptic PSD-95 SSDs are aligned with pre-synaptic RIM1/2 SSDs into trans-synaptic nanocolumns at excitatory synapses in hippocampal

neurons (Tang et al., 2016). As a common pre-synaptic protein for both excitatory and inhibitory synapses, RIM1/2 may play an important role in regulating the inhibitory synaptic transmission as well. However, it is not clear yet how p-gephyrin sites are spatially organized in relation to pre-synaptic RIM1/2. Do RIM1/2 and gephyrin also form trans-synaptic nanocolumns at inhibitory synapses? Do GlyRs or GABA_ARs have same or different proximity to RIM1/2 at mixed synapses? How are their spatial relationships modulated in response to altered neuronal network activity? To answer the questions, we investigated the spatial correlation of RIM1/2 with post-synaptic components at mixed inhibitory synapses in the following experiments.

3.2.4 RIM1/2 forms pre-synaptic SSDs that are aligned with post-synaptic p-gephyrin SSDs

We conducted two-color dSTORM imaging of RIM1/2 labeled with A647 and p-gephyrin labeled with Cy3B. The reconstructed synaptic images indicate that RIM1/2 molecules are organized heterogeneously at the AZ, forming subsynaptic domains (Figure 27). The synaptic complex presented from the side view also indicate that the gephyrin SSDs are mostly aligned with RIM1/2 SSDs, forming putative trans-synaptic nanocolumns (Figure 27.B). These observations demonstrate that trans-synaptic nanocolumns also exist at mixed inhibitory synapses in spinal cord neurons.

Next, we quantified the RIM1/2 SSDs and gephyrin SSDs for all the synapses in our experiments (number of synapses: 536). More than half of the RIM1/2 clusters have three or more SSDs, and less than 20% of the clusters have only one RIM1/2 SSD (Figure 28.A). In contrast, the majority of p-gephyrin clusters have one or two SSDs. And there is a weak correlation between the RIM1/2 SSD number and gephyrin SSD number per synapse. This suggests that pre- and post-synaptic proteins may be subjects to different spatial regulations. Moreover, both RIM1/2 SSD and gephyrin SSD counts per synapse are correlated to their whole cluster size (Figure 28.B).

In order to examine whether RIM1/2 SSDs and p-gephyrin SSDs are aligned across the pre- and post-synaptic compartments, we selected the synapses with

RIM1/2 and gephyrin clusters arranged side by side from a cross-section view (Figure 27.B). These 48 synapses were well reconstructed from dSTORM detections and exhibited representative pre- and post-synaptic alignment of RIM1/2 SSDs and gephyrin SSDs. With these synapses, we quantified the fraction of gephyrin SSDs which are aligned with RIM1/2 SSDs per synapse, and vice versa (Figure 28.C). For the majority of synapses, all the gephyrin SSDs are juxtaposed with RIM1/2 SSDs, and all the RIM1/2 SSDs are juxtaposed with gephyrin SSDs. Moreover, for the aligned RIM1/2 SSD and gephyrin SSD pairs, we measured the distances between their peak intensity. The distances between RIM1/2 SSD and gephyrin SSD are generally similar (mean \pm SD = 99 ± 23 nm, Figure 28.C), despite the variability of synaptic structures. This distance measurement accounts for the distance between RIM1/2 and pre-synaptic membrane (37 ± 4 nm, Dani et al. 2010), the synaptic cleft (~ 20 nm, Harris and Weinberg 2012), the distance between gephyrin and post-synaptic membrane (21.7 ± 8.5 nm, Triller et al. 1985), and the primary and secondary antibodies on each side (~ 10 nm of a single antibody, Maidorn et al. 2016). Due to the uncertainty of the orientations of the antibodies, we can count the size of one antibody on each side. Then the distance between the two fluorophores at pre- and post-synaptic compartments adds up to ~ 99 nm, which is in good agreement with our experimental data.

Therefore, in a quantitative manner, we demonstrated that p-gephyrin SSDs are aligned with RIM1/2 SSDs, forming trans-synaptic nanocolumns at inhibitory synapses in cultured spinal cord neurons.

3.2.5 GlyRs and GABA_ARs are differentially re-aligned to pre-synaptic vesicle release sites during increased neuronal activity

Our earlier study showed that the spatial correlation between GlyRs, GABA_ARs and p-gephyrin is increased after increasing the neuronal activity by 4-AP treatment. In addition, gephyrin as a common scaffold plays an important role in regulating synaptic GlyRs and GABA_ARs. Thus, the pre- and post-synaptic alignment of p-gephyrin SSDs with RIM1/2 SSDs implies that these trans-synaptic nanocolumns may regulate the spatial relationship of the inhibitory receptors and vesicle release sites during altered neuronal activity. Therefore, we

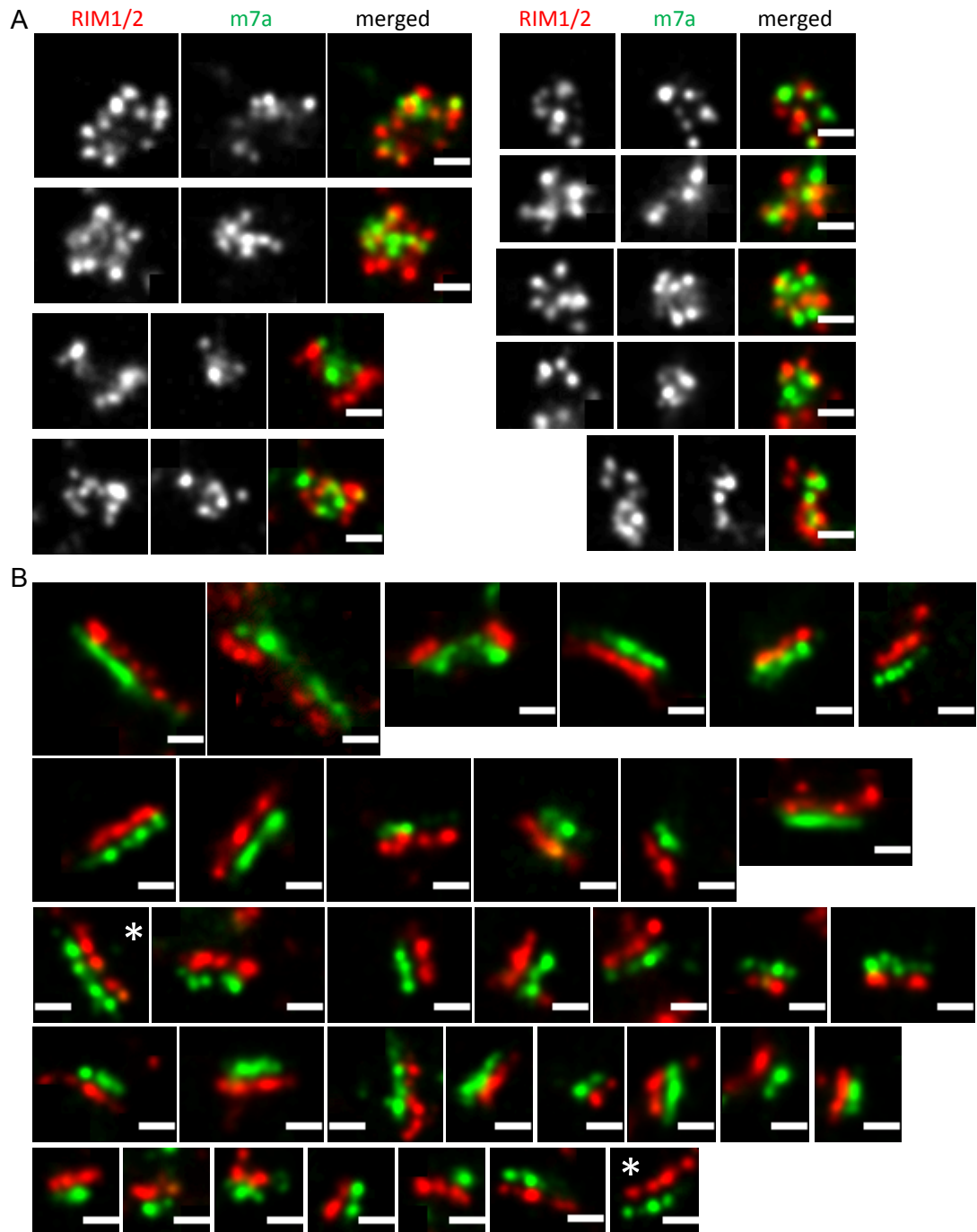


Figure 27. Reconstructed two-color dSTORM images showing the alignment of RIM1/2 and p-gephyrin.

Representative images of RIM1/2 (red) and gephyrin (green) clusters at synapses in spinal cord neurons, shown as *en face* view (A) or side view (B). RIM1/2 was labeled with A647 and gephyrin with Cy3B. Scale bar: 200 nm.

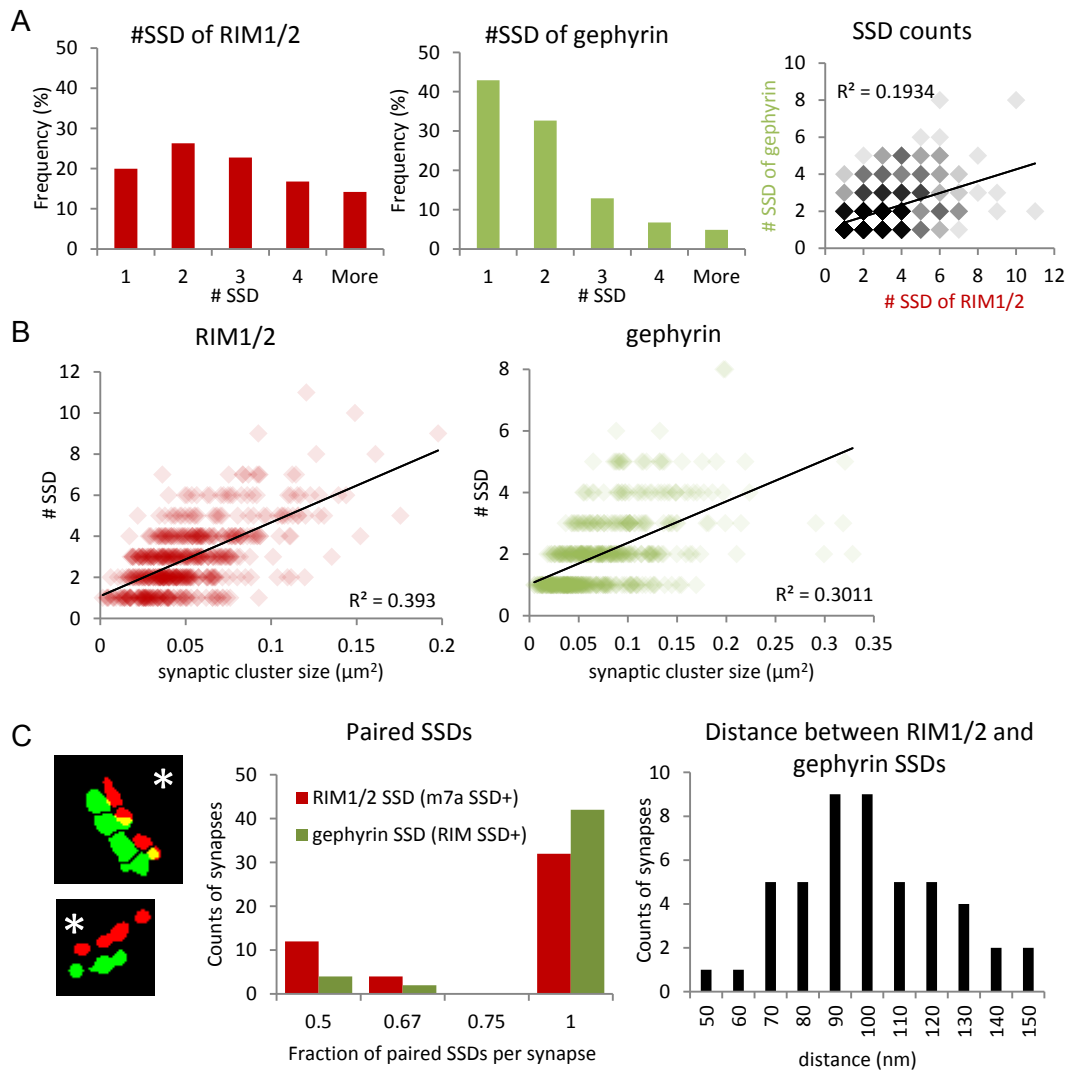


Figure 28. The alignment of post-synaptic gephyrin SSDs with pre-synaptic RIM1/2 SSDs at inhibitory synapses. (continued in next page)

(continued)

Figure 28. The alignment of post-synaptic gephyrin SSDs with pre-synaptic RIM1/2 SSDs at inhibitory synapses.

(A) SSD counts per cluster for RIM1/2 and gephyrin clusters in dSTORM images. RIM1/2 clusters tend to contain more SSDs than gephyrin. More than 50% of the RIM1/2 clusters contain ≥ 3 SSDs, while less than 30% of gephyrin clusters contain ≥ 3 SSDs. There is a weak correlation between RIM1/2 SSD counts and gephyrin SSD counts (Pearson's $R^2=0.1934$). (B) The SSD counts of RIM1/2 clusters and gephyrin clusters are moderately correlated to their synaptic cluster size (Pearson's $R^2=0.393$ and $R^2=0.3011$, respectively). (C) Forty eight synapses detected in side view were measured for their SSD alignment and the distance between RIM1/2 and gephyrin SSDs. Left: segmented RIM1/2 SSDs (red) and gephyrin SSDs (green) showing their apposition at synapses. Asterisks indicate the corresponding synapses in Figure 27. Middle: gephyrin SSDs are mostly paired with RIM1/2 SSDs (42 out of 48 synapses have all the gephyrin SSDs paired with RIM1/2 SSDs, and 32 out of 48 synapses have all the RIM1/2 SSDs paired with gephyrin SSDs). Right: for the paired SSDs of RIM1/2 and gephyrin, the distance between their intensity peaks was measured and averaged for each synapse (mean \pm SD = 99 ± 23 nm). Number of synapses: $n=536$ in (A) and (B); $n=48$ in (C); from three independent experiments.

investigated the spatial correlation of the inhibitory receptors and RIM1/2 using the same pharmacological approach and two-color dSTORM as described above.

3.2.5.1 Pre-synaptic RIM1/2 content is not changed by increased neuronal activity with 4-AP

We conducted pharmacological treatment with TTX and 4-AP in dissociated spinal cord neurons as described above. Cells were stained for RIM1/2, together with GlyRs and GABA_ARs to identify the mixed inhibitory synapses, and then subjected to conventional fluorescence microscopy (Figure 29.A). The integrated intensity of RIM1/2 clusters which co-localized with GlyRs and GABA_ARs is slightly decreased by 4-AP treatment compared to the control and TTX conditions (Figure 29.B). In agreement with our earlier results, GlyR cluster intensity was marginally reduced by 4-AP treatment, while GABA_AR cluster intensity was strongly decreased. Furthermore, the intensity ratio of RIM1/2 over GlyR clusters did not show a difference after the treatment, while the intensity ratio of GABA_AR/GlyR and GABA_AR/RIM1/2 was decreased in the 4-AP condition (Figure 29.C). This suggests that both RIM1/2 and GlyR amount is not changed by the increased neuronal activity, while the GABA_AR amount was reduced at the same PSDs.

3.2.5.2 Increased spatial association of GlyRs but not GABA_ARs with RIM1/2 after increasing neuronal activity

Next, we examined the spatial association of GlyRs with RIM1/2 and GABA_ARs with RIM1/2 by pairwise two-color dSTORM. For each experiment, triple staining of GlyRs, GABA_ARs and RIM1/2 was performed to identify the mixed inhibitory synapses. Only the target pairs of the receptor and RIM1/2 stained with A647 and Cy3B were subjected to two-color dSTORM. The third component was labeled with Alexa 488, and only imaged with conventional microscopy.

In the reconstructed synaptic structures, GlyR SSDs can be aligned with RIM1/2 SSDs (Figure 30.A). Their spatial association as measured with ICQ was increased by 4-AP treatment compared to the TTX treated condition (Figure 30.B). Moreover, the SSD counts per synaptic cluster did not change for either GlyR or RIM1/2 clusters (Figure 30.C). Given that the synaptic accumulation of

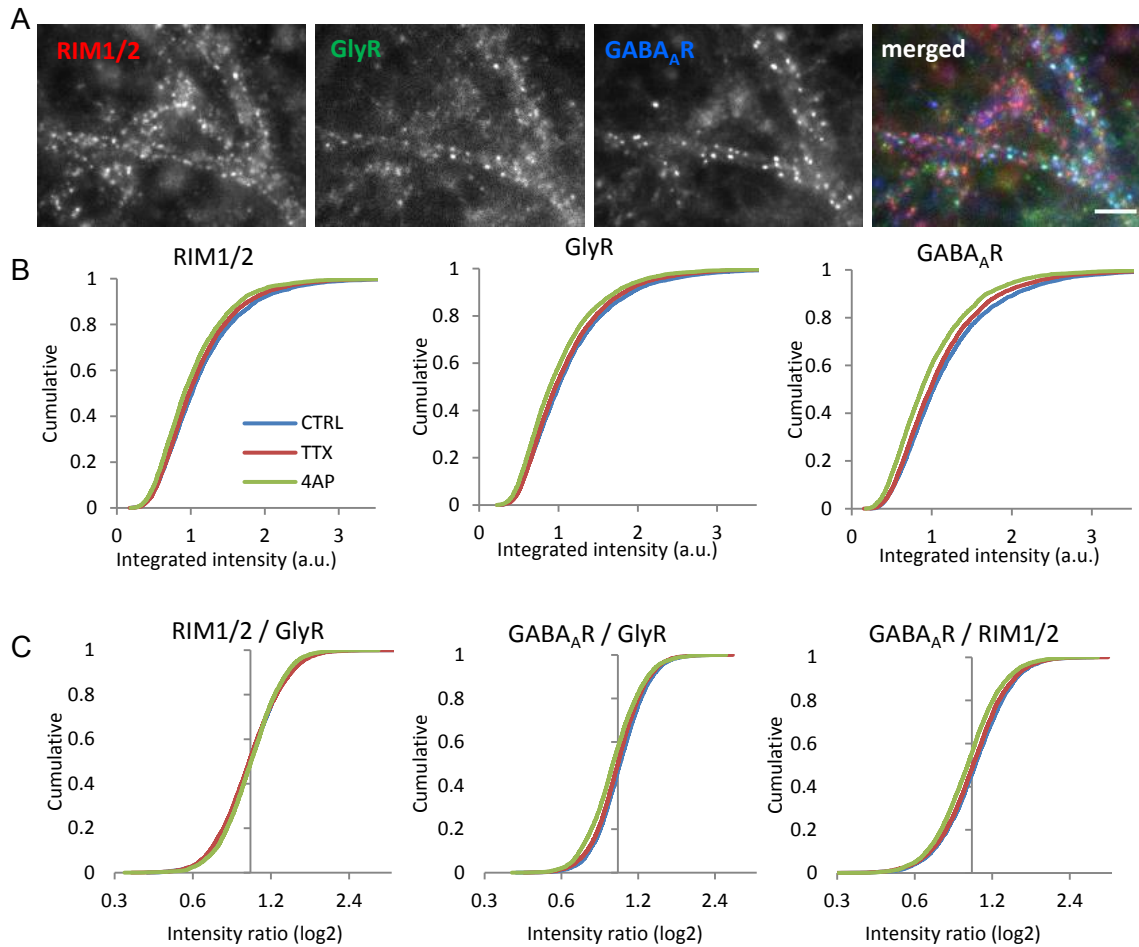


Figure 29. No change in the synaptic accumulation of RIM1/2 at mixed inhibitory synapses by 4-AP treatment.

(A) Triple staining of RIM1/2, GlyRs and GABA_ARs at mixed inhibitory synapses in spinal cord neurons. Scale bar: 5 μ m. (B) The intensity of RIM1/2 was not changed (Kolmogorov-Smirnov test, $p > 0.01$) and GlyR clusters are marginally reduced (Kolmogorov-Smirnov test, $p < 0.01$), while that of GABA_ARs is decreased ($p < 0.01$) by 4-AP treatment, compared to TTX condition. (C) The intensity ratio of RIM1/2 / GlyR was not changed, that of GABA_AR/GlyR was reduced ($p < 0.01$), and that of GABA_AR / RIM1/2 was reduced ($p < 0.01$). Number of synapses: $n=3972$ in non-treated (CTRL) group, $n=5406$ in TTX condition, $n=4408$ in 4-AP condition; from two independent experiments.

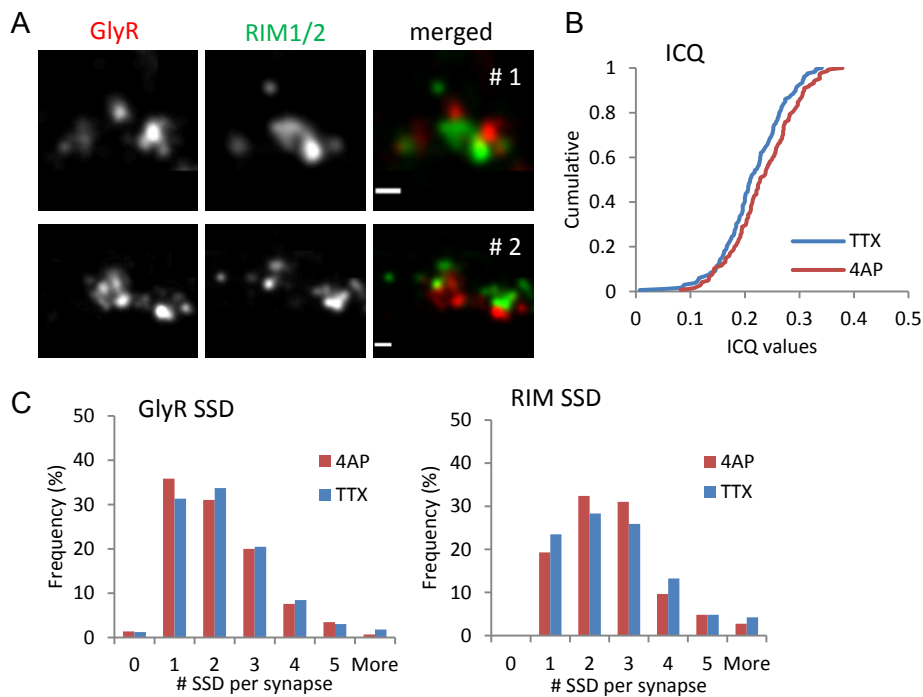


Figure 30. Increased spatial correlation of GlyRs and RIM1/2 by 4-AP treatment.

(A) Synaptic clusters of GlyRs labeled with A647 and RIM1/2 labeled with Cy3B in dSTORM images. Scale bar: 100 nm. (B) The spatial correlation of GlyRs and RIM1/2 is increased by 4-AP treatment compared to TTX condition, as shown by ICQ measurements (t-test, $p < 0.01$). (C) The SSD measurements of GlyR and RIM1/2 clusters in the dSTORM images. No difference was detected between the SSD counts in the two. Number of synapses: $n=166$ in TTX, $n=145$ in 4-AP conditions, from two independent experiments.

GlyRs and RIM1/2 are both not changed by 4-AP treatment, our results suggest that GlyRs may undergo intra-synaptic re-distribution to form a stronger association with pre-synaptic RIM1/2 molecules during increased neuronal activity. This increased spatial association could potentially increase the glycinergic neurotransmission in order to maintain the level of neuronal inhibition.

Similar to GlyRs, GABA_AR SSDs can also be aligned with RIM1/2 SSDs (Figure 31.A). However, no difference in the spatial association of GABA_AR and RIM1/2 was detected by ICQ measurement after the treatment (Figure 31.B). The SSD numbers of GABA_AR and RIM1/2 clusters were also not changed by the treatment (Figure 31.C). Given that GABA_ARs are removed from the synaptic sites after 4-AP treatment, the loss of GABA_AR seems to have no effect on their spatial relationship with pre-synaptic RIM1/2. Therefore, it is possible that GABA_AR is generally less associated with RIM1/2 than GlyRs at mixed inhibitory synapses.

3.2.6 Summary of the results on mixed inhibitory synapses

We investigated the intra-synaptic organization of the key proteins at mixed inhibitory synapses (GlyR, GABA_AR, gephyrin, RIM1/2) in dissociated spinal cord neurons, with the optimized protocol of two-color dSTORM. Furthermore, we examined the implications of their intra-synaptic organization in the neuronal activity with the two-color dSTORM. We also examined the changes in their synaptic accumulation during altered neuronal network activity, with conventional microscopy. Here, we recapitulated the results of the experiments on the mixed inhibitory synapses.

In the conventional microscopy experiments, the synaptic content of p-gephyrin and GABA_AR was reduced by 4-AP treatment, compared to the TTX condition, while that of GlyR, total gephyrin and RIM1/2 was not changed (Table 1). We also found that TTX treatment did not have strong impact on the synaptic accumulation of these synaptic components, compared to the non-treated control condition. Therefore, we used TTX conditions as comparison with 4-AP treatment in the two-color dSTORM experiments.

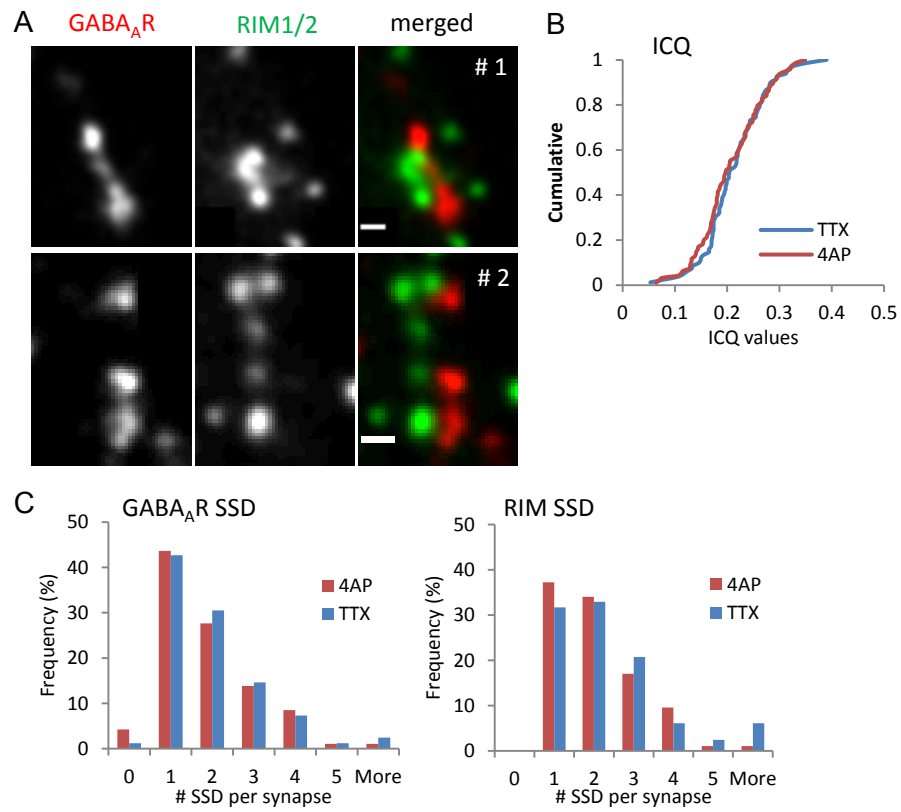


Figure 31. No change in the spatial correlation of GABA_ARs and RIM1/2 by 4-AP treatment.

(A) Synaptic clusters of GABA_ARs labeled with A647 and RIM1/2 labeled with Cy3B in dSTORM images. Scale bar: 100 nm. (B) ICQ measurements did not show a difference in the spatial correlation of GABA_ARs and RIM1/2 between 4-AP and TTX conditions (t-test, $p=0.462$). (C) The SSD measurements of GABA_AR and RIM1/2 clusters in the dSTORM images. No difference was detected between the two treatments in the SSD counts. Number of synapses: $n=82$ in TTX, $n=94$ in 4-AP conditions, from two independent experiments.

In the two-color dSTORM experiments, we observed a highly heterogeneous distribution of GlyRs, GABA_ARs, gephyrin and RIM1/2 at inhibitory synapses. All of these synaptic components form subsynaptic domains (SSDs). And p-gephyrin SSDs are often juxtaposed with RIM1/2 SSDs, forming putative trans-synaptic nanocolumns at inhibitory synapses. Using H-watershed approach, we quantified the SSDs and examined their implication in the neuronal activity. The SSD counts in GlyR, GABA_AR, gephyrin and RIM1/2 clusters showed no difference between 4-AP and TTX treated conditions in all the experiments. The size of their SSDs varies a lot across different experiments due to the impact of dyes. But we do observe a consistent larger GlyR SSDs after 4-AP treatment compared to TTX treatment.

To get an overview of the basal spatial correlation level of the synaptic components, we put together the ICQ measurements of paired synaptic components from non-treated conditions or TTX treated conditions (Figure 32). The basal spatial correlation of a pre- and post-synaptic component pair is consistently lower than that of a post-synaptic component pair, except that of GlyRs and GABA_ARs. The relatively low basal spatial correlation of GlyRs and GABA_ARs may indicate their competition for gephyrin binding sites and synaptic space. The ICQ measurement for p-gephyrin and total gephyrin is generally higher than that for gephyrin and GlyRs, which is as expected. These data not only showed the different spatial correlation levels between different synaptic components, but also proved the feasibility of using ICQ measurement to detect the changes in the spatial correlation.

Using ICQ method, we measured the changes in the spatial correlation of the synaptic proteins during increased neuronal network activity by 4-AP treatment. The spatial correlation between GlyRs and p-gephyrin, GABA_ARs and p-gephyrin, GlyRs and GABA_ARs was increased at the post-synaptic compartment after 4-AP treatment, compared to the TTX condition (Table 2). Moreover, GlyRs appeared to have stronger correlation with pre-synaptic RIM1/2 after 4-AP treatment. However, the spatial correlation of GABA_ARs and RIM1/2 was not changed.

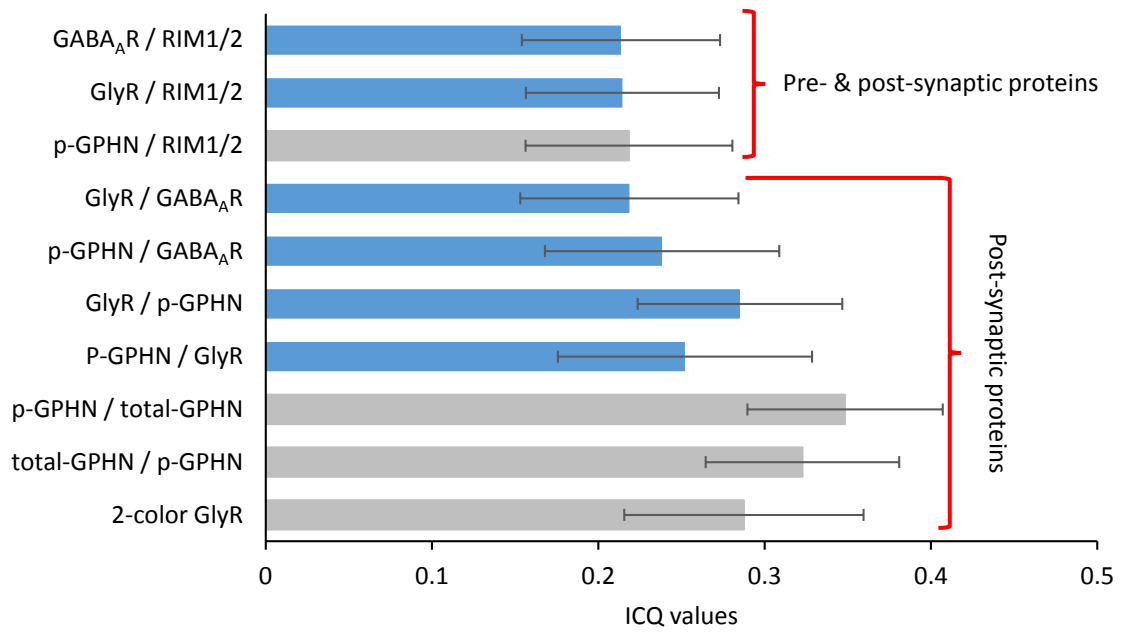


Figure 32. The spatial correlation of synaptic proteins measured by ICQ.

Grey bars: without any treatment; blue bars: TTX treated conditions.

Table 1. Summary of the changes in synaptic molecule amount at mixed synapses with altered neuronal activity.

(Comparing 4-AP to TTX)	Synaptic molecule amount
Total gephyrin	No change
p-gephyrin	Decreased
GlyRs	No change
GABA _A Rs	Decreased
RIM1/2	No change

(TTX condition is taken as control. Results are from the conventional microscopy experiments with TTX or 4-AP treatment.)

Table 2. Summary of the changes in spatial correlation between synaptic proteins with altered neuronal activity, measured by ICQ.

(Comparing 4-AP to TTX)	ICQ
GlyRs & p-gephyrin	Increased
GlyRs & p-gephyrin (reversed color)	Increased
GABA _A Rs & p-gephyrin	Increased
GABA _A Rs & GlyRs	Increased
RIM1/2 & GlyRs	Increased
RIM1/2 & GABA _A Rs	No change

(TTX condition is taken as control. Results are from two-color dSTORM experiments with TTX or 4-AP treatment.)

Chapter 4

4 Discussion

In my PhD project, I have adopted state-of-the-art super-resolution optical microscopy to study the internal structures of inhibitory synapses. Owing to the complexity of the technique and the particular properties of synapses, I developed an optimized two-color dSTORM protocol and carefully evaluated the influence of the dyes. With the obtained approaches, I then examined the intra-synaptic organization of GlyRs and GABA_ARs at the same PSD, and their re-organization in response to neuronal network activity. This is the first time that the different receptor types at mixed inhibitory synapses have been closely investigated in such detail at single molecule resolution using super-resolution optical microscopy.

In this chapter, I first critically review the subject of subsynaptic domain (SSD). Then I discuss my biological findings and their implications in the regulation of mixed inhibitory synaptic activity. Finally, I also discuss the technical and analytical challenges that I encountered and propose alternative approaches.

4.1 A critical review of sub-synaptic domains (SSDs)

We have observed SSDs of GlyRs, GABA_ARs, gephyrin and RIM1/2 at inhibitory synapses. The SSD counts per cluster are generally in the range of that has been reported in the literature. However, we found that the SSD segmentation and characterization can be affected by the dyes and the analysis methods. Also, there exists some ambiguity in the scientific literature about the definition of SSDs. Therefore, I reviewed the literature in detail and critically discuss the multiple aspects of SSDs. Our review article on this topic has been recently published (Yang and Specht, 2019)(also see Appendix 6).

4.1.1 What is a subsynaptic domain?

Terminology and definition

A major source of confusion is that different names have been used in the literature to describe subsynaptic domains. Among these, the terms nanodomain,

nanocluster, subcluster, subdomain and nanomodule have been used in an interchangeable manner (e.g. Broadhead et al. 2016; Haas et al. 2018; Hruska et al. 2018; Macgillavry et al. 2013; Nair et al. 2013). The lack of a clear and unified terminology has made it difficult to refer to specific molecular structures and to be aware of the differences and similarities between studies. Regarding the choice of words, the term cluster should best be avoided, because it can also refer to the clustering algorithms that are widely used for image analysis of SMLM data (Nicovich et al., 2017). The prefix nano is redundant, because synapses themselves have diameters of only a few hundred nanometers. Furthermore, nanodomain has been widely used to describe the high Ca^{2+} ion concentrations in the proximity of an open calcium channel (Augustine et al., 2003; Eggermann et al. 2013; Ghelani and Sigrist 2018).

We therefore refer to these structures as subsynaptic domain or SSD (Crosby et al., 2019) for the following reasons: (1) the term is self-explanatory, referring to a space that is smaller than the whole synaptic compartment and that is occupied by a given type of molecules; (2) it is flexible in that it can be equally applied to membrane receptors, scaffold and signaling proteins, whether they are pre-synaptic or post-synaptic. We define SSD as a sub-compartment of the synapse in which the density of a specific synaptic protein is higher than in the surrounding area, and that is typically observed with super-resolution microscopy. We believe that the term subsynaptic domain could thus provide some clarity in defining specific molecular entities at synapses.

SSD size and protein copy numbers

The most basic feature of SSDs that holds biologically relevant information is their size and the copy number of proteins that they contain. A wide range of sizes was detected by SMLM and STED microscopy (Table 3). For instance, SSDs of excitatory scaffold proteins in cultured hippocampal neurons have a diameter of ~80 nm as judged by coordinate-based SMLM analysis (MacGillavry et al., 2013), whereas an average diameter of 120 nm was measured in reconstructed super-resolution images (Nair et al., 2013). STED microscopy detected SSDs of PSD-95 with a diameter of 200 nm (Fukata et al., 2013). These differences in SSD size are likely due to the different resolution of the imaging systems and the

application of a threshold during image processing. A comparative study of PSD-95 in hippocampal tissue using PALM and STED determined median SSD diameters of 126 nm and 158 nm, respectively, exemplifying the impact of the imaging approach (Broadhead et al., 2016). The typical diameter of the whole PSD in hippocampal neurons ranges from 100 nm to 800 nm, with a mean of about 300 nm (Arellano et al., 2007; Harris & Stevens, 1989). Therefore, the lower limit of SSD sizes of ~50 nm reflects the image resolution of the super-resolution imaging techniques, while the upper limit corresponds to the size of the entire synapse. Given that synapse sizes vary substantially across the central nervous system, an interesting question is whether SSDs of different synaptic proteins have stereotypical sizes that are the same at different types of synapses (see Crosby et al. 2019).

Information about protein copy numbers is essential to establish the structural basis of SSD formation. To date, there are hardly any quantitative data about SSD molecule numbers. Subsynaptic domains of AMPARs have been estimated to contain an average of ~20 receptor complexes (Nair et al., 2013). Due to the limited accessibility of the epitopes for immunolabelling, however, the actual number of receptors per SSD could be higher. This could have an effect on the role of SSDs in synaptic function, since the number of active receptors is directly related to the strength of synaptic transmission (Fukazawa & Shigemoto, 2012; Masugi-Tokita et al., 2007; Tarusawa et al., 2009).

Table 3. Size and protein copy numbers of SSDs and PSDs obtained with different experimental techniques.

Structure	Diameter (nm)	Molecule numbers	Technique	Synapse type	References	
SSD	50-130 *		SMLM	Excitatory, hippocampal	Broadhead et al., 2016; Chamma et al., 2016 a,b; Haas et al., 2018; MacGillivray et al., 2013; Nair et al., 2013	
	130-760 *		STED	Excitatory, hippocampal and cortical	Broadhead et al., 2016; Hruska et al., 2018; Nair et al., 2013	
	~ 300 *		SIM	Inhibitory, hippocampal	Crosby et al., 2019	
	70 *	~ 20 AMPARs / SSD *	STORM	Excitatory, hippocampal	Nair et al., 2013	
PSD	300 (100-800) #		EM	Excitatory, hippocampal	Bourne & Harris 2011; Harris & Stevens 1989	
			EM	Excitatory, cortical	Arellano, 2007; Santuy et al., 2018	
	290 (110-650) #		EM	Inhibitory, hippocampal and cortical	Bourne & Harris 2011; Santuy et al., 2018	
	350 (110-700) #		EM	Inhibitory, various CNS regions	Fukazawa & Shigemoto, 2012; Masugi-Tokita et al., 2007; Tarusawa et al., 2009	
PSD		50 (0-200) AMPARs #	EM	Excitatory, various CNS regions	Nusser et al., 1997, 1998	
			30 (0-200) GABA _A Rs #	Inhibitory, cerebellar and hippocampal		
			30 (40-500) PSD-95 #	Biochemistry, TIRF microscopy	Excitatory, various brain regions	Sheng & Kim, 2011; Sugiyama et al. 2005
			30 (40-500) Gephyrin #	SMLM (decay recordings)	Inhibitory, spinal cord	Patrizio et al. 2017; Specht et al., 2013

* Mean values obtained in the cited studies; # mean (range in brackets). Values were taken directly or calculated from those reported in the cited studies.

Number of SSDs per synapse

Most synapses contain only one SSD or no SSD at all. More specifically, a single SSD was detected in 50% to 80% of synapses imaged with SMLM, SIM or STED microscopy, less than 20% had more than three SSDs, and six SSDs was the upper limit (Broadhead et al. 2016; Chamma et al., 2016 a, b; Crosby et al. 2019; Hruska et al. 2018; MacGillavry et al. 2013; Nair et al. 2013; Pennacchietti et al., 2017a). It is likely that the different imaging techniques and analyses again have an effect on the detection of multiple SSDs. This raises the question whether the SSD simply reflects the center of mass of the protein assembly, and if so, whether the presence of single or multiple SSDs actually matter for the regulation of synaptic function.

There exists a positive correlation between the number of SSDs and the size of the PSD or the dendritic spine (Crosby et al., 2019; Fukata et al., 2013; Hruska et al., 2018; Nair et al., 2013). EM studies have revealed a large variability in PSD area, ranging from 100 to 800 nm in diameter (Table 3). More than half of the PSDs are small ($<0.05 \mu\text{m}^2$), which is similar to the fraction of synapses with only one SSD (Arellano et al., 2007). Moreover, the number of AMPAR molecules is positively correlated with the PSD size, and large complex PSDs have a higher density of AMPARs than small, non-perforated PSDs (Fukazawa & Shigemoto, 2012; Ganeshina et al., 2004; Shinohara et al., 2008). Together, these data indicate that SSDs may only play a role at large PSDs, reflecting the superior strength of these synapses.

Trans-synaptic nanocolumns

From the viewpoint of neuron connectivity, pre-synaptic and post-synaptic SSDs can be aligned to form trans-synaptic structural units that regulate synaptic function (Biederer et al., 2017; Chen et al., 2018). Such an organization has been observed at excitatory synapses using 3D-SMLM, and was suitably named trans-synaptic nanocolumn (Tang et al., 2016). SMLM studies have further shown that synaptic adhesion complexes such as neuroligin and neurexin are also organized in SSDs, suggesting that they contribute to the formation of trans-synaptic nanocolumns (Haas et al., 2018; Perez de Arce et al., 2015). The term

nanocolumn therefore refers to a specific concept, namely the alignment of pre- and post-synaptic SSDs that brings together different functional elements. Future studies are expected to explore the possible role of nanocolumns in synaptic plasticity.

The dynamics of SSDs

The hypothesis that SSDs regulate synaptic transmission implies that SSDs adapt dynamically to changes in synaptic strength. Indeed, live SMLM in cultured neurons has revealed the mobility and morphological changes of SSDs. Synaptic scaffolds undergo dynamic changes on a timescale of 5-10 minutes, displaying marked differences in the number, position and shape of SSDs at different time points (Nair et al., 2013; Rodriguez et al., 2017; Specht et al., 2013). STED microscopy further showed that these morphological changes occurred both *in vitro* and *in vivo* (Hruska et al., 2018; Wegner et al., 2018). The dynamics of SSDs are in agreement with the exchange of individual proteins at synaptic and extra-synaptic sites, which is a hallmark of the dynamic synapse (Choquet & Triller, 2013; Delgado & Selvin, 2018). Therefore, SSDs are momentary representations of the protein distribution and need to be viewed as dynamic snapshots rather than rigid structural units.

4.1.2 How to detect SSDs with SMLM

The identification of SSDs consists in detecting small numbers of densely packed molecules in a confined space with a high local background from neighboring molecules with lower density. Despite these challenges, SMLM is well suited to resolve the internal organization of small structures such as synapses at single molecule level. In the following, we discuss the relevant factors of the image acquisition and data analysis that have an impact on the identification of SSDs.

Image acquisition

SMLM techniques aim to record large numbers of single fluorophore detections from densely labelled structures, while ensuring that the signals are sufficiently sparse to be well separated. STORM, PALM and uPAINT have all been employed for detecting SSDs. The three techniques have the same intrinsic challenges when

it comes to the ultrastructure of synapses, chief among them being the fluorophore. Most fluorophores are detected repeatedly due to their fluorescence lifetime, photo-switching and blinking. This can create dense clusters of redundant detections that are easily mistaken for SSDs. The blinking behavior of the fluorophores (organic dyes or fluorescent proteins) is dependent on their photo-physical and photo-chemical properties, and it can be modulated by the laser power and the composition of the imaging buffer (Dempsey et al., 2011; Endesfelder et al., 2011; Nahidiazar et al., 2016; van de Linde et al., 2011). Sub-optimal imaging conditions such as inefficient laser illumination or an incompatible buffer system can result in artificial clustering (Annibale et al., 2011b; Burgert et al., 2015; Nahidiazar et al., 2016). Even with an optimized imaging protocol, different fluorophores will produce different representations of the analyzed structure (Baddeley & Bewersdorf, 2018; Dempsey et al., 2011). The evaluation of the number and the size of SSDs is therefore strongly dependent on the fluorophores, and control experiments with different fluorophores are crucial to validate the experimental findings (Yang & Specht, 2020). In addition to the fluorophores, attention should also be drawn to the labelling strategies used for sample preparation. The distance between the fluorophores and the actual positions of the target molecules (e.g. due the size of antibodies used for labelling), and under-sampling due to a limited labelling efficiency can add to the uncertainties in the identification of SSDs (Deschout et al., 2014; Maidorn et al., 2016).

Image segmentation

Depending on the type of SMLM data (pointillist or reconstructed super-resolution images), different algorithms have been adopted for segmenting SSDs. For coordinates-based data, a local density threshold is generally applied. The local density can for instance be defined as the number of detections within a radius of five times the mean nearest neighbor distance of all the detections within each synapse, and SSDs are identified as regions above a certain threshold (Macgillavry et al. 2013; Pennacchietti et al., 2017a; Tang et al. 2016). As regards the reconstructed images, an intensity threshold may be adopted instead. For example, wavelet segmentation has been used to identify SSDs at synapses in the

whole field of view (Chamma et al., 2016 a,b; Nair et al. 2013). Similarly, watershed segmentation can be employed to segment SSDs of individual synapses in reconstructed SMLM images or deconvoluted STED images (Broadhead et al., 2016; Dzyubenko et al., 2016). In my own experiments, I have generally applied H-watershed segmentation to generate SSDs of receptor and scaffold proteins at inhibitory synapses. The difficulty of all these approaches is that the detected size and the number of SSDs are directly dependent on the algorithms and the chosen parameters, which makes an accurate identification of SSDs challenging.

Dealing with small molecule numbers and the variability of synapses

Synapses exhibit a large variability not only in size, but also in terms of molecule numbers. Neurotransmitter receptors such as AMPARs or GABA_ARs have relatively low copy numbers, with an average of ~50 receptor complexes per synapse (ranging up to 200 copies; Table 3). The main scaffold proteins at excitatory and inhibitory synapses outnumber the receptors by a factor of four to five. PSD-95 and gephyrin molecules amount to 40-500 per synapse, with an average of ~300 copies (Patrizio et al., 2017b; Sheng & Kim, 2011; Specht et al., 2013; Sugiyama et al., 2005). The low copy numbers of synaptic proteins, especially receptors, makes the identification of SSDs with SMLM challenging, since the labelling of the structures is often rather faint. At the same time, the high local density of synaptic proteins can further reduce the efficiency of immunolabelling due to epitope masking. The overall receptor density at synapses is in the order of 700 AMPARs/ μm^2 for the whole PSD (50 AMPARs / 0.07 μm^2). An average SSD with a diameter of 70 nm (area of 0.0038 μm^2) contains about 20 AMPARs, resulting in an estimated density of ~5000 AMPAR complexes/ μm^2 (Nair et al., 2013). Considering the molecular size of the receptor complexes (10 nm \times 20 nm; Patriarchi et al., 2018), 20 AMPARs would occupy a membrane area of at least 0.004 μm^2 . This means that the receptors are very densely packed inside the SSD, adding to the uncertainties that result from the stochasticity of the immunolabelling and fluorophore detection.

Alternative approaches

Given the rapid advances in super-resolution imaging technologies, promising alternatives for the investigation of complex structures such as synapses are quickly emerging. Among these, smaller probes such as nanobodies have been produced to bypass the limitations of labelling density and to minimize the distance between the fluorophores and the target proteins (Chamma et al., 2016a; Maidorn et al. 2016). DNA-PAINT allows multi-color SMLM imaging (Nieves et al., 2018). DNA origami standards provide a more precise way for calibrating protein copy numbers given that the absolute quantification of molecules at SSDs is faced with large stochasticity of the imaging technique (Zanacchi et al., 2017). Furthermore, new algorithms are being developed to segment synaptic clusters in coordinates-based datasets more efficiently (Baddeley & Bewersdorf, 2018; Nicovich et al., 2017). In collaboration with Felipe Delestro and Auguste Genovesio (IBENS), we have developed a versatile approach based on DBSCAN for cluster identification and the analysis of dual-color pointillist dSTORM datasets (SRclusters, see Figure 17 and Appendix 3).

4.2 The intra-synaptic spatial organization of mixed inhibitory synapses and its functional implications

I observed that gephyrin, GABA_ARs and RIM1/2 are heterogeneously distributed at inhibitory synapses and form SSDs in dissociated spinal cord neurons. This is similar with the recent studies on GABAergic inhibitory synapses in dissociated hippocampal neurons (Crosby et al. 2019; Pennacchietti et al., 2017a). Moreover, I found that GlyRs also exhibit similar heterogeneous distribution and SSDs at inhibitory PSDs. At mixed inhibitory synapses, GlyRs and GABA_ARs are not fully intermingled and their SSDs can occupy different spaces. This gives rise to the possibility that the intra-synaptic organization of the receptors can serve as a regulator for synaptic activity.

4.2.1 The intra-synaptic organization of GlyRs and GABA_ARs at mixed PSDs is differentially regulated

The cultured spinal cord neurons showed low basal network activity in our calcium imaging experiments. TTX application blocked the basal calcium signals completely, while 4-AP increased the frequency of the calcium signals. This effect was persistent for at least 20 minutes. In the conventional microscopy

experiments, the synaptic amount of GlyRs, GABA_ARs or gephyrin was not changed after one hour of TTX treatment. However, the amount of GABA_ARs and p-gephyrin was reduced at the post-synaptic sites, while that of GlyRs and total gephyrin was not changed (Table 1). In the two-color dSTORM experiments, the spatial correlation between GlyRs, GABA_ARs and p-gephyrin was increased after 4-AP treatment compared to TTX treatment (Table 2). Given that the amount of both GABA_ARs and p-gephyrin was reduced, the elevated spatial correlation between these three proteins may indicate an intra-synaptic re-organization at the mixed PSDs during elevated neuronal network activity.

4.2.1.1 The accumulation of GlyRs and GABA_ARs at mixed PSDs is differentially regulated by excitatory activity

In my experiments, 4-AP treatment reduced the synaptic amount of GABA_ARs and p-gephyrin, consistent with previous studies in our laboratory using hippocampal neurons (Bannai et al., 2009; Niwa et al., 2012). However, the synaptic amount of GlyRs and total gephyrin was not changed by the 4-AP treatment (Table 1). On the other hand, the synaptic amount of gephyrin, GlyRs and GABA_ARs did not change with TTX treatment compared to the non-treated condition. This is not surprising, because the baseline activity in our spinal cord cultures was generally low, and variations in the baseline activity level can be large (Figure 21-22). Therefore, in my experiments, the 4-AP and TTX treatments were taken as two representative conditions for high and low activity level respectively. In conclusion, the synaptic accumulation of GlyRs and GABA_ARs were differentially regulated by network activity.

A previous study in our laboratory showed that the diffusion coefficient of GlyRs was increased by TTX treatment in dissociated spinal cord neurons, while that of GABA_AR γ 2 subunits was not changed (Lévi et al., 2008). Interestingly, in hippocampal neurons where inhibitory synapses accommodate only GABA_ARs, TTX treatment reduces the diffusion coefficient of synaptic GABA_AR γ 2 subunits (Bannai et al., 2009). Different baseline activity in these cultures might contribute to the discrepancy in these observations. Alternatively, it is possible that the receptor dynamics may be differentially regulated at pure GABAergic synapses and mixed inhibitory synapses. On the other hand, 4-AP treatment increased the

diffusion coefficient of synaptic GABA_AR γ 2 subunits in hippocampal neurons (Bannai et al., 2009). However, it is not yet known if and how 4-AP treatment influences the GABA_AR and GlyR mobility at mixed inhibitory synapses in spinal cord neurons. Given that TTX treatment changes the diffusion coefficient (Lévi et al., 2008) but not the synaptic accumulation of GlyRs in spinal cord neurons, the diffusion coefficient may be not directly related to the synaptic accumulation of receptors.

Furthermore, TTX treatment was shown to reduce synaptic amount of GABA_AR α 2 subunits in dissociated spinal cord neurons, compared to the non-treated condition (Specht et al., 2013). However, in my experiments, TTX treatment did not change the synaptic amount of GABA_AR β 3 subunits compared to the non-treated condition. In addition, a recent study has shown that an alanine point mutation of gephyrin at serine 270 sites (S270A) increased the synaptic amount of GABA_AR α 2 subunits and gephyrin molecules in hippocampal neurons (Battaglia et al., 2018). However, the reduced phosphorylation at S270 sites by 4-AP treatment decreased the synaptic GABA_AR β 3 subunits in my study. This suggests that different GABA_AR subunits may be differently regulated in response to neuronal network activity.

GABA_AR β 3 subunits have been shown to play crucial roles in inhibitory synaptic transmission and their deficiency is involved in several pathogenesis (Culiat et al. 1995; Ferguson et al. 2007; Houston et al., 2008; Houston and Smart 2006; Nguyen and Nicoll 2018; Petrini et al. 2014; Saliba et al., 2012). This distinguishes GABA_AR β 3 subunits as important subjects for future studies.

4.2.1.2 Increased intra-synaptic spatial correlation of GlyRs, GABA_ARs and gephyrin at mixed PSDs by excitatory activity

In hippocampal neurons, chemical induction of inhibitory long-term potentiation (iLTP) increased the number of gephyrin SSDs (Pennacchietti et al., 2017a). In a recent study using structured illumination microscopy (SIM), both GABA_AR SSD counts and gephyrin SSD counts were increased after bicuculline treatment (Crosby et al., 2019). Bicuculline, as a GABA_AR antagonist, blocks inhibition and increases neuronal activity. When the gephyrin clusters were disrupted by

dominant negative expression of gephyrin, both gephyrin SSD and GABA_AR SSD counts were reduced. In addition, the SSD size was not changed in both experimental manipulations (Crosby et al., 2019). Therefore, it was suggested that SSDs may be building blocks of inhibitory synapses.

In my experiments, I did not observe any changes in the SSD counts of the inhibitory synaptic components after the pharmacological treatments. However, I observed changes in the SSD size due to the treatments. These different observations may be attributed to the differences between hippocampal neurons and spinal cord neurons, or to the differences in the pharmacological treatments adopted in these studies. Another important factor is the choice of imaging methods and analytical approaches (see below). Despite the fact that SIM improves the resolution by two-fold without suffering from the stochasticity of fluorescent blinking, it may not be sufficient to detect the true SSD size. In fact, the average SSD size was about 300 nm in diameter measured with SIM (Crosby et al., 2019). This SSD size is close to the size of inhibitory PSDs (~350 nm) measured by electron microscopy (Bourne & Harris, 2011; Santuy et al., 2018). In our study, we found that the SSD size was strongly influenced by the choice of dyes, which impedes a conclusion about the SSD size measured in our experiments. On the other hand, the analytical approaches may influence the results of SSD segmentation. Pennacchietti and colleagues used coordinate-based data derived from PALM imaging to segment SSDs from the synaptic clusters, by applying a threshold to the local density (Pennacchietti et al., 2017a). In our study, we applied H-watershed to the synaptic clusters in the rendered images for SSD segmentation. Because weak signals may be enhanced during image rendering, the SSD counts were probably overestimated in our results, especially in the images with down-regulated protein levels.

Therefore, the hypothesis that SSDs are building blocks for inhibitory synapses requires further investigation. There is still room for improvements in the SSD detection (see below). However, given the changes in the spatial correlation of GlyRs, GABA_ARs and p-gephyrin, what we can conclude is that the spatial relationships of inhibitory synaptic proteins plays a role in regulating synaptic activity. The heterogeneous distribution of GlyRs and GABA_ARs at mixed

inhibitory synapses may not be a random phenomenon, but appears to be closely regulated by neuronal activity.

Given the changes in the synaptic amount of p-gephyrin and its spatial correlation with the receptors in our experiments, gephyrin phosphorylation at S270 sites may be a key regulator for the intra-synaptic organization of GlyRs and GABA_ARs. In addition, other auxiliary proteins, such as the GABA_AR regulatory protein Lhfpl (GARLH) and the GDP/GTP-exchange factor collybistin, are also important in regulating synaptic clustering of gephyrin and GABA_ARs (Davenport et al. 2017; Heller et al. 2012; Kins et al., 2000; Papadopoulos and Soykan 2011; Saiepour et al. 2010; Yamasaki et al. 2017). Their potential roles in regulating receptors at mixed inhibitory synapses remain to be studied in the future.

4.2.2 Trans-synaptic nanocolumns at inhibitory synapses and potential roles of adhesion proteins

Trans-synaptic nanocolumns have been reported at excitatory synapses, incorporating the SSDs of pre-synaptic Bassoon, RIM1/2 and post-synaptic AMPARs, PSD-95, GKAP, Shank and Homer into one trans-synaptic unit (Tang et al., 2016). Similarly, I observed a trans-synaptic alignment of RIM1/2 SSDs with p-gephyrin SSDs at inhibitory synapses in spinal cord neurons (Figure 27). Given that the majority of inhibitory synapses in dissociated spinal cord neurons are mixed synapses (Dumoulin et al., 2000), the trans-synaptic nanocolumns most likely exist at mixed inhibitory synapses. When the neuronal network activity was increased by 4-AP treatment, the p-gephyrin level was reduced at synaptic sites. How the trans-synaptic alignment of RIM1/2 SSDs and p-gephyrin SSDs is affected by the altered activity remains an open question. Moreover, gephyrin phosphorylation at S270 does not occupy the entire gephyrin lattice (see section 3.1.4.2). Therefore, it will also be interesting to further investigate how the gephyrin lattice as a whole is correlated to pre-synaptic RIM1/2 SSDs.

It is important to point out that the synapses are dynamic structures and are continuously changing in living neurons. After fixation of the cells, we only get a snapshot of a certain status of the synapses. In live neurons, gephyrin clusters can move laterally on the dendritic shaft in the range of micrometers, and the pre-

synaptic compartments also move accordingly (Dobie and Craig, 2011; Hanus et al., 2006; Kuriu et al., 2012). This means that some trans-synaptic signals are needed to maintain the coordinated pre- and post-synaptic mobility. Synaptic cell adhesion molecules may be the key regulators in anchoring pre- and post-synaptic compartments during this movement. Many synaptic adhesion molecules are known to play important roles in synaptic function (Missler et al., 2012). However, which adhesion molecules are responsible for the coordinated mobility at inhibitory synapses is still unknown.

In addition to the mobility of the whole synapses, SMLM and STED microscopy have revealed that the intra-synaptic organization also changes over time, exhibiting differences in the synaptic morphology and SSD organization (Hruska et al., 2018; Nair et al., 2013; Rodriguez et al., 2017; Specht et al., 2013; Wegner et al., 2018). Under these circumstances, whether the trans-synaptic nanocolumns are maintained through the morphological changes and the lateral mobility of synapses remains to be investigated. It is likely that the trans-synaptic nanocolumns are maintained by the synaptic adhesion molecules. Synaptic cell adhesion molecule 1 (SynCAM1) and Ephrin type-B receptor 2 (EphB2) were shown to form SSDs as well (Perez de Arce et al., 2015). SynCAM1 SSDs mostly are located at the periphery of excitatory synapses, while EphB2 is enriched deeper within the PSD. Another study has shown that neuroligin-1 and leucine-rich repeat transmembrane neuronal protein 2 (LRRTM2) can also form SSDs at excitatory synapses (Chamma et al., 2016a). Neuroligin-1 molecules are generally located closer to the PSDs than LRRTM2. Owing to the different locations of these different synaptic adhesion molecules, they might play different roles in maintaining the alignment of the whole synapses and the trans-synaptic nanocolumns. A recent study has revealed that neuroligin-1 SSDs were integrated into the trans-synaptic nanocolumns of RIM1/2 and AMPARs at excitatory synapses (Haas et al., 2018). Expression of a C-terminally truncated neuroligin-1 disrupted the trans-synaptic nanocolumns and impaired the synaptic transmission. However, little is known so far about the roles of synaptic adhesion molecules in inhibitory trans-synaptic nanocolumns. The synaptic adhesion molecules responsible for the coordinated synapse mobility and the trans-synaptic nanocolumns at inhibitory synapses remain to be investigated.

4.2.3 Differential trans-synaptic alignment of GlyRs and GABA_ARs to pre-synaptic vesicle releasing sites

We found that 4-AP or TTX treatment did not change the amount of synaptic RIM1/2 compared to the non-treatment condition (Table 1). However, the spatial correlation between RIM1/2 and GlyRs was increased by 4-AP compared to TTX treatment, while the spatial correlation between RIM1/2 and GABA_ARs did not change (Table 2). This finding suggests that the relative locations of GlyRs and GABA_ARs to pre-synaptic vesicle release sites could be differentially regulated. We know that the synaptic amount of GABA_ARs and p-gephyrin are decreased by 4-AP treatment compared to the TTX condition, but not that of GlyRs and total gephyrin. Under these circumstances, if the trans-synaptic nanocolumns are somehow maintained, it may imply that GlyRs rather than GABA_ARs are recruited to the trans-synaptic nanocolumns after 4-AP treatment.

A recent study using SIM showed that GABA_AR SSDs are closely correlated with p-gephyrin SSDs as well as RIM1/2 SSDs at inhibitory synapses in hippocampal neurons (Crosby et al., 2019). This suggests that GABA_ARs may be incorporated in the trans-synaptic nanocolumns at GABAergic synapses. However, at mixed inhibitory synapses, a different mechanism may exist to differentially incorporate GlyRs and GABA_ARs into the trans-synaptic nanocolumns.

At excitatory synapses, AMPARs and NMDARs also exist at the same PSDs. Interestingly, it appears that AMPARs are more enriched in the PSD-95 SSDs than NMDARs (MacGillavry et al., 2013). In fact, there is evidence showing that AMPARs are incorporated into trans-synaptic nanocolumns (Tang et al., 2016). At these synapses, AMPARs and NMDARs share the same neurotransmitters, glutamate, released from the same pre-synaptic terminal. This suggests that they may compete for glutamate binding after vesicle release. It is known that the activation and neurotransmission of AMPARs and NMDARs are different in several ways, such as ligand binding affinity, current kinetics and voltage-dependency. However, it is possible that their spatial organization within the synapses also takes part in the receptors' access to the ligand and thus channel opening. At mixed inhibitory synapses, the increased spatial correlation of GlyRs, but not GABA_ARs, with both p-gephyrin and RIM1/2 by 4-AP treatment suggests

that GlyRs might be closely incorporated into trans-synaptic nanocolumns. Moreover, GlyRs and GABA_ARs are activated by two different neurotransmitters, glycine and GABA respectively. This suggests that they do not compete for ligand binding in the same way as the excitatory receptors. There is still some way to go before we can fully understand the role of intra-synaptic organization of two types of receptors at the same PSDs both for inhibitory and excitatory synapses.

4.3 Limitations in the current study and alternative approaches

Since the application of SMLM on synaptic clusters was first published in 2010 (Dani et al., 2010), SMLM has been adopted in many studies of the ultra-structure of synapses and proven to be a powerful tool. The ten-fold improvement of image resolution is appealing. However, it is still a young technique, especially in the field of investigating synaptic clusters. Due to the intrinsic stochasticity of the signals in SMLM and the complexity of synaptic structures (see section 1.2.2), we are faced with many challenges in the data acquisition and analysis. In this section, I discussed the limitations of my experiments as a result of the technical constraints, and also proposed alternative approaches and directions for future improvements.

First of all, I found that the impact of dyes on the detection of synaptic clusters in dSTORM is not trivial. In fact, the dyes have strong influence on the characterization of synaptic cluster size, the number of SSDs per clusters and the SSD size (Figure 15-17). This raises the question: can we actually measure the size of synaptic clusters and SSDs with dSTORM? An estimation of the clusters size and a comparison of the size between different experimental conditions may be more feasible. However, we found that the changes in the clusters size by the treatment are sometimes not consistent, when the same protein is labeled with a different dye (Figure 23-24). Therefore, despite the powerful resolution of dSTORM, there is still much room for improvement for a more precise estimation of synaptic cluster and SSD size.

Secondly, the data processing and analysis approaches can also have major effect on the cluster characterization. Both coordinate-based and image-based data analysis revealed the strong effect of the dyes on the synaptic cluster and SSD

sizes (Figure 16-17). However, different analytical techniques resulted in different measurements of SSD counts per synaptic cluster in the same dataset. In the rendered images, the pixel intensity of the clusters can be differently enhanced between images during the rendering step. As a consequence, synaptic clusters rendered from small number of localizations in one image may have the same intensity with other clusters rendered from many localizations in another image. This can cause an over-estimation of SSD counts with the H-watershed analysis, especially for the images with relative low number of localizations. In the results presented here, the SSD segmentation was mostly done with H-watershed using image-based datasets. Therefore, a different approach to segment SSDs is preferable in order to verify the observations in my experiments. For that purpose, we have developed the program SRclusters which makes use of coordinate-based data. In SRclusters, we adopted a weighted DBSCAN approach for SSD segmentation (see Appendix 3). This analysis will be applied to my dataset in the near future. Alternatively, a thresholding of the local density of localizations in the synaptic clusters using the coordinate-based data can potentially be implemented for SSD segmentation (also see section 4.3; Macgillavry et al. 2013; Pennacchietti et al., 2017a).

For the spatial correlation of synaptic clusters in the two channels, we mostly employed ICQ measurements using image-based datasets. Since the ICQ method measures the number of pixels in which the intensity in two channels changes in synchrony, rather than the total intensity of the clusters in the two channels, it is less affected by the image rendering. ICQ thus proved to be quite efficient in our experiments. However, there are still some concerns when using ICQ for the spatial correlation measurement of pre- and post-synaptic proteins. The separation of pre- and post-synaptic clusters can be evident in the dSTORM images, especially when the synapses are seen from the side in cross-section. Under these circumstances, the ICQ method may fall short in the precise measurement of the spatial correlation level. In SRclusters, a distance score is used to indicate the spatial correlation of two clusters in the two channels. This may be a better way to measure the correlation between structures that are separated by a small distance (i.e. the synaptic cleft or the plasma membrane).

This brings me to the last point. Synaptic clusters are three dimensional structures. When imaged in two dimensional mode, the 3-D structures are projected to 2-D. This causes the loss of information in the third dimension. When the synapses are seen from *en face* view, we may have better focus of one protein than the other in the two-color dSTORM imaging. This effect may be further enhanced by the inclined illumination. When the synapses are seen in side view, the 2-D projection of 3-D structures may cause the merging of different SSDs. Therefore, 3-D imaging with two-color dSTORM is certainly preferable for the synaptic clusters. We have set up a 3-D two-color dSTORM imaging protocol (see Appendix 4). However, these techniques are challenging and require further optimization. I have therefore not yet used 3D imaging systematically. I plan to do the experiments in 3D to confirm the most important findings of my research. Future development of 3-D image processing and cluster characterization approaches will allow me to accomplish a quantitative study of 3-D synaptic clusters.

4.4 Future directions and perspectives

At mixed inhibitory synapses, GlyRs and GABA_ARs undergo re-organization during altered neuronal activity, however, their SSD counts did not change. The differential changes in the molecular amount and spatial organization between GlyRs and GABA_ARs during the altered neuronal activity may underlie the precise control of the synaptic activity. For example, the increased spatial correlation of GlyRs and RIM1/2 might indicate an increase in the glycinergic miniature IPSCs in the neurons. Further electrophysiology and simulation studies can potentially validate this hypothesis. More studies on the GlyR/GABA_AR co-transmission in the future can be foreseen, providing more insights into their precise functional regulations.

We have also demonstrated the existence of SSDs of GlyRs, GABA_ARs, gephyrin and RIM1/2 at inhibitory synapses in spinal cord neurons. RIM1/2 and p-gephyrin SSDs formed trans-synaptic nanocolumns at inhibitory synapses. These observations are in line with what has been seen at excitatory synapses, where RIM1/2 and PSD-95 SSDs, together with other proteins in the active zone and the post-synaptic density, form trans-synaptic nanocolumns. Inhibitory and excitatory synapses may therefore share similar structural organization, as SSDs could be

important regulators of synaptic function. SSDs as dynamic structural units provide another angle to interpret synaptic functions. However, the identification and characterization of SSDs is complicated by technical difficulties. Future development of analytical methods will therefore be required to understand the formation of SSDs and their functions at synapses.

SMLM is a powerful tool to study synaptic structures. Yet, the complexity in the application of SMLM to synaptic structures calls for more attention to evaluating the strategies in practice. I believe that more attention has to be paid to the technical and analytical development in this particular application. Future developments of SMLM methodologies will certainly promote the study of the ultra-structure of synapses.

References

- Alvarez, F. J. (2017). Gephyrin and the regulation of synaptic strength and dynamics at glycinergic inhibitory synapses. *Brain Res Bull*, *129*, 50–65.
- Anderson, W. B., Graham, B. A., Beveridge, N. J., Tooney, P. A., Brichta, A. M., & Callister, R. J. (2009). Different forms of glycine- and GABAA -receptor mediated inhibitory synaptic transmission in mouse superficial and deep dorsal horn neurons. *Mol Pain*, *5*(65), 1–16.
- Andronov, L., Orlov, I., Lutz, Y., Vonesch, J., & Klaholz, B. P. (2016). ClusterViSu , a method for clustering of protein complexes by Voronoi tessellation in super-resolution microscopy. *Sci Rep*, *6*(24084), 1–9.
- Annibale, P., Scarselli, M., Greco, M., & Radenovic, A. (2012). Identification of the factors affecting co-localization precision for quantitative multicolor localization microscopy. *Optical Nanoscopy*, *1*(9).
- Annibale, P., Vanni, S., Scarselli, M., Rothlisberger, U., & Radenovic, A. (2011a). Identification of clustering artifacts in photoactivated localization microscopy. *Nat Methods*, *8*(7), 527–528.
- Annibale, P., Vanni, S., Scarselli, M., Rothlisberger, U., & Radenovic, A. (2011b). Quantitative Photo Activated Localization Microscopy: Unraveling the effects of photoblinking. *PLoS One*, *6*(7), 1–8.
- Apostolides, P. F., & Trussell, L. O. (2013). Rapid, Activity-Independent Turnover of Vesicular Transmitter Content at a Mixed Glycine/GABA Synapse. *J Neurosci*, *33*(11), 4768–4781.
- Arellano, J. I., Benavides-Piccione, R., DeFelipe, J., & Yuste, R. (2007). Ultrastructure of dendritic spines: correlation between synaptic and spine morphologies. *Front Neurosci*, *1*(1), 131–143.
- Aubrey, K. R. (2016). Presynaptic control of inhibitory neurotransmitter content in VIAAT containing synaptic vesicles. *Neurochem Int*, *98*, 94–102.
- Aubrey, K. R., Rossi, F. M., Ruivo, R., Alboni, S., Bellenchi, G. C., Goff, A. Le, Gasnier B., Supplisson, S. (2007). The Transporters GlyT2 and VIAAT Cooperate to Determine the Vesicular Glycinergic Phenotype. *J Neurosci*, *27*(23), 6273–6281.
- Aubrey, K. R., & Supplisson, S. (2018). Heterogeneous Signaling at GABA and glycine co-releasing terminals. *Front Synaptic Neurosci*, *10*(40), 1–13.
- Augustine, G. J., Santamaria, F., & Tanaka, K. (2003). Local Calcium Signaling in Neurons. *Neuron*, *40*, 331–346.
- Baddeley, D., & Bewersdorf, J. (2018). Biological Insight from Super-Resolution

- Microscopy: What We Can Learn from Localization-Based Images. *Ann Rev Biochem*, 87(1), 965–989.
- Bannai, H., Lévi, S., Schweizer, C., Inoue, T., Launey, T., Racine, V., Sibarita J.-B., Mikoshiba K., Triller, A. (2009). Activity-Dependent Tuning of Inhibitory Neurotransmission Based on GABAAR Diffusion Dynamics. *Neuron*, 62(5), 670–682.
- Bates, M., Huang, B., Dempsey, G. T., & Zhuang, X. (2007). Multicolor super resolution imaging with photoswitchable fluorescent probes. *Science*, 317(5845), 1749–1753.
- Battaglia, S., Renner, M., Russeau, M., Côme, E., Tyagarajan, S. K., & Lévi, S. (2018). Activity-dependent inhibitory synapse scaling is determined by gephyrin phosphorylation and subsequent regulation of GABA A receptor diffusion. *ENeuro*, 5(1), 0203–0217.
- Betz, H., & Laube, B. (2006). Glycine receptors: Recent insights into their structural organization and functional diversity. *J Neurochem*, 97(6), 1600–1610.
- Betzig, E., Patterson, G. H., Sougrat, R., Lindwasser, O. W., Olenych, S., Bonifacino, J. S., Davidson M.W., Lippincott-Schwartz J., Hess, H. F. (2006). Imaging Intracellular Fluorescent Proteins at Nanometer Resolution. *Science*, 313(5793), 1642–1646.
- Biederer, T., Kaeser, P. S., & Blanpied, T. A. (2017). Transcellular Nanoalignment of Synaptic Function. *Neuron*, 96(3), 680–696.
- Bohlhalter, S., Mohler, H., & Fritschy, J. (1994). Inhibitory neurotransmission in rat spinal cord: co-localization of glycine- and GABA_A-receptors at GABAergic synaptic contacts demonstrated by triple immunofluorescence staining. *Brain Res*, 642(1–2), 59–69.
- Bonansco, C., & Fuenzalida, M. (2016). Plasticity of Hippocampal Excitatory-Inhibitory Balance: Missing the Synaptic Control in the Epileptic Brain. *Neural Plast*, 2016, 1–13.
- Bourne, J. N., & Harris, K. M. (2011). Coordination of size and number of excitatory and inhibitory synapses results in a balanced structural plasticity along mature hippocampal CA1 dendrites during LTP. *Hippocampus*, 21(4), 354–373.
- Bowery, N., & Smart, T. (2006). GABA and glycine as neurotransmitters: A brief history. *Br J Pharmacol*, 147, 109–119.
- Brady, M. L., & Jacob, T. C. (2015). Synaptic Localization of $\alpha 5$ GABA(A) Receptors via Gephyrin Interaction Regulates Dendritic Outgrowth and Spine Maturation. *Dev Neurobiol*, 75(11), 1241–1251.

- Broadhead, M. J., Horrocks, M. H., Zhu, F., Muresan, L., Benavides-piccione, R., DeFelipe, J., Fricker D., Kopanitsa M.V., Duncan R.R., Klenerman D., Komiyama N.H., Lee S.F., Grant, S. G. N. (2016). PSD95 nanoclusters are postsynaptic building blocks in hippocampus circuits. *Sci Rep*, 6(24626), 1–14.
- Brocher, J. (2014). Qualitative and Quantitative Evaluation of Two New Histogram Limiting Binarization Algorithms. *Int J Im Process*, 8(2), 30–48.
- Burgert, A., Letschert, S., Doose, S., & Sauer, M. (2015). Artifacts in single-molecule localization microscopy. *Histochem Cell Biol*, 144, 123–131.
- Burzomato, V., Groot-Kormelink, P. J., Sivilotti, L. G., & Beato, M. (2003). Stoichiometry of recombinant heteromeric glycine receptors revealed by a pore-lining region point mutation. *Receptors Channels*, 9(6), 353–361.
- Calamai, M., Specht, C. G., Heller, J., Alcor, D., Machado, P., Vannier, C., & Triller, A. (2009). Gephyrin Oligomerization Controls GlyR Mobility and Synaptic Clustering. *J Neurosci*, 29(24), 7639–7648.
- Cantaut-Belarif, Y., Antri, M., Pizzarelli, R., Colasse, S., Vaccari, I., Soares, S., ... Bessis, A. (2017). Microglia control the glycinergic but not the GABAergic synapses via prostaglandin E2 in the spinal cord. *J Cell Biol*, 216(9), 2979–2989.
- Cantaut-Belarif, Y., Antri, M., Vaccari, I., Pizzarelli, R., Colasse, S., Soares, S., Renner M., Dallel R., Triller A., Bessis, A. (2017). Microglia control the glycinergic but not the GABAergic synapses via prostaglandin E2 in the spinal cord. *J Cell Biol*, 216(9), 2979–2989.
- Chamma, I., Letellier, M., Butler, C., Tessier, B., Lim, K. H., Gauthereau, I., Choquet D., Sibarita J.-B., Park S., Sainlos M., Thoumine, O. (2016a). Mapping the dynamics and nanoscale organization of synaptic adhesion proteins using monomeric streptavidin. *Nat Commun*, 7(10773), 1–15.
- Chamma, I., Levet, F., Sibarita, J.-B., Sainlos, M., & Thoumine, O. (2016b). Nanoscale organization of synaptic adhesion proteins revealed by single-molecule localization microscopy. *Neurophotonics*, 3(4), 041810.
- Chaudhry, F. A., Reimer, R. J., Bellocchio, E. E., Danbolt, N. C., Osen, K. K., Edwards, R. H., & Storm-Mathisen, J. (1998). The Vesicular GABA Transporter, VGAT, Localizes to Synaptic Vesicles in Sets of Glycinergic as Well as GABAergic Neurons. *J Neurosci*, 18(23), 9733–9750.
- Chen, H., Tang, A. H., & Blanpied, T. A. (2018). Subsynaptic spatial organization as a regulator of synaptic strength and plasticity. *Curr Opin Neurobiol*, 51, 147–153.
- Chéry, N., & De Koninck, Y. (1999). Junctional versus Extrajunctional Glycine

- and GABA A Receptor-Mediated IPSCs in Identified Lamina I Neurons of the Adult Rat Spinal Cord. *J Neurosci*, 19(17), 7342–7355.
- Choquet, D. (2010). Fast AMPAR trafficking for a high-frequency synaptic transmission. *Eur J Neurosci*, 32(2), 250–260.
- Choquet, D., & Triller, A. (2013). The Dynamic Synapse. *Neuron*, 80(3), 691–703.
- Coltharp, C., Yang, X., & Xiao, J. (2014). Quantitative analysis of single-molecule superresolution images. *Curr Opin Struct Biol*, 28(1), 112–121.
- Coull, J. A., Boudreau, D., Bachand, K., Prescott, S. A., Nault, F., Sik, A., De Koninck P., De Koninck, Y. (2003). Trans-synaptic shift in anion gradient in spinal lamina I neurons as a mechanism of neuropathic pain. *Nature*, 424(6951), 938-942.
- Crosby, K. C., Gookin, S. E., Garcia, J. D., Hahm, K. M., Dell'Acqua, M. L., & Smith, K. R. (2019). Nanoscale Subsynaptic Domains Underlie the Organization of the Inhibitory Synapse. *Cell Rep*, 26(12), 3284–3297.
- Culiat, C. T., Stubbs, L. J., Woychik, R. P., Russell, L. B., Johnson, D. K., & Rinchik, E. M. (1995). Deficiency of the beta3 subunit of the type A gamma-aminobutyric acid receptor causes cleft palate in mice. *Nat Genet*, 11(3), 344–346.
- Dahan, M., Lévi, S., Luccardini, C., Rostaing, P., Riveau, B., & Triller, A. (2003). Diffusion Dynamics of Glycine Receptors Revealed by Single-Quantum Dot Tracking. *Science*, 302(5644), 442–445.
- Dani, A., Huang, B., Bergan, J., Dulac, C., & Zhuang, X. (2010). Super-resolution Imaging of Chemical Synapses in the Brain. *Neuron*, 68(5), 843–856.
- Davenport, E. C., Pendolino, V., Kontou, G., McGee, T. P., Sheehan, D. F., López-Doménech, G., Farrant M., Kittler, J. T. (2017). An Essential Role for the Tetraspanin LHFPL4 in the Cell-Type-Specific Targeting and Clustering of Synaptic GABAARs. *Cell Rep*, 21(1), 70–83.
- De Chaumont, F., Dallongeville, S., Chenouard, N., Hervé, N., Pop, S., Provoost, T., Meas-Yedid V., Pankajakshan P., Lecomte T., Le Montagner Y., Lagache T., Dufour A., Olivo-Marin, J.-C. (2012). Icy: An open bioimage informatics platform for extended reproducible research. *Nat Methods*, 9(7), 690–696.
- Dejanovic, B., & Schwarz, G. (2014). Neuronal Nitric Oxide Synthase-Dependent S-Nitrosylation of Gephyrin Regulates Gephyrin Clustering at GABAergic Synapses. *J Neurosci*, 34(23), 7763–7768.
- Dejanovic, B., Semtner, M., Ebert, S., Lamkemeyer, T., Neuser, F., Meier, J. C., & Schwarz, G. (2014). Palmitoylation of Gephyrin Controls Receptor Clustering and Plasticity of GABAergic Synapses. *Plos One*, 12(7),

e1001908.

- Delgado, J. Y., & Selvin, P. R. (2018). A Revised View on the Role of Surface AMPAR Mobility in Tuning Synaptic Transmission: Limitations, Tools, and Alternative Views. *Front Synaptic Neurosci*, *10*(21), 1–12.
- Dempsey, G. T., Vaughan, J. C., Chen, K. H., Bates, M., Zhuang, X., & Graham T. Dempsey, Joshua C. Vaughan, Kok Hao Chen, Mark Bates, and X. Z. (2011). Evaluation of fluorophores for optimal performance in localization-based super-resolution imaging. *Nat Methods*, *8*(12), 1027–1036.
- Deschout, H., Zanicchi, F. C., Mlodzianoski, M., Diaspro, A., Bewersdorf, J., Hess, S. T., & Braeckmans, K. (2014). Precisely and accurately localizing single emitters in fluorescence microscopy. *Nat Methods*, *11*(3), 253–266.
- Dobie, F. A., & Craig, A. M. (2011). Inhibitory Synapse Dynamics: Coordinated Presynaptic and Postsynaptic Mobility and the Major Contribution of Recycled Vesicles to New Synapse Formation. *J Neurosci*, *31*(29), 10481–10493.
- Doty, R. L. (2012). Olfaction in Parkinson’s disease and related disorders. *Neurobiol Dis*, *46*(3), 527–552.
- Dufour, A., Tell, F., Kessler, J. P., & Baude, A. (2010). Mixed GABA-glycine synapses delineate a specific topography in the nucleus tractus solitarii of adult rat. *J Physiol*, *588*(7), 1097–1115.
- Dugué, G. P., Dumoulin, A., Triller, A., & Dieudonne, S. (2005). Target-Dependent Use of Coreleased Inhibitory Transmitters at Central Synapses. *J Neurosci*, *25*(28), 6490–6498.
- Dumoulin, A., Lévi, S., Riveau, B., Gasnier, B., & Triller, A. (2000). Formation of mixed glycine and GABAergic synapses in cultured spinal cord neurons. *Eur J Neurosci*, *12*, 3883–3892.
- Dumoulin, Andréa, Rostaing, P., Bedet, C., Lévi, S., Isambert, M. F., Henry, J. P., Triller A., Gasnier, B. (1999). Presence of the vesicular inhibitory amino acid transporter in GABAergic and glycinergic synaptic terminal boutons. *J Cell Sci*, *112*, 811–823.
- Dumoulin, Andrea, Triller, A., & Dieudonne, S. (2001). IPSC Kinetics at Identified GABAergic and Mixed GABAergic and Glycinergic Synapses onto Cerebellar Golgi Cells. *J Neurosci*, *21*(16), 6045–6057.
- Dumoulin, Andrea, Triller, A., & Kneussel, M. (2010). Cellular transport and membrane dynamics of the glycine receptor. *Front Mol Neurosci*, *2*(28), 1–11.
- Dunn, K. W., Kamocka, M. M., & McDonald, J. H. (2011). A practical guide to evaluating colocalization in biological microscopy. *Am J Physiol Cell*

Physiol, 300(4), C723–C742.

Durisic, N., Godin, A. G., Wever, C. M., Heyes, C. D., Lakadamyali, M., & Dent, J. A. (2012). Stoichiometry of the Human Glycine Receptor Revealed by Direct Subunit Counting. *J Neurosci*, 32(37), 12915–12920.

Dutertre, S., Becker, C. M., & Betz, H. (2012). Inhibitory glycine receptors: An update. *J Biol Chem*, 287(48), 40216–40223.

Dzyubenko, E., Rozenberg, A., Hermann, D. M., & Faissner, A. (2016). Colocalization of synapse marker proteins evaluated by STED-microscopy reveals patterns of neuronal synapse distribution in vitro. *J Neurosci Methods*, 273, 149–159.

Eggermann, E., Bucurenciu, I., Goswami, S. P., & Jonas, P. (2013). Europe PMC Funders Group Nanodomain coupling between Ca²⁺ channels and sensors of exocytosis at fast mammalian synapses. *Nat Rev Neurosci*, 13(1), 7–21.

Endesfelder, U., & Heilemann, M. (2014). Art and artifacts in single-molecule localization microscopy: beyond attractive images. *Nat Methods*, 11(3), 235–238.

Endesfelder, U., Malkusch, S., Flottmann, B., Mondry, J., Liguzinski, P., Verveer, P. J., & Heilemann, M. (2011). Chemically induced photoswitching of fluorescent probes-A general concept for super-resolution microscopy. *Molecules*, 16(4), 3106–3118.

Essrich, C., Lorez, M., Benson, J. A., Fritschy, J.-M., & Lüscher, B. (1998). Postsynaptic clustering of major GABA A receptor subtypes requires the γ 2 subunit and gephyrin. *Nat Neurosci*, 1(7), 563–571.

Ferguson, C., Hardy, S. L., Werner, D. F., Hileman, S. M., Delorey, T. M., & Homanics, G. E. (2007). New insight into the role of the β 3 subunit of the GABAA-R in development, behavior, body weight regulation, and anesthesia revealed by conditional gene knockout. *BMC Neurosci*, 8(85), 1–13.

Fischl, M. J., & Burger, R. M. (2014). Glycinergic transmission modulates GABAergic inhibition in the avian auditory pathway. *Front Neural Circuits*, 8(19), 1–13.

Fricke, F., Beaudouin, J., Eils, R., & Heilemann, M. (2015). One, two or three? Probing the stoichiometry of membrane proteins by single-molecule localization microscopy. *Sci Rep*, 5(14072), 1–8.

Fritschy, J. M., Panzanelli, P., & Tyagarajan, S. K. (2012). Molecular and functional heterogeneity of GABAergic synapses. *Cell Mol Life Sci*, 69(15), 2485–2499.

Fukata, Y., Dimitrov, A., Boncompain, G., Vielemeyer, O., Perez, F., & Fukata,

- M. (2013). Local palmitoylation cycles define activity-regulated postsynaptic subdomains. *J Cell Biol*, 202(1), 145–161.
- Fukata, Y., & Fukata, M. (2017). Epilepsy and synaptic proteins. *Curr Opin Neurobiol*, 45, 1–8.
- Fukazawa, Y., & Shigemoto, R. (2012). Intra-synapse-type and inter-synapse-type relationships between synaptic size and AMPAR expression. *Curr Opin Neurobiol*, 22(3), 446–452.
- Ganeshina, O., Berry, R. W., Petralia, R. S., Nicholson, D. A., & Geinisman, Y. (2004). Synapses with a segmented, completely partitioned postsynaptic density express more AMPA receptors than other axospinous synaptic junctions. *Neuroscience*, 125(3), 615–623.
- Gao, R., & Penzes, P. (2015). Common Mechanisms of Excitatory and Inhibitory Imbalance in Schizophrenia and Autism Spectrum Disorders. *Curr Mol Med*, 15(2), 146–167.
- Gasnier, B. (2000). The loading of neurotransmitters into synaptic vesicles. *Biochimie*, 82, 327–337.
- Geiman, E. J., Zhang, W., Fritschy, J.-M., & Alvarez, F. J. (2002). Glycine and GABAA receptor subunits on renshaw cells: Relationship with presynaptic neurotransmitters and postsynaptic gephyrin clusters. *J Comp Neurol*, 444(3), 275–289.
- Gerrow, K., & Triller, A. (2010). Synaptic stability and plasticity in a floating world. *Curr Opin Neurobiol*, 20(5), 631–639.
- Ghelani, T., & Sigrist, S. J. (2018). Coupling the Structural and Functional Assembly of Synaptic Release Sites. *Front Neuroanat*, 12(81), 1–20.
- Giannone, G., Hosy, E., Levet, F., Constals, A., Schulze, K., Sobolevsky, A. I., Rosconi M.P., Gouaux E., Tampe R., Choquet D., Cognet, L. (2010). Dynamic superresolution imaging of endogenous proteins on living cells at ultra-high density. *Biophys J*, 99(4), 1303–1310.
- Glebov, O. O., Jackson, R. E., Winterflood, C. M., Owen, D. M., Barker E. A., Doherty P., Ewers H., Burrone, J. (2017). Nanoscale Structural Plasticity of the Active Zone Matrix Modulates Presynaptic Function. *Cell Rep*, 18(11), 2715–2728.
- Gonzalez-Forero, D., & Alvarez, F. J. (2005). Differential Postnatal Maturation of GABAA, Glycine Receptor, and Mixed Synaptic Currents in Renshaw Cells and Ventral Spinal Interneurons. *J Neurosci*, 25(8), 2010–2023.
- Gonzalez-Forero, D., Pastor, A. M., Geiman, E. J., Benitez-Temino, B., & Alvarez, F. J. (2005). Regulation of Gephyrin Cluster Size and Inhibitory Synaptic Currents on Renshaw Cells by Motor Axon Excitatory Inputs. *J*

- Neurosci*, 25(2), 417–429.
- Gouzer, G., Specht, C. G., Allain, L., Shinoe, T., & Triller, A. (2014). Benzodiazepine-dependent stabilization of GABA A receptors at synapses. *Mol Cell Neurosci*, 63, 101–113.
- Granger, A. J., Wallace, M. L., & Sabatini, B. L. (2017). Multi-transmitter neurons in the mammalian central nervous system. *Curr Opin Neurobiol*, 45, 85–91.
- Groeneweg, F. L., Trattnig, C., Kuhse, J., Nawrotzki, R. A., & Kirsch, J. (2018). Gephyrin: a key regulatory protein of inhibitory synapses and beyond. *Histochem Cell Biol*, 150(5), 489–508.
- Grudzinska, J., Schemm, R., Haeger, S., Nicke, A., Schmalzing, G., Betz, H., & Laube, B. (2005). The beta Subunit Determines the Ligand Binding Properties of Synaptic Glycine Receptors. *Neuron*, 45(5), 727–739.
- Grünewald, N., Jan, A., Salvatico, C., Kress, V., Renner, M., Triller, A., Specht C.G., Schwarz, G. (2018). Sequences Flanking the Gephyrin-Binding Site of GlyR β Tune Receptor Stabilization at Synapses. *ENeuro*, 5(1), 1–17.
- Gustafsson, M. G. L. (2000). Surpassing the lateral resolution limit by a factor of two using structured illumination microscopy. *J Microsc*, 198(2), 82–87.
- Ha, T., & Tinnefeld, P. (2012). Photophysics of Fluorescence Probes for Single Molecule Biophysics and Super-Resolution Imaging. *Annu Rev Phys Chem*, 63(2), 595–617.
- Haas, K. T., Compans, B., Letellier, M., Bartol, T. M., Grillo-Bosch, D., Sejnowski, T. J., Sainlos M., Choquet D., Thoumine O., Hosy, E. (2018). Pre-post synaptic alignment through neuroligin-1 tunes synaptic transmission efficiency. *ELife*, 7, 1–22.
- Hannan, S., Minere, M., Harris, J., Izquierdo, P., Thomas, P., Tench, B., & Smart, T. G. (2019). GABAAR isoform and subunit structural motifs determine synaptic and extrasynaptic receptor localisation. *Neuropharmacology*, xxx(xxx), xxx.
- Hanus, C., Ehrensperger, M.-V., & Triller, A. (2006). Activity-Dependent Movements of Postsynaptic Scaffolds at Inhibitory Synapses. *J Neurosci*, 26(17), 4586–4595.
- Harris, K. M., & Stevens, J. K. (1989). Dendritic spines of CA1 pyramidal cells in the rat hippocampus serial electron microscopy with reference to their biophysical characteristics. *J Neurosci*, 9(8), 2982–2997.
- Harris, K. M., & Weinberg, R. J. (2012). Ultrastructure of Synapses in the Mammalian Brain. *Cold Spring Harb Perspect Biol*, 4(5), 1–30.

- Harvey, R. J., Depner, U. B., Wässle, H., Ahmadi, S., Heindl, C., Reinold, H., Smart T.G., Harvey K., Schutz B., Abo-Salem O.M., Zimmer A., Poisbeau P., Welzl H., Wolfer D.P., Betz H., Zeilhofer H.U., Müller, U. (2004). GlyR $\alpha 3$: An Essential Target for Spinal PGE 2-Mediated Inflammatory Pain Sensitization. *Science*, 304(5672), 884–887.
- Harvey, R. J., & Yee, B. K. (2013). Glycine transporters as novel therapeutic targets in schizophrenia, alcohol dependence and pain. *Nat Rev Drug Discov*, 12(11), 866–885.
- Heilemann, M., Linde, S. Van De, Sch, M., Kasper, R., Seefeldt, B., Mukherjee, A., Tinnefeld P., Sauer, M. (2008). Subdiffraction-resolution fluorescence imaging with conventional fluorescent probes. *Angew Chem Int Ed Engl*, 47(33), 6172–6176.
- Hell, S. W., Sahl, S. J., Bates, M., Zhuang, X., Heintzmann, R., Booth, M. J., ... Cordes, T. (2015). The 2015 super-resolution microscopy roadmap. *J Physics D: Appl Phys*, 48(44), 443001.
- Heller, E. A., Zhang, W., Selimi, F., Earnheart, J. C., Slimak, M. A., Santos-Torres, J., Ibanez-Tallon I., Aoki C., Chait B.T., Heintz, N. (2012). The Biochemical Anatomy of Cortical Inhibitory Synapses. *PLoS One*, 7(6), e39572.
- Hennekinne, L., Colasse, S., Triller, A., & Renner, M. (2013). Differential Control of Thrombospondin over Synaptic Glycine and AMPA Receptors in Spinal Cord Neurons. *J Neurosci*, 33(28), 11432–11439.
- Herweg, J., & Schwarz, G. (2012). Splice-specific Glycine Receptor Binding, Folding, and Phosphorylation of the Scaffolding Protein Gephyrin. *J Biol Chem*, 287(16), 12645–12656.
- Hess, S. T., Girirajan, T. P. K. K., & Mason, M. D. (2006). Ultra-high resolution imaging by fluorescence photoactivation localization microscopy. *Biophys J*, 91(11), 4258–4272.
- High, B., Cole, A. A., Chen, X., & Reese, T. S. (2015). Electron microscopic tomography reveals discrete transclefth elements at excitatory and inhibitory synapses. *Front Synaptic Neurosci*, 7(9), 1–9.
- Houston, C. M., Hosie, A. M., & Smart, T. G. (2008). Distinct Regulation of beta2 and beta3 Subunit-Containing Cerebellar Synaptic GABA(A) Receptors by Calcium/Calmodulin-Dependent Protein Kinase II. *J Neurosci*, 28(30), 7574–7584.
- Houston, C. M., & Smart, T. G. (2006). CaMK-II modulation of GABAA receptors expressed in HEK293, NG108-15 and rat cerebellar granule neurons. *Eur J Neurosci*, 24(9), 2504–2514.

- Hruska, M., Henderson, N., Le Marchand, S. J., Jafri, H., & Dalva, M. B. (2018). Synaptic nanomodules underlie the organization and plasticity of spine synapses. *Nat Neurosci*, *21*(5), 671–682.
- Imlach, W. L., Bhola, R. F., Mohammadi, S. A., & Christie, M. J. (2016). Glycinergic dysfunction in a subpopulation of dorsal horn interneurons in a rat model of neuropathic pain. *Sci Rep*, *6*(37104), 1–14.
- Ishibashi, H., Yamaguchi, J., Nakahata, Y., & Nabekura, J. (2013). Dynamic regulation of glycine-GABA co-transmission at spinal inhibitory synapses by neuronal glutamate transporter. *J Physiol*, *591*(16), 3821–3832.
- Izeddin, I., Specht, C. G., Lelek, M., Darzacq, X., Triller, A., Zimmer, C., & Dahan, M. (2011). Super-resolution dynamic imaging of dendritic spines using a low-affinity photoconvertible actin probe. *PLoS One*, *6*(1), e15611.
- Jonas, P., Bischofberger, J., & Sandkühler, J. (1998). Co-release of Two Fast Neurotransmitters at a Central Synapse. *Science*, *281*(5375), 419–424.
- Juge, N., Muroyama, A., Hiasa, M., Omote, H., & Moriyama, Y. (2009). Vesicular inhibitory amino acid transporter is a Cl⁻/γ-aminobutyrate co-transporter. *J Biol Chem*, *284*(50), 35073–35078.
- Kaila, K., Price, T. J., Payne, J. A., Puskarjov, M., & Voipio, J. (2014). Cation-chloride cotransporters in neuronal development, plasticity and disease. *Nat Rev Neurosci*, *15*(10), 637–654.
- Kasaragod, V. B., & Schindelin, H. (2018). Structure–Function Relationships of Glycine and GABAA Receptors and Their Interplay With the Scaffolding Protein Gephyrin. *Front Mol Neurosci*, *11*(317), 1–21.
- Kasugai, Y., Swinny, J. D., Roberts, J. D. B., Dalezios, Y., Fukazawa, Y., Sieghart, W., Shigemoto R., Somogyi, P. (2010). Quantitative localisation of synaptic and extrasynaptic GABA A receptor subunits on hippocampal pyramidal cells by freeze-fracture replica immunolabelling. *Eur J Neurosci*, *32*(11), 1868–1888.
- Katsurabayashi, S., Kubota, H., Higashi, H., Akaike, N., & Ito, Y. (2004). Distinct profiles of refilling of inhibitory neurotransmitters into presynaptic terminals projecting to spinal neurones in immature rats. *J Physiol*, *560*(2), 469–478.
- Keller, A. F., Coull, J. A. M., Chery, N. ge, Poisbeau, P., & Koninck, Y. De. (2001). Region-specific developmental specialization of GABA-glycine cosynapses in laminae I-II of the rat spinal dorsal horn. *J Neurosci*, *21*(20), 7871–7880.
- Khanna, R., Li, Q., Sun, L., Collins, T. J., & Stanley, E. F. (2006). N type Ca²⁺ channels and RIM scaffold protein covary at the presynaptic transmitter release face but are components of independent protein complexes.

- Neuroscience*, 140(4), 1201–1208.
- Kim, E. Y., Schrader, N., Smolinsky, B., Bedet, C., Vannier, C., Schwarz, G., & Schindelin, H. (2006). Deciphering the structural framework of glycine receptor anchoring by gephyrin. *EMBO J*, 25(6), 1385–1395.
- Kins, S., Betz, H., & Kirsch, J. (2000). Collybistin, a newly identified brain-specific GEF, induces submembrane clustering of gephyrin. *Nat Neurosci*, 3(1), 22–29.
- Klar, T. A., Jakobs, S., Dyba, M., Egner, A., & Hell, S. W. (2000). Fluorescence microscopy with diffraction resolution barrier broken by stimulated emission Physical Principles and Setup. *Proc Natl Acad Sci U S A*, 97(15), 8206–8210.
- Kneussel, M., & Betz, H. (2000a). Clustering of inhibitory neurotransmitter receptors at developing postsynaptic sites : the membrane activation model. *Trends Neurosci*, 23(9), 429–435.
- Kneussel, M., & Betz, H. (2000b). Receptors , gephyrin and gephyrin-associated proteins : novel insights into the assembly of inhibitory postsynaptic membrane specializations. *J Physiol*, 525(1), 1–9.
- Knoflach, F., Hernandez, M., & Bertrand, D. (2016). GABA A receptor-mediated neurotransmission: Not so simple after all. *Biochem Pharmacol*, 115, 10–17.
- Kowalczyk, S., Winkelmann, A., Smolinsky, B., Benjamin, F., Neundorff, I., Schwarz, G., & Meier, J. C. (2013). Direct binding of GABAA receptor β 2 and β 3 subunits to gephyrin. *Eur J Neurosci*, 37(4), 544–554.
- Kuhse, J., Kalbouneh, H., Schlicksupp, A., Mükusch, S., Nawrotzki, R., & Kirsch, J. (2012). Phosphorylation of gephyrin in hippocampal neurons by cyclin-dependent kinase CDK5 at Ser-270 is dependent on collybistin. *J Biol Chem*, 287(37), 30952–30966.
- Kuriu, T., Inoue, A., Bito, H., Sobue, K., & Okabe, S. (2006). Differential Control of Postsynaptic Density Scaffolds via Actin-Dependent and -Independent Mechanisms. *J Neurosci*, 26(29), 7693–7706.
- Kuriu, Toshihiko, Yanagawa, Y., & Konishi, S. (2012). Activity-dependent coordinated mobility of hippocampal inhibitory synapses visualized with presynaptic and postsynaptic tagged-molecular markers. *Mol Cell Neurosci*, 49(2), 184–195.
- Laine, R. F., Schierle, G. S. K., Van De Linde, S., & Kaminski, C. F. (2016). From single-molecule spectroscopy to super-resolution imaging of the neuron: A review. *Methods Appl Fluoresc*, 4(2).
- Langosch, D., Thomas, L., & Betz, H. (1988). Conserved quaternary structure of ligand-gated ion channels: the postsynaptic glycine receptor is a pentamer. *Proc Natl Acad Sci*, 85(19), 7394–7398.

- Legendre, P. (2001). The glycinergic inhibitory synapse. *Cell Mol Life Sci*, 58(5–6), 760–793.
- Lehmann, M., Lichtner, G., Klenz, H., & Schmoranzler, J. (2016). Novel organic dyes for multicolor localization-based super-resolution microscopy. *J Biophotonics*, 9(1–2), 161–170.
- Lelek, M., Di Nunzio, F., Henriques, R., Charneau, P., Arhel, N., & Zimmer, C. (2012). Superresolution imaging of HIV in infected cells with FIAsh-PALM. *Proc Natl Acad Sci U S A*, 109(22), 8564–8569.
- Levet, F., Hosy, E., Kechkar, A., Butler, C., Beghin, A., Choquet, D., & Sibarita, J. (2015). SR-Tesseler: a method to segment and quantify localization-based super-resolution microscopy data. *Nat Methods*, 12(11), 1065–1071.
- Lévi, S., Chesnoy-Marchais, D., Sieghart, W., Triller, A. (1999). Synaptic Control of Glycine and GABAA Receptors and Gephyrin Expression in Cultured Motoneurons. *J Neurosci*, 19(17), 7434–7449.
- Lévi, Sabine, Le Roux, N., Eugène, E., & Poncer, J. C. (2015). Benzodiazepine ligands rapidly influence GABAA receptor diffusion and clustering at hippocampal inhibitory synapses. *Neuropharmacology*, 88, 199–208.
- Lévi, Sabine, Logan, S. M., Tovar, K. R., & Craig, A. M. (2004). Gephyrin Is Critical for Glycine Receptor Clustering But Not for the Formation of Functional GABAergic Synapses in Hippocampal Neurons. *J Neurosci*, 24(1), 207–217.
- Lévi, Sabine, Schweizer, C., Bannai, H., Pascual, O., Charrier, C., & Triller, A. (2008). Homeostatic Regulation of Synaptic GlyR Numbers Driven by Lateral Diffusion. *Neuron*, 59(2), 261–273.
- Li, J., Casteels, T., Frogne, T., Collombat, P., Hecksher-sørensen, J., & Kubicek, S. (2017). Artemisinin Target GABA(A) Receptor Signaling and Impair alpha Cell Identity. *Cell*, 168(1–2), 86–100.
- Li, Q., Lau, A., Morris, T. J., Guo, L., Fordyce, C. B., & Stanley, E. F. (2004). A Syntaxin 1, Gαo, and N-Type Calcium Channel Complex at a Presynaptic Nerve Terminal: Analysis by Quantitative Immunocolocalization. *J Neurosci*, 24(16), 4070–4081.
- Li, T. P., Song, Y., MacGillavry, H. D., Blanpied, T. A., & Raghavachari, S. (2016). Protein Crowding within the Postsynaptic Density Can Impede the Escape of Membrane Proteins. *J Neurosci*, 36(15), 4276–4295.
- Lim, R., Alvarez, F. J., & Walmsley, B. (2000). GABA mediates presynaptic inhibition at glycinergic synapses in a rat auditory brainstem nucleus. *J Physiol*, 525(2), 447–459.
- Linsalata, A. E., Chen, X., Winters, C. A., & Reese, T. (2014). Electron

- Tomography on γ -Aminobutyric Acid-ergic Synapses Reveals a Discontinuous Postsynaptic Network of Filaments. *J Comp Neurol*, 522(4), 921–936.
- Liu, K. K. L., Hagan, M. F., & Lisman, J. E. (2017). Gradation (approx. 10 size states) of synaptic strength by quantal addition of structural modules. *Philos Trans R Soc Lond B Biol Sci*, 372(1715).
- Lu, T., Rubio, M. E., & Trussell, L. O. (2007). Glycinergic Transmission Shaped by the Corelease of GABA in a Mammalian Auditory Synapse. *Neuron*, 57(4), 524–535.
- Lynch, J. W. (2004). Molecular structure and function of the glycine receptor chloride channel. *Physiol Rev*, 84(4), 1051–1095.
- MacGillavry, H. D., Song, Y., Raghavachari, S., & Blanpied, T. A. (2013). Nanoscale scaffolding domains within the postsynaptic density concentrate synaptic ampa receptors. *Neuron*, 78(4), 615–622.
- Maidorn, M., Rizzoli, S. O., & Opazo, F. (2016). Tools and limitations to study the molecular composition of synapses by fluorescence microscopy. *Biochem J*, 473(20), 3385–3399.
- Malkusch, S., & Heilemann, M. (2016). Extracting quantitative information from single-molecule super-resolution imaging data with LAMA-LocAlization Microscopy Analyzer. *Sci Rep*, 6(34486), 1–4.
- Maric, H. M., Kasaragod, V. B., Hausrat, T. J., Kneussel, M., Tretter, V., Strømgaard, K., & Schindelin, H. (2014). Molecular basis of the alternative recruitment of GABA A versus glycine receptors through gephyrin. *Nat Commun*, 5(5767), 1–11.
- Maric, H., Mukherjee, J., Tretter, V., Moss, S. J., & Schindelin, H. (2011). Gephyrin-mediated γ -Aminobutyric Acid Type A and Glycine Receptor Clustering Relies on a Common Binding Site. *J Biol Chem*, 286(49), 42105–42114.
- Masch, J.-M., Steffens, H., Fischer, J., Engelhardt, J., Hubrich, J., Keller-Findeisen, J., ... Hell, S. W. (2018). Robust nanoscopy of a synaptic protein in living mice by organic-fluorophore labeling. *Proc Natl Acad Sci U S A*, 115(34), E8047–E8056.
- Masugi-Tokita, M., Tarusawa, E., Watanabe, M., Molnar, E., Fujimoto, K., & Shigemoto, R. (2007). Number and Density of AMPA Receptors in Individual Synapses in the Rat Cerebellum as Revealed by SDS-Digested Freeze-Fracture Replica Labeling. *J Neurosci*, 27(8), 2135–2144.
- Mcdonald, J. H., & Dunn, K. W. (2013). Statistical tests for measures of colocalization in biological microscopy. *J Microsc*, 252(3), 295–302.

- McIntire, S. L., Reimer, R. J., Schuske, K., Edwards, R. H., & Jorgensen, E. M. (1997). Identification and characterization of the vesicular GABA transporter. *Nature*, 389(6653), 870–876.
- Medelin, M., Rancic, V., Cellot, G., Laishram, J., Veeraraghavan, P., Rossi, C., Muzio L., Sivilotti L., Ballerini, L. (2016). Altered development in GABA co-release shapes glycinergic synaptic currents in cultured spinal slices of the SOD1G93A mouse model of amyotrophic lateral sclerosis. *J Physiol*, 594(13), 3827–3840.
- Meye, F. J., Soiza-Reilly, M., Smit, T., Diana, M. A., Schwarz, M. K., & Mameli, M. (2016). Shifted pallidal co-release of GABA and glutamate in habenula drives cocaine withdrawal and relapse. *Nat Neurosci*, 19(8), 1019–1024.
- Meyer, D., Bonhoeffer, T., & Scheuss, V. (2014). Balance and stability of synaptic structures during synaptic plasticity. *Neuron*, 82(2), 430–443.
- Meyer, G., Kirsch, J., Betz, H., & Langosch, D. (1995). Identification of a gephyrin binding motif on the glycine receptor b subunit. *Neuron*, 15(3), 563–572.
- Missler, M., Südhof, T. C., & Biederer, T. (2012). Synaptic Cell Adhesion. *Cold Spring Harb Perspect Biol*, 4(4), a005694–a005694.
- Mitchell, K., Spike, R., & Todd, A. (1993). An immunocytochemical study of glycine receptor and GABA in laminae I-III of rat spinal dorsal horn. *J Neurosci*, 13(6), 2371–2381.
- Moore, L. A., & Trussell, L. O. (2017). Corelease of Inhibitory Neurotransmitters in the Mouse Auditory Midbrain. *J Neurosci*, 37(39), 9453–9464.
- Moss, S. J., & Smart, T. G. (2001). Constructing inhibitory synapses. *Nat Rev Neurosci*, 2(4), 240–250.
- Mukherjee, J., Kretschmannova, K., Gouzer, G., Maric, H., Ramsden, S., Tretter, V., Harvey K., Davies P.A., Triller A., Schindelin H., Moss, S. J. (2011). The residence time of GABAARs at inhibitory synapses is determined by direct binding of the receptor $\alpha 1$ subunit to gephyrin. *J Neurosci*, 31(41), 14677–14687.
- Muller, E., Corronc, L., Triller, A., Legendre, P., Le Corronc, H., Triller, A., & Legendre, P. (2006). Developmental dissociation of presynaptic inhibitory neurotransmitter and postsynaptic receptor clustering in the hypoglossal nucleus. *Mol Cell Neurosci*, 32(3), 254–273.
- Nabekura, J., Katsurabayashi, S., Kakazu, Y., Shibata, S., Matsubara, A., Jinno, S., Mizoguchi Y., Sasaki A., Ishibashi, H. (2004). Developmental switch from GABA to glycine release in single central synaptic terminals. *Nat Neurosci*, 7(1), 17–23.

- Nahidiyar, L., Agronskaia, A. V., Broertjes, J., van den Broek, B., & Jalink, K. (2016). Optimizing imaging conditions for demanding multi-color super resolution localization microscopy. *PLoS One*, *11*(7), 1–18.
- Nair, D., Hosy, E., Petersen, J. D., Constals, A., Giannone, G., Choquet, D., & Sibarita, J. (2013). Super-Resolution Imaging Reveals That AMPA Receptors Inside Synapses Are Dynamically Organized in Nanodomains Regulated by PSD95. *J Neurosci*, *33*(32), 13204–13224.
- Narahashi, T. (2008). Review Tetrodotoxin: A brief history. *Proc Jpn Acad, Ser B*, *84*(5), 147–154.
- Nawrotzki, R., Islinger, M., Vogel, I., Völkl, A., & Kirsch, J. (2012). Expression and subcellular distribution of gephyrin in non-neuronal tissues and cells. *Histochem Cell Biol*, *137*(4), 471–482.
- Nelson, S. B., & Valakh, V. (2015). Excitatory/Inhibitory Balance and Circuit Homeostasis in Autism Spectrum Disorders. *Neuron*, *87*(4), 684–698.
- Nerlich, J., Kuenzel, T., Keine, C., Korenic, A., Rubsamen, R., & Milenkovic, I. (2014). Dynamic Fidelity Control to the Central Auditory System: Synergistic Glycine/GABAergic Inhibition in the Cochlear Nucleus. *J Neurosci*, *34*(35), 11604–11620.
- Nguyen, Q. A., & Nicoll, R. A. (2018). The GABAAR receptor β Subunit Is Required for Inhibitory Transmission. *Neuron*, *98*(4), 718–725.e3.
- Nicovich, P. R., Owen, D. M., & Gaus, K. (2017). Turning single-molecule localization microscopy into a quantitative bioanalytical tool. *Nat Protoc*, *12*(3), 453–461.
- Nieves, D., Gaus, K., & Baker, M. (2018). DNA-Based Super-Resolution Microscopy: DNA-PAINT. *Genes*, *9*(12), 621.
- Niwa, F., Bannai, H., Arizono, M., Fukatsu, K., Triller, A., & Mikoshiba, K. (2012). Gephyrin-Independent GABAAR Mobility and Clustering during Plasticity. *PLoS One*, *7*(4), e36148.
- Nusser, Z., Cull-Candy, S., & Farrant, M. (1997). Differences in synaptic GABA(A) receptor number underlie variation in GABA mini amplitude. *Neuron*, *19*(3), 697–709.
- Nusser, Z., Hájos, N., Somogyi, P., & Mody, I. (1998). Increased number of synaptic GABA(A) receptors underlies potentiation at hippocampal inhibitory synapses. *Nature*, *395*(6698), 172–177.
- Nutt, D. (2006). GABA receptors: subtypes, regional distribution, and function. *J Clin Sleep Med*, *2*(2), S7-11.
- O'Brien, J. A., & Berger, A. J. (1999). Cotransmission of GABA and Glycine to

- Brain Stem Motoneurons. *J Neurophysiol*, 82(3), 1638–1641.
- O'Brien, J. A., & Berger, A. J. (2001). The Nonuniform Distribution of the GABA(A) Receptor $\alpha 1$ Subunit Influences Inhibitory Synaptic Transmission to Motoneurons within a Motor Nucleus. *J Neurosci*, 21(21), 8482–8494.
- Oertner, T. G., & Matus, A. (2005). Calcium regulation of actin dynamics in dendritic spines. *Cell Calcium*, 37(5), 477–482.
- Olsen, R. W., & Seighart, W. (2008). International Union of Pharmacology. LXX. Subtypes of gamma-aminobutyric acid(A) receptors: classification on the basis of subunit composition, pharmacology, and function. *Pharmacol Rev*, 60(3), 243–260.
- Pageon, S. V., Nicovich, P. R., Mollazade, M., Tabarin, T., & Gaus, K. (2016). Clus-DoC: a combined cluster detection and colocalization analysis for single-molecule localization microscopy data. *Mol Biol Cell*, 27(22), 3627–3636.
- Papadopoulos, T., & Soykan, T. (2011). The Role of Collybistin in Gephyrin Clustering at Inhibitory Synapses: Facts and Open Questions. *Front Cell Neurosci*, 5(11), 1–10.
- Patriarchi, T., Buonarati, O. R., & Hell, J. W. (2018). Postsynaptic localization and regulation of AMPA receptors and Cav1.2 by $\beta 2$ adrenergic receptor/PKA and Ca²⁺/CaMKII signaling. *EMBO J*, 37, e99771.
- Patrizio, A., Renner, M., Pizzarelli, R., Triller, A., & Specht, C. G. (2017a). Alpha subunit-dependent glycine receptor clustering and regulation of synaptic receptor numbers. *Scientific Reports*, 7(1), 1–11.
- Patrizio, A., Renner, M., Pizzarelli, R., Triller, A., & Specht, C. G. (2017b). Alpha subunit-dependent glycine receptor clustering and regulation of synaptic receptor numbers. *Sci Rep*, 7(1), 1–11.
- Pennacchietti, F., Gould, T. J., & Hess, S. T. (2017b). The Role of Probe Photophysics in Localization- Based Superresolution Microscopy. *Biophys J*, 113, 2037–2054.
- Pennacchietti, F., Vascon, S., Nieuw, T., Rosillo, C., Das, S., Tyagarajan, S. K., Diaspro A., Del Bue A., Petrini E.M., Barberis A., Cella Zancchi, F. (2017a). Nanoscale Molecular Reorganization of the Inhibitory Postsynaptic Density Is a Determinant of GABAergic Synaptic Potentiation. *J Neurosci*, 37(7), 1747–1756.
- Perez de Arce, K., Schrod, N., Metzbower, S. W. R., Allgeyer, E., Kong, G. K. W., Tang, A. H., Krupp A.J., Stein V., Liu X., Bewersdorf J., Blanpied T.A., Lucic V., Biederer, T. (2015). Topographic Mapping of the Synaptic Cleft into Adhesive Nanodomains. *Neuron*, 88(6), 1165–1172.

- Petrini, E. M., Ravasenga, T., Hausrat, T. J., Iurilli, G., Olcese, U., Racine, V., Sibarita J.-B., Jacob T.C., Moss S.J., Benfenati F., Medini P., Kneussel M., Barberis, A. (2014). Synaptic recruitment of gephyrin regulates surface GABAA receptor dynamics for the expression of inhibitory LTP. *Nat Commun*, 5(3921), 1–19.
- Pizzarelli, R., & Cherubini, E. (2011). Alterations of GABAergic Signaling in Autism Spectrum Disorders. *Neural Plast*, 2011(297153), 1–12.
- Rahman, J., Latal, A. T., Besser, S., Hirrlinger, J., Hulsman, S., & Hülsmann, S. (2013). Mixed miniature postsynaptic currents resulting from co-release of glycine and GABA recorded from glycinergic neurons in the neonatal respiratory network. *Eur J Neurosci*, 37(8), 1229–1241.
- Renner, M., Schweizer, C., Bannai, H., Triller, A., & Lévi, S. (2012). Diffusion Barriers Constrain Receptors at Synapses. *PLoS One*, 7(8), e43032.
- Renner, M., Specht, C. G., & Triller, A. (2008). Molecular dynamics of postsynaptic receptors and scaffold proteins. *Curr Opin Neurobiol*, 18(5), 532–540.
- Rodriguez, P. C., Almeida, L. G., & Triller, A. (2017). Continuous rearrangement of the postsynaptic gephyrin scaffolding domain: a super-resolution quantified and energetic approach. *BioRxiv*.
- Ross, G. W., Petrovitch, H., Abbott, R. D., Tanner, C. M., Popper, J., Masaki, K., Launer L., White, L. R. (2008). Association of olfactory dysfunction with risk for future Parkinson's disease. *Ann Neurol*, 63(2), 167–173.
- Rousseau, C. V., Dugue, G. P., Dumoulin, A., Mugnaini, E., Dieudonne, S., & Diana, M. A. (2012). Mixed Inhibitory Synaptic Balance Correlates with Glutamatergic Synaptic Phenotype in Cerebellar Unipolar Brush Cells. *J Neurosci*, 32(13), 4632–4644.
- Russier, M., Kopysova, I. L., Ankri, N., Ferrand, N., & Debanne, D. (2002). GABA and glycine co-release optimizes functional inhibition in rat brainstem motoneurons in vitro. *J Physiol*, 541(1), 123–137.
- Rust, M. J., Bates, M., & Zhuang, X. (2006). Sub-diffraction-limit imaging by stochastic optical reconstruction microscopy (STORM). *Nat Methods*, 3(10), 793–795.
- Sagné, C., El Mestikawy, S., Isambert, M. F., Hamon, M., Henry, J. P., Giros, B., & Gasnier, B. (1997). Cloning of a functional vesicular GABA and glycine transporter by screening of genome databases. *FEBS Letters*, 417(2), 177–183.
- Saiepour, L., Fuchs, C., Patrizi, A., Sassoe-Pognetto, M., Harvey, R. J., & Harvey, K. (2010). Complex Role of Collybistin and Gephyrin in GABAA Receptor

- Clustering. *J Biol Chem*, 285(38), 29623–29631.
- Saiyed, T., Paarmann, I., Schmitt, B., Haeger, S., Sola, M., Schmalzing, G., Weissenhorn W., Betz, H. (2007). Molecular Basis of Gephyrin Clustering at Inhibitory Synapses. *J Biol Chem*, 282(8), 5625–5632.
- Saliba, R. S., Kretschmannova, K., & Moss, S. J. (2012). Activity-dependent phosphorylation of GABA(A) receptors regulates receptor insertion and tonic current. *EMBO J*, 31(13), 2937–2951.
- Salvatico, C., Specht, C. G., & Triller, A. (2015). Synaptic receptor dynamics: From theoretical concepts to deep quantification and chemistry in cellulo. *Neuropharmacology*, 88, 2–9.
- Santuy, A., Rodríguez, J.-R., DeFelipe, J., & Merchán-Pérez, A. (2018). Study of the Size and Shape of Synapses in the Juvenile Rat Somatosensory Cortex with 3D Electron Microscopy. *ENeuro*, 5(1), 0377–0317.
- Schaefer, N., Roemer, V., Janzen, D., & Villmann, C. (2018). Impaired Glycine Receptor Trafficking in Neurological Diseases. *Front Mol Neurosci*, 11, 1–24.
- Scheefhals, N., & MacGillavry, H. D. (2018). Functional organization of postsynaptic glutamate receptors. *Mol Cell Neurosci*, 91, 82–94.
- Schermelleh, L., Heintzmann, R., & Leonhardt, H. (2010). A guide to super-resolution fluorescence microscopy. *J Cell Biol*, 190(2), 165–175.
- Schindelin, J., Arganda-Carreras, I., Frise, E., Kaynig, V., Longair, M., Pietzsch, T., Preibisch S., Rueden C., Saalfeld S., Schmid B., Tinevez J.Y., White D.J., Hartenstein V., Eliceiri K., Tomancak P., Cardona, A. (2012). Fiji: An open-source platform for biological-image analysis. *Nat Methods*, 9(7), 676–682.
- Schwarz, G., Mendel, R. R., & Ribbe, M. W. (2009). Molybdenum cofactors, enzymes and pathways. *Nature*, 460(7257), 839–847.
- Selten, M., van Bokhoven, H., & Nadif Kasri, N. (2018). Inhibitory control of the excitatory/inhibitory balance in psychiatric disorders. *F1000Res*, 7(23), 1–16.
- Sergé, A., Bertaux, N., Rigneault, H., & Marguet, D. (2008). Dynamic multi-target tracing to probe spatiotemporal cartography of cell membrane. *Nat Methods*, 5(8), 687–694.
- Shabel, S. J., Proulx, C. D., Piriz, J., & Malinow, R. (2014). Mood regulation. GABA/glutamate co-release controls habenula output and is modified by antidepressant treatment. *Science*, 345(6203), 1494–1498.
- Sharma, K., Fong, D. K., & Craig, A. M. (2006). Postsynaptic protein mobility in dendritic spines: Long-term regulation by synaptic NMDA receptor

- activation. *Mol Cell Neurosci*, 31(4), 702–712.
- Sheng, M., & Kim, E. (2011). The Postsynaptic Organization of Synapses. *Cold Spring Harb Perspect Biol*, 3, 1–20.
- Shinohara, Y., Hirase, H., Watanabe, M., Itakura, M., Takahashi, M., & Shigemoto, R. (2008). Left-right asymmetry of the hippocampal synapses with differential subunit allocation of glutamate receptors. *Proc Natl Acad Sci U S A*, 105(49), 19498–19503.
- Shivanandan, A., Unnikrishnan, J., & Radenovic, A. (2015). Accounting for Limited Detection Efficiency and Localization Precision in Cluster Analysis in Single Molecule Localization Microscopy. *PLoS One*, 10(3), e0118767.
- Shrivastava, A. N., Triller, A., & Sieghart, W. (2011). GABA(A) receptors: post-synaptic co-localization and cross-talk with other receptors. *Front Cell Neurosci*, 5(7), 1–12.
- Sieben, C., Douglass, K. M., Guichard, P., & Manley, S. (2018). Super-resolution microscopy to decipher multi-molecular assemblies. *Curr Opin Struct Biol*, 49, 169–176.
- Sigel, E., & Steinmann, M. E. (2012). Structure, function, and modulation of GABAA receptors. *J Biol Chem*, 287(48), 40224–40231.
- Sola, M., Bavro, V. N., Timmins, J., Franz, T., Ricard-Blum, S., Schoehn, G., Ruigrok R.W., Paarmann I., Saiyed T., O'Sullivan G.A., Schmitt B., Betz H., Weissenhorn, W. (2004). Structural basis of dynamic glycine receptor clustering by gephyrin. *EMBO J*, 23(13), 2510–2519.
- Specht, C. G., Izeddin, I., Rodriguez, P. C., Beheiry, M. El, Rostaing, P., Darzacq, X., Dahan M., Triller, A. (2013). Quantitative Nanoscopy of Inhibitory Synapses : Counting Gephyrin Molecules and Receptor Binding Sites. *Neuron*, 79(2), 308–321.
- Specht, C. G., & Triller, A. (2008). The dynamics of synaptic scaffolds. *Bioessays*, 30(3), 1062–1074.
- Spitzer, N. C. (2010). How GABA generates depolarization. *J Physiol*, 588(5), 757–758.
- Südhof, T. C. (2012). The Presynaptic Active Zone. *Neuron*, 75(1), 11–25.
- Sugiyama, Y., Kawabata, I., Sobue, K., & Okabe, S. (2005). Determination of absolute protein numbers in single synapses by a GFP-based calibration technique. *Nat Methods*, 2(9), 677–684.
- Sydor, A. M., Czymmek, K. J., Puchner, E. M., & Mennella, V. (2015). Super-Resolution Microscopy: From Single Molecules to Supramolecular Assemblies. *Trends Cell Biol*, 25(12), 730–748.

- Takazawa, T., Choudhury, P., Tong, C.-K., Conway, C. M., Scherrer, G., Flood, P. D., Mukai J., MacDermott, A. B. (2017). Inhibition Mediated by Glycinergic and GABAergic Receptors on Excitatory Neurons in Mouse Superficial Dorsal Horn Is Location-Specific but Modified by Inflammation. *J Neurosci*, 37(9), 2336–2348.
- Takazawa, T., & MacDermott, A. B. (2010). Synaptic pathways and inhibitory gates in the spinal cord dorsal horn. *Ann N Y Acad Sci*, 1198, 153–158.
- Tang, A. H., Chen, H., Li, T. P., Metzbower, S. R., MacGillavry, H. D., & Blanpied, T. A. (2016). A trans-synaptic nanocolumn aligns neurotransmitter release to receptors. *Nature*, 536(7615), 210–214.
- Tarusawa, E., Matsui, K., Budisantoso, T., Molnar, E., Watanabe, M., Matsui, M., Fukazawa Y., Shigemoto, R. (2009). Input-Specific Intrasynaptic Arrangements of Ionotropic Glutamate Receptors and Their Impact on Postsynaptic Responses. *J Neurosci*, 29(41), 12896–12908.
- Thevenaz, P., Ruttiman, U. E., & Unser, M. (1998). A Pyramid Approach to Sub-Pixel Registraion based on Intensity. *IEEE Trans. Im Process*, 7(1), 27–41.
- Todd, A. J., Watt, C., Spike, R. C., & Sieghart, W. (1996). Colocalization of GABA, glycine, and their receptors at synapses in the rat spinal cord. *J Neurosci*, 16(3), 974–982.
- Treiman, D. M. (2001). GABAergic mechanisms in epilepsy. *Epilepsia*, 42(3), 8–12.
- Tretter, V., Jacob, T. C., Mukherjee, J., Fritschy, J., Pangalos, M. N., & Moss, S. J. (2008). The Clustering of GABA(A) Receptor Subtypes at Inhibitory Synapses is Facilitated via the Direct Binding of Receptor $\alpha 2$ Subunits to Gephyrin. *J Neurosci*, 28(6), 1356–1365.
- Tretter, V., Kerschner, B., Milenkovic, I., Ramsden, S. L., Ramerstorfer, J., Saiepour, L., Maric H.M., Moss S.J., Schindelin H., Harvey R.J., Seighart W., Harvey, K. (2011). Molecular Basis of the γ -Aminobutyric Acid A Receptor $\alpha 3$ Subunit Interaction with the Clustering Protein Gephyrin. *J Biol Chem*, 286(43), 37702–37711.
- Tretter, V., Mukherjee, J., Maric, H.-M., Schindelin, H., Sieghart, W., & Moss, S. J. (2012). Gephyrin, the enigmatic organizer at GABAergic synapses. *Front Cell Neurosci*, 6(23), 1–16.
- Triller, A, Cluzaud, F., Pfeiffer, F., Betz, H., & Korn, H. (1985). Distribution of glycine receptors at central synapses: an immunoelectron microscopy study. *J Cell Biol*, 101(2), 683–688.
- Triller, Antoine, & Choquet, D. (2008). New Concepts in Synaptic Biology Derived from Single-Molecule Imaging. *Neuron*, 59(3), 359–374.

- Triller, Antoine, Cluzaud, F., & Korn, H. (1987). Gamma-Aminobutyric Acid-containing Terminals Can Be Apposed to Glycine Receptors at Central Synapses. *J Cell Biol*, *104*(4), 947–956.
- Tritsch, N. X., Granger, A. J., & Sabatini, B. L. (2016). Mechanisms and functions of GABA co-release. *Nat Rev Neurosci*, *17*(3), 139–145.
- Turkowsky, B., Virant, D., & Endesfelder, U. (2016). From single molecules to life: microscopy at the nanoscale. *Anal Bioanal Chem*, *408*(25), 6885–6911.
- Tyagarajan, S. K., & Fritschy, J. (2014). Gephyrin: a master regulator of neuronal function? *Nat Rev Neurosci*, *15*(3), 141–156.
- Vaaga, C. E., Borisovska, M., & Westbrook, G. L. (2014). Dual-transmitter neurons: Functional implications of co-release and co-transmission. *Curr Opin Neurobiol*, *29*, 25–32.
- van de Linde, S., Löschberger, A., Klein, T., Heidbreder, M., Wolter, S., Heilemann, M., & Sauer, M. (2011). Direct stochastic optical reconstruction microscopy with standard fluorescent probes. *Nat Protoc*, *6*(7), 991–1009.
- van de Linde, S., Wolter, S., Heilemann, M., & Sauer, M. (2010). The effect of photoswitching kinetics and labeling densities on super-resolution fluorescence imaging. *J Biotechnol*, *149*(4), 260–266.
- van Zundert, B., Castro, P., & Aguayo, L. G. (2005). Glycinergic and GABAergic synaptic transmission are differentially affected by gephyrin in spinal neurons. *Brain Res*, *1050*, 40–47.
- Vangindertael, J., Camacho, R., Sempels, W., Mizuno, H., Dedecker, P., & Janssen, K. P. F. (2018). Methods and Applications in Fluorescence - An introduction to optical super-resolution microscopy for the adventurous biologist. *Methods Appl Fluoresc*, *6*(2), 55.
- Wang, S., Moffitt, J. R., Dempsey, G. T., Xie, X. S., & Zhuang, X. (2014). Characterization and development of photoactivatable fluorescent proteins for single-molecule-based superresolution imaging. *Proc Natl Acad Sci U S A*, *111*(23), 8452–8457.
- Wegner, W., Mott, A. C., Grant, S. G. N., Steffens, H., & Willig, K. I. (2018). In vivo STED microscopy visualizes PSD95 sub-structures and morphological changes over several hours in the mouse visual cortex. *Sci Rep*, *8*(219), 1–11.
- Wojcik, S. M., Katsurabayashi, S., Guillemin, I., Friauf, E., Rosenmund, C., Brose, N., & Rhee, J. S. (2006). A Shared Vesicular Carrier Allows Synaptic Corelease of GABA and Glycine. *Neuron*, *50*(4), 575–587.
- Wong, M. (2010). Too Much Inhibition Leads to Excitation in Absence Epilepsy. *Epilepsy Currents*, *10*(5), 131–133.

- Xu, J., Ma, H., & Liu, Y. (2017). Stochastic optical reconstruction microscopy (STORM). *Curr Protoc Cytom*, *81*(12), 1–12.
- Yamasaki, T., Hoyos-Ramirez, E., Martenson, J. S., Morimoto-Tomita, M., & Tomita, S. (2017). GARLH Family Proteins Stabilize GABAA Receptors at Synapses. *Neuron*, *93*(5), 1138–1152.
- Yang, X., & Specht, C. G. (2019). Subsynaptic Domains in Super-Resolution Microscopy: The Treachery of Images. *Frontiers in Molecular Neuroscience*, *12*(July).
- Yang, X., & Specht, C. G. (2020). Practical guidelines for two-color SMLM of synaptic proteins in cultured neurons. In Y. Okada & N. Yamamoto (Eds.), *NeuroMethods: Single Molecule microscopy* (p. xxxx). Springer.
- Yang, Z., Taran, E., Webb, T. I., & Lynch, J. W. (2012). Stoichiometry and subunit arrangement of $\alpha 1\beta$ glycine receptors as determined by atomic force microscopy. *Biochemistry*, *51*(26), 5229–5231.
- Zacchi, P., Antonelli, R., & Cherubini, E. (2014). Gephyrin phosphorylation in the functional organization and plasticity of GABAergic synapses. *Front Cell Neurosci*, *8*(103), 1–9.
- Zanacchi, F. C., Manzo, C., Alvarez, A. S., Derr, N. D., Garcia-Parajo, M. F., & Lakadamyali, M. (2017). A DNA origami platform for quantifying protein copy number in super-resolution. *Nat Methods*, *14*(8), 789–792.
- Zeilhofer, H. U., Möhler, H., & Di Lio, A. (2009). GABAergic analgesia: new insights from mutant mice and subtype-selective agonists. *Trends Pharmacol Sci*, *30*(8), 397–402.
- Zhang, L., & McBain, C. J. (1995). Potassium conductances underlying repolarization and after-hyperpolarization in rat CA1 hippocampal interneurons. *Journal Physiol*, *488*(3), 661–672.

Appendix Table 1. Antibodies

Antibodies	Source	Identifier
mouse monoclonal mAb7a gephyrin	Synaptic system	Cat.No. 147011
rat monoclonal mAb7a gephyrin	Synaptic system	Cat.No. 147208
rabbit polyclonal gephyrin	Synaptic system	Cat.No.147002
rabbit polyclonal GlyR α 1	Triller A. lab	# 2353
mouse monoclonal GABA _A R β 3	UC Davis/NIH NeuroMab Facility	Cat.No.75-149, RRID: AB_2109585
rabbit polyclonal RIM1/2	Synaptic system	Cat.No. 140203
guinea pig polyclonal RIM1/2	Synaptic system	Cat.No. 140205
unconjugated donkey anti-mouse IgG (H+L)	Jackson ImmunoResearch	Cat.No. 715-005-151
unconjugated donkey anti-rabbit IgG (H+L)	Jackson ImmunoResearch	Cat.No. 711-005-152
unconjugated donkey anti-rat IgG (H+L)	Jackson ImmunoResearch	Cat.No. 712-005-153
unconjugated donkey anti-guinea pig IgG (H+L)	Jackson ImmunoResearch	Cat.No. 706-005-148
Alexa 647-conjugated goat anti-rat IgG (H+L)	Invitrogen	Cat.No. A21247, RRID: AB_141778
Alexa 647-conjugated donkey anti-rabbit IgG (H+L)	Jackson ImmunoResearch	Cat.No. 711-605-152, RRID: AB_2492288
Alexa 647-conjugated donkey anti-mouse IgG (H+L)	Jackson ImmunoResearch	Cat.No. 715-605-151, RRID: AB_2340863
Alexa 647-conjugated donkey anti-guinea pig IgG (H+L)	Jackson ImmunoResearch	Cat.No. 706-605-148, RRID:AB_2340476
Alexa 647-conjugated donkey anti-rat IgG (H+L)	Jackson ImmunoResearch	Cat.No. 712-605-153, RRID: AB_2340694
CY3-conjugated goat anti-mouse IgG (H+L)	Jackson ImmunoResearch	Cat.No. 115-165-166, RRID: AB_2338692
CY3-conjugated goat anti-rabbit IgG (H+L)	Jackson ImmunoResearch	Cat.No. 111-165-144, RRID: AB_2338006
Alexa 488-conjugated donkey anti-rat IgG (H+L)	Invitrogen	Cat.No. A21208, RRID:AB_2535794
Alexa 488-conjugated donkey anti-rat IgG (H+L)	Jackson ImmunoResearch	Cat.No. 712-545-153, RRID: AB_2340648
Alexa 488-conjugated goat anti-mouse IgG (H+L)	Jackson ImmunoResearch	Cat.No. 115-545-166, RRID: AB_2338852
Alexa 488-conjugated goat anti-rabbit IgG (H+L)	Jackson ImmunoResearch	Cat.No. 111-545-144, RRID:AB_2338052
Alexa 568-conjugated goat anti-guinea pig IgG (H+L)	Invitrogen	Cat.No. A11075, RRID: AB_2534119

Appendix Table 2. List of two-color dSTORM dataset

Two-color dSTORM of	Targets	Dyes	Treatments	Independent experiments
GlyR	GlyR α 1	Alexa 647	No treatment	2
		Cy3B		
Gephyrin	m7a	Alexa 647 or Cy3B	No treatment	3
	rbGPHN	Cy3B or Alexa 647		
Gephyrin and GlyR	m7a	Alexa 647	No treatment	3
	GlyR α 1	Cy3B		
Gephyrin and RIM1/2	m7a	Cy3B	No treatment	3
	RIM1/2	Alexa 647		
Gephyrin and GlyR	m7a	Alexa 647	TTX or 4-AP	3
	GlyR α 1	Cy3B		
	GABA _A R β 3	Alexa 488 * #		
Gephyrin and GlyR	m7a	Cy3B	TTX or 4-AP	2
	GlyR α 1	Alexa 647		
	GABA _A R β 3	Alexa 488 * #		
Gephyrin and GABA _A R	m7a	Alexa 647	TTX or 4-AP	3
	GABA _A R β 3	Cy3B		
	GlyR α 1	Alexa 488 * #		
GlyR and GABA _A R	GlyR α 1	Alexa 647	TTX or 4-AP	2
	GABA _A R β 3	Cy3B		
	m7a	Alexa 488 * #		
RIM1/2 and GlyR	GlyR α 1	Alexa 647	TTX or 4-AP	2
	RIM1/2	Cy3B		
	GABA _A R β 3	Alexa 488 #		
RIM1/2 and GABA _A R	GABA _A R β 3	Alexa 647	TTX or 4-AP	2
	RIM1/2	Cy3B		
	GlyR α 1	Alexa 488 #		

indicates the third labeling, which was not subject to dSTORM imaging, but only used as a marker.

* indicates this labeling was done in one of the repeating experiments.

Appendix 3: SRclusters protocol

SRclusters

--- Coordinates based two-color dSTORM data analysis tool

The SRclusters program is self-explanatory. It is written in Python language based on Jupyter Notebook. The main algorithms adopted here are the density-based spatial clustering of applications with noise (DBSCAN) and the nearest neighbor distance (NND).

[1] Preparation of input files.

Matlab 2012b, SrInput2.

Both the MTT mat file and drift corrected file are needed, and in the same folder. The drift corrected file should be named as “###_DC.mat”.

The transformation of mat file to SR_input csv file:

In mat file: coordinates (x, y, z) are in pixels, intensity is the alpha value from the Gaussian fitting.

In SR_input file: coordinates (x,y,z) are in nanometers, Intensity is the calculated photon number.

See the table below for the calculation details. Consult your microscope engineer when the setup is modified for the correct parameters (Pre-amp, EM gain, quantum efficiency, Gaussian fitting details for alpha values).

Updated on 2019.04.25

Input file for 2D

frame	x	y	z	r_x	r_y	intensity
	(drift corrected)	(drift corrected)	--	(radius_x)	(radius_y)	(photon counts)

$$\alpha_{\text{real}} = \alpha_{\text{MTT}} * (2 * \pi * \sigma_{\text{PSF}} / \sqrt{\pi}) = 3.545 * \sigma_{\text{PSF}} * \alpha_{\text{MTT}} \quad \leftarrow (\sigma_{\text{PSF}} \text{ in pixel})$$

$$\sigma_{\text{PSF}} \text{ (nm)} = \text{pixel-size (nm)} * \sigma_{\text{PSF}} \text{ (pxl)} = 160 * \sigma_{\text{PSF}} \text{ (pxl)} \quad \leftarrow (\text{with } 100 \times \text{ magnification})$$

$$N^{\circ} \text{ Photons (FR)} = \alpha_{\text{real}} * \text{Pre-amp} / (\text{EM gain} * \text{QE}) = \alpha_{\text{real}} * 4.59 / (300 * 0.94);$$

$$N^{\circ} \text{ Photons (R)} = \alpha_{\text{real}} * \text{Pre-amp} / (\text{EM gain} * \text{QE}) = \alpha_{\text{real}} * 4.59 / (300 * 0.96);$$

$$N^{\circ} \text{ Photons} = \alpha_{\text{peak}} * \text{Pre-amp} / (\text{EM gain} * \text{QE})$$

$$\alpha_{\text{peak}} = \alpha_{\text{MTT}} / (\sigma_{\text{PSF}} * \sqrt{2\pi}) = 0.4 * \alpha_{\text{MTT}} / \sigma_{\text{PSF}} \quad \leftarrow (\sigma_{\text{PSF}} \text{ in pixel})$$

$$\text{Precision} = \sigma_{\text{PSF}} / \sqrt{N} \quad \leftarrow (\sigma_{\text{PSF}} \text{ in nm})$$

(Note that opening the csv files in EXCEL may change the format and cause error when loading files to SRclusters in the Step01.)

[2] SRclusters on Jupyter Notebook.

<http://bioclusts02.bioclust.biologie.ens.fr:7777/srclusters/login>

Password: XXXXXXXXXX

To interact with all the figures, change `%matplotlib inline` to `%matplotlib nbagg`. Note that the program will run very slowly on the interactive mode.

To save images, right click on the image and save.

In [], it always goes as [channel 1, channel 2].

Step01 – Cluster and Register:

Plot color code: blue- first channel (channel 0), red- second channel (channel 1).

In `names = [ch0, ch1]`, Do not use `'_'`, use `'-'` instead, otherwise errors will occur later, because the program extract the channel names from the file name based on the separation by `'_'`.

Set names, paths, DBSCAN variables (distance, amount), intensity threshold, beads amount.

Step02 – Remove beads:

Set persistence threshold: when the value <1 , it is the percentage; when the value >1 , it is the number of frames.

The persistence threshold can be arbitrarily adjusted for each image to include proper clusters, because the number of detections for different protein under different conditions can be dramatically different, in addition to the stochasticity of dSTORM detection.

Step3 – Paring clusters:

Set path, `max_dist` (distance between the centroid of paired clusters), `min_points` (the sum of the points from two clusters in a pair).

The `min_points` can be arbitrarily adjusted to include all the proper synapses.

Step04 – Feature extraction:

- (1) Set path and `process_list = []`, choosing the good synaptic pairs according to step03 and reference images.

(2) Global synaptic cluster features:

Features --- all features are imported from networkx, based on 'graph', except for npoints which are extracted independently from the input files.

Diameter (the maximum eccentricity): calculating by the nodes (which are localizations here), not in nanometer scale.

Radius (the minimum eccentricity): by the nodes, not in nanometer scale.

Ncenters (number of points where the eccentricity equal to radius).

Nperiphery (number of points where the eccentricity is equal to the diameter).

Density (is 0 for a graph without edges and 1 for a complete graph).

Npoints (number of points/localizations in this cluster).

Nedges (number of connections on the Delaunay triangulation).

Hull area (area of the bounding polygon).

Hull density (number of points/hull area).

Eigen ratio (ratio between the biggest and smaller Eigen values of the co-variance matrix. A value of 1 would mean a perfectly round cluster, and 0 an infinitely elongated cluster).

Npoints: extracted from the coordinates by counting the number of coordinates for each cluster.

Hull Area: corresponding to the Hull Volume in the graph, is the area of the cluster, in nm².

Hull density is calculated from the **Npoints/Hull Area**.

(3) Spatial correlation and distributional heterogeneity with NND:

Set nneighbors = [], it is applied to both intra-cluster and inter-cluster NND measurement.

2-channel correlation:

Score = absolute (intermean0-intermean1); for each pair.

Another score {abs (intermean0-intermean1) + abs (interSD0-interSD1)} has linear relationship with score {abs (intermean0-intermean1)}, thus not adopted.

Inter-cluster NND: Mean0, std0, CoefVar0, Mean1, std1, CoefVar1. (0=channel 0, 1=channel 1).

Intra-cluster NND: Mean0, std0, CoefVar0, Mean1, std1, CoefVar1. (0=channel 0, 1=channel 1).

Normality (statistics) --- from SciPy.org

== (Skewness² + Kurtosis²) --- Larger values, more normal distribution.

For both intra-cluster and inter-cluster NND.

(4) Subsynaptic domain (SSD) segmentation with modified DBSCAN: eps = [,], min_samples =[,].

Parameter “min_sample” is adjusted by the density of the cluster:

--- (min_sample input) * (Hull density).

Subclusters (number of subclusters segmented from each cluster, using modified DBSCAN with density).

Parameters output:

Copy “zipfiles.ipynb” in to the data folder and run the script. The zipped file is saved under the same path. Download the zipped file. (If the saving process was done by several times, the second batch of zipped files is compressed into the previous zipped file.)

List of output files:



...Red arrows indicate the final data files.

Statistics---

[Global features]. “_features.csv”

Combined all the data into one excel file. **#pairs filtered** according to epi images.

For ‘_features’, removed ‘ncenters’, ‘nperiphery’, ‘density’, ‘nedges’, ‘NormalityPValue’.

Split the two channels [0, 1].

Cluster size information: **Hull Area.

Detection number information: **npoints, Hull Density.

****Subcluster counts**.

Distributional heterogeneity: InnerDistMean, InnerDistStd, CoefficientOfVariation, **NormalityStatistics.

Statistics---

[Spatial correlation of two channels]. “_inter_distances.csv”

** Spatial correlation: Mean0, std0, CoefVar0, Mean1, std1, CoefVar1, **Score**.

Statistics ---

[Subcluster features].”_features_sub0.csv” & “_features_sub1.csv”

Subcluster features: npoints, Hull Area, Density, Eigen ratio. For each channel.

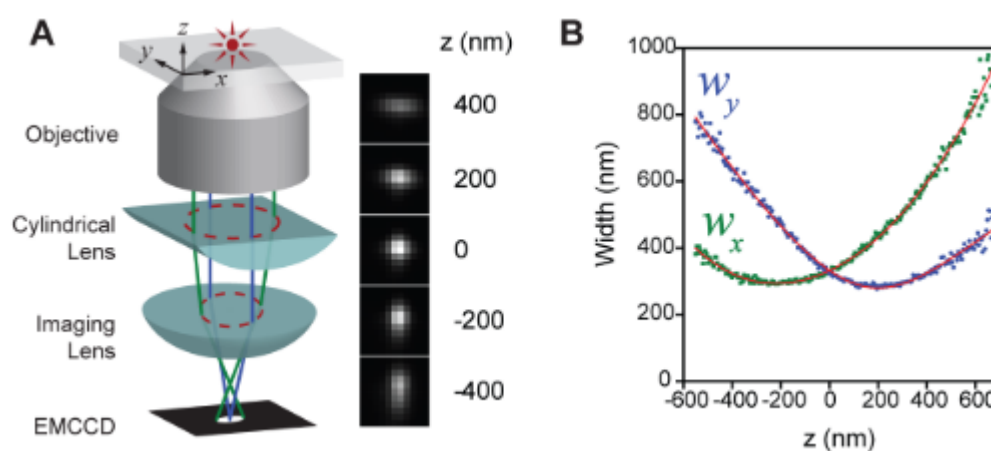
Appendix 4. Two-color 3D dSTORM

Two-color 3D dSTORM

1. Introduction: the basic principle of 3D super-resolution imaging

Three dimensional (3D) dSTORM imaging shares many intrinsic properties with two dimensional (2D) dSTORM as discussed in this thesis main text. However, 3D imaging allows us to obtain the information of the third dimension, thus producing more realistic representations of the biological structures than 2D.

In the 3D dSTORM imaging mode, a cylindrical lens is introduced to the light emission path, introducing optical astigmatism to the single molecule signals (Appendix Figure 1.A). With astigmatism, the point spread functions (PSFs) of these single molecule signals are elongated either in the x or in the y directions, depending on their z positions. The width of the PSFs is measured in the x and y dimensions (W_x and W_y), and the position in z dimension can be calculated from the difference between W_x and W_y (Appendix Figure 1.B).

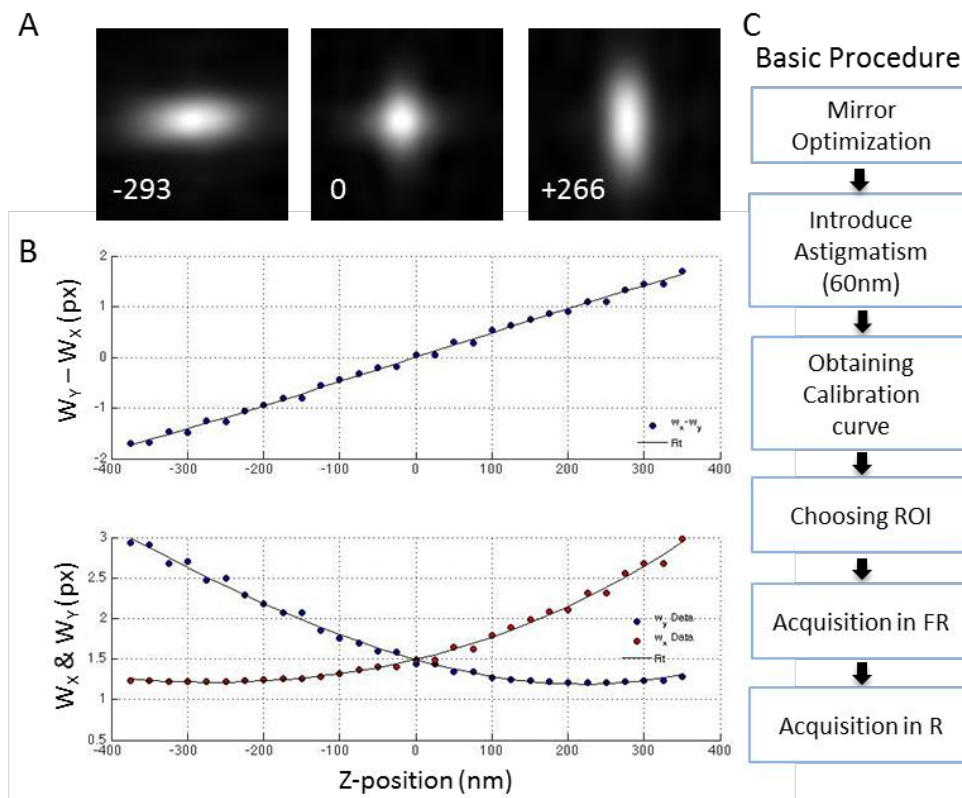


Appendix Figure 1. The basic principle of three dimensional STORM. (A) The illustration shows a cylindrical lens inserted into the emission light path (left), and that signals at different z position exhibit different PSF shapes (right). (B) The calibration curve with the PSF width in x and y dimension, from which the z position is calculated. From Huang 2008.

2. A two-color 3D dSTORM scheme

To enable the 3D imaging of synaptic clusters in my doctoral project, I have set up a two-color 3D dSTORM imaging procedure (Appendix Figure 2). A

deformable mirror (MicAO 3DSR, Imagine Optics) was introduced into the emission light path on our microscope setup, instead of cylindrical lens. The deformable mirror can introduce astigmatism into the light path, and it can also be adjusted to minimize other optical aberrations. The two-color 3D dSTORM imaging procedure is basically similar to the 2D dSTORM Appendix Figure 2.C). In addition to that, the deformable mirror needs to be optimized at the beginning of the recordings, then a user-defined astigmatism is introduced and a calibration recording with a bead is taken for producing the calibration curve.



Appendix Figure 2. A two-color 3D dSTORM imaging scheme. (A) The point spread function of the signals from one bead imaged in different z depth (-293 nm, 0, +266 nm), with respect to the calibration curve. (B) The calibration curves obtained with the deformable mirror. (C) The two-color 3D dSTORM imaging procedure. At the beginning, the deformable mirror needs to be optimized to minimize the optical aberrations in the light path. The optimization is performed using a fluorescent bead as marker. Then a user-defined astigmatism is introduced and calibration curve is obtained with the bead. Afterwards, recordings in the two channels are performed as in the two-color 2D dSTORM imaging.

3. Conclusion

The two-color 3D dSTORM imaging allows us to image the synaptic clusters in three dimension, which can avoid the imaging artefacts due to the 2D projection in the 2D imaging mode. It will be interesting to continue the 3D imaging, in order to further confirm the important findings in my work presented in the thesis.

Reference

Huang, B., Wang, W., Bates, M., & Zhuang, X. (2008). Three-Dimensional Super-Resolution Imaging by Stochastic Optical Reconstruction Microscopy. *Science*, 319(5864), 810–813.

Appendix 5: Yang and Specht 2020

Yang, X., & Specht, C. G. (2020). Practical guidelines for two-color SMLM of synaptic proteins in cultured neurons. In Y. Okada & N. Yamamoto (Eds.), *NeuroMethods: Single Molecule microscopy* (p. xxxx). Springer.

1 **Practical guidelines for two-color SMLM of synaptic proteins in cultured neurons**

2 **Xiaojuan Yang¹ and Christian G Specht^{1*}**

3 ¹ École Normale Supérieure, PSL Research University, CNRS, Inserm, Institute of Biology
4 (IBENS), Paris 75005, France

5 * **Correspondence:** Tel. 0033-1-44322300, E-mail: specht@biologie.ens.fr

6 **Running title:** Two-color SMLM of synapses.

7 **Abstract**

8 The application of single molecule localization microscopy (SMLM) to the study of synaptic
9 proteins has shown that the postsynaptic density (PSD) is organized heterogeneously in
10 nanodomains that are thought to play important roles in neurotransmission and synaptic
11 plasticity. However, the dense packing of neurotransmitter receptors and scaffold proteins at
12 synapses, together with the small total number of target molecules make SMLM of synaptic
13 components particularly challenging. Here, we discuss the technical difficulties of SMLM
14 imaging that are specific to synapses. We present a method for dual-color direct stochastic
15 optical reconstruction microscopy (dSTORM) of two inhibitory synaptic proteins, the glycine
16 receptor (GlyR) and the scaffold protein gephyrin (GPHN), highlighting strategic choices and
17 practical solutions for imaging quality control. Our aim is to provide biologists with
18 guidelines for the implementation of two-color dSTORM imaging of synaptic proteins from
19 sample preparation to data analysis.

20 **Keywords**

21 Super-resolution, single molecule localization microscopy (SMLM), two-color dSTORM,
22 synaptic proteins, nanoclusters, correlation analysis.

23 **1. Introduction**

24 **1.1 Overview of SMLM techniques**

25 In conventional optical microscopy, the lateral resolution is limited by the wavelength (λ) and
26 the numerical aperture (NA) of the objective. The minimal distance between two resolvable
27 points is several hundred nanometers due to the diffraction limit ($d \approx 0.61 \lambda/NA$).

28 Conventional fluorescence microscopy therefore cannot gain detailed information on sub-
29 diffraction-limit structures such as synapses, which have a size of only a few hundred
30 nanometers. The advancement of super-resolution fluorescence microscopy allows
31 researchers to probe nanometer-scale structural details. Single molecule localization
32 microscopy (SMLM) takes advantage of the blinking behavior of fluorophores (Fig. 1A) to
33 calculate the precise position of individual molecules. During imaging, the fluorophores are
34 first pushed into a non-fluorescent OFF state, then a sparse subset of fluorophores are re-
35 activated by a low dose of UV light or spontaneously in the presence of reducing agents in the
36 imaging buffer to gain a temporal separation of the signals. These sparse single detections are
37 fitted mathematically during image processing, attaining a localization precision of ~ 10 nm.
38 Super-resolution images can then be reconstructed by superimposing all the detections from
39 the recording.

40 SMLM differs from conventional optical microscopy very significantly and there are some
41 definitions in SMLM that biologists should be aware of. The first one is the localization
42 precision. It is the precision with which single detections are localized by fitting with a
43 Gaussian distribution or other algorithms. The localization precision can be approximated by
44 Δ/\sqrt{N} , where Δ is the full width at half-maximum (FWHM) of the point spread function (PSF)
45 and N is the number of collected photons [1], [2]. Note that the localization precision is also
46 affected by background noise, in other words, the signal to noise ratio (SNR). The second

47 concept is the localization density, which is the number of localizations per spatial unit. It
48 relies on the labeling density, as well as the blinking properties of the fluorophores. It has
49 been proposed that the labeling density should be sufficiently high to meet the Nyquist-
50 Shannon criterion [3], [4]. According to this criterion, the sampling must be at least two times
51 denser than the achieved spatial resolution. However, this is not always the case in SMLM,
52 because fluorophore localizations are not classical samples as in conventional microscopy but
53 stochastic events [5]. The detection of redundant information due to multiple switching cycles
54 of the fluorophores means that the number of detections is much higher than the actual
55 sampling of independent targets. Baddeley and Bewersdorf demonstrated that significantly
56 higher localization density, empirically exceeding by 5-fold the Nyquist-Shannon criterion,
57 are therefore needed to attain the best spatial resolution [5]. The third definition is the spatial
58 resolution, which is not as clear a concept any more as in conventional microscopy.
59 Canonically, it refers to how well two objects can be distinguished, which is strongly
60 dependent on the wavelength and the objective. In SMLM, it usually means the resolving
61 power for two objects in the reconstructed images. Then, both the localization precision as
62 well as the localization density are determinants of the spatial resolution.

63 SMLM techniques include stochastic optical reconstruction microscopy (STORM) [6] and
64 photo-activated localization microscopy (PALM) [7], [8]. The main difference between
65 STORM and PALM is the labeling technique, where endogenous proteins are stained with
66 organic dyes in STORM and target proteins are tagged with fluorescent proteins in PALM,
67 respectively. Both organic dyes and fluorescent proteins can be induced to blink under
68 different conditions. In STORM, the blinking of fluorescent dyes requires particular imaging
69 buffers and high illumination intensity. In PALM, the blinking of fluorescent proteins is
70 achieved by sequential photo-activation/conversion with UV light in buffered salt solutions.
71 PALM is thus preferable for live-cell imaging, because the STORM imaging buffers are

72 detrimental to living cells. However, labeling with fluorescent proteins requires the
73 expression of recombinant fusion proteins, which may potentially change the target protein's
74 function. Moreover, organic dyes usually have narrower excitation/emission spectra and
75 higher photon emission compared to fluorescent proteins. Therefore, STORM is more suitable
76 for multi-color imaging and to gain a better localization precision.

77 There are two versions of STORM imaging, N-STORM [6] and direct STORM (dSTORM)
78 [9]. N-STORM adopts a pair of dyes, one with a short wavelength (green) and another with a
79 longer wavelength (red), to act as activator and reporter, respectively. The pair of dyes are
80 conjugated to the same antibody at close proximity. During imaging, a red laser is used to
81 excite the red dyes and to switch them into the OFF state, while a green laser at low intensity
82 excites the green dyes that in turn activate the red fluorophores. Note that no UV light is
83 needed in N-STORM. For dual-color imaging, the two target proteins are labeled with the
84 same reporter dye (e.g. Alexa Fluor 647), but different activator dyes are used to selectively
85 visualize the two targets [10]. There are, however, a few drawbacks of using activator/reporter
86 dye pairs in STORM. Firstly, it is difficult to control precisely the ratio of activator and
87 reporter dyes on the same antibody. Secondly, by using two wavelengths for a single target
88 protein, N-STORM leaves limited options of dyes for multi-color imaging. Thirdly and most
89 importantly, the commonly used reporter dye Alexa Fluor 647 can blink spontaneously in the
90 imaging buffer without laser activation, making N-STORM susceptible to contaminating
91 detections from other channels. This is particularly problematic for dense structures such as
92 synaptic protein assemblies, because there is no efficient way to identify and remove the
93 contaminating detections. In dSTORM, only single fluorophores (reporter dyes) are used for
94 one color imaging, and their activation is tuned by a low dose of UV light and reducing agents
95 in the imaging buffer. The spectral separation of the fluorophores affords a larger choice of

96 dyes, making dSTORM more favorable for implementing dual-color super-resolution imaging
97 of synaptic proteins.

98 **1.2 SMLM applications in neurobiology**

99 SMLM techniques have been successfully applied to many biological structures, providing
100 new insights into their sub-cellular organization and functions [5], [11], [12]. Baddeley and
101 Bewersdorf classified the analyzed structures into three categories with increasing difficulties:
102 (1) well-isolated repetitive or stereotypic structures, (2) more complex but still isolated
103 structures, and (3) complex and closely spaced structures [5]. This classification is a good
104 way to illustrate how the level of difficulty can vary for different structures, meaning that
105 labeling, imaging and the data analysis need to be optimized for a given molecular complex.
106 Stereotypic structures allow combining the information from many structures to reconstruct
107 composite images, and are hence less demanding in terms of the labeling density and
108 detection efficiency. On the other hand, variable structures like synapses need to be treated
109 individually. Therefore, it is not surprising that most SMLM studies to date have been
110 conducted on stereotypic structures such as filaments and nuclear pore complex (NPC), and
111 only limited numbers of studies have been carried out on complex structures such as gene loci
112 or synapses.

113 One of the most striking discoveries that has been achieved thanks to SMLM imaging was the
114 identification of periodic actin rings in neuronal dendrites and axons by Xu and colleagues
115 [13]. These actin rings are evenly distributed along axons and connected by spectrin
116 tetramers, forming a periodic cytoskeletal structure. The periodic organization is also found in
117 the axon initial segment (AIS), providing a robust structural scaffold [14]. Similarly, the
118 dendritic spine neck was shown to contain periodic actin structures, as demonstrated by
119 another super-resolution imaging technique, namely stimulated emission depletion (STED)

120 microscopy[15]. The discovery of the periodic actin cytoskeleton in neurons has led to
121 substantial further research and has fundamental consequences for our understanding of the
122 morphogenesis of neurons. Another successful application of SMLM is the description of the
123 eight-fold symmetry of the NPC and the orientation of its Y-shaped component [16]–[18].
124 Due to their stereotypic structure and well-known features, NPCs as well as sparsely
125 distributed microtubule filaments are commonly used to assess the performance of newly
126 developed fluorophores, probes, algorithms, etc.

127 Synapses are of great interest in SMLM due to their small size and important roles in neuronal
128 activity. SMLM investigations have provided important insights into synaptic function. Dani
129 and colleagues have examined pre- and post-synaptic protein assemblies with SMLM,
130 confirming a layered molecular organization of different synaptic components [19]. This
131 arrangement may explain the different kinetic properties of excitatory scaffold proteins, where
132 proteins that are located at a greater distance from the synaptic membrane have faster
133 exchange rates [20]. It has also been shown by SMLM that post-synaptic scaffold proteins are
134 organized in nanodomains that undergo dynamic changes and regulate the strength of
135 neuronal transmission at excitatory[21]–[23] and inhibitory synapses [24]–[26]. This synaptic
136 nano-architecture was also observed *in vivo* and has been confirmed using different super-
137 resolution imaging techniques [27], [28]. It was further proposed that pre- and post-synaptic
138 nanodomains are aligned in so-called trans-synaptic nanocolumns[29]. Synaptic adhesion
139 molecules are likely to coordinate these trans-synaptic complexes [30], [31]. Finally, SMLM
140 has been used to determine the absolute numbers of scaffold proteins and neurotransmitter
141 receptor complexes at synapses, providing new types of quantitative information about the
142 regulation of synaptic structure and function [24], [32], [33].

143 **1.3 Difficulties of applying two-color dSTORM to synaptic proteins**

144 SMLM has shown great promise in revealing the nanometer-scale architecture of synapses
145 and the dynamic re-organization during synaptic plasticity. However, SMLM is a complex
146 technology and has some intrinsic limitations that need to be taken into consideration for the
147 experimental design (see section 2). In addition, the unique character of synaptic protein
148 clusters poses particular challenges to the acquisition of reliable SMLM data and to obtaining
149 statistically meaningful results.

150 First of all, the size of synapses is of the same order as the diffraction limit, with only a few
151 hundred nanometers in diameter, which makes it difficult to obtain resolvable sparse blinking
152 events during imaging. Even when the overall blinking in the field of view (region of interest,
153 ROI) is sparse, there can still be many overlapping blinking events at synaptic sites. The
154 assignment of multiple signals to a single detection necessarily causes wrong representations
155 in the super-resolved image. Second, synapses have large structural variability in terms of
156 cluster shape and molecule numbers. As a consequence, individual synaptic clusters cannot be
157 combined and population averaging is not applicable. Each synaptic cluster needs to be
158 treated individually, which increases the difficulties of data analysis. Furthermore, given the
159 stochastic nature inherent to dSTORM, the variations in detection efficiency and localization
160 density of synaptic clusters in the same ROI can be large, not to mention the variations among
161 different ROIs. Therefore, extraordinary scrutiny is required to assess the quality of the
162 imaging data. Thirdly, even though synapses are densely packed compartments, the copy
163 numbers of many of their components are quite small, with receptors in the order of tens and
164 scaffold proteins in order of hundreds of molecules per synapse. Small numbers of target
165 proteins make it difficult to attain sufficiently dense labeling and hence efficient sampling of
166 the synapse in order to reconstruct a representative super-resolution image. Fourth, synaptic

167 proteins undergo dynamic changes and re-organization during synaptic plasticity, which adds
168 to the difficulties of SMLM data interpretation. Given the variability and plasticity of
169 synapses, large sample sizes (number of synapses) are needed for meaningful data
170 interpretation. However, synapses are usually well separated along the dendrites and
171 sometimes only a few synapses can be recorded in one ROI due to the high magnification
172 used for imaging, which limits the data output and consequently increases the time required
173 for the experiments. In addition to the aspects mentioned above, the detection of two synaptic
174 components in parallel dramatically increases the complexity of the experiments, because it
175 not only requires the achievement of good imaging quality of two channels, but also the
176 implementation of more complicated data processing and analysis tools.

177 Owing to the complexity of the technology and the unique properties of any research target,
178 each application of SMLM has to be optimized and the imaging quality closely controlled
179 (section 4.3). We strongly recommend that a suitable biological question is formulated in the
180 first place, and that factors such as the spatial resolution, sampling efficiency and data output
181 of the SMLM recordings are weighed against the reproducibility and expected magnitude of
182 the observed effect. In our case, we hypothesize that different neurotransmitter receptors and
183 scaffold proteins occupy specific sub-domains at inhibitory synapses. Our aim is to compare
184 the distributions of these inhibitory synaptic proteins on a scale of tens of nanometers using
185 dual-color dSTORM imaging.

186 In spinal cord neurons, fast inhibition is mainly mediated by two types of receptors, glycine
187 receptors (GlyR) and γ -aminobutyric acid (GABA) type A receptors (GABA_AR). The
188 neurotransmitters glycine and GABA are co-released from the same presynaptic terminals
189 [34], [35] and the two types of receptors coexist at the same postsynaptic densities (PSD)
190 [36]–[40]. At the PSD, both GlyRs and GABA_ARs bind to the inhibitory synaptic scaffold

191 protein gephyrin. They share a common binding site but have different binding affinities for
192 gephyrin [41]–[44]. Besides, the accumulation of the two types of receptors at synapses can
193 be differentially regulated; for example, microglial prostaglandin E2 modulates GlyR
194 diffusion dynamics but not GABA_ARs [45]. GlyR- and GABA_AR-mediated postsynaptic
195 currents have different kinetic properties, with GlyR currents exhibiting fast decay times and
196 GABA_ARs decaying more slowly [35], [44], [46]. Together, the co-transmission and the
197 independent regulation of GlyRs and GABA_ARs at mixed inhibitory synapses may modulate
198 the time course and amplitude of fast inhibition in spinal cord neurons. Recently, super-
199 resolution fluorescence microscopy has revealed that gephyrin molecules form nanodomains
200 that are dynamically re-organized during inhibitory synaptic plasticity [24], [26], [28]. On the
201 other hand, it was shown that excitatory scaffold proteins are also organized in nanodomains
202 that in turn regulate the distribution of excitatory neurotransmitter receptors [21], [22].
203 Therefore, our goal is to investigate the spatial relationship between GlyRs, GABA_ARs and
204 gephyrin at mixed inhibitory synapses. Whether GlyRs and GABA_ARs occupy the same or
205 separate sub-synaptic compartments in relation to the gephyrin distribution has profound
206 consequences for the understanding of the mechanism of co-transmission at mixed inhibitory
207 synapses.

208 The intrinsic challenges that we encountered when applying SMLM to inhibitory synaptic
209 proteins led us to the method described here (Fig. 1B, C). We found that a practical guideline
210 for biologists to set up quality-controlled SMLM experiments was imperative yet missing. In
211 this article, we describe the crucial considerations for implementing two-color dSTORM of
212 synaptic proteins and provide biology-oriented strategies to assess the imaging quality. We
213 also present a workflow for data analysis with freely-accessible and ready-to-use software.
214 We hope that these guidelines can help biologists set up their own workflow to study synaptic
215 structures or similarly complex cellular compartments.

216 **2. Sample preparation for two-color dSTORM**

217 **2.1 Labeling strategies**

218 With a localization precision of single molecules in the order of 10 nm, the size of the probes
219 used for labeling can impact the quality of dSTORM data in several ways (Fig. 2).

220 Commercial primary and secondary antibodies are easy to access and convenient for
221 immunostaining, hence they are commonly used to label endogenous proteins in SMLM
222 experiments. However, the average size of full-length IgG is about 10 nm, which is similar to
223 the single molecule localization precision in dSTORM. The combination of primary and
224 secondary antibodies can add a distance of up to 20 nm between the epitope and the
225 fluorophores. If the orientation of the antibodies bound to the target proteins is random, the
226 detected synaptic clusters can be blurred and the resolution of the super-resolution images is
227 lessened. Moreover, the bulky size of antibodies can limit the labeling density due to the
228 masking of epitopes in the crowded synaptic environment, which reduces the sampling
229 efficiency. And finally, the cross-linking effect of primary and secondary antibodies may
230 potentially induce clustering artefacts that only become apparent on the nanometer scale,
231 especially when using live-staining of membrane proteins such as neurotransmitter receptors
232 (Fig. 2A).

233 Different approaches can be adopted to overcome the drawbacks of using conventional
234 antibodies in dSTORM. For example, antigen-binding fragments (Fab) can be used instead of
235 whole IgG as secondary labels. Primary antibodies can also be conjugated directly with
236 fluorescent dyes, omitting secondary antibodies altogether [31]. Alternatively, single-domain
237 antibody fragments derived from camelid or shark antibodies, so-called nanobodies, have
238 recently caught a lot of attention due to their favorable small size [47] (Fig. 2B). If combined
239 with specific protein tags, dye-conjugated nanobodies can be used as a modular detection

240 system that generates less epitope-displacement and can give better spatial resolution [48]–
241 [50], however, this requires modification and recombinant expression of the target proteins.
242 Unfortunately, none of these approaches can be easily implemented. Coupling primary
243 antibodies with organic dyes is prone to reduce the binding efficacy and may even affect
244 antibody specificity, whereas the production of specific nanobodies for a target protein can be
245 time-consuming. Nevertheless, the use of small sized probes is certainly preferable whenever
246 there is availability.

247 Due to the practical limitations mentioned above, we propose to start using conventional
248 immunostaining with primary and secondary antibodies that have been previously used and
249 validated by classical fluorescent microscopy, which is also the case in our experiments. Even
250 though we obtain a slightly lower resolution with conventional antibody labeling of GlyR and
251 gephyrin clusters than with smaller probes, we expect that any significant changes in the
252 synaptic distribution of the receptors and scaffold proteins in response to regulatory processes
253 can still be detected. In addition to using commercial dye-conjugated secondary antibodies,
254 we have also coupled unconjugated secondary antibodies with succinimidyl ester (NHS ester)
255 derivatives of fluorescent dyes, in order to better control the dye/protein ratio of this
256 fluorophore (D/P ratio ranging from 1 to 4). By reducing the amount of redundant information
257 arising from different dyes on the same antibody, this approach increases the sampling
258 efficiency of independent target proteins.

259 **2.2 Choice of fluorescent dyes and imaging buffers**

260 Fluorescent dyes are the most critical factors for the imaging quality of multi-color dSTORM.
261 As shown in Figure 1A, fluorophores can switch between the ON and the OFF state. The
262 excited fluorophores (S1) can either emit red-shifted light and return to ground state (S0) or
263 enter into the OFF state. Fluorophores in the OFF state can enter the ON state spontaneously

264 (with low efficiency), and the activation can be accelerated by activation lasers and reducing
265 agents in the imaging buffer. Generally, all dyes can be activated by light of shorter
266 wavelength and almost all dyes can be activated by UV light with different efficiency. The
267 ON/OFF switching of fluorophores is stochastic, and the duration that fluorophores remain in
268 the OFF state can last from sub-milliseconds to minutes or even hours. Since the ability to
269 separate blinking events both spatially and temporally during imaging is key to obtaining
270 accurate dSTORM data, the photophysical properties of the dyes have a decisive impact on
271 the experimental outcomes. Artifacts that occur in the reconstructed images as a consequence
272 of an insufficient separation of blinking events are difficult to be identified and removed
273 during data processing, and can lead to false conclusions [51]–[53].

274 The blinking behavior of the dyes is dependent on the illumination intensity and reducing
275 agents in the imaging buffer. In dSTORM imaging, a high power of excitation laser light is
276 needed to keep most fluorophores in the OFF state while inducing efficient and sparse
277 blinking of the fluorophores [54], [55]. The presence of oxygen in the imaging buffer causes
278 the irreversible bleaching of fluorophores and is therefore deleterious for dSTORM imaging.
279 It has also been demonstrated that the blinking performance of many dyes is superior in low
280 oxygen buffers containing reducing agent such as thiols to assist the activation from the OFF
281 to the ON state [55]–[57]. Therefore, most dSTORM imaging buffers contain an enzymatic
282 oxygen scavenging system as well as millimolar concentrations of the thiols β -
283 mercaptoethylamine (MEA) or β -mercaptoethanol (see Appendix for buffer compositions).
284 Most commonly, oxygen removal is achieved with a glucose oxidase based enzymatic system
285 (Gloxy buffer), which works optimally for carbocyanine dyes [58]. Rhodamine dyes usually
286 do not blink well without oxygen, thus an oxyrase-based buffer (OxEA) permitting low level
287 oxygen is preferred for multicolor dSTORM imaging with rhodamine dyes [59]. Meanwhile,
288 novel organic dyes are being developed in an attempt to further improve the fluorophore

289 performance [60]–[63], and there are quite a range of commercially available dyes for
290 dSTORM. However, due to their photochemical differences in addition to their spectral
291 properties, identifying a pair of compatible dyes that behave equally well in the same imaging
292 system is not trivial [58], [59], especially when both target proteins require the best possible
293 imaging qualities.

294 The characterization of the blinking performance of the dyes is therefore indispensable and
295 should be taken into account for the experimental design. Empirically, the performance of
296 dyes can be assessed according to the following principles: (1) at the beginning of the
297 dSTORM recording, the activated fluorophores can be easily pushed into the OFF state in
298 reducing and oxygen-depleted buffer conditions under strong illumination; (2) the
299 fluorophores in the OFF state can be efficiently activated into the ON state by UV light or
300 reducing agents; (3) the dyes can go through several ON/OFF switching cycles, which ensures
301 that sufficient detections can be recorded; (4) the duration of the fluorescence emission should
302 not be persistent (longer than a few image frames) in order to avoid repetitive detections of
303 the same fluorophore during a single blinking event; (5) the dyes should be sufficiently bright
304 to obtain a high localization precision of the single molecule signals. Since all of the above
305 parameters are dependent on the imaging conditions, the optimization of the laser intensities
306 and the buffer composition can substantially improve the blinking performance of the
307 fluorescent dyes.

308 As a starting point, we strongly recommend the carbocyanine dye Alexa Fluor 647 in the far-
309 red channel. Alexa 647 is commonly used in dSTORM due to its excellent photophysical
310 properties that satisfy the five requirements mentioned above. Moreover, appropriate blinking
311 of Alexa 647 can be achieved in various buffer conditions, and there is generally very little
312 background fluorescence in biological samples in the far-red channel. To determine the

313 second color for two-color dSTORM, we have tested several rhodamine dyes (Atto 488,
314 Alexa Fluor 488, Alexa Fluor 568) and carbocyanine dyes (Cy3B) emitting in the green or the
315 red channel in different imaging buffers, to evaluate their compatibility with Alexa 647 in
316 sequential two-color dSTORM. As expected, Gloxy and OxEA buffers stand out of merely
317 MEA-containing buffers and PBS. In the green channel, Atto 488 performed better than
318 Alexa 488 in Gloxy buffer. The concern of using green dyes is that biological samples often
319 have a high level of fluorescence background in this part of the spectrum, and that the higher
320 energy of the green light accelerates the bleaching of the fluorescent beads used as fiducial
321 markers (section 2.3). In the red channel, Alexa 568 blinks nicely in OxEA buffer but less
322 well in Gloxy buffer. Cy3B on the other hand works better in Gloxy buffer. Also, Alexa 647
323 performs optimally in Gloxy buffer but fails to exhibit sufficient spontaneous blinking in
324 OxEA buffer without UV activation. Therefore, we chose Alexa 647 and Cy3B in Gloxy
325 buffer as the optimal imaging system. Since our two-color dSTORM recordings are done
326 sequentially (Fig. 1B,C), this combination of dyes allows us to omit UV activation during the
327 imaging of Alexa 647 due to its spontaneous blinking, thus avoiding any undesired bleaching
328 of Cy3B or the beads. In the second stage, Cy3B is imaged in the red channel with an
329 increasing 405 nm illumination to dynamically adjust the number of fluorophores in the ON
330 state. It is recommended to prepare fresh imaging buffer before the dSTORM recordings,
331 since aging buffers tend to induce less and slower blinking events. Optionally, a very stable
332 glucose-oxidase based imaging buffer is commercially available from Abbelight (Smart kit).

333 **2.3 Fluorescent beads as fiducial markers**

334 Drift correction and two-channel registration are important factors for reconstructing super-
335 resolution images as well as co-localization analysis of synaptic components [64]. Fluorescent
336 beads are generally used as fiducial markers in two-color dSTORM imaging for both drift

337 correction and image registration. Since the recordings can take up to 30 minutes, the
338 microscope stage can drift dramatically in the x/y plane by up to tens of micrometers due to
339 mechanical and thermal effects (Fig. 3). Though the perfect focusing system of our Nikon Ti
340 microscope minimizes the drift in the axial direction, the lateral drift can lead to false
341 structural representations that demand correction. For stereotypic or densely labeled
342 structures, the drift correction can also be achieved by using the structures themselves as
343 landmarks. However, in the case of sparse synaptic clusters, there are too few detections for
344 drift correction using the clusters themselves. Using beads for drift correction is therefore our
345 best option. For sequential two-color dSTORM, two-channel registration is also mandatory,
346 because both lateral drift and spectral differences result in a mismatch between the
347 reconstructed images in the two channels. Using beads as independent fiducial markers
348 induces less bias in the two-channel alignment than using the synaptic clusters.

349 During sample preparation, we attach multicolor beads (100 nm, TetraSpeck microspheres,
350 ThermoFisher) non-specifically to the coverslips. To this aim, the fixed and labeled samples
351 are incubated for about one minute with an excess of beads ($\sim 10^6 \mu\text{l}^{-1}$ in PBS) and rinsed,
352 before mounting the coverslips in imaging buffer. The number of attached beads strongly
353 depends on the density of cellular material on the coverslip, and can be controlled by
354 adjusting the dilution of the beads, the incubation duration and the amount of rinsing. Too few
355 beads will make it difficult to find suitable ROIs and too many beads can mask the signals
356 coming from the fluorophores (Fig. 1C). The attachment of beads on the coverslip is non-
357 specific, meaning that the beads are not always stationary. This is seen as jittering of the
358 beads during imaging, and sometimes the beads can even detach and move out of the field of
359 view (Fig. 3B, bead #1). Beads are usually very bright and produce precisely localized
360 detections. However, when their signals are saturated, the positions of the beads are not fitted
361 accurately, introducing errors in the drift correction. Consequently, strong laser illumination is

362 needed at the beginning of the recording to partially bleach the beads. Note that the pre-
363 bleaching of the beads can result in a loss of signals from the sample fluorophores. In short,
364 saturated or moving beads should be avoided as markers, and using more than one bead in the
365 ROI can improve the precision of drift correction (Fig. 3). In the ideal case, we aim to record
366 about two to three stable and non-saturated beads per field of view.

367 **2.4 Primary spinal cord neuron culture and immunocytochemistry**

368 All procedures using animals follow the regulations of the French Ministry of Agriculture and
369 the Direction départementale des services vétérinaires de Paris (Ecole Normale Supérieure,
370 Animalerie des Rongeurs, license B 75-05-20). Primary spinal cord neuron cultures were
371 prepared from embryonic Sprague Dawley rats on day 14 of gestation (E14) as described
372 previously[24], with some modifications. Cells were plated on 18 mm glass coverslips
373 (thickness 0.16 mm, No. 1.5, VWR #6310153) that were pre-washed with ethanol and coated
374 with 70 µg/ml poly-DL-ornithine. Dissociated neurons were seeded at a density of 4×10^4
375 cells/cm² in Neurobasal medium (ThermoFisher) supplemented with B-27, 2 mM glutamine,
376 5 U/ml penicillin and 5 µg/ml streptomycin. Neurons were cultured at 37°C with 5% CO₂, and
377 the medium was replenished twice a week by replacing half of the volume with BrainPhys
378 neuronal medium (Stemcell Technologies) supplemented with SM1 and antibiotics. Usually,
379 spinal cord neurons developed mature neurites after two weeks in culture, at which point they
380 were used for immunocytochemistry.

381 Spinal cord neurons were fixed with 100% methanol at -20°C for 10 minutes or with pre-
382 warmed (37°C) 4% paraformaldehyde (PFA) in PBS for 15 minutes. Unspecific binding sites
383 were blocked with 3% BSA in PBS (blocking buffer) for at least 30 minutes. The cells were
384 then incubated with primary antibodies diluted in blocking buffer for 1 hour at room
385 temperature or overnight at 4°C, followed by several washing steps in PBS and incubation

386 with secondary antibodies in blocking buffer for 1 hour at room temperature in the dark. In
387 the experiments described here, the following primary antibodies were used: mouse
388 monoclonal mAb7a (Synaptic Systems, #147011, at 1:500 dilution) and rabbit polyclonal
389 (Synaptic Systems, #147002, 1:500) antibodies against gephyrin, as well as custom-made
390 rabbit polyclonal antibody against the GlyR subunit $\alpha 1$ (A. Triller lab, #2353, 1:500 to
391 1:1000). The secondary antibodies were Alexa Fluor 647-conjugated donkey anti-mouse IgG
392 (Jackson ImmunoResearch, #715-605-151, 1:500 to 1:1000) and Alexa Fluor 647-conjugated
393 donkey anti-rabbit IgG (Jackson ImmunoResearch, #711-605-152, 1:500 to 1:1000). In
394 addition, unconjugated donkey anti-mouse IgG (Jackson ImmunoResearch, #715-005-151)
395 and donkey anti-rabbit IgG (Jackson ImmunoResearch, #711-005-152) secondary antibodies
396 were coupled with Cy3B mono-reactive NHS ester (PA63101, GE Healthcare) according to
397 the supplier's protocol, purified using size exclusion columns (Illustra NAP-5 columns,
398 #17085302, GE Healthcare) and used at a dilution of 1:50 to 1:100 for immunolabeling.

399 The choice of fixatives, concentrations of primary and secondary antibodies, as well as
400 buffering solutions and incubation times can all affect dSTORM imaging [65]–[67]. Even
401 though the primary neuron culture and the immunocytochemistry procedures are standard
402 protocols, optimization of the sample preparation is important for dSTORM, since the
403 requirements are not the same as for conventional fluorescence microscopy. For example,
404 Cy3B-tagged secondary antibodies with low dye/protein ratio ($D/P \approx 1-4$) give more discrete
405 blinking profiles in our dSTORM recordings, even if the total fluorescence intensity of the
406 labeled synapses is reduced. Fixatives such as PFA can contribute to background
407 fluorescence. We have therefore quenched the fluorescence background with 50 mM NH_4Cl
408 after fixation. Membrane molecules may retain a certain level of residual mobility after
409 chemical fixation that can be detected in super-resolution images [68]. In these cases, it is
410 recommended to increase fixation times, as long as this does not interfere with the access of

411 the antibodies to the epitopes. Where necessary, membrane proteins such as neurotransmitter
412 receptors can also be stained by live-cell immunocytochemistry to enhance epitope
413 recognition. However, care should be taken to avoid the artificial clustering of the membrane
414 proteins due to the crosslinking effect of secondary antibodies [69]. Finally, samples should
415 always be protected from light and kept at 4°C for no longer than two days prior to dSTORM
416 imaging.

417 **3. Sequential two-color dSTORM imaging**

418 **3.1 Microscope setup**

419 The STORM setup is built on an inverted Nikon Eclipse Ti microscope with a perfect
420 focusing system (PFS) to minimize the axial drift of the microscope stage, and equipped with
421 a 100× oil immersion objective (HP APO TIRF 100× oil, NA 1.49, Nikon). The setup
422 includes several continuous laser lines with emission wavelengths at 640 nm, 561 nm, 532
423 nm, 488 nm and 405 nm (Coherent), with nominal maximum power of 1W, 1W, 500 mW,
424 500 mW and 120 mW, respectively (Fig. 4). The lasers are combined in an external platform
425 and controlled via an acousto-optic tunable filter (AOTF) to apply fast illumination pulses and
426 to set the laser intensity. The laser beam is expanded with a total internal reflection
427 fluorescence (TIRF) arm that controls the inclination angle of the excitation light, and is
428 focused on the back focal plane of the objective. The emission of the fluorescent dyes is
429 captured with an electron multiplying charge-coupled device (EMCCD) camera (Andor iXon
430 897 Ultra, 512 x 512 pixels chip) using a multiple wavelength dichroic mirror and appropriate
431 band pass filters (Semrock FF02-684/24 for Alexa 647, FF01-607/36 for Cy3B) in the
432 emission light path. Conventional fluorescence images were taken with a mercury lamp
433 (Intensilight C-HGFIE, Nikon) that emits a broad spectrum of wavelengths, using the

434 corresponding band pass filters (FF01-650/13 for Alexa 647, FF01-560/25 for Cy3B) in the
435 excitation light path. All the elements are controlled by NIS-Elements software (Nikon).

436 **3.2 Imaging procedure**

437 The dSTORM imaging workflow is illustrated in Figure 1B and C. On the day of imaging,
438 labeled neuron cultures on glass coverslips are incubated with 100 nm beads, and mounted on
439 glass slides with a cavity (diameter 15-18 mm, depth 0.6-0.8 mm) containing freshly prepared
440 Gloxy imaging buffer. Coverslips are sealed with silicone rubber (Picodent twinsil speed 22).
441 We search for ROIs containing several synaptic clusters and fiducial beads under the
442 illumination of the mercury lamp instead of lasers to minimize the bleaching of the
443 fluorophores. Reference images are taken in the far-red and in the red channel with the lamp.
444 The effective magnification of these images is 100x, resulting in a pixel size of 160 nm.
445 Sequential two-color dSTORM is then carried out first in the far-red channel for Alexa 647
446 signals, followed by the red channel for Cy3B. In the beginning of each recording, the field of
447 view is briefly pre-bleached to push the fluorophores into the OFF state and to dampen the
448 brightness of the beads. At least 20000 frames with an exposure time of 50 milliseconds are
449 recorded in each channel. We use highly inclined illumination rather than TIRF to reduce the
450 background fluorescence while avoiding interferences and inhomogeneous illumination. In
451 the far-red channel, the 640 nm laser is used for illumination at an intensity of approximately
452 2.7 kW/cm^2 , resulting in the spontaneous blinking of Alexa 647 fluorophores in the absence
453 of 405 nm laser activation in Gloxy buffer. In the red channel, Cy3B dyes are imaged with the
454 561 nm laser at an intensity of 4 kW/cm^2 . The blinking of Cy3B is supported by low-intensity
455 activation with the 405 nm laser ($\sim 0.01 \text{ kW/cm}^2$ power). The total acquisition time needed
456 for each ROI is about one hour.

457 **3.3 Determining the length of imaging**

458 The primary goal of SMLM imaging is to record as many blinking events as possible from the
459 fluorophores. However, it is practically impossible to detect all the signals in dSTORM
460 because of the random ON/OFF switching cycles of the organic dyes. Some fluorophores can
461 stay in the OFF state for long periods that exceed the recording time. In fact, the multiple
462 switching cycles produce redundant data where each fluorophore can be detected several
463 times. The target proteins are usually labeled with several fluorophores through primary and
464 secondary antibody staining, which produces further redundant information about the position
465 of the same target protein. In addition, the number of detection artefacts (i.e. non-specific
466 fluorescence background) increases with the number of image frames, whereas the actual
467 fluorophore blinking events decrease over time. Therefore, it is neither necessary nor
468 advisable to extend the duration of the recordings and aim to detect all the blinking events
469 from the fluorophores. It is only important to record sufficient independent localizations from
470 which representative structures can be reconstructed. We have therefore adopted the
471 following reasoning to determine the imaging length of our recordings: what is the minimal
472 number of frames from which the reconstructed structures have visibly good agreement with
473 the images reconstructed from much longer recordings?

474 For two-color dSTORM imaging of GlyRs and gephyrin labeled with Alexa 647 and Cy3B,
475 respectively, we recorded 30000 frames in the far-red and 40000 frames in the red channel,
476 until there remained few blinking events at the end of the recordings (Fig. 5). We then split
477 the whole stacks into consecutive sub-stacks of 10000 frames from which we reconstructed
478 separate images and compared their similarity. GlyR clusters reconstructed from the first
479 10000 frames agree well with those in the second and third sub-stacks. Image reconstructions
480 made of the first 20000 frames give very similar representation as 30000 frames. This

481 illustrates that Alexa 647 fluorophores undergo multiple ON/OFF switching cycles that give
482 rise to relatively stable long-term blinking, and that the sub-synaptic distribution of labeled
483 GlyRs at synapses can be captured within 20000 frames (Fig. 5A). In the red channel, the
484 gephyrin clusters from the first two sub-stacks of 10000 images are again quite similar,
485 however, the reconstruction of the third sub-stack produces a less detailed representation.
486 Clearly, Cy3B fluorophores have fewer blinking cycles, meaning that the number of
487 independent detections declines over time, despite the use of the 405 nm activation laser. As a
488 result, the gephyrin clusters reconstructed from 30000 and from 40000 frames are essentially
489 indistinguishable. We therefore set the recording time in the red channel to 30000 frames
490 (Fig. 5B). From the temporal profile of the reconstructed clusters in the two channels, we can
491 also gain some insights into the blinking performance of the dyes. If the clusters reconstructed
492 from the sub-stacks are similar, this implies that the switching cycles of the fluorophores are
493 relatively dispersed throughout the recording (also see Fig. 6A), confirming that the two dyes
494 are suitable for dSTORM imaging of synaptic proteins.

495 **4. Data analysis and quality assessment**

496 **4.1 Image pre-processing**

497 Critical processing steps of the raw imaging data include single particle detection, drift
498 correction, two-channel registration and image reconstruction (Fig. 1B). Single particle
499 detection is realized by applying Gaussian fitting of the PSF of each fluorophore signal to
500 determine the molecule coordinates. To this aim, we use an adapted version of the multiple-
501 target tracing (MTT) program [70] in Matlab 2012b (MathWorks), as described by Izeddin et
502 al [3]. The lateral drift is corrected with the program PALMvis [71] in Matlab 2012b using
503 beads as fiducial markers. A sliding window of 100 to 1000 frames is applied to calculate the

504 average position of the beads, and the systematic x/y drift over time is estimated with a
505 temporal resolution of 5-50 s based on the average displacement of the beads (Fig. 3). The
506 calculated drift of the stage is then applied to the whole image to correct the coordinates of all
507 the single fluorophore localizations. At this stage, we obtain the final coordinates of the
508 localizations, and the two-channel registration can now be done by aligning the beads that
509 were chosen as fiducial markers. Nevertheless, we can go one step further and render the
510 SMLM images as density-based representations of the fluorophore detections. The drift-
511 corrected coordinates are converted into rendered images by representing each localization as
512 a Gaussian function with the same intensity and with a standard deviation ($\sigma = 15$ nm) that is
513 derived from the average localization precision of the detections. Super-resolution images are
514 generally displayed with a pixel size of 10 nm to balance file size versus representation
515 precision. In the rendered super-resolution images, the pixel intensities ultimately represent
516 the density of localizations and the images have zero background. Finally, the two super-
517 resolution images are aligned using the TurboReg plugin[72] in Fiji [73].

518 Alternative tools are available for all the processing steps described above [74]. For example,
519 ThunderSTORM [75] and QuickPALM [76] are commonly used for signal detection and
520 SMLM image reconstruction, and are freely accessible as plugins in Fiji. For more
521 information about the software and programs designed for SMLM, please also see the website
522 of the Biomedical Imaging Group of the EPFL (Lausanne, Switzerland;
523 <http://bigwww.epfl.ch/smlm/software>).

524 **4.2 Statistical analysis**

525 Both types of datasets from SMLM can be used for statistical analysis, namely the coordinate-
526 based pointillist data and the rendered super-resolution image data. Each type of datasets has
527 its own strengths and drawbacks for analysis. The coordinate-based pointillist data in

528 principle make the best use of single molecule localizations. However, the localization
529 precision is usually neglected in the analytical methods developed so far. Moreover, cluster
530 segmentation, feature extraction and spatial correlation analysis based on the pointillist data
531 may demand qualified programming skills. On the other hand, the rendered super-resolution
532 images give more intuitive information, and can be analyzed using common image processing
533 tools such as ImageJ that are widely known to researchers. More importantly, in the rendered
534 images, pixel values represent the density of the localizations, taking into account the
535 localization precision. Since the SMLM coordinates are not the actual positions of the
536 fluorophores but only calculated positions, they can also be understood as localization
537 probabilities. The inclusion of the localization precision in image rendering thus produces
538 more realistic representations. In addition, pixels that do not contain any localizations have
539 the value of zero. In other words, there is no background in the rendered super-resolution
540 images. Thus there is no need for background subtraction or thresholding, which is one of the
541 major difficulties in fluorescent image processing.

542 Different algorithms and software are available for analyzing coordinate-based pointillist data.
543 For instance, density-based spatial clustering of applications with noise (DBSCAN) and
544 Voronoï tessellation have been exploited for spatial clustering and segmentation of SMLM
545 data [77]. The advantage of the two algorithms is that they do not make any assumptions
546 about the shape of the structures, which is very suitable for segmenting synaptic clusters in
547 SMLM data. To quantify the co-localization of two proteins, coordinate-based co-localization
548 (CBC) [78], [79] enables single molecule correlation analysis of dual-color pointillist data.
549 These algorithms have been implemented in different open-source software for SMLM data
550 analysis, such as Clus-Doc, LAMA and so on [80]–[83]. However, using these tools can be
551 problematic, because they are often not suited to the specific demands. In our case, we did not
552 find any suitable analysis tool that would allow us to perform individual cluster-based

553 analysis, which is essential for the comparison of synaptic GlyR and gephyrin clusters. In
554 contrast, individual synaptic clusters in the rendered super-resolution images can be easily
555 obtained with classical image processing. With the powerful image analysis platforms Fiji
556 [73] and Icy [84], image-based analysis of individual synaptic clusters is relatively
557 straightforward. Therefore, we suggest to begin with image-based SMLM analysis.

558 In the following, we describe an image-based analysis workflow using exclusively open
559 source tools that allow biologists to extract relevant information. With the help of simple
560 macros in Fiji [73] to record commands and construct basic programs, a set of experimental
561 data, namely two-color recordings of ten cells with about one hundred synapses, can be
562 analyzed in one day using this workflow.

563 First, the reference images are converted into binary masks with the Icy spot detector plugin,
564 choosing appropriate parameters to select well focused and brightly labeled synaptic puncta.
565 The combined area of synaptic masks in the two channels is obtained by calculating the sum
566 of the binary images with Fiji and used to identify the synaptic clusters in the super-resolution
567 images. Since out-of-focus synapses and background fluorescence can also appear as clusters
568 in dSTORM images, using the mask to pre-select synaptic clusters is necessary. However, it
569 should be kept in mind that this process can potentially introduce a certain bias in the
570 analysis, since small and weakly labeled synaptic clusters may be lost. This is not an issue in
571 our case, because our aim is to directly compare the sub-synaptic distributions of different
572 synaptic components within the same synapse. The dual-color dSTORM recordings can
573 therefore be considered as paired data. Therefore, the selection of synaptic clusters based on
574 the labeling intensity is a legitimate approach.

575 Since our super-resolution images are reconstructed from detection coordinates, there may be
576 a substantial mismatch between the two super-resolution images and the reference images.

577 Drift correction and chromatic differences add to the mismatch between the images.
578 Therefore, in the second step, the super-resolution images and the combined mask image are
579 aligned with TurboReg plugin in Fiji. Also, the pixel size of the low resolution mask (160 nm)
580 has to be artificially enhanced to match that of the rendered dSTORM images (10 nm). After
581 image registration, the masks for individual synapses are applied to the super-resolution
582 images to crop the individual synaptic clusters in Fiji. At this point, we obtain individual
583 synaptic cluster pairs of GlyRs and gephyrin, on which we can perform further cluster
584 analysis.

585 To characterize the spatial correlation of GlyR and gephyrin clusters, we employ the intensity
586 correlation analysis (ICA) plugin in Fiji as described by Li et al [85]. In this analysis, the
587 variations of the intensities for each pixel between two images are compared in order to
588 identify correlated changes that reflect the co-localization of the two proteins. Intensity
589 correlation quotients (ICQ) between -0.5 and +0.5 are calculated for each synaptic cluster,
590 where -0.5 indicates a mutually exclusive distribution, zero a random distribution, and +0.5 a
591 perfect positive correlation between the two proteins. Moreover, the ICA plugin also
592 calculates the Pearson correlation coefficient (Pearson's R) which measures the linear
593 correlation of the intensity of each pixel between the two images, providing additional
594 information.

595 To characterize the internal synaptic distribution of GlyRs and gephyrin, we carry out H-
596 watershed analysis to segment the subclusters using the interactive H-watershed plugin
597 developed by Benoit Lombardot (http://imagej.net/Interactive_Watershed) in Fiji. H-
598 watershed finds local maxima with one parameter, H, allowing the detection of subcluster
599 peaks and the segmentation of the subclusters from each other. After segmentation, the
600 features of the binary synaptic subclusters are extracted using extended particle analyzer

601 (EPA) [86] in Fiji. We can thus obtain detailed information about synaptic GlyR and gephyrin
602 subclusters under various experimental conditions. For example, changes in the number and
603 area of the subclusters per synapse reveal how the distribution of GlyRs and gephyrin within
604 the PSD is regulated during inhibitory synaptic plasticity.

605 **4.3 Strategies for imaging quality assessment**

606 The evaluation of individual factors (dyes, buffers, probes, laser power and so on) is
607 important for understanding their influence on the quality of the dSTORM data. However, the
608 final image quality depends on the combined effect of these factors that are heavily inter-
609 dependent. Therefore, a joined assessment of the imaging data is necessary to estimate the
610 capability of the protocol to answer the biological question or hypothesis. We propose to
611 carry out the following types of control experiments to evaluate the performance of the
612 chosen experimental approach (Fig 6).

613 First, we recorded the blinking behavior of the two dyes conjugated to IgG in order to
614 estimate the degree of redundant detections and the appearance of fake nanoclusters. We
615 carried out two-color dSTORM imaging of two secondary antibodies, conjugated with either
616 Alexa 647 or Cy3B dye. Clean glass coverslips were incubated for one hour with Alexa 647-
617 conjugated donkey anti-mouse IgG and Cy3B-conjugated donkey anti-rabbit IgG that were
618 diluted in 3% BSA and mounted with beads and imaging buffer. We then performed
619 sequential two-color dSTORM imaging as described above and characterized the clusters
620 produced by single secondary antibodies in the two channels (Fig. 6A). Both A647-IgG and
621 Cy3B-IgG produced nanometer scale clusters with a wide variability in the number of
622 detections per cluster as well as cluster size. From the temporal profiles of the blinking
623 events, we can infer the photophysical behavior of the dyes. For Alexa 647, the blinking
624 events are brief and dispersed across the entire recording. Cy3B fluorophores on the other

625 hand display relatively few blinking events, some of which have persistent ON times,
626 resulting in large bursts of repetitive detections during a single blinking event. As a
627 consequence, Cy3B produces detection densities that are less quantitative than those of Alexa
628 647. The diameter of the clusters produced by single IgG is around 40 to 120 nm, which is
629 similar to the size of the nanodomains proposed for synaptic proteins [21]–[23], [29].
630 Therefore, the detection density and the size of the clusters from single probes used for
631 labeling has to be taken into account during data analysis and interpretation when
632 characterizing nanodomains of synaptic proteins.

633 Next, we assessed the consistency of two-color dSTORM imaging of synaptic proteins by
634 labeling GlyR clusters in spinal cord neurons with the same antibody against the GlyR α 1
635 subunit and with two different secondary antibodies, namely Alexa 647-conjugated donkey
636 anti-rabbit and Cy3B-conjugated donkey anti-rabbit IgG. We then analyzed the spatial
637 correlation of GlyR clusters detected in the two channels. As expected, both Pearson's
638 coefficient and ICA showed strong positive correlation, demonstrating that Alexa 647 and
639 Cy3B produce similarly good representations of the same GlyR cluster (Fig. 6B). We further
640 looked into the internal organization of the GlyR clusters detected by the two dyes. The super-
641 resolution clusters of GlyR were segmented using H-watershed to detect the sub-synaptic
642 GlyR distribution. The subcluster counts detected by either Alexa 647 or Cy3B showed
643 moderate correlation and Cy3B tended to produce more subclusters. Concomitantly, the areas
644 of the subclusters detected by Alexa 647 were significantly larger than the ones detected by
645 Cy3B. This shows that the different photophysical properties of Alexa 647 and Cy3B dyes
646 have considerable impact on the sub-synaptic structural representation in dSTORM.

647 Third, we tested the effect of dye reversal on the detection of synaptic clusters (Fig. 6C). We
648 used two different primary antibodies that recognize the same synaptic protein, gephyrin.

649 Primary mouse monoclonal mAb7a (m7a) and rabbit polyclonal antibodies against gephyrin
650 (rbGPHN) were labeled, in one case with Cy3B-conjugated donkey anti-mouse IgG and
651 Alexa 647-conjugated donkey anti-rabbit IgG (condition 1), and in the other case with Alexa
652 647-conjugated donkey anti-mouse IgG and Cy3B-conjugated donkey anti-rabbit IgG
653 (condition 2). We then compared the spatial correlation of the gephyrin clusters in the two
654 channels between the two conditions, as well as the subclusters. The second experimental
655 condition showed significantly stronger correlation than the first condition, as judged from the
656 Pearson's R and ICQ values. As to the sub-synaptic organization of gephyrin, the subcluster
657 counts per synapse detected by Cy3B were again higher than those of Alexa 647-labeled
658 clusters in both conditions. Interestingly, the sizes of the subclusters probed with rbGPHN-
659 A647 were much larger than with m7a-Cy3B in the first condition. However, this difference
660 was not seen in the second condition with reversed dyes. Under the same circumstances, it
661 would be expected that the two conditions give the same degree of co-localization and that
662 gephyrin subclusters detected by Alexa 647 would generally occupy larger areas than with
663 Cy3B, which is not the case in our results. Given that m7a and rbGPHN detect different
664 epitopes of gephyrin, one possible explanation for this unexpected finding is that the two
665 epitopes are not distributed homogeneously at synapses, which is part of our ongoing
666 research. Our data also illustrate the necessity of control experiments with reversed dyes to
667 validate the experimental findings.

668 **5. Conclusion**

669 SMLM is a powerful technology that allows the characterization of biological samples with a
670 resolution on the nanometer scale. Based on our own experiences we strongly recommend to
671 consider the technical difficulties and limitations of the technique in the experimental design,
672 in particular when SMLM is applied to complex biological structures. The methodological

673 framework discussed in this chapter is applicable to synapses and similarly complex
674 structures alike. We also propose that the quality of the reconstructed images and the
675 relevance of the extracted parameters be critically assessed before drawing far-reaching
676 conclusions, and that the results of these assessments and control experiments should be
677 included where possible in scientific publications.

678 **Acknowledgement**

679 We thank Manuel Maidorn and Felipe Opazo for the illustrations in Figure 2 [47], and Ignacio
680 Izeddin for Figure 4. Our research is funded by grants (to Antoine Triller, IBENS, Paris)
681 from the Agence Nationale de la Recherche (ANR-12-BSV4-0019-01, ANR-11-IDEX-0001-
682 02, ANR-10-LABX-54) and the European Research Council (ERC, PlastInhib). XY is
683 supported by the China Scholarship Council (CSC).

684 **Appendix: imaging buffers**

685 Gloxy buffer: 0.5 mg/ml glucose oxidase, 40 μ g/ml catalase, 0.5 M D-glucose, 50 mM β -
686 mercaptoethylamine (MEA), in PBS pH 7.4, degased with N₂ [3].

687 OxEA buffer: 3% (v/v) oxyrase (EC-Oxyrase, Sigma-Aldrich), 1 M sodium DL-lactate, 50
688 mM MEA, in PBS pH 8.0 [59].

689 **6. References**

- 690 [1] R. E. Thompson, D. R. Larson, and W. W. Webb, "Precise Nanometer Localization
691 Analysis for Individual Fluorescent Probes," *Biophys. J.*, vol. 82, no. May, pp. 2775–
692 2783, 2002.
- 693 [2] B. Huang, "Super-resolution optical microscopy: multiple choices," *Curr. Opin. Chem.*
694 *Biol.*, vol. 14, no. 1, pp. 10–14, 2010.

- 695 [3] I. Izeddin *et al.*, “Super-resolution dynamic imaging of dendritic spines using a low-
696 affinity photoconvertible actin probe,” *PLoS One*, vol. 6, no. 1, 2011.
- 697 [4] S. Van De Linde *et al.*, “Direct stochastic optical reconstruction microscopy with
698 standard fluorescent probes,” *Nat. Protoc.*, vol. 6, no. 7, pp. 34–38, 2011.
- 699 [5] D. Baddeley and J. Bewersdorf, “Biological Insight from Super-Resolution
700 Microscopy: What We Can Learn from Localization-Based Images,” *Annu. Rev.*
701 *Biochem.*, vol. 87, pp. 965–89, 2018.
- 702 [6] M. J. Rust, M. Bates, and X. Zhuang, “Stochastic optical reconstruction microscopy
703 (STORM) provides sub-diffraction-limit image resolution,” *Nat. Methods*, vol. 3, no.
704 10, pp. 793–795, 2006.
- 705 [7] E. Betzig *et al.*, “Imaging Intracellular Fluorescent Proteins at Nanometer Resolution,”
706 *Science (80-.)*, vol. 313, no. 5793, pp. 1642–1645, 2006.
- 707 [8] S. T. Hess, T. P. K. Girirajan, and M. D. Mason, “Ultra-High Resolution Imaging by
708 Fluorescence Photoactivation Localization Microscopy,” *Biophys. J.*, vol. 91, no. 11,
709 pp. 4258–4272, 2006.
- 710 [9] M. Heilemann *et al.*, “Subdiffraction-resolution fluorescence imaging with
711 conventional fluorescent probes,” *Angew. Chemie - Int. Ed.*, vol. 47, pp. 6172–6176,
712 2008.
- 713 [10] M. Bates, B. Huang, G. T. Dempsey, X. Zhuang, and T. Dempsey, “Multicolor Super-
714 Resolution Imaging with Photo-Switchable Probes Fluorescent,” *Science (80-.)*, vol.
715 317, no. 5845, pp. 1749–1753, 2007.
- 716 [11] Haining Zhong, “Applying superresolution localization-based microscopy to neurons,”
717 *Synapse*, vol. 69, pp. 283–294, 2015.
- 718 [12] A. M. Sydor, K. J. Czymmek, E. M. Puchner, and V. Mennella, “Super-Resolution
719 Microscopy: From Single Molecules to Supramolecular Assemblies,” *Trends Cell*

- 720 *Biol.*, vol. 25, no. 12, pp. 730–748, 2015.
- 721 [13] K. Xu, G. Zhong, and X. Zhuang, “Actin, Spectrin, and Associated Proteins Form a
722 Periodic Cytoskeletal Structure in Axons,” *Science (80-.)*, 2013.
- 723 [14] C. Leterrier, J. Potier, G. Caillol, and C. Debarnot, “Nanoscale Architecture of the
724 Axon Initial Segment Reveals an Organized and Robust Scaffold,” *Cell Rep.*, vol. 13,
725 pp. 2781–2793, 2015.
- 726 [15] J. Bär, O. Kobler, B. Van Bommel, and M. Mikhaylova, “Periodic F-actin structures
727 shape the neck of dendritic spines,” *Sci. Rep.*, vol. 6, no. November, pp. 1–9, 2016.
- 728 [16] A. Loschberger *et al.*, “Super-resolution imaging visualizes the eightfold symmetry of
729 gp210 proteins around the nuclear pore complex and resolves the central channel with
730 nanometer resolution,” *J. Cell Sci.*, vol. 125, no. 3, pp. 570–575, 2012.
- 731 [17] A. Szyborska, A. De Marco, N. Daigle, V. C. Cordes, J. A. G. Briggs, and J.
732 Ellenberg, “Nuclear Pore Scaffold Structure Analyzed by Super-Resolution
733 Microscopy and Particle Averaging,” *Science (80-.)*, vol. 341, no. 6146, pp. 655–658,
734 2013.
- 735 [18] and B. R. Jordi Broeken, Hannah Johnson, Diane S. Lidke, Sheng Liu, Robert P.J.
736 Nieuwenhuizen, Sjoerd Stallinga, Keith A. Lidke, “Resolution improvement by 3D
737 particle averaging in localization microscopy,” *Methods Appl Fluoresc*, vol. 3, 2015.
- 738 [19] A. Dani, B. Huang, J. Bergan, and C. Dulac, “Super-resolution Imaging of Chemical
739 Synapses in the Brain,” *Neuron*, vol. 68, no. 5, pp. 843–856, 2010.
- 740 [20] T. Kuriu, A. Inoue, H. Bito, K. Sobue, and S. Okabe, “Differential Control of
741 Postsynaptic Density Scaffolds via Actin-Dependent and -Independent Mechanisms,”
742 *J. Neurosci.*, vol. 26, no. 29, pp. 7693–7706, 2006.
- 743 [21] H. D. MacGillavry, Y. Song, S. Raghavachari, and T. A. Blanpied, “Nanoscale
744 scaffolding domains within the postsynaptic density concentrate synaptic ampa

- 745 receptors,” *Neuron*, vol. 78, no. 4, pp. 615–622, 2013.
- 746 [22] D. Nair, E. Hosy, J. D. Petersen, A. Constals, G. Giannone, and D. Choquet, “Super-
747 Resolution Imaging Reveals That AMPA Receptors Inside Synapses Are Dynamically
748 Organized in Nanodomains Regulated by PSD95,” *J. Neurosci.*, vol. 33, no. 32, pp.
749 13204–13224, 2013.
- 750 [23] K. T. Haas *et al.*, “Pre-post synaptic alignment through neuroligin-1 tunes synaptic
751 transmission efficiency,” *Elife*, vol. 7, pp. 1–22, 2018.
- 752 [24] C. G. Specht *et al.*, “Quantitative Nanoscopy of Inhibitory Synapses : Counting
753 Gephyrin Molecules and Receptor Binding Sites,” *Neuron*, vol. 79, no. 2, pp. 308–321,
754 2013.
- 755 [25] A. T. Pamela C. Rodriguez, Leandro G. Almeida, “Continuous rearrangement of the
756 postsynaptic gephyrin scaffolding domain: a super-resolution quantified and energetic
757 approach,” *bioRxiv*, 2017.
- 758 [26] F. Pennacchietti *et al.*, “Nanoscale Molecular Reorganization of the Inhibitory
759 Postsynaptic Density Is a Determinant of GABAergic Synaptic Potentiation,” *J.*
760 *Neurosci.*, vol. 37, no. 7, pp. 1747–1756, 2017.
- 761 [27] M. J. Broadhead *et al.*, “PSD95 nanoclusters are postsynaptic building blocks in
762 hippocampus circuits,” *Sci. Rep.*, vol. 6, no. 24626, 2016.
- 763 [28] E. Dzyubenko, A. Rozenberg, D. M. Hermann, and A. Faissner, “Colocalization of
764 synapse marker proteins evaluated by STED-microscopy reveals patterns of neuronal
765 synapse distribution in vitro,” *J. Neurosci. Methods*, vol. 273, pp. 149–159, 2016.
- 766 [29] A. H. Tang, H. Chen, T. P. Li, S. R. Metzbower, H. D. MacGillavry, and T. A.
767 Blanpied, “A trans-synaptic nanocolumn aligns neurotransmitter release to receptors,”
768 *Nature*, vol. 536, no. 7615, 2016.
- 769 [30] K. P. De Arce *et al.*, “Topographic Mapping of the Synaptic Cleft into Adhesive

- 770 Nanodomains Report Topographic Mapping of the Synaptic Cleft into Adhesive
771 Nanodomains,” *Neuron*, vol. 88, pp. 1165–1172, 2015.
- 772 [31] I. Chamma *et al.*, “Mapping the dynamics and nanoscale organization of synaptic
773 adhesion proteins using monomeric streptavidin,” *Nat. Commun.*, vol. 7, no. 10773,
774 2016.
- 775 [32] F. Fricke, J. Beaudouin, R. Eils, and M. Heilemann, “One, two or three? Probing the
776 stoichiometry of membrane proteins by single-molecule localization microscopy,” *Sci.*
777 *Rep.*, vol. 5, no. 14072, 2015.
- 778 [33] A. Patrizio, M. Renner, R. Pizzarelli, A. Triller, and C. G. Specht, “Alpha subunit-
779 dependent glycine receptor clustering and regulation of synaptic receptor numbers,”
780 *Sci. Rep.*, vol. 7, no. 1, pp. 1–11, 2017.
- 781 [34] P. Jonas, J. Bischofberger, and J. Sandkühler, “Corelease of two fast neurotransmitters
782 at a central synapse,” *Science (80-.)*, vol. 281, no. 5375, pp. 419–424, 1998.
- 783 [35] K. R. Aubrey, “Presynaptic control of inhibitory neurotransmitter content in VIAAT
784 containing synaptic vesicles,” *Neurochem. Int.*, vol. 98, pp. 94–102, 2016.
- 785 [36] A. Triller, F. Cluzaud, and H. Korn, “Gamma-Aminobutyric Acid-containing
786 Terminals Can Be Apposed to Glycine Receptors at Central Synapses,” *J. Cell Biol.*,
787 vol. 104, pp. 947–956, 1987.
- 788 [37] S. Bohlhalter, H. Mohler, and J. Fritschy, “Inhibitory neurotransmission in rat spinal
789 cord : co-localization of glycine- and GABAA-receptors at GABAergic synaptic
790 contacts demonstrated by triple immunofluorescence staining,” *Brain Res.*, vol. 642,
791 pp. 59–69, 1994.
- 792 [38] A. J. Todd, C. Watt, R. C. Spike, and W. Sieghart, “Colocalization of GABA, glycine,
793 and their receptors at synapses in the rat spinal cord,” *J. Neurosci.*, vol. 16, no. 3, pp.
794 974–982, 1996.

- 795 [39] A. Dumoulin, S. Levi, B. Riveau, B. Gasnier, and A. Triller, “Formation of mixed
796 glycine and GABAergic synapses in cultured spinal cord neurons,” *Eur J Neurosci*,
797 vol. 12, pp. 3883–3892, 2000.
- 798 [40] A. N. Shrivastava, A. Triller, and W. Sieghart, “GABAA Receptors: Post-Synaptic Co-
799 Localization and Cross-Talk with Other Receptors,” *Front. Cell. Neurosci.*, vol. 5, no.
800 7, pp. 1–12, 2011.
- 801 [41] G. Meyer, J. Kirsch, H. Betz, and D. Langosch, “Identification of a Gephyrin Binding
802 Motif on the Glycine Receptor β Subunit,” *Neuron*, vol. 15, pp. 563–572, 1995.
- 803 [42] H. Maric, J. Mukherjee, V. Tretter, S. J. Moss, and H. Schindelin, “Gephyrin-mediated
804 γ -Aminobutyric Acid Type A and Glycine Receptor Clustering Relies on a Common
805 Binding Site,” *J. Biol. Chem.*, vol. 286, no. 49, pp. 42105–42114, 2011.
- 806 [43] W. S. and S. J. M. Verena Tretter, Jayanta Mukherjee , Hans-Michael Maric , Hermann
807 Schindelin, “Gephyrin , the enigmatic organizer at GABAergic synapses,” *Front. Cell.*
808 *Neurosci.*, vol. 6, pp. 1–16, 2012.
- 809 [44] F. J. Alvarez, “Gephyrin and the regulation of synaptic strength and dynamics at
810 glycinergic inhibitory synapses,” *Brain Res. Bull.*, 2016.
- 811 [45] Y. Cantaut-Belarif *et al.*, “Microglia control the glycinergic but not the GABAergic
812 synapses via prostaglandin E2 in the spinal cord,” *J. Cell Biol.*, vol. 216, no. 9, pp.
813 2979–2989, 2017.
- 814 [46] M. Russier, I. L. Kopysova, N. Ankri, N. Ferrand, and D. Debanne, “GABA and
815 glycine co-release optimizes functional inhibition in rat brainstem motoneurons in
816 vitro,” *J. Physiol.*, vol. 541, no. 1, pp. 123–137, 2002.
- 817 [47] M. Maidorn, S. O. Rizzoli, and F. Opazo, “Tools and limitations to study the molecular
818 composition of synapses by fluorescence microscopy,” *Biochem. J.*, vol. 473, pp.
819 3385–3399, 2016.

- 820 [48] J. Ries, C. Kaplan, E. Platonova, H. Eghlidi, and H. Ewers, “A simple , versatile
821 method for GFP-based microscopy via nanobodies,” *Nat. Methods*, vol. 9, no. 6, 2012.
- 822 [49] E. Platonova, C. M. Winterflood, A. Junemann, D. Albrecht, J. Faix, and H. Ewers,
823 “Single-molecule microscopy of molecules tagged with GFP or RFP derivatives in
824 mammalian cells using nanobody binders,” *Methods*, vol. 88, pp. 89–97, 2015.
- 825 [50] T. Pleiner *et al.*, “Nanobodies : site-specific labeling for super-resolution imaging ,
826 rapid epitope- mapping and native protein complex isolation,” *Elife*, vol. 4, 2015.
- 827 [51] P. Annibale, S. Vanni, M. Scarselli, U. Rothlisberger, and A. Radenovic,
828 “Identification of clustering artifacts in photoactivated localization microscopy,” *Nat.*
829 *Methods*, vol. 8, no. 7, pp. 527–528, 2011.
- 830 [52] P. Annibale, S. Vanni, M. Scarselli, U. Rothlisberger, and A. Radenovic, “Quantitative
831 Photo Activated Localization Microscopy : Unraveling the Effects of Photoblinking,”
832 *PLoS One*, vol. 6, no. 7, 2011.
- 833 [53] A. Burgert, S. Letschert, S. Doose, and M. Sauer, “Artifacts in single-molecule
834 localization microscopy,” *Histochem. Cell Biol.*, vol. 144, pp. 123–131, 2015.
- 835 [54] S. Van De Linde, S. Wolter, M. Heilemann, and M. Sauer, “The effect of
836 photoswitching kinetics and labeling densities on super-resolution fluorescence
837 imaging,” *J. Biotechnol.*, vol. 149, no. 4, pp. 260–266, 2010.
- 838 [55] S. van de Linde, I. Krstić, T. Prisner, S. Doose, M. Heilemann, and M. Sauer,
839 “Photoinduced formation of reversible dye radicals and their impact on super-
840 resolution imaging.,” *Photochem. Photobiol. Sci.*, vol. 10, no. 4, pp. 499–506, 2011.
- 841 [56] J. Vogelsang *et al.*, “A Reducing and Oxidizing System Minimizes Photobleaching and
842 Blinking of Fluorescent Dyes,” *Angew. Chemie - Int. Ed.*, vol. 47, pp. 5465–5469,
843 2008.
- 844 [57] T. Ha and P. Tinnefeld, “Photophysics of Fluorescence Probes for Single Molecule

845 Biophysics and Super-Resolution Imaging,” *Annu Rev Phys Chem*, vol. 63, no. 2, pp.
846 595–617, 2012.

847 [58] G. T. Dempsey, J. C. Vaughan, K. H. Chen, M. Bates, and X. Zhuang, “Evaluation of
848 fluorophores for optimal performance in localization-based super-resolution imaging,”
849 vol. 8, no. 12, 2011.

850 [59] L. Nahidiyar, A. V. Agronskaia, J. Broertjes, B. Den Van Broek, and K. Jalink,
851 “Optimizing imaging conditions for demanding multi-color super resolution
852 localization microscopy,” *PLoS One*, vol. 11, no. 7, pp. 1–18, 2016.

853 [60] and S. C. B. Qinsi Zheng, Manuel F. Juettea, Steffen Jockusch, Michael R.
854 Wasserman, Zhou Zhou, Roger B. Altman, “Ultra-stable organic fluorophores for
855 single-molecule research,” *Chem Soc Rev*, vol. 43, no. 4, pp. 1044–1056, 2014.

856 [61] and M. Y. B. Natalia G. Zhegalova, Shawn He, Haiying Zhou, David M. Kim,
857 “Minimization of self-quenching fluorescence on dyes conjugated to biomolecules with
858 multiple labeling sites via asymmetrically charged NIR fluorophores,” *Contrast Media
859 Mol Imaging*, vol. 9, no. 5, pp. 355–362, 2014.

860 [62] J. B. Grimm *et al.*, “Bright photoactivatable fluorophores for single- molecule
861 imaging,” *Nat. Methods*, 2016.

862 [63] M. Lehmann, G. Lichtner, H. Klenz, and J. Schmoranzer, “Novel organic dyes for
863 multicolor localization-based super-resolution microscopy,” *J. Biophotonics*, vol. 9, no.
864 1–2, pp. 161–170, 2016.

865 [64] M. G. and A. R. Paolo Annibale, Marco Scarselli, “Identification of the factors
866 affecting co-localization precision for quantitative multicolor localization microscopy,”
867 *Opt. nanoscopy*, 2012.

868 [65] K. N. Richter *et al.*, “Glyoxal as an alternative fixative to formaldehyde in
869 immunostaining and super-resolution microscopy,” *EMBO J.*, pp. 1–21, 2017.

- 870 [66] T. A. Stanly *et al.*, “Critical importance of appropriate fixation conditions for faithful
871 imaging of receptor microclusters,” *Biol. Open*, vol. 5, no. 9, pp. 1343–1350, 2016.
- 872 [67] D. R. Whelan and T. D. M. Bell, “Image artifacts in Single Molecule Localization
873 Microscopy : why optimization of sample preparation protocols matters,” *Sci. Rep.*,
874 vol. 5, no. 07924, pp. 1–10, 2015.
- 875 [68] K. A. K. Tanaka *et al.*, “Membrane molecules mobile even after chemical fixation,”
876 *Nat. Methods*, vol. 7, no. 11, pp. 865–866, 2010.
- 877 [69] I. Brünig, E. Scotti, C. Sidler, and J. M. Fritschy, “Intact sorting, targeting, and
878 clustering of γ -aminobutyric acid A receptor subtypes in hippocampal neurons in
879 vitro,” *J. Comp. Neurol.*, vol. 443, pp. 43–55, 2002.
- 880 [70] H. R. & D. M. Arnauld Serge, Nicolas Bertaux, “Dynamic multi-target tracing to probe
881 spatiotemporal cartography of cell membrane,” *Nat. Methods*, vol. 5, no. 8, pp. 687–
882 694, 2008.
- 883 [71] M. Lelek, F. Di Nunzio, R. Henriques, P. Charneau, N. Arhel, and C. Zimmer,
884 “Superresolution imaging of HIV in infected cells with FIAsh-PALM,” *Proc. Natl.*
885 *Acad. Sci.*, vol. 109, no. 22, pp. 8564–8569, 2012.
- 886 [72] P. Thevenaz, U. E. Ruttiman, and M. Unser, “A Pyramid Approach to Sub-Pixel
887 Registraion based on Intensity,” *IEEE Trans. Image Process.*, vol. 7, no. 1, pp. 27–41,
888 1998.
- 889 [73] J. Schindelin *et al.*, “Fiji: An open-source platform for biological-image analysis,” *Nat.*
890 *Methods*, vol. 9, no. 7, pp. 676–682, 2012.
- 891 [74] D. Sage *et al.*, “Quantitative evaluation of software packages for single-molecule
892 localization microscopy,” *Nat. Methods*, vol. 12, no. 8, pp. 717–724, 2015.
- 893 [75] M. Ovesný, P. Křížek, J. Borkovec, Z. Švindrych, and G. M. Hagen,
894 “ThunderSTORM: A comprehensive ImageJ plug-in for PALM and STORM data

- 895 analysis and super-resolution imaging,” *Bioinformatics*, vol. 30, no. 16, pp. 2389–2390,
896 2014.
- 897 [76] R. Henriques, M. Lelek, E. F. Fornasiero, F. Valtorta, C. Zimmer, and M. M. Mhlanga,
898 “QuickPALM: 3D real-time photoactivation nanoscopy image processing in ImageJ,”
899 *Nat. Methods*, vol. 7, no. 5, pp. 339–340, 2010.
- 900 [77] P. R. Nicovich, D. M. Owen, and K. Gaus, “Turning single-molecule localization
901 microscopy into a quantitative bioanalytical tool,” *Nat. Protoc.*, vol. 12, no. 3, pp. 453–
902 461, 2017.
- 903 [78] S. Malkusch, U. Endesfelder, J. Mondry, M. Gelléri, P. J. Verveer, and M. Heilemann,
904 “Coordinate-based colocalization analysis of single-molecule localization microscopy
905 data,” *Histochem. Cell Biol.*, vol. 137, pp. 1–10, 2012.
- 906 [79] M. Georgieva, D. I. Cattoni, J. Fiche, T. Mutin, D. Chamousset, and M. Nollmann,
907 “Nanometer resolved single-molecule colocalization of nuclear factors by two-color
908 super resolution microscopy imaging,” *METHODS*, 2016.
- 909 [80] S. V Paeon, P. R. Nicovich, M. Mollazade, T. Tabarin, K. Gaus, and D. Lidke, “Clus-
910 DoC : a combined cluster detection and colocalization analysis for single-molecule
911 localization microscopy data,” *molbiolcel*, vol. 27, pp. 3627–3636, 2016.
- 912 [81] S. Malkusch and M. Heilemann, “Extracting quantitative information from single-
913 molecule super- resolution imaging data with LAMA – LocAlization Microscopy
914 Analyzer,” *Sci. Rep.*, vol. 6, 2016.
- 915 [82] F. Levet *et al.*, “SR-Tesseler : a method to segment and quantify localization-based
916 super-resolution microscopy data,” *Nat. Methods*, vol. 12, no. 11, 2015.
- 917 [83] L. Andronov, I. Orlov, Y. Lutz, and J. Vonesch, “ClusterViSu , a method for clustering
918 of protein complexes by Voronoi tessellation in super- resolution microscopy,” *Sci.*
919 *Rep.*, vol. 6, 2016.

- 920 [84] F. De Chaumont *et al.*, “Icy: An open bioimage informatics platform for extended
921 reproducible research,” *Nat. Methods*, vol. 9, no. 7, pp. 690–696, 2012.
- 922 [85] and E. F. S. Qi Li, Anthony Lau, Terence J. Morris, Lin Guo, Christopher B. Fordyce,
923 “A Syntaxin 1, Gαo, and N-Type Calcium Channel Complex at a Presynaptic Nerve
924 Terminal: Analysis by Quantitative Immunocolocalization,” *J. Neurosci.*, vol. 24, no.
925 16, pp. 4070–4081, 2004.
- 926 [86] J. Brocher, “Qualitative and Quantitative Evaluation of Two New Histogram Limiting
927 Binarization Algorithms,” *Int. J. Image Process.*, vol. 8, no. 2, pp. 30–48, 2014.
- 928

929 **Figure1. Sequential two-color dSTORM imaging of synaptic proteins.**

930 **A.** Simplified Jablonski diagram, showing the switching cycle of fluorophores. After
931 excitation to the S1 state, the fluorophores can either return to the ground state (S0) by
932 emitting longer wavelength light, or they enter the non-fluorescence OFF state. Fluorophores
933 in the OFF state are re-activated by UV light or spontaneously in the presence of reducing
934 agents in the imaging buffer.

935 **B.** Experimental workflow for two-color dSTORM imaging and data analysis.

936 **C.** Representative images of two-color dSTORM recordings. From left to right:
937 epifluorescence reference images, acquisition of image stacks with single fluorophore
938 blinking events, pointillist dSTORM images reconstructed from single fluorophore
939 localizations (after drift correction), and rendered super-resolution images in the far-red
940 (Alexa 647) and the red channel (Cy3B). Arrowheads point to beads in the region of interest
941 (ROI) used for drift correction. Scale: 2 μm .

942

943 **Figure 2. The effect of the probe size.**

944 **A.** The large size of primary and secondary antibodies limits their access to all the epitopes
945 and keeps the fluorophores at a distance from the target proteins. Live labeling with
946 antibodies may also cause artificial clustering of membrane proteins.

947 **B.** Small monovalent probes such as nanobodies circumvent these limitations, avoiding
948 epitope masking, signal de-localization and crosslinking. The epitope-binding interface is
949 shown in magenta, organic dyes in red, labeling probes in green, and target proteins in blue.
950 These illustrations were originally published by Maidorn, Rizzoli & Opazo in the
951 Biochemical Journal (2016, <https://doi.org/10.1042/BCJ20160366>) [47], and were reproduced
952 with the kind permission of the authors and the publisher.

953

954 **Figure 3. Drift correction with beads as fiducial markers.**

955 **A.** Apparent drift in the X and Y directions of three beads that were attached to the coverslip
956 (red, green and blue traces). The bright green trace represents the average drift of the three
957 beads that is used for correction, calculated with a sliding window of 500 frames.

958 **B.** Projection of the detection coordinates of the three beads before drift correction (left
959 panels) and bead #3 after drift correction (right). Note that the lateral drift of the beads can
960 differ; bead #1 is lost after frame 16000, and #2 is less bright and therefore has lower
961 localization precision.

962

963 **Figure 4. dSTORM microscope setup with its main components.**

964 The lasers are collimated in an external platform and controlled with an acousto-optic tunable
965 filter (AOTF) that sets the illumination intensity and temporal sequence. The laser beam is
966 expanded within the total internal reflection fluorescence (TIRF) arm that focuses the light on
967 the back focal plane of the objective and also controls the inclination angle of the excitation
968 light. The emission light from the fluorophores on the sample coverslip is captured with an
969 EMCCD camera. This illustration was kindly provided by Ignacio Izeddin (ESPCI, Paris).

970

971 **Figure 5. Determining the optimal length of dSTORM recordings.**

972 **A.** Long dSTORM recordings of 30000 frames were acquired under optimized imaging
973 conditions until there were few remaining blinking events from GlyRs labeled with Alexa 647
974 (GlyR-A647). The reconstructed GlyR clusters from independent substacks of 10000 frames
975 were compared to define the ideal length of recording. The good agreement between the three
976 substacks indicates that 10000 frames are sufficient to reconstruct the synaptic clusters with
977 Alexa 647 fluorophores.

978 **B.** For Cy3B-labeled gephyrin clusters, the first two substacks were similar and matched the
979 reconstructed image of the entire stack (40000 frames), however, the third substack showed
980 incomplete sampling. To ensure sufficient detections of Cy3B signals, we determined an
981 optimal imaging length of 30000 frames for this channel. Yellow boxes show the masks of
982 individual synaptic clusters produced from the epifluorescence images. Scale: 500 nm.

983

984 **Figure 6. Strategies for evaluating the quality of dSTORM imaging.**

985 **A.** Blinking properties of the dyes: dSTORM imaging was done on sparsely distributed
986 secondary antibodies coupled with Alexa 647 (A647-IgG) or Cy3B (Cy3B-IgG). We
987 observed a large variability in the number of detections per dye-coupled IgG, with clusters of
988 up to hundreds of detections (left graph). Representative time traces of single A647-IgG and
989 Cy3B-IgG detections in dSTORM show that the blinking of Alexa 647 is more dispersed than
990 that of Cy3B (top right: the upper boxes show the number of detections per frame, the lower
991 boxes the cumulative detections). Dye-coupled IgGs produce apparent nanoclusters with
992 diameters ranging from 40 nm to 120 nm, as a result of multiple detections with limited
993 localization precision (bottom right panel).

994 **B.** Co-localization control: dSTORM imaging of GlyR clusters in spinal cord neurons (fixed
995 with 4% PFA) that were labeled with the same primary antibody and two different secondary
996 antibodies (GlyR-A647 and GlyR-Cy3B). Super-resolution clusters of GlyR detected with
997 Alexa 647 and Cy3B showed high level of spatial correlation tested by Pearson's coefficient
998 R (mean \pm SD: 0.52 ± 0.18) and ICQ (0.29 ± 0.07). GlyR sub-clusters were analyzed by H-
999 watershed segmentation (lower images). We observed a moderate positive correlation
1000 between the numbers of sub-clusters detected with Alexa 647 and Cy3B (middle panel: darker
1001 spots represent more synapses). The subcluster area was significantly larger when detected
1002 with Alexa 647 than with Cy3B (Kolmogorov-Smirnov test, $p < 0.0001$, $n = 180$ synapses

1003 with 767 subclusters for GlyR-A647 and 874 subclusters for GlyR-Cy3B, from two
1004 independent experiments). Scale: 200 nm.

1005 **C. Dye reversal experiment: two-color dSTORM imaging of gephyrin in spinal cord neurons**
1006 (fixed with cold methanol) that were labeled with two different primary antibodies against
1007 gephyrin, followed by two combinations of secondary antibodies. The antibody combination
1008 rbGPHN-Cy3B/m7a-A647 (n = 174 synapses) gave a significantly higher spatial correlation
1009 of gephyrin clusters in the two channels than the combination with reversed dyes (rbGPHN-
1010 A647/m7a-Cy3B, n = 148), as shown by Pearson's coefficient (Mann-Whitney U test, p =
1011 0.00262) and ICQ (p < 0.00001). Subcluster counts per synapse were systematically higher
1012 when clusters were detected with Cy3B than with Alexa 647 regardless of the primary
1013 antibodies (paired t-test, p < 0.0001 for both combinations, data are shown as mean ± SD).
1014 Subcluster areas detected by rbGPHN-A647 were significantly larger than by m7a-Cy3B
1015 (Kolmogorov-Smirnov test, p < 0.0001, n = 321 subclusters for rbGPHN-A647 and 403 for
1016 m7a-Cy3B), while the difference was not detected with the other antibody combination (p =
1017 0.425, n = 578 for rbGPHN-Cy3B and 504 for m7a-A647). Data were from three imaging
1018 experiments using two different spinal cord cultures. Scale: 100 nm.

1019

Fig. 1

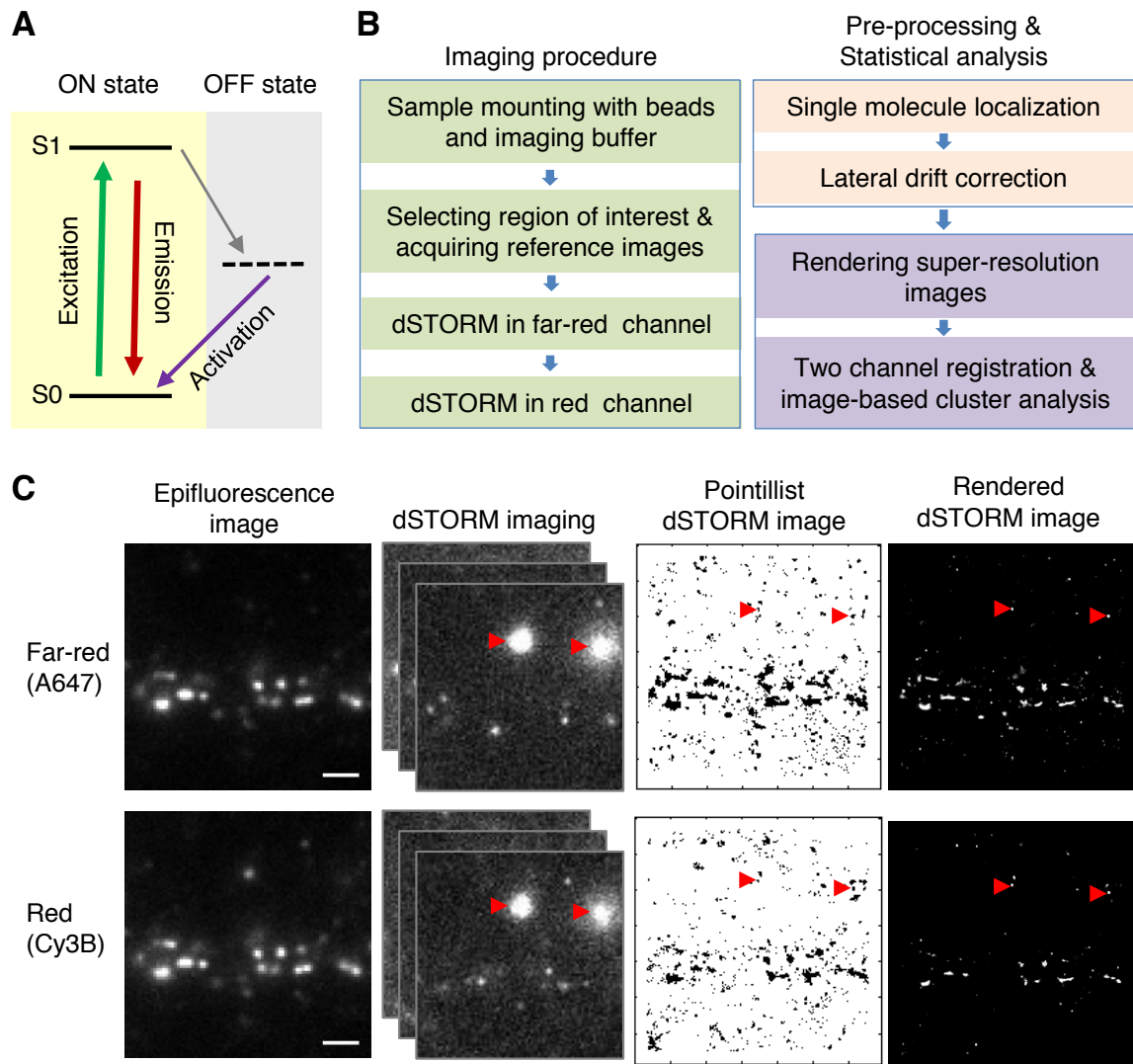
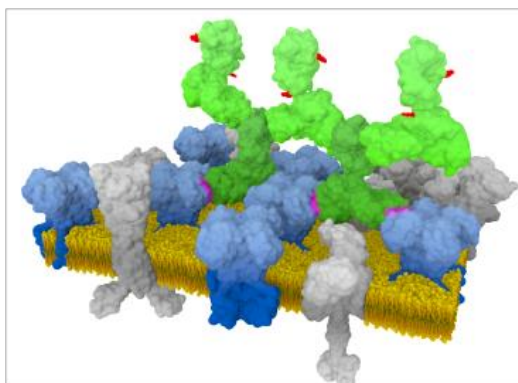


Fig. 2

A



B

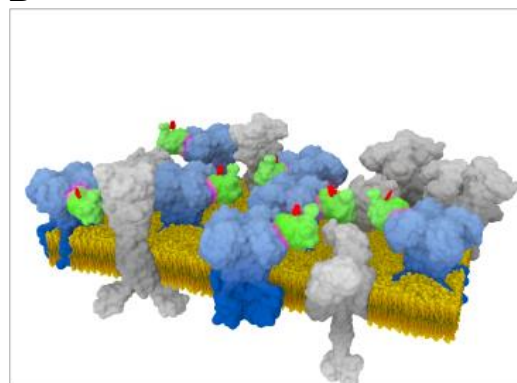


Fig. 3

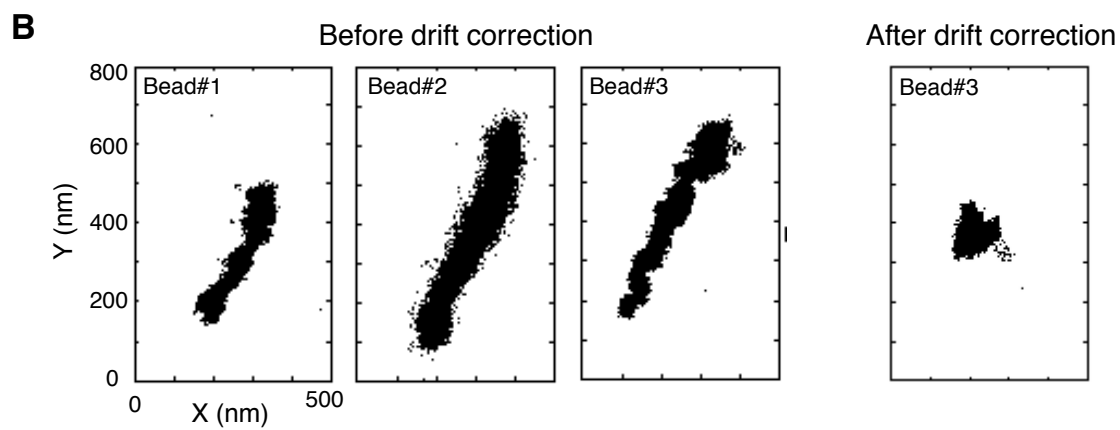
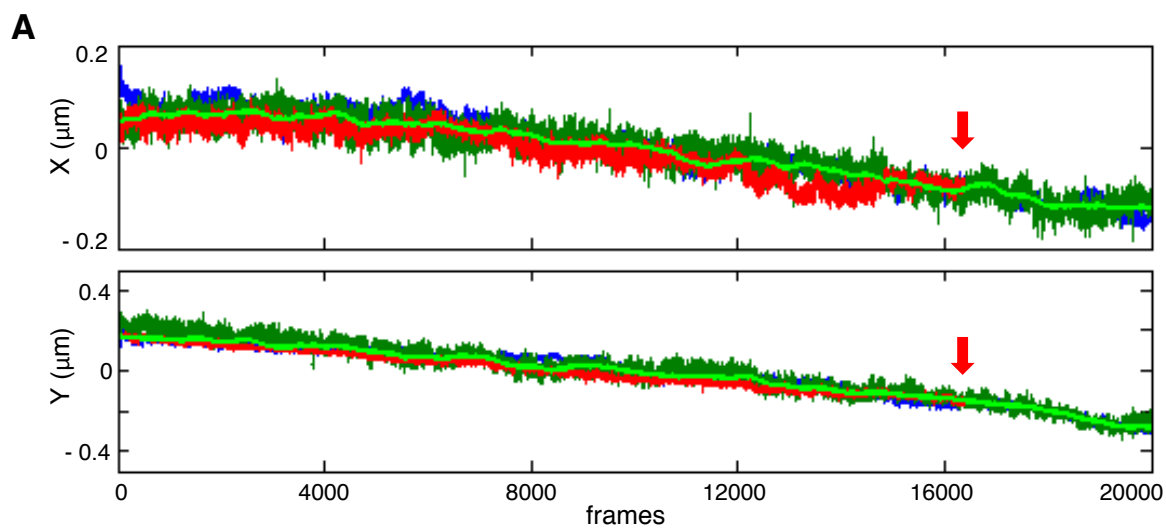


Fig. 4

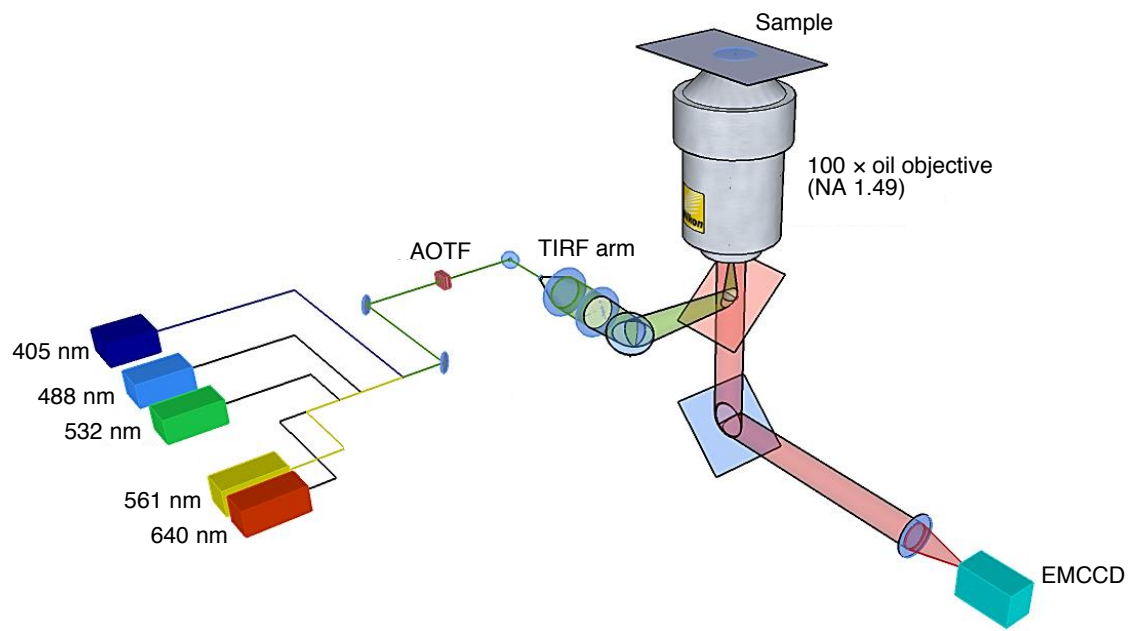


Fig. 5

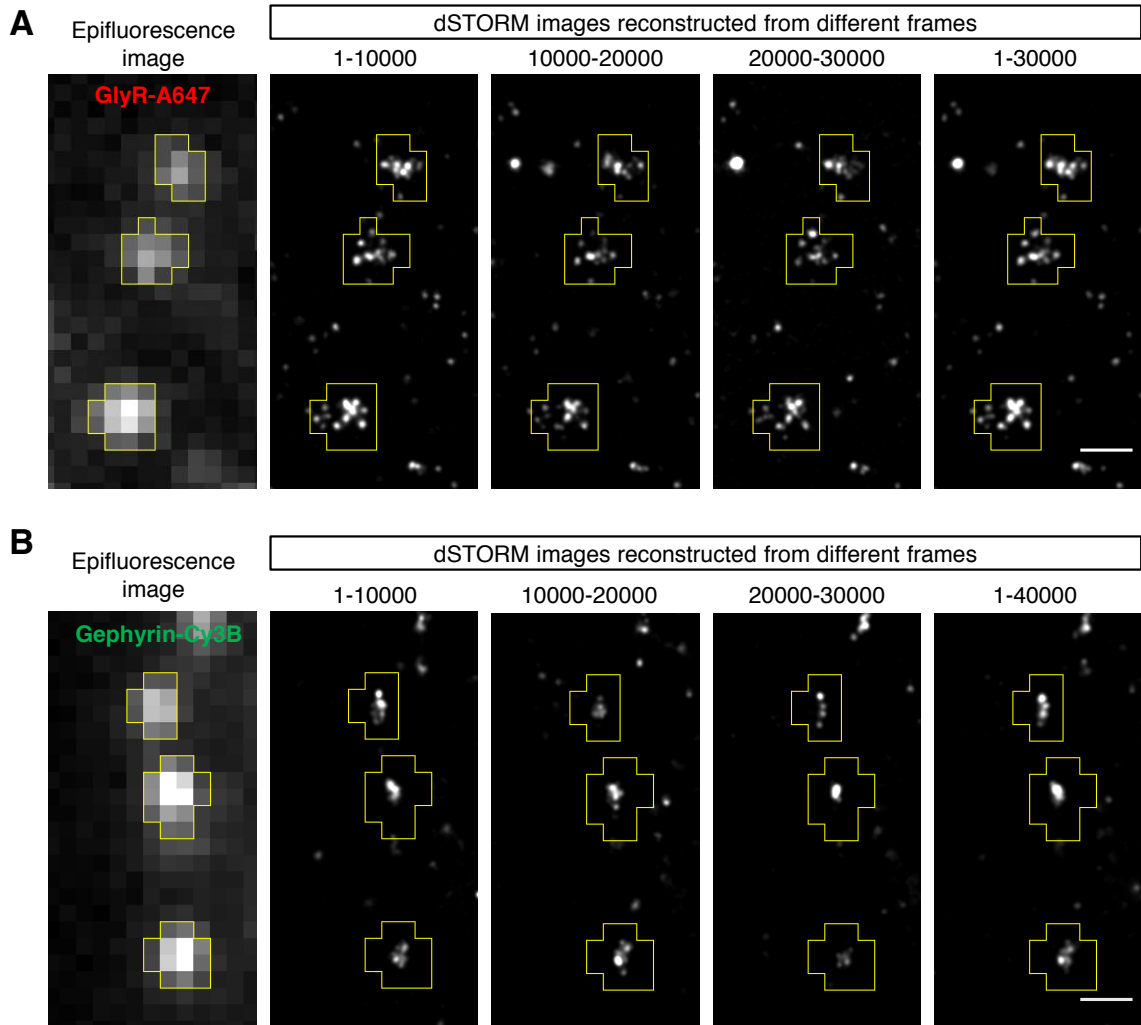
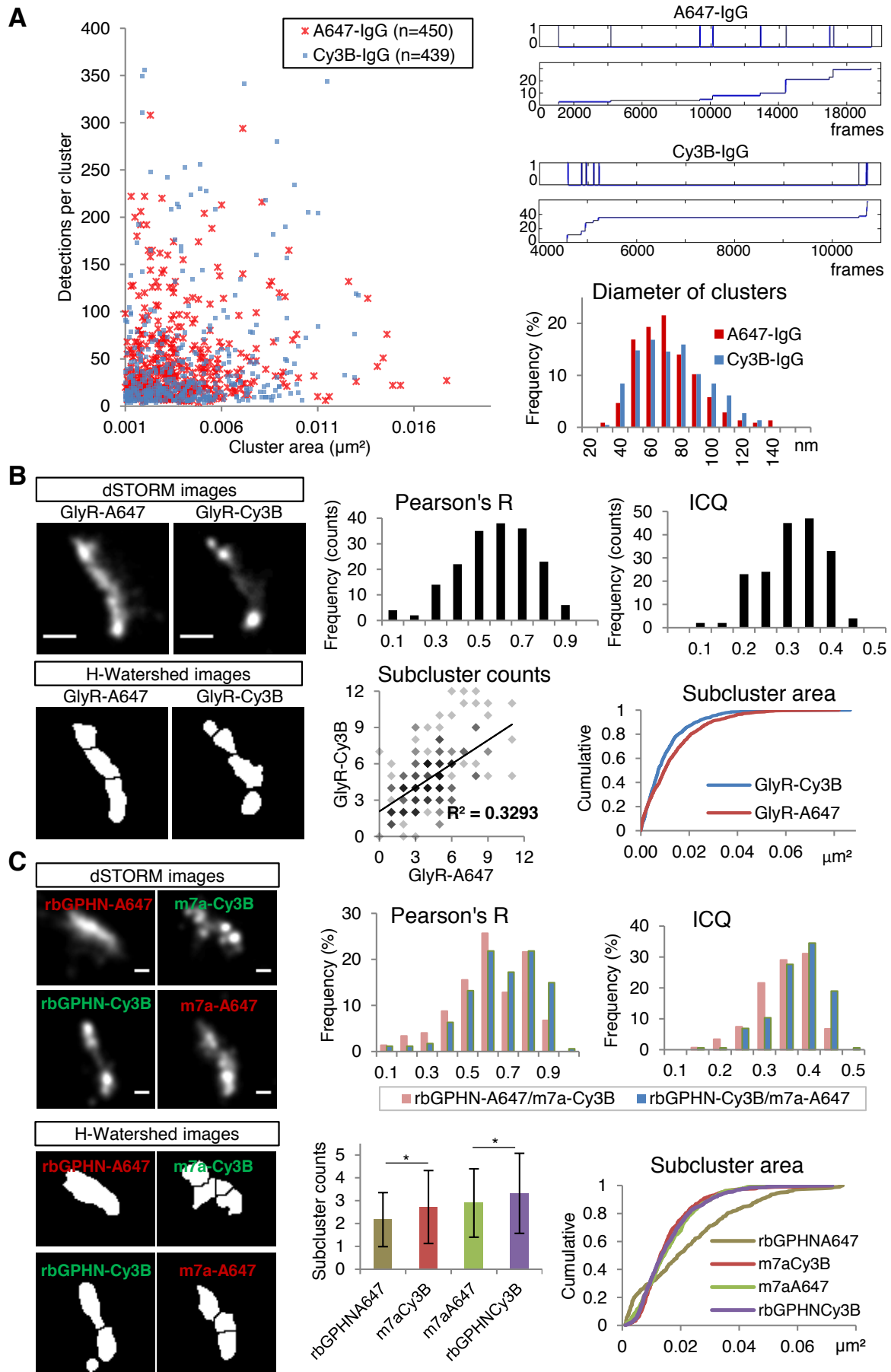


Fig. 6



Appendix 6. Yang and Specht 2019

Yang, X., & Specht, C. G. (2019). Subsynaptic Domains in Super-Resolution Microscopy: The Treachery of Images. *Frontiers in Molecular Neuroscience*, 12(July).



Subsynaptic Domains in Super-Resolution Microscopy: The Treachery of Images

Xiaojuan Yang and Christian G. Specht*

École Normale Supérieure, PSL Research University, CNRS, Inserm, Institute of Biology (IBENS), Paris, France

The application of super-resolution optical microscopy to investigating synaptic structures has revealed a highly heterogeneous and variable intra-synaptic organization. Dense subsynaptic protein assemblies named subsynaptic domains or SSDs have been proposed as structural units that regulate the efficacy of neuronal transmission. However, an in-depth characterization of SSDs has been hampered by technical limitations of super-resolution microscopy of synapses, namely the stochasticity of the signals during the imaging procedures and the variability of the synaptic structures. Here, we synthesize the available evidence for the existence of SSDs at central synapses, as well as the possible functional relevance of SSDs. In particular, we discuss the possible regulation of co-transmission at mixed inhibitory synapses as a consequence of the subsynaptic distribution of glycine receptors (GlyRs) and GABA_A receptors (GABA_ARs).

LAY ABSTRACT

Super-resolution imaging strategies bypass the resolution limit of conventional optical microscopy and have given new insights into the distribution of proteins at synapses in the central nervous system. Neurotransmitter receptors and scaffold proteins appear to occupy specialized locations within synapses that we refer to as subsynaptic domains or SSDs. Interestingly, these SSDs are highly dynamic and their formation seems to be related to the remodeling of synapses during synaptic plasticity. It was also shown that SSDs of pre- and post-synaptic proteins are aligned in so-called nanocolumns, highlighting the role of SSDs in the regulation of synaptic transmission. Despite recent advances, however, the detection of SSDs with super-resolution microscopy remains difficult due to the inherent technical limitations of these approaches that are discussed in this review article.

Keywords: subsynaptic domain (SSD), super-resolution microscopy, single molecule localization microscopy (SMLM), inhibitory receptors, gephyrin

OPEN ACCESS

Edited by:

Andrea Barberis,
Istituto Italiano di Tecnologia, Italy

Reviewed by:

Carlos B. Duarte,
University of Coimbra, Portugal
Josef Kittler,
University College London,
United Kingdom

*Correspondence:

Christian G. Specht
christian.specht@inserm.fr

Received: 13 April 2019

Accepted: 12 June 2019

Published: 02 July 2019

Citation:

Yang X and Specht CG
(2019) Subsynaptic Domains in
Super-Resolution Microscopy: The
Treachery of Images.
Front. Mol. Neurosci. 12:161.
doi: 10.3389/fnmol.2019.00161

INTRODUCTION

Single molecule localization microscopy (SMLM) bypasses the diffraction limit by detecting signals from a sparse subset of molecules that are temporally separated, thus achieving a spatial resolution of single molecules of 10–40 nm (Schermerle et al., 2010; Turkowyd et al., 2016; Sieben et al., 2018). SMLM includes several related techniques, namely STORM, PALM and uPAINT (Betzig et al., 2006; Hess et al., 2006; Rust et al., 2006; Giannone et al., 2010).

In 2010, Dani et al. (2010) measured the laminar distribution of synaptic proteins using multicolor three-dimensional (3D) STORM, demonstrating the capability of SMLM to visualize the ultra-structure of synapses (Specht et al., 2014). This marks the beginning of super-resolution optical imaging of synaptic structures. Numerous studies have since applied SMLM to explore the heterogeneity and complexity of protein assemblies at synapses. Another type of super-resolution optical microscopy achieves sub-diffraction resolution by means of structured excitation, such as stimulated emission depletion (STED; Klar et al., 2000) and structured illumination microscopy (SIM; Gustafsson, 2000). Regardless of the different working principles, super-resolution microscopy techniques have yielded significant insights into the distribution of synaptic proteins on the nanometer scale. Given their wide-field, volumetric imaging strategies, three-dimensional and quantitative information can be gained from a large sample size.

In 2013, several groups reported independently that different synaptic proteins are distributed heterogeneously at synapses (MacGillavry et al., 2013; Nair et al., 2013; Specht et al., 2013). SMLM images showed that the excitatory scaffold protein PSD-95 occupies subdomains within the post-synaptic density (PSD) that regulate AMPAR clustering (MacGillavry et al., 2013; Nair et al., 2013). The existence of PSD-95 subdomains was confirmed with STED microscopy both *in vitro* and *in vivo* (Broadhead et al., 2016; Dzyubenko et al., 2016; Hruska et al., 2018; Masch et al., 2018; Wegner et al., 2018). Likewise, subsynaptic domains of gephyrin were shown to play a role in inhibitory plasticity at GABAergic synapses (Pennacchietti et al., 2017; Crosby et al., 2019). These findings point towards a mechanism whereby subsynaptic domains drive the recruitment of neurotransmitter receptors to specific locations within the PSD, thus regulating synaptic transmission.

SMLM and STED microscopy have also shown that pre-synaptic proteins of the active zone (AZ) and synaptic adhesion proteins display subsynaptic distributions (Perez de Arce et al., 2015; Chamma et al., 2016a,b; Tang et al., 2016; Glebov et al., 2017; Haas et al., 2018). Using multicolor 3D-STORM, Tang et al. (2016) demonstrated that subsynaptic domains of RIM1/2 are aligned with those of PSD-95, an arrangement that is referred to as trans-synaptic nanocolumn. The alignment of pre- and post-synaptic elements appears to be due to neuroligin/neurexin adhesion complexes (Perez de Arce et al., 2015; Haas et al., 2018). These exciting observations not only demonstrate the power of SMLM to visualize the ultra-structures of synapses but also point towards possible roles of subsynaptic domains in synaptic function (reviewed in Biederer et al., 2017; Liu et al., 2017; Chen et al., 2018; Scheefhals and MacGillavry, 2018).

Despite these advances, the concept of subsynaptic domains remains ambiguous, not least because the technical and biological limitations in identifying subsynaptic domains have not been sufficiently scrutinized. Here, we review the available evidence for the existence of subsynaptic domains, highlighting the factors that need to be taken into account in detecting small protein assemblies using SMLM. We then discuss the possible role of subsynaptic domains in the regulation of glycinergic

and GABAergic co-transmission based on recent data from inhibitory synapses.

WHAT IS A SUBSYNAPTIC DOMAIN?

Terminology and Definition

A major source of confusion is that different names have been used in the literature to describe subsynaptic domains. Among these, the terms nanodomain, nanocluster, subcluster, subdomain and nanomodule have been used in an interchangeable manner (e.g., MacGillavry et al., 2013; Nair et al., 2013; Broadhead et al., 2016; Haas et al., 2018; Hruska et al., 2018). The lack of a clear and unified terminology has made it difficult to refer to specific molecular structures and to be aware of the differences and similarities between studies. Regarding the choice of words, the term *cluster* should best be avoided, because it can also refer to the clustering algorithms that are widely used for image analysis of SMLM data (Nicovich et al., 2017). The prefix *nano* is redundant because synapses themselves have diameters of only a few hundred nanometers. Furthermore, *nanodomain* has been widely used to describe the high Ca^{2+} ion concentrations in the proximity of an open calcium channel (Augustine et al., 2003; Eggermann et al., 2013; Ghelani and Sigrist, 2018).

We, therefore, refer to these structures as *subsynaptic domain* or *SSD* (Crosby et al., 2019) for the following reasons: (1) the term is self-explanatory, referring to a space that is smaller than the whole synaptic compartment and that is occupied by a given type of molecules; and (2) it is flexible in that it can be equally applied to membrane receptors, scaffold and signaling proteins, whether they are pre-synaptic or post-synaptic. We define SSD as a sub-compartment of the synapse in which the density of a specific synaptic protein is higher than in the surrounding area, and that is typically observed with super-resolution microscopy. We believe that the term SSD could thus provide some clarity in defining specific molecular entities at synapses.

SSD Size and Protein Copy Numbers

The most basic feature of SSDs that holds biologically relevant information is their size and the copy number of proteins that they contain. A wide range of sizes was detected by SMLM and STED microscopy (**Table 1**). For instance, SSDs of excitatory scaffold proteins in cultured hippocampal neurons have a diameter of ~ 80 nm as judged by coordinate-based SMLM analysis (MacGillavry et al., 2013), whereas an average diameter of 120 nm was measured in reconstructed super-resolution images (Nair et al., 2013). STED microscopy detected SSDs of PSD-95 with a diameter of 200 nm (Fukata et al., 2013). These differences in SSD size are likely due to the different resolution of the imaging systems and the application of a threshold during image processing. A comparative study of PSD-95 in hippocampal tissue using PALM and STED determined median SSD diameters of 126 nm and 158 nm, respectively, exemplifying the impact of the imaging approach (Broadhead et al., 2016). The typical diameter of the whole PSD in hippocampal neurons ranges from 100 nm to 800 nm, with a mean of about 300 nm (Harris and Stevens, 1989; Arellano et al., 2007). Therefore, the

lower limit of SSD sizes of ~50 nm reflects the image resolution of the super-resolution imaging techniques, while the upper limit corresponds to the size of the entire synapse. Given that synapse sizes vary substantially across the central nervous system, an interesting question is whether SSDs of different synaptic proteins have stereotypical sizes that are the same at different types of synapses (see Crosby et al., 2019).

Information about protein copy numbers is essential to establish the structural basis of SSD formation. To date, there are hardly any quantitative data about SSD molecule numbers. SSDs of AMPARs have been estimated to contain an average of ~20 receptor complexes (Nair et al., 2013). Due to the limited accessibility of the epitopes for immunolabeling, however, the actual number of receptors per SSD could be higher. This could have an effect on the role of SSDs in synaptic function since the number of active receptors is directly related to the strength of synaptic transmission (Masugi-Tokita et al., 2007; Tarusawa et al., 2009; Fukazawa and Shigemoto, 2012).

Number of SSDs Per Synapse

Most synapses contain only one SSD or no SSD at all. More specifically, a single SSD was detected in 50% to 80% of synapses imaged with SMLM, SIM or STED microscopy, less than 20% had more than three SSDs, and six SSDs was the upper limit (MacGillavry et al., 2013; Nair et al., 2013; Broadhead et al., 2016; Chamma et al., 2016a,b; Pennacchiotti et al., 2017; Hruska et al., 2018; Crosby et al., 2019). It is likely that the different imaging techniques and analyses again have an effect on the detection of multiple SSDs. This raises the question whether the SSD simply reflects the center of mass of the protein assembly, and if so, whether the presence of single or multiple SSDs actually matter for the regulation of synaptic function.

There exists a positive correlation between the number of SSDs and the size of the PSD or the dendritic spine (Fukata et al., 2013; Nair et al., 2013; Hruska et al., 2018; Crosby et al., 2019). EM studies have revealed a large variability in PSD area, ranging from 100 nm to 800 nm in diameter (Table 1). More than half of the PSDs are small (<0.05 μm²), which is similar to the fraction of synapses with only one SSD (Arellano et al., 2007). Moreover, the number of AMPAR molecules is positively correlated with the PSD size, and large complex PSDs have a higher density of AMPARs than small, non-perforated PSDs (Ganeshina et al., 2004; Shinohara et al., 2008; Fukazawa and Shigemoto, 2012). Together, these data indicate that SSDs may only play a role at large PSDs, reflecting the superior strength of these synapses.

Trans-synaptic Nanocolumns

From the viewpoint of neuron connectivity, pre-synaptic and post-synaptic SSDs can be aligned to form trans-synaptic structural units that regulate synaptic function (Biederer et al., 2017; Chen et al., 2018). Such an organization has been observed at excitatory synapses using 3D-SMLM, and was suitably named *trans-synaptic nanocolumn* (Tang et al., 2016). SMLM studies have further shown that synaptic adhesion complexes such as neuroligin and neurexin are also organized in SSDs, suggesting that they contribute to the formation of trans-synaptic nanocolumns (Perez de Arce et al., 2015; Haas et al., 2018). The

TABLE 1 | Size and protein copy numbers of SSDs and PSDs obtained with different experimental techniques.

Structure	Diameter (nm)	Molecule numbers	Technique	Synapse type	References
SSD	50–130*		SMLM	Excitatory, hippocampal	MacGillavry et al. (2013), Nair et al. (2013), Broadhead et al. (2016), Chamma et al. (2016a,b) and Haas et al. (2018)
	130–760*		STED	Excitatory, hippocampal and cortical	Nair et al. (2013), Broadhead et al. (2016) and Hruska et al. (2018)
	~300*		SIM	Inhibitory, hippocampal	Crosby et al. (2019)
	70*	~20 AMPARs/SSD*	STORM	Excitatory, hippocampal	Nair et al. (2013)
PSD	300 (100–800)#		EM	Excitatory, hippocampal	Harris and Stevens (1989) and Bourne and Harris (2011)
	290 (110–650)#		EM	Excitatory, cortical	Arellano et al. (2007) and Santuy et al. (2018)
	350 (110–700)#		EM	Inhibitory, hippocampal and cortical	Bourne and Harris (2011) and Santuy et al. (2018)
		50 (0–200) AMPARs#	EM	Excitatory, various CNS regions	Masugi-Tokita et al. (2007), Tarusawa et al. (2009) and Fukazawa and Shigemoto (2012)
		30 (0–200) GABA _A Rs#	Electrophysiology, EM	Inhibitory, cerebellar and hippocampal	Nusser et al. (1997, 1998)
		30 (40–500) PSD-95#	Biochemistry, TIRF microscopy	Excitatory, various brain regions	Sugiyama et al. (2005) and Sheng and Kim (2011)
		30 (40–500) Gephyrin#	SMLM (decay recordings)	Inhibitory, spinal cord	Specht et al. (2013) and Patrizio et al. (2017)

*Mean values obtained in the cited studies; # mean (range in brackets). Values were taken directly or calculated from those reported in the cited studies.

term nanocolumn, therefore, refers to a specific concept, namely the alignment of pre- and post-synaptic SSDs that brings together different functional elements. Future studies are expected to explore the possible role of nanocolumns in synaptic plasticity.

The Dynamics of SSDs

The hypothesis that SSDs regulate synaptic transmission implies that SSDs adapt dynamically to changes in synaptic strength. Indeed, live SMLM in cultured neurons has revealed the mobility and morphological changes of SSDs. Synaptic scaffolds undergo dynamic changes on a timescale of 5–10 min, displaying marked differences in the number, position and shape of SSDs at different time points (Nair et al., 2013; Specht et al., 2013; Rodriguez et al., 2017). STED microscopy further showed that these morphological changes occurred both *in vitro* and *in vivo* (Hruska et al., 2018; Wegner et al., 2018). The dynamics of SSDs are in agreement with the exchange of individual proteins at synaptic and extra-synaptic sites, which is a hallmark of the dynamic synapse (Choquet and Triller, 2013; Delgado and Selvin, 2018). Therefore, SSDs are momentary representations of the protein distribution and need to be viewed as dynamic snapshots rather than rigid structural units.

HOW TO DETECT SUBSYNAPTIC DOMAINS WITH SMLM

The identification of SSDs consists in detecting small numbers of densely packed molecules in a confined space with a high local background from neighboring molecules with lower density. Despite these challenges, SMLM is well suited to resolve the internal organization of small structures such as synapses at single molecule level. In the following, we discuss the relevant factors of the image acquisition and data analysis that have an impact on the identification of SSDs.

Image Acquisition

SMLM techniques aim to record large numbers of single fluorophore detections from densely labeled structures, while ensuring that the signals are sufficiently sparse to be well separated. STORM, PALM and uPAINT have all been employed for detecting SSDs. The three techniques have the same intrinsic challenges when it comes to the ultrastructure of synapses, chief among them being the fluorophore. Most fluorophores are detected repeatedly due to their fluorescence lifetime, photo-switching and blinking. This can create dense clusters of redundant detections that are easily mistaken for SSDs. The blinking behavior of the fluorophores (organic dyes or fluorescent proteins) is dependent on their photo-physical and photo-chemical properties, and it can be modulated by the laser power and the composition of the imaging buffer (Dempsey et al., 2011; Endesfelder et al., 2011; van de Linde et al., 2011; Nahidiazar et al., 2016). Sub-optimal imaging conditions such as inefficient laser illumination or an incompatible buffer system can result in artificial clustering (Annibale et al., 2011; Burgert et al., 2015; Nahidiazar et al., 2016). Even with an optimized imaging protocol, different fluorophores will produce different representations of the analyzed structure (Dempsey

et al., 2011; Baddeley and Bewersdorf, 2018). The evaluation of the number and the size of SSDs is therefore strongly dependent on the fluorophores, and control experiments with different fluorophores are crucial to validate the experimental findings (Yang and Specht, in press). In addition to the fluorophores, attention should also be drawn to the labeling strategies used for sample preparation. The distance between the fluorophores and the actual positions of the target molecules (e.g., due to the size of antibodies used for labeling), and under-sampling due to a limited labeling efficiency can add to the uncertainties in the identification of SSDs (Deschout et al., 2014; Maidorn et al., 2016).

Image Segmentation

Depending on the type of SMLM data (pointillist or reconstructed super-resolution images), different algorithms have been adopted for segmenting SSDs. For coordinates-based data, a local density threshold is generally applied. The local density can for instance be defined as the number of detections within a radius of five times the mean nearest neighbor distance of all the detections within each synapse, and SSDs are identified as regions above a certain threshold (MacGillivray et al., 2013; Tang et al., 2016; Pennacchiotti et al., 2017). As regards the reconstructed images, an intensity threshold may be adopted instead. For example, wavelet segmentation has been used to identify SSDs at synapses in the whole field of view (Nair et al., 2013; Chamma et al., 2016a,b). Similarly, watershed segmentation can be employed to segment SSDs of individual synapses in reconstructed SMLM images or deconvoluted STED images (Broadhead et al., 2016; Dzyubenko et al., 2016). The difficulty of all these approaches is that the detected size and the number of SSDs are directly dependent on the algorithms and the chosen parameters, which makes an accurate identification of SSDs challenging.

Dealing With Small Molecule Numbers and the Variability of Synapses

Synapses exhibit a large variability not only in size but also in terms of molecule numbers. Neurotransmitter receptors such as AMPARs or GABA_ARs have relatively low copy numbers, with an average of ~50 receptor complexes per synapse (ranging up to 200 copies; **Table 1**). The main scaffold proteins at excitatory and inhibitory synapses outnumber the receptors by a factor of four to five. PSD-95 and gephyrin molecules amount to 40–500 per synapse, with an average of ~300 copies (Sugiyama et al., 2005; Sheng and Kim, 2011; Specht et al., 2013; Patrizio et al., 2017). The low copy numbers of synaptic proteins, especially receptors, makes the identification of SSDs with SMLM challenging since the labeling of the structures is often rather faint. At the same time, the high local density of synaptic proteins can further reduce the efficiency of immunolabeling due to epitope masking. The overall receptor density at synapses is in the order of 700 AMPARs/ μm^2 for the whole PSD (50 AMPARs/ $0.07 \mu\text{m}^2$). An average SSD with a diameter of 70 nm (area of $0.0038 \mu\text{m}^2$) contains about 20 AMPARs, resulting in an estimated density of ~5,000 AMPAR complexes/ μm^2 (Nair et al., 2013). Considering the molecular size of the receptor complexes (10 nm × 20 nm;

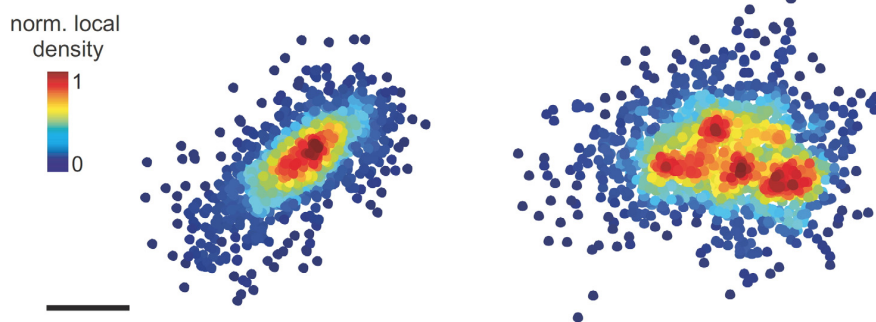


FIGURE 1 | Pointillist images showing synaptic gephyrin clusters with one SSD (left) or four SSDs (right). The points represent the detections of single fluorophores from PALM imaging. Scale bar: 100 nm (adapted with permission from Pennacchietti et al., 2017).

Patriarchi et al., 2018), 20 AMPARs would occupy a membrane area of at least $0.004 \mu\text{m}^2$. This means that the receptors are very densely packed inside the SSD, adding to the uncertainties that result from the stochasticity of the immunolabeling and fluorophore detection.

Alternative Approaches

Given the rapid advances in super-resolution imaging technologies, promising alternatives for the investigation of complex structures such as synapses are quickly emerging. Among these, smaller probes such as nanobodies have been produced to bypass the limitations of labeling density and to minimize the distance between the fluorophores and the target proteins (Chamma et al., 2016a; Maidorn et al., 2016). DNA-PAINT allows multi-color SMLM imaging (Nieves et al., 2018). DNA origami standards provide a more precise way for calibrating protein copy numbers given that the absolute quantification of molecules at SSDs is faced with large stochasticity of the imaging technique (Zanacchi et al., 2017). Furthermore, new algorithms are being developed to segment synaptic clusters in coordinates-based datasets more efficiently (Nicovich et al., 2017; Baddeley and Bewersdorf, 2018).

THE EMERGING ROLE OF SSDs IN INHIBITORY SYNAPTIC TRANSMISSION

Electron microscopy of symmetric synapses has revealed a discontinuous network of filaments at the inhibitory PSD and in the synaptic cleft (Linsalata et al., 2014; High et al., 2015). Super-resolution optical microscopy confirmed that the inhibitory scaffold protein gephyrin forms synaptic clusters of variable morphology that can undergo dynamic changes and may contain SSDs (Specht et al., 2013; Dzyubenko et al., 2016; Pennacchietti et al., 2017; Crosby et al., 2019). SMLM imaging in cultured hippocampal neurons further revealed that extra-synaptic gephyrin molecules are recruited to synaptic sites during NMDA-induced inhibitory long-term potentiation (Pennacchietti et al., 2017). The increase in molecule density was accompanied by an increased fraction of gephyrin clusters with multiple SSDs (Figure 1). More recently, Crosby et al. (2019) conducted a comprehensive analysis of pre- and postsynaptic

components using 3D-SIM, reaching a resolution of ~ 120 nm laterally and ~ 300 nm axially. It was shown that GABA_ARs form SSDs with an average diameter of ~ 300 nm that are closely associated with SSDs of gephyrin and pre-synaptic RIM (Crosby et al., 2019). This implies the existence of trans-synaptic nanocolumns as an organizing principle of inhibitory synapses. Given that the measured size of the SSDs was close to the resolution limit, the concept of nanocolumns at inhibitory synapses will require further validation. Nonetheless, these studies strongly suggest that the internal organization of inhibitory synapses plays an important role in regulating synaptic transmission.

Unlike the cortex and hippocampus where fast neuronal inhibition is mainly mediated by GABA_ARs, both glycine and GABA receptors coexist at synapses in the brainstem and the spinal cord. Gephyrin provides binding sites for the immobilization of both types of receptor (reviewed in Choi and Ko, 2015; Alvarez, 2017; Groeneweg et al., 2018; Specht, 2019). Several GABA_AR subunits bind to gephyrin, albeit with a lower affinity than the GlyR β subunit (e.g., Maric et al., 2011; Kowalczyk et al., 2013). We do not yet know whether GlyRs and GABA_ARs form SSDs at mixed synapses, and if so, how they are related to the SSDs of gephyrin. Mixed inhibitory synapses are activated by the co-release of glycine and GABA from presynaptic vesicles (Jonas et al., 1998; Aubrey and Supplisson, 2018). This creates a situation, where the exact position of GlyRs and GABA_ARs relative to the pre-synaptic release site can have a strong impact on the efficacy of the agonists and thus the activity of the receptors. Through its capacity to resolve the spatial organization of mixed inhibitory synapses, SMLM may provide answers to these open questions.

OUTLOOK

The concept of SSDs as dynamic units underlying synaptic strength provides a new angle to interpret the function of synapses. SMLM and other super-resolution imaging techniques are powerful tools to investigate the internal organization of synapses. Given the intrinsic stochasticity of SMLM and the inherent variability of synaptic protein assemblies, however, the identification and characterization of SSDs demand great

scrutiny in the experimental and analytical procedures. Super-resolution techniques may still have some way to go before we can truly resolve the fast molecular processes at synapses.

AUTHOR CONTRIBUTIONS

All authors listed have made a substantial, direct and intellectual contribution to the work, and approved it for publication.

REFERENCES

- Alvarez, F. J. (2017). Gephyrin and the regulation of synaptic strength and dynamics at glycinergic inhibitory synapses. *Brain Res. Bull.* 129, 50–65. doi: 10.1016/j.brainresbull.2016.09.003
- Annibale, P., Vanni, S., Scarselli, M., Rothlisberger, U., and Radenovic, A. (2011). Identification of clustering artifacts in photoactivated localization microscopy. *Nat. Methods* 8, 527–528. doi: 10.1038/nmeth.1627
- Arellano, J. I., Benavides-Piccione, R., DeFelipe, J., and Yuste, R. (2007). Ultrastructure of dendritic spines: correlation between synaptic and spine morphologies. *Front. Neurosci.* 1, 131–143. doi: 10.3389/neuro.01.1.1.010.2007
- Aubrey, K. R., and Supplisson, S. (2018). Heterogeneous signaling at GABA and glycine co-releasing terminals. *Front. Synaptic Neurosci.* 10:40. doi: 10.3389/fnsyn.2018.00040
- Augustine, G. J., Santamaria, F., and Tanaka, K. (2003). Local calcium signaling in neurons. *Neuron* 40, 331–346. doi: 10.1016/s0896-6273(03)00639-1
- Baddeley, D., and Bewersdorf, J. (2018). Biological insight from super-resolution microscopy: what we can learn from localization-based images. *Annu. Rev. Biochem.* 87, 965–989. doi: 10.1146/annurev-biochem-060815-014801
- Betzig, E., Patterson, G. H., Sougrat, R., Lindwasser, O. W., Olenych, S., Bonifacino, J. S., et al. (2006). Imaging intracellular fluorescent proteins at nanometer resolution. *Science* 313, 1642–1645. doi: 10.1126/science.1127344
- Biederer, T., Kaeser, P. S., and Blanpied, T. A. (2017). Transcellular nanoalignment of synaptic function. *Neuron* 96, 680–696. doi: 10.1016/j.neuron.2017.10.006
- Bourne, J. N., and Harris, K. M. (2011). Coordination of size and number of excitatory and inhibitory synapses results in a balanced structural plasticity along mature hippocampal CA1 dendrites during LTP. *Hippocampus* 21, 354–373. doi: 10.1002/hipo.20768
- Broadhead, M. J., Horrocks, M. H., Zhu, F., Muresan, L., Benavides-Piccione, R., DeFelipe, J., et al. (2016). PSD95 nanoclusters are postsynaptic building blocks in hippocampus circuits. *Sci. Rep.* 6:24626. doi: 10.1038/srep24626
- Burgert, A., Letschert, S., Doose, S., and Sauer, M. (2015). Artifacts in single-molecule localization microscopy. *Histochem. Cell Biol.* 144, 123–131. doi: 10.1007/s00418-015-1340-4
- Chamma, I., Letellier, M., Butler, C., Tessier, B., Lim, K. H., Gauthereau, I., et al. (2016a). Mapping the dynamics and nanoscale organization of synaptic adhesion proteins using monomeric streptavidin. *Nat. Commun.* 7:10773. doi: 10.1038/ncomms10773
- Chamma, I., Levet, F., Sibarita, J.-B., Sainlos, M., and Thoumine, O. (2016b). Nanoscale organization of synaptic adhesion proteins revealed by single-molecule localization microscopy. *Neurophotonics* 3:041810. doi: 10.1117/1.nph.3.4.041810
- Chen, H., Tang, A. H., and Blanpied, T. A. (2018). Subsynaptic spatial organization as a regulator of synaptic strength and plasticity. *Curr. Opin. Neurobiol.* 51, 147–153. doi: 10.1016/j.conb.2018.05.004
- Choi, G., and Ko, J. (2015). Gephyrin: a central GABAergic synapse organizer. *Exp. Mol. Med.* 47:e158. doi: 10.1038/emmm.2015.5
- Choquet, D., and Triller, A. (2013). The dynamic synapse. *Neuron* 80, 691–703. doi: 10.1016/j.neuron.2013.10.013
- Crosby, K. C., Gookin, S. E., Garcia, J. D., Hahn, K. M., Dell'Acqua, M. L., and Smith, K. R. (2019). Nanoscale subsynaptic domains underlie the organization of the inhibitory synapse. *Cell Rep.* 26, 3284.e3–3297.e3. doi: 10.1016/j.celrep.2019.02.070

FUNDING

XY is supported by the China Scholarship Council (CSC).

ACKNOWLEDGMENTS

We thank Andrea Barberis (IIT, Genoa) for the permission to reproduce the pointillist image in **Figure 1**.

- Dani, A., Huang, B., Bergan, J., Dulac, C., and Zhuang, X. (2010). Super-resolution imaging of chemical synapses in the brain. *Neuron* 68, 843–856. doi: 10.1016/j.neuron.2010.11.021
- Delgado, J. Y., and Selvin, P. R. (2018). A revised view on the role of surface AMPAR mobility in tuning synaptic transmission: limitations, tools, and alternative views. *Front. Synaptic Neurosci.* 10:21. doi: 10.3389/fnsyn.2018.00021
- Dempsey, G. T., Vaughan, J. C., Chen, K. H., Bates, M., and Zhuang, X. (2011). Evaluation of fluorophores for optimal performance in localization-based super-resolution imaging. *Nat. Methods* 8, 1027–1036. doi: 10.1038/nmeth.1768
- Deschout, H., Cella Zanacchi, F., Mlodzianoski, M., Diaspro, A., Bewersdorf, J., Hess, S. T., et al. (2014). Precisely and accurately localizing single emitters in fluorescence microscopy. *Nat. Methods* 11, 253–266. doi: 10.1038/nmeth.2843
- Dzyubenko, E., Rozenberg, A., Hermann, D. M., and Faissner, A. (2016). Colocalization of synapse marker proteins evaluated by STED-microscopy reveals patterns of neuronal synapse distribution *in vitro*. *J. Neurosci. Methods* 273, 149–159. doi: 10.1016/j.jneumeth.2016.09.001
- Eggermann, E., Bucurenciu, I., Goswami, S. P., and Jonas, P. (2013). Europe PMC funders group nanodomain coupling between Ca²⁺ channels and sensors of exocytosis at fast mammalian synapses. *Nat. Rev. Neurosci.* 13, 7–21. doi: 10.1038/nrn3125
- Endesfelder, U., Malkusch, S., Flottmann, B., Mondry, J., Liguzinski, P., Verveer, P. J., et al. (2011). Chemically induced photoswitching of fluorescent probes—A general concept for super-resolution microscopy. *Molecules* 16, 3106–3118. doi: 10.3390/molecules16043106
- Fukata, Y., Dimitrov, A., Boncompain, G., Vilemeyer, O., Perez, F., and Fukata, M. (2013). Local palmitoylation cycles define activity-regulated postsynaptic subdomains. *J. Cell Biol.* 202, 145–161. doi: 10.1083/jcb.201302071
- Fukazawa, Y., and Shigemoto, R. (2012). Intra-synapse-type and inter-synapse-type relationships between synaptic size and AMPAR expression. *Curr. Opin. Neurobiol.* 22, 446–452. doi: 10.1016/j.conb.2012.01.006
- Ganeshina, O., Berry, R. W., Petralia, R. S., Nicholson, D. A., and Geinisman, Y. (2004). Synapses with a segmented, completely partitioned postsynaptic density express more AMPA receptors than other axospinous synaptic junctions. *Neuroscience* 125, 615–623. doi: 10.1016/j.neuroscience.2004.02.025
- Ghelani, T., and Sigrist, S. J. (2018). Coupling the structural and functional assembly of synaptic release sites. *Front. Neuroanat.* 12:81. doi: 10.3389/fnana.2018.00081
- Giannone, G., Hosy, E., Levet, F., Constals, A., Schulze, K., Sobolevsky, A. I., et al. (2010). Dynamic superresolution imaging of endogenous proteins on living cells at ultra-high density. *Biophys. J.* 99, 1303–1310. doi: 10.1016/j.bpj.2010.06.005
- Glebov, O. O., Jackson, R. E., Winterflood, C. M., Owen, D. M., Barker, E. A., Doherty, P., et al. (2017). Nanoscale structural plasticity of the active zone matrix modulates presynaptic function. *Cell Rep.* 18, 2715–2728. doi: 10.1016/j.celrep.2017.02.064
- Groeneweg, F. L., Trattig, C., Kuhse, J., Nawrotzki, R. A., and Kirsch, J. (2018). Gephyrin: a key regulatory protein of inhibitory synapses and beyond. *Histochem. Cell Biol.* 150, 489–508. doi: 10.1007/s00418-018-1725-2
- Gustafsson, M. G. L. (2000). Surpassing the lateral resolution limit by a factor of two using structured illumination microscopy. *J. Microsc.* 198, 82–87. doi: 10.1046/j.1365-2818.2000.00710.x
- Haas, K. T., Compans, B., Letellier, M., Bartol, T. M., Grillo-Bosch, D., Sejnowski, T. J., et al. (2018). Pre-post synaptic alignment through neuroligin-1

- tunes synaptic transmission efficiency. *ELife* 7:e31755. doi: 10.7554/elifelife.31755
- Harris, K. M., and Stevens, J. K. (1989). Dendritic spines of CA 1 pyramidal cells in the rat hippocampus serial electron microscopy with reference to their biophysical characteristics. *J. Neurosci.* 9, 2982–2997. doi: 10.1523/JNEUROSCI.09-08-02982.1989
- Hess, S. T., Girirajan, T. P. K., and Mason, M. D. (2006). Ultra-high resolution imaging by fluorescence photoactivation localization microscopy. *Biophys. J.* 91, 4256–4272. doi: 10.1529/biophysj.106.091116
- High, B., Cole, A. A., Chen, X., and Reese, T. S. (2015). Electron microscopic tomography reveals discrete transleft elements at excitatory and inhibitory synapses. *Front. Synaptic Neurosci.* 7:9. doi: 10.3389/fnsyn.2015.00009
- Hruska, M., Henderson, N., Le Marchand, S. J., Jafri, H., and Dalva, M. B. (2018). Synaptic nanomodules underlie the organization and plasticity of spine synapses. *Nat. Neurosci.* 21, 671–682. doi: 10.1038/s41593-018-0138-9
- Jonas, P., Bischofberger, J., and Sandkühler, J. (1998). Corelease of two fast neurotransmitters at a central synapse. *Science* 281, 419–424. doi: 10.1126/science.281.5375.419
- Klar, T. A., Jakobs, S., Dyba, M., Egner, A., and Hell, S. W. (2000). Fluorescence microscopy with diffraction resolution barrier broken by stimulated emission Physical Principles and Setup. *Proc. Natl. Acad. Sci. U S A* 97, 8206–8210. doi: 10.1073/pnas.97.15.8206
- Kowalczyk, S., Winkelmann, A., Smolinsky, B., Förstera, B., Neundorff, I., Schwarz, G., et al. (2013). Direct binding of GABA_A receptor β 2 and β 3 subunits to gephyrin. *Eur. J. Neurosci.* 37, 544–554. doi: 10.1111/ejn.12078
- Linsalata, A. E., Chen, X., Winters, C. A., and Reese, T. (2014). Electron tomography on γ -aminobutyric acid-ergic synapses reveals a discontinuous postsynaptic network of filaments. *J. Comp. Neurol.* 522, 921–936. doi: 10.1002/cne.23453
- Liu, K. K. L., Hagan, M. F., and Lisman, J. E. (2017). Gradation (approx. 10 size states) of synaptic strength by quantal addition of structural modules. *Philos. Trans. R. Soc. B Biol. Sci.* 372:20160328. doi: 10.1098/rstb.2016.0328
- MacGillavry, H. D., Song, Y., Raghavachari, S., and Blanpied, T. A. (2013). Nanoscale scaffolding domains within the postsynaptic density concentrate synaptic ampa receptors. *Neuron* 78, 615–622. doi: 10.1016/j.neuron.2013.03.009
- Maidorn, M., Rizzoli, S. O., and Opazo, F. (2016). Tools and limitations to study the molecular composition of synapses by fluorescence microscopy. *Biochem. J.* 473, 3385–3399. doi: 10.1042/bcj20160366
- Maric, H., Mukherjee, J., Tretter, V., Moss, S. J., and Schindelin, H. (2011). Gephyrin-mediated γ -aminobutyric acid type A and glycine receptor clustering relies on a common binding site. *J. Biol. Chem.* 286, 42105–42114. doi: 10.1074/jbc.M111.303412
- Masch, J.-M., Steffens, H., Fischer, J., Engelhardt, J., Hubrich, J., Keller-Findeisen, J., et al. (2018). Robust nanoscopy of a synaptic protein in living mice by organic-fluorophore labeling. *Proc. Natl. Acad. Sci. U S A* 115, E8047–E8056. doi: 10.1073/pnas.1807104115
- Masugi-Tokita, M., Tarusawa, E., Watanabe, M., Molnár, E., Fujimoto, K., and Shigemoto, R. (2007). Number and density of AMPA receptors in individual synapses in the rat cerebellum as revealed by SDS-digested freeze-fracture replica labeling. *J. Neurosci.* 27, 2135–2144. doi: 10.1523/JNEUROSCI.2861-06.2007
- Nahidiazar, L., Agronskaia, A. V., Broertjes, J., van den Broek, B., and Jalink, K. (2016). Optimizing imaging conditions for demanding multi-color super resolution localization microscopy. *PLoS One* 11:e0158884. doi: 10.1371/journal.pone.0158884
- Nair, D., Hossy, E., Petersen, J. D., Constals, A., Giannone, G., Choquet, D., et al. (2013). Super-resolution imaging reveals that AMPA receptors inside synapses are dynamically organized in nanodomains regulated by PSD95. *J. Neurosci.* 33, 13204–13224. doi: 10.1523/JNEUROSCI.2381-12.2013
- Nicovich, P. R., Owen, D. M., and Gaus, K. (2017). Turning single-molecule localization microscopy into a quantitative bioanalytical tool. *Nat. Protoc.* 12, 453–460. doi: 10.1038/nprot.2016.166
- Nieves, D. J., Gaus, K., and Baker, M. A. B. (2018). DNA-based super-resolution microscopy: DNA-PAINT. *Genes* 9:E621. doi: 10.3390/genes9120621
- Nusser, Z., Cull-Candy, S., and Farrant, M. (1997). Differences in synaptic GABA_A receptor number underlie variation in GABA mini amplitude. *Neuron* 19, 697–709. doi: 10.1016/s0896-6273(00)80382-7
- Nusser, Z., Hájos, N., Somogyi, P., and Mody, I. (1998). Increased number of synaptic GABA_A receptors underlies potentiation at hippocampal inhibitory synapses. *Nature* 395, 172–177. doi: 10.1038/25999
- Patriarchi, T., Buonarati, O. R., and Hell, J. W. (2018). Postsynaptic localization and regulation of AMPA receptors and Cav1.2 by β 2 adrenergic receptor/PKA and Ca²⁺/CaMKII signaling. *EMBO J.* 37:e99771. doi: 10.15252/embj.201899771
- Patrizio, A., Renner, M., Pizzarelli, R., Triller, A., and Specht, C. G. (2017). Alpha subunit-dependent glycine receptor clustering and regulation of synaptic receptor numbers. *Sci. Rep.* 7:10899. doi: 10.1038/s41598-017-11264-3
- Pennacchietti, F., Vascon, S., Nieuws, T., Rosillo, C., Das, S., Tyagarajan, S. K., et al. (2017). Nanoscale molecular reorganization of the inhibitory postsynaptic density is a determinant of gabaergic synaptic potentiation. *J. Neurosci.* 37, 1747–1756. doi: 10.1523/jneurosci.0514-16.2016
- Perez de Arce, K., Schrod, N., Metzbower, S. W. R. R., Allgeyer, E., Kong, G. K. W., Tang, A. H., et al. (2015). Topographic mapping of the synaptic cleft into adhesive nanodomains. *Neuron* 88, 1165–1172. doi: 10.1016/j.neuron.2015.11.011
- Rodriguez, P. C., Almeida, L. G., and Triller, A. (2017). Continuous rearrangement of the postsynaptic gephyrin scaffolding domain: a super-resolution quantified and energetic approach. *BioRxiv* [Preprint]. 33. doi: 10.1101/193698
- Rust, M. J., Bates, M., and Zhuang, X. (2006). Sub-diffraction-limit imaging by stochastic optical reconstruction microscopy (STORM). *Nat. Methods* 3, 793–795. doi: 10.1038/nmeth929
- Santuy, A., Rodríguez, J.-R., DeFelipe, J., and Merchán-Pérez, A. (2018). Study of the size and shape of synapses in the juvenile rat somatosensory cortex with 3d electron microscopy. *eNeuro* 5:ENEURO.0377-17.2017. doi: 10.1523/eneuro.0377-17.2017
- Scheefhals, N., and MacGillavry, H. D. (2018). Functional organization of postsynaptic glutamate receptors. *Mol. Cell. Neurosci.* 91, 82–94. doi: 10.1016/j.mcn.2018.05.002
- Schermelleh, L., Heintzmann, R., and Leonhardt, H. (2010). A guide to super-resolution fluorescence microscopy. *J. Cell Biol.* 190, 165–175. doi: 10.1083/jcb.201002018
- Sheng, M., and Kim, E. (2011). The postsynaptic organization of synapses. *Cold Spring Harb. Perspect. Biol.* 3:a005678. doi: 10.1101/cshperspect.a005678
- Shinohara, Y., Hirase, H., Watanabe, M., Itakura, M., Takahashi, M., and Shigemoto, R. (2008). Left-right asymmetry of the hippocampal synapses with differential subunit allocation of glutamate receptors. *Proc. Natl. Acad. Sci. U S A* 105, 19498–19503. doi: 10.1073/pnas.0807461105
- Sieben, C., Douglass, K. M., Guichard, P., and Manley, S. (2018). Super-resolution microscopy to decipher multi-molecular assemblies. *Curr. Opin. Struct. Biol.* 49, 169–176. doi: 10.1016/j.sbi.2018.03.017
- Specht, C. G. (2019). Fractional occupancy of synaptic binding sites and the molecular plasticity of inhibitory synapses. *Neuropharmacology* doi: 10.1016/j.neuropharm.2019.01.008 [Epub ahead of print].
- Specht, C. G., Izeddin, I., and Dahan, M. (2014). “Visualizing the ultrastructures and dynamics of synapses by single-molecule nanoscopy,” in *Nanoscale Imaging of Synapses. Neuromethods, Vol 84*, eds U. V. Nägerl and A. Triller (New York, NY: Humana Press), 75–91.
- Specht, C. G., Izeddin, I., Rodríguez, P. C., El Beheiry, M., Rostaing, P., Darzacq, X., et al. (2013). Quantitative nanoscopy of inhibitory synapses: counting gephyrin molecules and receptor binding sites. *Neuron* 79, 308–321. doi: 10.1016/j.neuron.2013.05.013
- Sugiyama, Y., Kawabata, I., Sobue, K., and Okabe, S. (2005). Determination of absolute protein numbers in single synapses by a GFP-based calibration technique. *Nat. Methods* 2, 677–684. doi: 10.1038/nmeth783
- Tang, A. H., Chen, H., Li, T. P., Metzbower, S. R., MacGillavry, H. D., and Blanpied, T. A. (2016). A trans-synaptic nanocolumn aligns neurotransmitter release to receptors. *Nature* 536, 210–214. doi: 10.1038/nature19058
- Tarusawa, E., Matsui, K., Budisantoso, T., Molnar, E., Watanabe, M., Matsui, M., et al. (2009). Input-specific intrasynaptic arrangements of ionotropic glutamate receptors and their impact on postsynaptic responses. *J. Neurosci.* 29, 12896–12908. doi: 10.1523/JNEUROSCI.6160-08.2009

- Turkowsky, B., Virant, D., and Endesfelder, U. (2016). From single molecules to life: microscopy at the nanoscale. *Anal. Bioanal. Chem.* 408, 6885–6911. doi: 10.1007/s00216-016-9781-8
- van de Linde, S., Löschberger, A., Klein, T., Heidbreder, M., Wolter, S., Heilemann, M., et al. (2011). Direct stochastic optical reconstruction microscopy with standard fluorescent probes. *Nat. Protoc.* 6, 991–1009. doi: 10.1038/nprot.2011.336
- Wegner, W., Mott, A. C., Grant, S. G. N., Steffens, H., and Willig, K. I. (2018). *In vivo* STED microscopy visualizes PSD95 sub-structures and morphological changes over several hours in the mouse visual cortex. *Sci. Rep.* 8:219. doi: 10.1038/s41598-017-18640-z
- Yang, X., and Specht, C. G. (in press). “Practical guidelines for two-color SMLM of synaptic proteins in cultured neurons,” in *Single Molecule Microscopy in Neurobiology*, eds Y. Okada and N. Yamamoto (New York, NY: Humana Press).
- Zanacchi, F. C., Manzo, C., Alvarez, A. S., Derr, N. D., Garcia-Parajo, M. F., and Lakadamyali, M. (2017). A DNA origami platform for quantifying protein copy number in super-resolution. *Nat. Methods* 14, 789–792. doi: 10.1038/nmeth.4342

Conflict of Interest Statement: The authors declare that the research was conducted in the absence of any commercial or financial relationships that could be construed as a potential conflict of interest.

Copyright © 2019 Yang and Specht. This is an open-access article distributed under the terms of the Creative Commons Attribution License (CC BY). The use, distribution or reproduction in other forums is permitted, provided the original author(s) and the copyright owner(s) are credited and that the original publication in this journal is cited, in accordance with accepted academic practice. No use, distribution or reproduction is permitted which does not comply with these terms.

RÉSUMÉ

La microscopie optique stochastique de reconstruction (STORM) contourne la limite de diffraction en enregistrant des signaux monomoléculaires spatialement et temporellement séparés, atteignant une résolution de ~10-40 nm. Dans mon étude, j'ai développé une stratégie d'imagerie et d'analyse de données dSTORM bicolore afin d'étudier l'ultrastructure des synapses inhibitrices mixtes. Mes résultats ont montré que les GlyRs, les GABA_ARs, la géphyrine et RIM1/2 présentent une organisation intra-synaptique hétérogène et forment des domaines sous-synaptiques (SSDs). Les GlyR et les GABA_AR ne sont pas complètement mélangés, mais peuvent occuper des espaces différents à la densité post-synaptique (PSD). De plus, les SSD de géphyrine post-synaptique sont alignées avec les SSD de RIM1/2 pré-synaptiques, formant des nanocolonnes trans-synaptiques. Au cours d'une activité neuronale élevée par traitement 4-AP, la corrélation spatiale entre les GlyRs, les GABA_ARs et la géphyrine a augmentée au PSD. De plus, la corrélation spatiale des GlyRs et RIM1/2 a également augmenté, tandis que celle des GABA_ARs et RIM1/2 n'a pas changé. Le nombre de SSD par synapse pour ces protéines synaptiques n'est pas modifié par 4-AP. Cette étude fournit un nouvel angle de compréhension des mécanismes sous-jacents à la co-transmission GABAergique/glycinergique.

MOTS CLÉS

Synapses inhibitrices mixtes, GlyR, GABA_AR, géphyrine, RIM1/2, co-transmission, domaine sous-synaptique (SSD), nanocolonne trans-synaptique, microscopie de localisation de molécule unique (SMLM), microscopie de reconstruction optique stochastique directe (dSTORM), dSTORM multi-couleur.

ABSTRACT

Stochastic optical reconstruction microscopy (STORM) bypasses the diffraction limit by recording spatially and temporally separated single molecule signals, achieving a resolution of ~10-40 nm. In my study, I have developed a two-color dSTORM imaging and data analysis strategy, in order to investigate the ultrastructure of mixed inhibitory synapses. My results show that GlyRs, GABA_ARs, gephyrin and RIM1/2 exhibit a heterogeneous intra-synaptic organization and form sub-synaptic domains (SSDs). GlyRs and GABA_ARs were not fully intermingled, but sometimes occupied different spaces at the post-synaptic density (PSD). In addition, post-synaptic gephyrin SSDs were aligned with pre-synaptic RIM1/2 SSDs, forming trans-synaptic nanocolumns. During elevated neuronal activity by 4-AP treatment, the spatial correlation between GlyRs, GABA_ARs and gephyrin was increased at the PSD. Moreover, the spatial correlation of GlyRs and RIM1/2 was also increased, while that of GABA_ARs and RIM1/2 did not change. The number of SSDs per synapse for these synaptic proteins was not changed by 4-AP. My study thus provides a new angle for understanding the mechanisms underlying GABAergic/glycinergic co-transmission.

KEYWORDS

Mixed inhibitory synapses, GlyR, GABA_AR, gephyrin, RIM1/2, co-transmission, subsynaptic domain (SSD), trans-synaptic nanocolumn, single molecule localization microscopy (SMLM), direct stochastic optical reconstruction microscopy (dSTORM), multi-color dSTORM.